A dissertation submitted to

MONDRAGON UNIBERTSITATEA

for the degree of

Doctor of Philosophy

MODELING FOR HARMONIC ANALYSIS OF AC OFFSHORE WIND POWER PLANTS

Author:

CARLOS RUIZ RODRIGUEZ

Supervisor:

GONZALO ABAD BIAIN

Mondragon Unibertsitatea

Department of Electronics and Informatics

Mondragon Unibertsitatea

December 2019

Abstract

This Ph.D. dissertation presents the work carried out on the modeling, for harmonic analysis, of AC offshore wind power plants (OWPP). The studies presented in this Ph.D. thesis are oriented to two main aspects regarding the harmonic analysis of this type of power system.

The first aspect is the modeling and validation of the main power components of an AC offshore wind power plant. Special emphasis is focused on the modeling of wind turbines, power transformers, submarine cables, and the interaction between them.

A proposal of a wind turbine harmonic model is presented in this dissertation to represent the behavior of a wind turbine and its harmonics, up to 5 kHz. The distinctive structure of this model consists of implementing a voltage source containing both the fundamental component and the harmonics emitted by the converter. For the case of transformer and submarine cables, the frequency-dependent behavior of certain parameters is modeled for frequencies up to 5 kHz as well. The modeling of the frequency-dependent characteristics, due to skin and proximity effect, is achieved by means of Foster equivalent networks for time-domain simulations.

Regarding the interaction between these power components, two complementary modeling approaches are presented. These are the Simulink®-based model and an analytical sequence network model of the passive components of the OWPP. A description of model development and parameterization is carried out for both modeling approaches considering a scenario that is defined according to a real offshore wind power plant.

On the other hand, the second aspect of this Ph.D. thesis is oriented to the analysis of the issues that appear in offshore wind power plants in relation to harmonic amplification risk, compliance of grid codes in terms of harmonics and power factor, and the design of effective solutions to improve the harmonic emission of the facility. The technical solutions presented in this Ph.D. thesis cover aspects regarding modulation strategies, design of the connection filter of the grid side converter and management of the operation point of the grid side converter of wind turbines. This last by means of changing the setpoint of certain variables. As inferred, these are solutions from the perspective of the wind turbine manufacturer.

Acknowledgements

Dedicated to My Parents,

María Rodríguez Rodríguez and Sergio Ruiz Amaya,

To whom I owe everything.

Acronyms

AC	Alternate Current
AIS	Air-Insulated Switchgear
APLC	Active Power Line Conditioner
APOD	Alternative Phase Opposite Disposition
CB-PWM	Carrier-Based PWM
CC	Cable Constants
CCM	Component Connection Method
CFD	Computational Fluid Dynamics
CHB	Cascaded H-Bridge
CP	Collection Point
DC	Direct Current
DFT	Discrete Fourier Transform
DHM	Dynamic Hysteresis Model
EMT	Electromagnetic Transient
EMTP	Electromagnetic Transient Program
EMTS	Electromagnetic Transient Simulation
FC	Flying Capacitor
FD	Frequency-Dependent
FDPi	Frequency-Dependent Pi
FEM	Finite Element Method
FRT	Fault Ride Through
GIS	Gas-Insulated Switchgear
GMTRAN	Geometric Mean Transformer
GSC	Grid Side Converter
GWEC	Global Wind Energy Council
HV	High Voltage
HVAC	High Voltage Alternate Current

HVDC	High Voltage Direct Current
HVRT	High Voltage Ride Through
IEC	International Electrotechnical Committee
IEEE	Institute of Electrical and Electronics Engineers
IGBT	Insulated Gate Bipolar Transistor
IPD	In-Phase Disposition
JA	Jiles-Atherton
KCL	Kirchoff Current Law
KVL	Kirchoff Voltage Law
LCC	Line Commutated Converter
LPF	Low Pass Filter
LS-PWM	Level-Shifted PWM
LV	Low Voltage
LVRT	Low Voltage Ride Through
MAF-PLL	Moving Average Filter PLL
MMC	Modular Multilevel Converter
MMF	Magnetomotive Force
MoM	Method of Moments
MPPT	Maximum Power Point Tracking
MV	Medium Voltage
OPP-PWM	Optimal Pulse Pattern PWM
OST	Offshore Substation Transformer
OWPP	Offshore Wind Power Plant
PCC	Point of Common Coupling
PI	Proportional-Integral
PLL	Phase Locked Loop
PMSG	Permanent Magnet Synchronous Generator
POD	Phase Opposite Disposition
PS-PWM	Phase-Shifted PWM
PWM	Pulse Width Modulation
SCADA	Supervisory Control and Data Acquisition

SCIG	Squirrel Cage Induction Generator
SCR	Short Circuit Ratio
SDFT	Sliding Discrete Fourier Transform
SHE-PWM	Selective Harmonic Elimination PWM
SHM-PWM	Selective Harmonic Mitigation PWM
SPWM	Sine PWM
STC	Saturable Transformer Component
THD	Total Harmonic Distortion
TRMS	True Root Mean Square
TRV	Transient Recovery Voltage
ULM	Universal Line Model
UMEC	Unified Magnetic Equivalent Circuit
UPQC	Unified Power Quality Conditioner
VF	Vector Fitting
VSC	Voltage Source Converter
WECC	Western Electricity Coordinating Council
WRSG	Wound Rotor Synchronous Generator
WT	Wind Turbine
WTT	Wind Turbine Transformer
XLPE	Cross-Linked Polyethylene
3L-NPC	Three-Level Neutral Point Clamped

Contents

Chapter 1

Introduction

This chapter gives a general perspective of the aspects that motivate the formulation of this Ph.D. thesis. The main objective and tasks of the Ph.D. thesis are presented. Finally, an outline of the document is presented.

1.1 Offshore Market Status 2018

According to the Global Wind Energy Council (GWEC), the global cumulative installed wind power capacity in 2018 was 23.1GW [1]. The current share of the total global offshore installations represents the 4% of the total 591 GW of wind capacity (onshore and offshore) installed [1]. By 2025, the share is expected to exceed 10% according to the forecast of the GWEC.

Fig. 1.1 shows the evolution of the global cumulative offshore wind capacity from year 2011 until 2018. From the 23.1 GW of installed offshore wind power capacity, United Kingdom has the 34% of this capacity, followed by Germany with the 28%, then China with a 20%, and the remaining 18% is installed in different countries around the world [1,2].

Globally, 4.5 GW of new offshore wind power was installed only in 2018 [1]. For the first time, China installed and connected more offshore capacity (1.8 GW) than any other country. The United Kingdom took the second place with 1.3 GW and Germany third place with 0.9 GW. The remaining capacity (0.5 GW) was installed in different countries around the world.
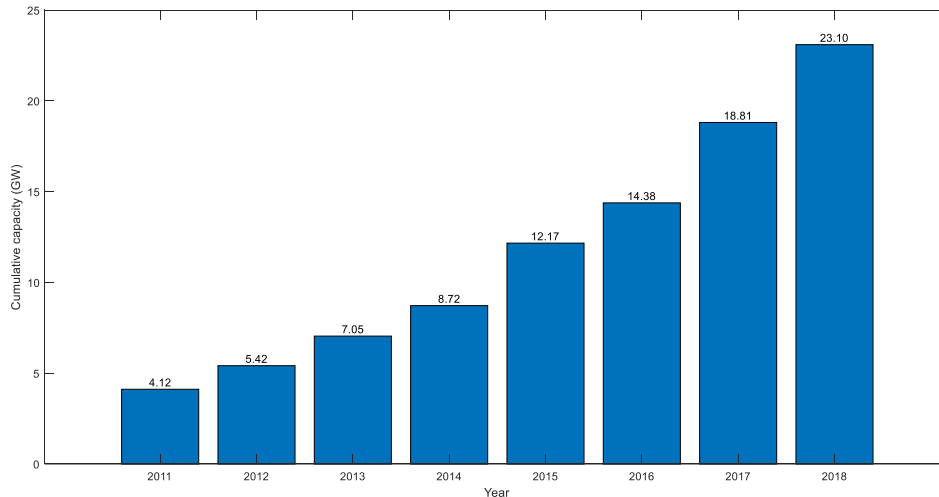
Fig. 1.1. Global cumulative offshore wind capacity (2011 to 2018). Source [1].

Offshore wind technology continues to advance

During 2018, the trend for larger offshore turbines continued. Following next, some key data supporting this trend [1,2]:

- General Electric had already introduced its Haliade X 12MW offshore turbine in 2017, expected to be commercially operational as of 2024/25.
- In 2018, MHI Vestas upgraded its turbine to 10 MW to be used for several projects in Netherlands, United Kingdom and the Vineyard project in USA.
- Goldwing introduced an 8-MW turbine for projects on the south east coast of China.
- Siemens Gamesa's 10 MW turbine is expected to be online by 2022.

1.2 Framework

The study of harmonics is of special interest in the case of OWPPs because of the special sensibility of this type of system to harmonic problems [3–5]. Some of the characteristics that make them susceptible to harmonic problems are given next.

- There is a high number of power converters that act as harmonic sources and contribute to the overall harmonic generation of the OWPP [5].
- Resonance problems become significant [3] in this type of system since they approach the low frequency range (few hundreds of Hertz).
- Due to passive components, e.g. the capacitance of long submarine cable and the inductance of transformers, series and parallel resonances occur. These resonances may either increase or decrease a given voltage or current harmonic.

2

- Low frequency resonances might overlap with the increasing bandwidth of power electronic converters, leading to possible harmonic instabilities if it is not properly addressed [6].

On top of that, not only OWPPs are susceptible to harmonic events, but certain characteristics of these systems vary with respect to other power generation systems. For example:

- Switching frequencies of power converters oriented to offshore applications are lower than other power converters, e.g. in distribution system scenarios. This is done to reduce power losses.
- The design of filters with lower cut-off frequencies and thus lower resonant frequencies.
- As the stability region is much related to the sampling frequency in power converters with LCL filters [7], the reduction of the switching frequency might indirectly affect the stability region of the converters.

The main effects of harmonics in OWPPs are [5]:

- Reduction in the efficiency of the generation and transmission of electric energy.
- Possibility of amplification of voltage and current harmonics as a consequence of series and parallel resonances.
- Control malfunction and possible loss of stability.
- Premature aging of system components (e.g. insulation being affected by voltage and/or temperature).
- Malfunctioning of protection systems, leading to the possible disconnection of feeders and the entire OWPP.

As a consequence of the previous characteristics and effects, harmonic studies of OWPPs are a key concern of the offshore wind industry, research centers and academia.

1.2.1 Modeling Guidelines for Harmonic Simulations in OWPPs

The evaluation of harmonics in power systems is halfway between electromagnetic transient simulations (EMTS) and RMS simulations [8], see Fig. 1.2.
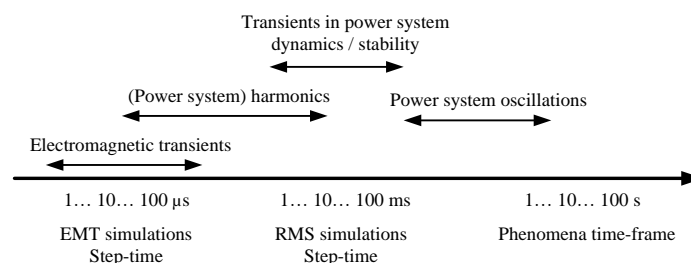
Fig. 1.2. Time-frame of different phenomena to be considered in modeling procedure and simulation of electrical phenomena. Source [8].

It is commonly accepted that power quality from harmonic perspective is investigated during steady-state operation [5].

To account for an appropriate harmonic assessment of an OWPP, it is required to consider three important factors in the modeling [9]. First, an accurate representation of the harmonics injected by the wind turbines. Second, the frequency-dependent characteristic of installed passive components, e.g. submarine cables and transformers. The third factor to consider is the evaluation of different operation points for each wind turbine. These operation points depend on wind conditions, wind farm layout, and requirements given by the grid operator (e.g. power factor requirements). Following these three factors, the core ideas of the modeling guidelines of the main power components of OWPPs are briefly covered next.

Modeling Guidelines of Main Power Components

Main modeling guidelines of wind turbines for harmonic simulations are given next.

- Conventional EMT models proposed for WTs are usually complex, highly detailed and generally confidential. The complexity of those models many times presents big constraints to analyze large power systems in terms of lack of information (provided by the manufacturer) and computational load.
- Due to the different approaches in electrical design taken by wind turbine manufacturers, it is convenient to represent the harmonics injected by the WT in a generic way. This is by means of a Thevenin or a Norton equivalent circuit. The equivalent circuit is to be provided for each harmonic component of interest to be included in the model. These recommendations are given by Dr. Lukasz Kocewiak and are summarized in Table 1.1 [10].

Table 1.1. Modeling guidelines for the wind turbine harmonic model. Source [10].

Representation	Description
Equivalent harmonic source	• Magnitude and phase angle of the spectral components must be represented for the frequency range of interest. • It is represented by an equivalent voltage or current source.
Equivalent impedance	• The equivalent impedance should include not only passive components of the wind turbines but also the grid side converter internal impedance given by the control scheme and operation point. • The equivalent impedance must be represented for the frequency range of interest as well.

Some key modeling guidelines of submarine cables and power transformers are given next.

- CIGRE Working Group (WG) 33-02 covers the representation of the most important power components taking into account the frequency range of the transient phenomena to be simulated [11].
- IEEE WG on modeling and analysis of system transients using digital programs and its task forces give modeling guidelines for several particular types of studies [12].

Table 1.2 provides a summary of modeling guidelines for the representation of submarine cables and power transformer according to the frequency range of interest [13].

Table 1.2. Modeling guidelines for power transformers and cables according to the frequency range of interest. Source [13].

Power Component	Frequency Range	
Transformer	**0.1 Hz to 3 kHz**	**50/60 Hz to 20 kHz**
	• Models must incorporate saturation effects, as well as core and winding losses. • Capacitive coupling can be neglected.	• Models must incorporate saturation effects, as well as core and winding losses. • Capactive coupling is important only for surge transfer.
	10 kHz to 3 MHz	**100 kHz to 50 MHz**
	• Core losses and saturation can be neglected. • Coupling between phases is mostly capacitive. • The influence of the short-circuit impedance is very important.	• Core losses and saturation can be neglected. • Coupling between phases is mostly capacitive. • The model should incorporate the surge impedance of the windings.
Cable	**0.1 Hz to 3 kHz**	**50/60 Hz to 20 kHz**
	• Multiphase model with lumped and constant parameters, including conductor asymmetry. • Frequency-dependence can be important for the ground mode propagation.	• Multiphase model with distributed parameters, including conductor asymmetry. • Frequency-dependence of parameters is important. • Frequency-dependent model in modal domain can be adopted. • Frequency-dependent model in phase domain can be used as well, Universal Line Model (ULM).
	10 kHz to 3 MHz	**100 kHz to 50 MHz**
	• Multiphase model with distributed parameters. • Frequency-dependence of parameters is very important. • ULM can be used to represent the behavior of the cable.	• Single-phase model with distributed parameters. • Frequency-dependence of parameters is important.

In general, the effects that have to be represented in submarine cables and transformers are:

- Electromagnetic fields: The effects of the electromagnetic fields are generally represented using a circuit approach. Magnetic field effects are modeled by means of inductors and coupling between them. On the contrary, electric field effects are represented by capacitors.

- Losses: Approaches that can be used to represent this effect include resistor(s) that can be linear, non-linear, or equivalent networks that consists of passive elements (resistors, inductors and capacitors). The last approach is generally used to include the frequency-dependent effect of a parameter in time-domain simulations. The frequency-dependent behavior in submarine cables and power transformers is consequence of skin- and proximity effect.

Modeling Parameterization in Specialized Software Tools

Table 1.3 shows the studied power system simulation tools and a brief description of the different approaches for the determination of the electrical parameters of the available models.

Table 1.3. Modeling options in current simulation tools for the power components analyzed in this Ph.D. thesis.

Power Component	Simulation Tools	Status of Simulation Tools (to date)
Wind Turbine	PSS-E [14] PSCAD [15] PSLF [16] TSAT [17] PowerWorld [18]	• For some of these simulation tools (PSS, PowerWorld, PSLF and TSAT) there are generic wind turbine models for different types of wind turbines. In addition, there are manufacturer specific wind turbine models that may be downloaded. • The model parameterization is simple for the generic wind turbine models. Guidelines regarding this aspect can be found in the WECC/IEC standards. • PSCAD offers many examples and ready-to-use models for wind turbine simulations.
Transformers	ATP-EMTP [19] EMTP-RV [20] PSCAD [15] PowerFactory [21]	• A supporting routine is usually available in most transient tools to obtain an unsaturated transformer model from nameplate data. • Fitting routines have been also implemented in some tools to obtain unsaturated high-frequency models from frequency response data. • Parameters for low- and mid frequency models are usually derived from nameplate data or standard tests and anhysteretic curve provided by the manufacturer. • There are, however, transformer models whose parameters cannot be derived from nameplate information only. • Users can also consider the possibility of estimating parameters from typical transformer geometry and physical properties.
Cables		• Electrical parameters are determined (as a function of frequency) from the cable geometry and from the physical properties of the different layers (conductor, insulation, screens, armour) of the cable. • Cable parameters are usually obtained by means of supporting routines, generally called Cable Constants (CC) routines. • CC routines are implemented in most transient simulation tools. Some software tools only consider some cable arrangements and types of cables. For those tools, specific routines must be done.

Up to now, Simulink® Power System Toolbox has not included models, at least in its library of models, that account for the frequency-dependent representation of submarine cables and power transformers. The reader is suggested to review reference [22] for detailed information on the power library components of Simulink® Power System Toolbox.

Generally, power system simulation tools (described in Table 1.3) do not include models to represent the wind turbine wake. To evaluate the impact of the wake effect in an OWPP, some commercial software tools have been studied in order to gain knowledge and compare some wake models. Table 1.4 shows the studied simulation tools and a brief description of their mean features.

Table 1.4. Simulation tools to represent the wake effect.

Phenomenon	Simulation Tools	Status of Simulation Tools (to date)
Wake Effect	WindPro [23] – WasP [24] WindSim [25] WindFarm [26]	• These simulation tools include a set of wake effect models for the estimation of energy production, turbulence modeling, wind farm layout optimization, and other studies. • Software intended for project design and planning of both single WT and large wind power plants (onshore and offshore). • Input variables are dependant on the type of model that is implemented. It is common for all of them to specify physical turbine parameters such as turbine diameter, hub height, thrust coefficient, location of each turbine, wind speed and direction, etc.

IEC Standards

Table 1.5 shows a recompilation of the most remarkable IEC standards of the power components studied in this Ph.D. thesis.

Table 1.5. Recopilation of the most remarkable IEC standards of the power components covered in this Ph.D. thesis.

Power Component	IEC Standards
Wind Turbine	**IEC 61400-3** Design requirements for offshore wind turbines, 2009.
	IEC 61400-12-1 Power performance measurements of electricity producing wind turbines, 2005.
	IEC 61400-21 Measurement and assessment of power quality characteristics of grid connected wind turbines, 2008.
	IEC 61400-27-1 Electrical simulation models of wind turbines, 2015.
Cable	**IEC 60228** Conductors of insulated cables, 2004.
	IEC 60287-X Electric cables. Calculation of the current rating, 2001.
Transformer	**IEC 60076-X** Power transformers, 2004.
	IEC 60079-16 Transforrmer for Wind Turbine Applications

1.2.2 Key References covering Harmonic Studies in OWPPs

The following is a brief summary of some key references, covering harmonic studies in OWPPs.

Doctoral Theses

- Reference [5] performed a measurement data analysis and deep study of harmonics in large offshore wind farms.
- Reference [27] covers the development of an evaluation and simulation methodology to define the most suitable layout depending on the size and location of each wind farm.
- Refence [28] covers methods and models to perform harmonic studies of wind power installations in a systematic way.

- Reference [29] developed and validated models of the power electronic converters, including the modular multi-level cascaded converter (MMCCs) for wind power integration (HVDC and STATCOM). This reference also developed a practice for harmonic stability assessment in OWPPs.

Papers

- Reference [30] performed a study with an equivalent model for an offshore WPP. Each section of cable is modeled as a lumped Pi model, which connects the sending end voltage and current with the receiving end voltage and current. The model of the collection grid is further reduced mathematically to become an equivalent model. The harmonic distortion is next obtained using this model.
- Reference [31] analyzed the parallel resonance phenomenon. The paper explores this phenomenon in wind parks and provides analytical expressions to determine parallel resonances.
- Reference [32] studied the resonances obtained from a system modeling. Parallel and series resonances are shown to occur at frequencies around a few hundred Hz. The paper also proposes a damping method with cascaded notch-filter to limit the peak values at the lower frequency resonances.
- Reference [33] contributed with expressions of WT equivalent harmonic impedance including current control of the grid side converter. The paper studied the effect of wind turbine converter control on wind power plant harmonic response and resonances.
- Following the same line, reference [34] investigated the interaction between the wind turbine control system and the wind farm structure in offshore wind farms.

1.2.3 Identified Guidelines for Potential Improvements

In references [5,6], some potential improvements have been pointed out and serve as input for this Ph.D. thesis. These are:

- Current industry practice relies on WT models provided by manufacturers. These models might be provided only for the rated power point, and it is not always clear how complete they are. In other words, if they include the PLL effects, the saturation of PI controllers, and other control logics and effects. Further, as these models are provided as black boxes, wind power plant developers do not have deep insights into the system.
- Corrective measures commonly imply the installation of passive components. However, solutions to face the potential harmonic problems from the perspective of the wind turbine manufacturer can be more advantageous in terms of efficiency, costs, and effectiveness. Examples of these wind turbine manufacturer oriented solutions are advanced control loops and appropriate tuning of controllers, implementation of modulation schemes that reduce the harmonic emission of WTs and of the entire OWPP, and others.

- Some factors introduce coupling terms between the sequence-networks in OWPPs [35]. The proximity effect and flat formation installation of three-phase single-core submarine cables are some examples of these factors. Thus, the fact the harmonic study is only performed with one-phase positive-sequence equivalent might compromise the accuracy of the method. Further studies need to be done to justify the approximation or to include the information of other sequences for appropriate harmonic studies.

1.2.4 Electrical Configuration Alternatives of OWPPs

Table 1.6 presents the alternatives of the electrical configuration of an OWPP together with an indication of which combinations are existing solutions and possible future solutions [36].

Table 1.6. Offshore wind power plants connection alternatives. Source [36].

OWPP connection alternatives		Collection Network	
		AC	DC
Transmission Link	AC	Common today	Unlikely option
	DC	Likely to become common	Possible future option

Current OWPPs have an AC collection network and depending on the transmission distance and power (mainly), the power is transferred through High-Voltage Alternating-Current (HVAC) or High-Voltage Direct-Current (HVDC).

According to the status of OWPP connection alternatives (Table 1.6), the studies carried out within the framework of this Ph.D. thesis are performed to OWPPs with AC collection networks and HVAC transmission links.

An overview of the electrical system of OWPPs is presented in chapter 2 of this dissertation.

1.3 Objectives

The main objective of this Ph.D. thesis is to increase the knowledge about AC offshore wind power plants. This increase of knowledge is oriented to the compliance of grid codes in terms of harmonics and power factor, and the design of effective solutions oriented to improve these aspects from the perspective of the wind turbine manufacturer. This goal is obtained by means of developing tools oriented to model the behavior of an offshore wind power plant.

In order to achieve the main goal, some tasks are defined below.

- Modeling and validation of the main power components of an offshore wind power plant. Special emphasis is focused on the modeling of wind turbines, power transformers and submarine cables, considering also the interaction between them,

or in other words, their global behavior. The modeling of wind turbines considers the injection of harmonics up to 5 kHz. For the case of transformers and submarine cables, the frequency-dependent behavior of certain parameters are modeled for frequencies up to 5 kHz as well.

- Definition of an offshore wind power plant base scenario according to information of a real offshore wind farm.

- Development of a Simulink-based model of the offshore wind power plant base scenario accounting for the models of the main power components, adopted or proposed, in task 1.

- Development of a sequence-network model (implemented in a *.m-file in Matlab®) of the passive elements of the offshore wind power plant in order to obtain the frequency response and be able to perform additional studies. Among these studies are the evaluation of changes in the frequency response when varying the electrical parameters of the main power components and when considering an OWPP with an asymmetrical layout.

- Analysis and evaluation of the issues that appear in offshore wind power plants in relation to harmonic amplification risk and the compliance of the grid codes in terms of harmonics.

- Design of technical solutions oriented to improve the aspects evaluated in previous task. The technical solutions addressed in this Ph.D. thesis cover aspects regarding modulation strategies, management of the operation point of wind turbines by means of changing the setpoint of certain variables, and the design of the GSC connection filter. As stated in the main goal, these are solutions from the perspective of the wind turbine manufacturer.

1.4 Contributions

At the end of the work carried out in this Ph.D. thesis, three main contributions can be highlighted. These are:

- A proposal of a wind turbine harmonic model that serves as a generic simulation tool for stakeholders within the wind power industry, to conduct harmonic studies and evaluate grid code compliance of a wind power plant (onshore and offshore) from the power quality perspective. Especially, this wind turbine harmonic model is intended to be used during the design stage of the wind power plant.

- The modeling of an entire offshore wind power plant to conduct harmonic studies and evaluate grid code compliance from the power quality perspective. The main power components are modeled to represent harmonics up to 5 kHz. This contribution results in several tools developed in Matlab®/Simulink® environment. Among these tools are: the Simulink®-based model of each power

component (wind turbine, power transformer, and submarine cable) and the OWPP, the sequence-network model of the passive components (grid side connection filter, power transformers, and submarine cables) of the OWPP in a *.m-file in Matlab®, the wake effect tool and the routines to parameterize the different main power components.

- Wind turbine manufacturer oriented solutions are proposed with the aim of improving the harmonic emission of an OWPP. A comparison of two modulation strategies, the typical Carrier-Based Pulse Width Modulation (CB-PWM) and the synchronous Selective Harmonic Elimination (SHE-PWM), is evaluated for an OWPP case scenario having a resonance at a low frequency value. The implementation of the particular solution of SHE-PWM modulation is presented together with complementary solutions to further improve the harmonic emission of the OWPP with this type of modulation strategy. Among these complementary solutions are the redesign of the grid side connection filter and the management of the operation point, i.e. amplitude modulation index and phase shift (between converter output voltage and grid voltage). This last solution is performed by means of changing the DC-link voltage setpoint of the grid side converter of each wind turbine, the reactive power setpoint of each wind turbine, or a combination of both strategies.

As a result of this Ph.D. thesis, one journal paper and a conference paper have been accepted. These scientific contributions are detailed in subsection 10.2.

1.5 Thesis outline

The document is divided into ten chapters. To give an overview of the document, a short outline is presented below.

Chapter 1: A brief description of the background is presented and the objectives of this Ph.D. thesis are detailed.

Chapter 2: The aim of this chapter is to provide an overview of the electrical system of AC offshore wind power plants.

Chapter 3: The development of a wind turbine harmonic model for harmonic analysis in power systems is covered in this chapter. For that purpose and based on generic wind turbine models, some changes and the implementation of additional structures are proposed to represent the harmonic emission of WTs for harmonics up to 5 kHz.

Chapter 4: This chapter briefly describes the best-known models of wind turbine wakes. Jensen's wake model is chosen to determine the mean wind speed at each wind turbine according to the spatial distribution of the OWPP and wind conditions.

Chapter 5: A Frequency-Dependent STC model of a three-phase two-winding transformer is presented in this chapter. The model is developed to represent the frequency-dependent behavior of some parameters for frequencies up to 5 kHz. The transformer model includes four main parameters. These are the frequency-dependent behavior of the winding resistance, the impedance of the transformer core, stray capacitances and the zero-sequence impedance.

Chapter 6: This chapter presents an alternative Frequency-Dependent Pi (FDPi) model that represents the steady-state and transients comprising frequencies up to 5 kHz. The model consists of cascaded FDPi sections, which incorporate both inductive coupling and the frequency-dependent characteristic of some series impedance terms of the conductive layers.

Chapter 7: Two complementary approaches to model an OWPP, the Simulink®-based model and an analytical sequence network model in state-space form, are covered in this chapter. A description of model development and parameterization is carried out for both modeling approaches. An OWPP base scenario is defined taking into account information of a real offshore wind power plant.

Chapter 8: The frequency response of an OWPP is studied in this chapter. Bode plots of transfer functions, relating voltage- and current variables of different points along the OWPP base scenario, are presented. A discussion about the risk of amplification of the harmonics injected by the WTs is performed according to the spectrums of the modulation strategies considered in this Ph.D. thesis, CB-PWM and SHE-PWM. Finally, changes in the frequency response of the OWPP base scenario are presented due to variation in electrical parameters of main power components and when considering an OWPP with an asymmetrical layout.

Chapter 9: The current-harmonic evaluation of an OWPP is presented in this chapter. The harmonic evaluation is performed by means of computing the spectrum of current signals, the total harmonic distortion (THDi) values, and the fulfillment of the BDEW grid code. Two main studies are done. First, the harmonic evaluation is performed by considering that wind turbines operate with the typical CB-PWM modulation. For this modulation strategy, the harmonic assessment is performed at wind turbine level and at OWPP level for several operation points. Second, WT manufacturer oriented solutions are proposed with the aim of improving the harmonic emission of the OWPP. The implementation of the particular solution of SHE-PWM modulation is presented together with complementary solutions to further improve the harmonic emission of the OWPP with this type of modulation strategy.

Chapter 10: Finally, conclusions and guidelines for future work are detailed.

Chapter 2

Overview of OWPP Electrical System

The aim of this chapter is to provide an overview of the electrical system of AC offshore wind power plants. First, a brief description of the main electrical components of an OWPP is carried out. Then, collection network topologies and transmission system technologies are described. Finally, typical grounding configurations in OWPPs are addressed, especially aspects describing the grounding of transformers, submarine cables, and grounding transformers.

2.1 Introduction

The interest in the use of offshore wind power is increasing considerably in the last years [3]. The main reason is that wind speed offshore is potentially higher than onshore, which leads to higher power production. Some countries promote the development of offshore wind power because it plays an important role in the national targets for reducing carbon dioxide (CO_2) emissions [2]. However, investment and maintenance costs for offshore wind power are much higher than those for onshore installations [3].

In offshore wind power plants (OWPPs), the power generated by wind turbines is collected through an inter-array connection, or collection network, to an offshore substation. This power is then transmitted to shore in either alternate current (AC) or direct current (DC)

form by means of a subsea transmission scheme. The transmission scheme sometimes consists of multiple links to increase the reliability of the installation.

The aim of this chapter is to provide an overview of the electrical system of offshore wind power plants. This chapter is structured as follows. Section 2.2 provides an overview of the main power components of OWPPs. These are wind turbines, transformers, submarine cables, and protection systems. Section 2.3 briefly describes the collection network topologies of OWPPs. Section 2.4 presents the transmission system technologies of OWPPs. Section 2.5 provides information about the typical grounding configurations in OWPPs. Finally, section 2.6 gives the chapter summary.

2.2   Main Power Components of OWPPs

The typical schematic of an OWPP is illustrated in Fig. 2.1. The wind turbines are connected to a medium-voltage (MV) collection network. This voltage is then step-up by a power transformer (located on the offshore platform) and transmitted to shore via submarine cables. Finally, the onshore substation adequates the voltage (if required) and provides special protection equipment to disconnect the OWPP from the power grid, due to a fault condition or maintenance.

Other types of equipment such as active and passive filtering, reactive power compensation and protections can be installed in different locations within the OWPP depending on factors such as security, harmonic mitigation, grid code requirements, maintenance, and others.
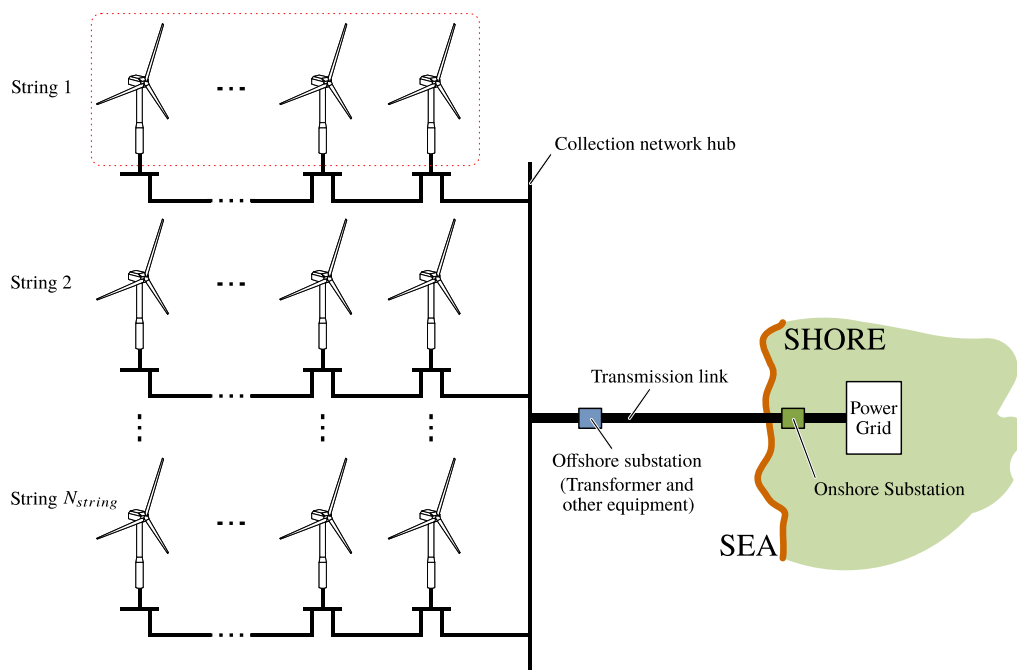
Fig. 2.1. Schematic of a typical Offshore Wind Power Plant.

The main power components of current OWPPs are briefly described below. It is worth to point out that state of the art modeling of wind turbines, power transformers and submarine cables is covered from chapter 3 to chapter 6. A description of the models used in this Ph.D. thesis is presented in these chapters.

2.2.1 Wind Turbines

There are four types of wind turbine configurations according to their ability to control speed [37]. These are:

- Type-1: Fixed speed wind turbine.
- Type-2: Partial variable speed wind turbine.
- Type-3: Variable speed wind turbine with reduced-capacity converter.
- Type-4: Variable speed wind turbine with full-capacity converter.

In general, the most commonly sold and installed technology in today's offshore market tends to be type-4 units [36]. In this sense, attention is focused on this type of wind turbine.

Fig. 2.2 shows the configuration of a type-4 wind turbine. In this configuration, the generator is connected to the grid via a full-capacity converter. With the use of the power converter, the generator is fully decoupled from the grid and can operate in full speed range. Squirrel Cage Induction Generator (SCIG), Wound Rotor Synchronous Generator (WRSG) and Permanent Magnet Synchronous Generator (PMSG) can be used for this type of configuration. The Three-Level Neutral Point Clamped (3L-NPC) converter is the most common converter topology of offshore wind turbines to date [4]. This type of wind turbine contains a chopper in the DC circuit to dissipate the generated power during grid faults. The grid side connection filter is required for power quality improvement in terms of harmonics.

The two main control functions of a type-4 wind turbine are the turbine control (or pitch-control) and the converter control [38,39], as depicted in Fig. 2.2.
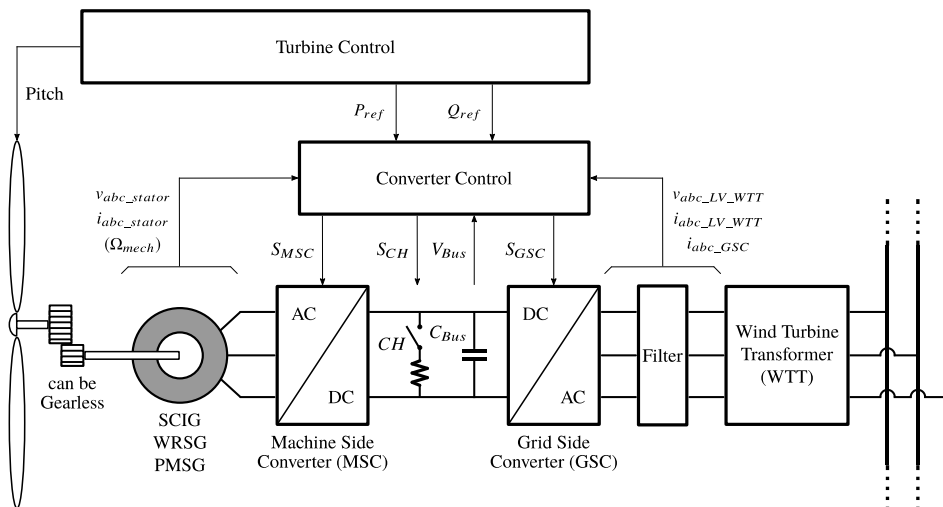
Fig. 2.2. Type-4 wind turbine schematic. Source [38].

Due to the configuration of this type of WT and the implemented control strategies, the main advantages of this type of wind turbine are [38]:

- The power extraction efficiency is increased with the addition of the full-capacity converter.
- Voltage- and frequency support and fault ride-through (FRT) capability can be provided by proper control of the converter.

The main disadvantage is the increased cost, due to the full-capacity converter, in comparison with other types of wind turbines [38]. Furthermore, it is a more complex system in comparison with type-1 and type-2 wind turbines.

Table 2.1 gives information about the manufacturer and power rating of WT models already operating in commissioned OWPPs.

Table 2.1. Wind turbines already operating in commissioned OWPPs. Source [36,40,41].

Manufacturer	Model	Power (MW)	Type of Generator
Vestas	V80/2000	2.0	DFIG
Siemens	SWT-2.3-82/93	2.3	SCIG
Winwind	WWD-3-100	3.0	PMSG
Sinovel	SL 3000/90	3.0	DFIG
Vestas	V90/3.0-Off	3.0	DFIG
Siemens	SWT-3.6-107	3.6	SCIG
Repower	5M	5.0	DFIG
Areva	M5000	5.0	PMSG
Siemens	SWT-6.0-120	6.0	PMSG
Alstom Power	Haliade 150	6.0	PMSG
Nordex	N150/6000	6.0	PMSG
Bard	Bard 6.5	6.5	PMSG
Dewind	DSME 7.0	7.0	PMSG
Mitsubishi PSE	SeaAngel	7.0	PMSG
Vestas	V164/7.0	7.0	PMSG
Gamesa	G14X	7.0	PMSG
Vestas	V164/8.8	8.8	PMSG

2.2.2 Power Transformers

Power transformers are needed in OWPPs to step-up the voltage of the wind turbines (typically from 690-3.3 kV to 10-36 kV) and for transmission link levels, typically from 10-36 kV to 110-150 kV. The goal of increasing the voltage is to reduce power losses (because the currents become lower) and capital costs (since smaller cross-section cables are required).

The design of power transformers for offshore applications does not differ much from those used in the conventional power system. The distinctive feature is the addition of extra corrosion protection because of the marine environment [42]. Transformers are made of copper windings that are wrapped around laminated iron cores. They can be mainly classified into two types according to the electrical insulation medium, liquid-filled and dry-type transformers [43]. Liquid-filled transformers use paper/liquid while dry-type transformers use air/resin.

Until a few years ago, dry-type transformers were installed in the vast majority of wind turbines because of their good fire behavior and compact dimensions. However, silicone and biodegradable liquid-filled transformers (replacing the mineral oil used in conventional liquid transformers) have been developed for modern WTs because their performance and reliability makes them particularly suited to offshore applications [43].

2.2.3 Submarine Cables

Submarine cables play an important role in the transmission of energy in OWPPs. They connect each WT to the collection point and provides a link between the offshore substation and shore.

Cross-Linked Polyethylene (XLPE) submarine cables are the most common type of cable used in OWPPs [4]. Fig. 2.3 shows the typical layout of currently available options of submarine cables for OWPPs. Fig. 2.3(a) and Fig. 2.3(b) show the cross-section of a single-core submarine cable and a three-core submarine cable, respectively.
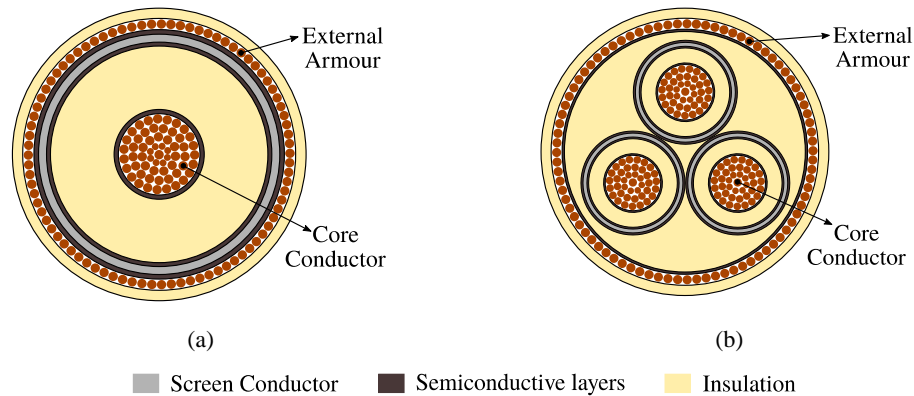
Fig. 2.3. Typical layout of currently available options of XLPE submarine cables for OWPPs. (a) Cross-section of a single-core submarine cable (b) Cross-section of a three-core submarine cable. Source [42].

For AC systems, three single-core submarine cables are installed to transmit large amounts of power with a voltage level up to 420 kV. These submarine cables are usually buried and arranged in tight trefoil formation. On the other hand, three-core designs are installed to transmit a smaller amount of power with voltage levels up to 225 kV [3]. Three-core designs are typically the preferred choice for the collection network (MVAC submarine cables) [42].

For DC systems, single-core submarine cables are generally installed for HVDC links.

A brief description of the cable-layers and their functionalities is addressed below. The reader is suggested to review references [44–46] for more information.

- **Core Conductor:** The main function of the core conductor is to allow the circulation of an electrical current. The size of the conductor or its cross-section depends mainly on the current flowing through it, the type of material (usually made of copper or aluminum) and the dielectric used. Power cable cores are usually stranded conductors in order to reduce the skin effect.

- **Insulation:** The insulation has two main functions. The first one is to ensure that there is not an electrical connection between conductors (core-screen and screen-armour). The second function is to keep the electric field between conductors uniform.

  In general, the insulator must be capable of withstanding the electric field of the cable for steady- and transient-state conditions.

  The most common polymer is the Cross-Linked Polyethylene (XLPE), which is used in the majority of high voltage cables manufactured today. The main reasons for its usage over other technologies are the higher allowable operating temperature and lower negative impact on the environment. It is less harmful than other technologies based on fluids, oil or gas.

- **Screen Conductor:** There are four main functions of this layer. First, it reduces the electric field outside each cable phase. Second, it provides a return path for the charging current. Third, it conducts fault currents to earth. Finally, it reduces the proximity effect.

  The size of the metallic screen depends on the value of the zero-sequence short-circuit current that the cable must withstand. Usually, the screens are made of copper wires together with an aluminum foil.

- **Semiconductive layers:** Semiconductive layers, between the core conductor and main insulator and between the insulation and screen, are used to ensure a cylindrical electric field and to avoid the formation of gaps between layers, thus preventing the occurrence of partial discharges.

- **External Armour:** Submarine cables have an external wire armour (conductive layer). The function of the armour is to endure the tensile force they experience during the installation. In addition, it can help to avoid a cable failure when a submarine cable is damaged in the sea by a third party.

Some of the major submarine cable manufacturers in the world include ABB, Nexans, Prysmian and NSW [2]. Table 2.2 shows values for 33 kV three-core XLPE submarine cables from Nexans manufacturer.

Table 2.2. Example values for a 33 kV, three-core XLPE submarine cable from Nexans. Source [47,48].

Cross-section (mm^2)	Current rating, Buried (A)	Transmission capacity, Buried (MVA)
95	352	20
120	399	23
150	446	25
185	502	28
240	581	33

2.2.4 Protection Systems

Existing protection systems, also called switchgears, can be classified into two types according to their insulation technology [49]. The first type is based on air-insulated switchgear (AIS). This type of protection system is predominantely used in conventional

onshore substations. The second type of protection system is based on gas-insulated switchgear (GIS) where the conductive elements are insulated by pressurized sulfur hexafluoride (SF_6) gas [49]. This kind of technology is the one used in OWPPs because of its compact structure and low maintenance in comparison with AIS switchgear technology.

The most relevant AC protection systems are circuit breakers, relays, fuses, meters and control switches. These elements need coordinated actions among them in order to ensure correct equipment operation, thus proper fault clearing. DC breakers are still an immature technology, thus in HVDC transmission systems, protection systems rely on circuit breakers on the AC side of the converters [47].

Medium-Voltage switchgears are used in offshore collection networks to protect both wind turbine equipment and main OWPP components, connect strings and control the connection and disconnection of individual wind turbines [42]. The number and type of protection used is different depending on the collection network topology and the required level of reliability, as shown in Fig. 2.4.

(a)   (b)

(c)   (d)

✗: Circuit breaker   ╱: Normally close switch   ∅: Normally open switch
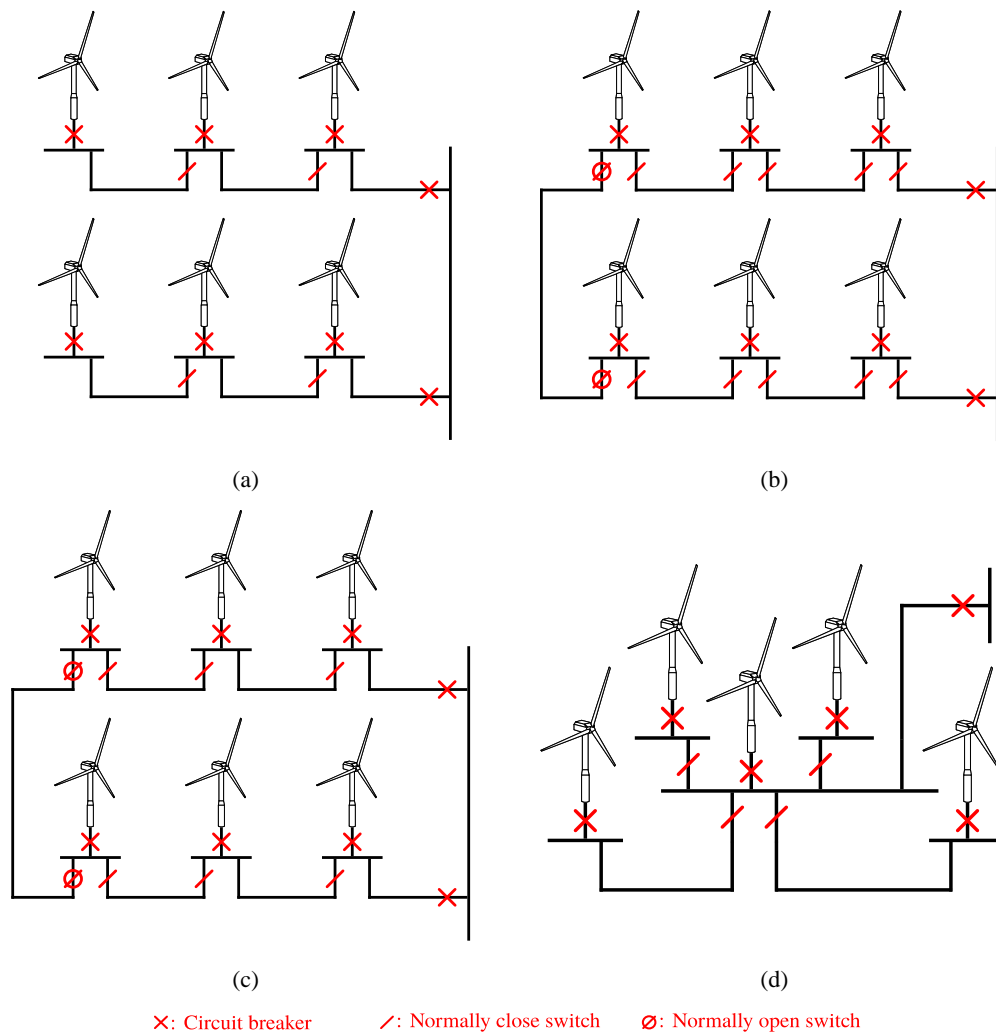
Fig. 2.4. Examples of configurations with circuit breakers and manual switches for different collection network topologies. (a) Radial topology. (b) Ring topology alternative 1. (c) Ring topology alternative 2. (d) Star topology. Source [42].

Each wind turbine has protections in the Low-Voltage (LV) and Medium-Voltage (MV) side. The LV protection clears internal wind turbine faults, while the MV protection is used to clear faults in the WT transformer and faults in the cable connected to the next turbine. The MV circuit breakers can be remotely operated from shore via Supervisory Control and Data Acquisition (SCADA) systems.

Protection elements on the offshore substation are used to protect against faults in the MV/HV transformer and disconnect feeders. The offshore substation transformer usually has additional protection for oil temperature, pressure, etc.

2.3 Collection Network Topologies of OWPPs

The overall function of the collection network is to gather the power coming from individual wind turbines. A collection network can be designed using different topologies, which depend on the size of the OWPP and the desired level of reliability [3,50]. These layouts are described next.

2.3.1 Radial

Fig. 2.4(a) shows the radial design of a collection network. In this topology, the wind turbines are connected to a single cable feeder within a string. The maximum number of WTs that can be connected to one feeder is determined by the ampacity of the cable and the rated power of the WTs.

This design offers the benefits of being simple and less expensive in comparison to other designs [27]. It is the less expensive because the total cable length required for connecting all the WTs with the collection network hub is the smallest.

The major drawback of this topology is its poor reliability as, in the case of a fault between the first WT and the hub of a feeder, all the power generated by the downstream WTs in the string will be lost.

2.3.2 Ring

There are two different ring designs, the single-sided and double-sided configuration [3,51]. The single-sided configuration is similar to the radial design but with an extra cable connection. For the case of the double-sided configuration, the last WT in one string is interconnected to the last WT of the next string as depicted in Fig. 2.4(b) or Fig. 2.4(c) [42].

Ringed layouts offer service reliability, compared to radial designs, by incorporating a redundant path for the power flow within a string. The main drawback of this additional feature comes at the expense of longer cable runs and higher cable rating requirements for each string.

2.3.3 Star

In the star topology, each WT is connected directly to a collection point, as shown in Fig. 2.4(d). The star design aims to reduce the cable ampacity requirements and to increase the reliability of the wind farm as a whole since one cable outage only affects one WT [27].

2.4 Transmission System Technologies of OWPPs

Offshore wind power transmission systems use submarine cables to transmit the power generated from the wind turbines of an OWPP to shore.

Fig. 2.5 shows the key offshore wind power transmission technologies use to date. These are Medium-Voltage Alternating-Current (MVAC), High-Voltage Alternating-Current (HVAC) and High-Voltage Direct-Current (HVDC). Fig. 2.6 shows the key factors that influence the choice of a transmission technology [3]. These factors are:

- Distance between OWPP and shore.
- Amount of power transmitted.

A brief description of the transmission technologies is shown below. For more details, the reader is suggested to review reference [3,4,42].
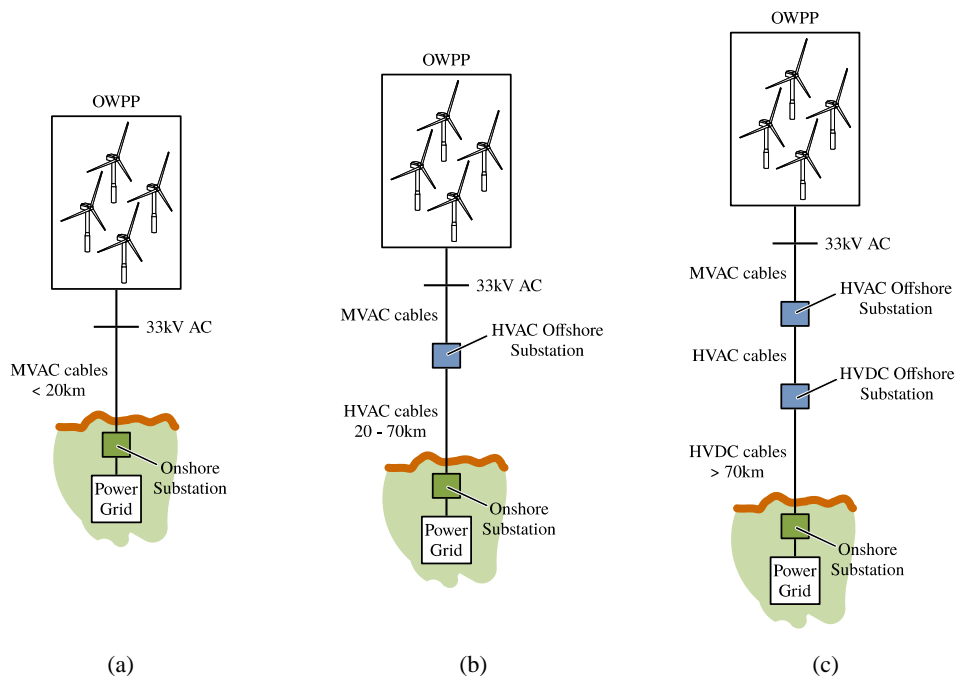
Fig. 2.5. Power transmission system technologies of an OWPP. (a) MVAC transmission system. (b) HVAC transmission system. (c) HVDC transmission system. Source [42].
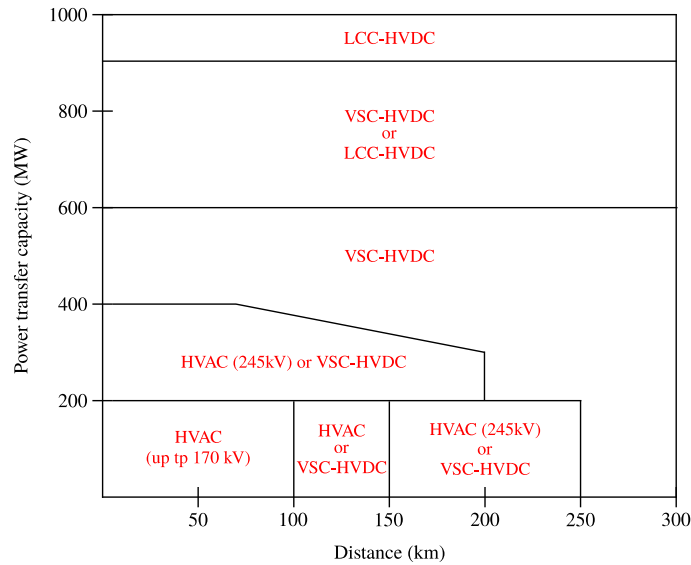
Fig. 2.6. Choice of transmission technology for different OWPP capacity and distance from shore. Source [3].

2.4.1 MVAC Transmission

MVAC transmission system is used to connect OWPPs that are close to shore, typically up to a distance of 20 km [42]. As depicted in Fig. 2.5(a), there is no need for installing an offshore substation. The onshore substation transformer steps-up the medium-voltage, typically 33 kV, to the required grid voltage. This system is the simplest for offshore wind power transmission [42].

2.4.2 HVAC Transmission

Fig. 2.5(b) shows a typical layout of an HVAC transmission link for an OWPP. HVAC transmission is suitable and commonly used for distances between 20 and 70 km [3,42]. In this system, the submarine cables of the collection network connect the WTs to the offshore substation. The offshore substation transformer steps-up the voltage of the collection point, which is typically of 33 kV, to a high-voltage level that is typically between 110 kV to 170 kV.

As depicted in Fig. 2.6, it is possible to use HVAC transmission for distances beyond 70 km and with voltages above 170 kV. For this case, reactive power compensation at both ends of the submarine cable is required, thus increasing the total costs of the transmission system [3,52].

2.4.3 HVDC Transmission

Fig. 2.5(c) shows a typical layout of an HVDC transmission system for an OWPP. In this type of transmission system, HVAC submarine cables connect the HVAC- and HVDC offshore substations. As pointed out in subsection 2.2.3, single-core submarine cables are installed for the HVDC link.

There are two different technologies of HVDC transmission systems. These are briefly described below.

Line-Commutated Converters (LCC)

LCC-HVDC transmission systems are based on power converters using thyristors as the switching element [53]. The basic building block of the converter is the well-known six-pulse thyristor bridge or the 12-pulse thyristor configuration [4]. Fig. 2.7 shows the schematic of a line-commuted power converter. This converter is capable of transferring the current in only one direction, but power can flow in both directions by reversing the voltage polarity via the control of the firing angle.
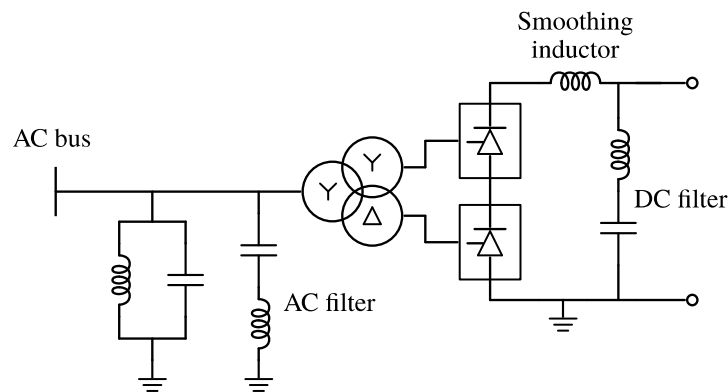
Fig. 2.7. Schematic of a Line-Commutated Converter (LCC). Source [4].

LCC-HVDC systems have the following main components at each end of the transmission line [4]:

- Tranformers: Substations at both ends need transformers in order to raise the voltage to the necessary level of the transmission line. It is usual to have both connections, star and delta, for the 12-pulse converter in order to cancel harmonics and reduce the size of the filter.
- LCC converter.
- AC and DC filters: LCC converters generate a high content of low order harmonics in the line currents. Thus, AC and DC filters are necessary. AC filters supply a portion of the reactive power needed by the LCC converter. The DC filter avoid the generation of circulating AC currents in the HVDC submarine cable.
- Capacitors or STATCOM: LCC converters require reactive power for proper operation. These elements are needed to compensate the reactive power demand in the grid.

LCC-HVDC is a mature technology that is suitable for transmitting high amounts of power over long distances [54]. LCC-HVDC requires strong grids to be connected to both ends of the converter stations, hence they are not suitable for offshore wind power transmission [42]. However, several research entities (universities, technological centers and manufacturers) are studying the applicability of this technology for large OWPPs [55].

Voltage Source Converters (VSC)

The schematic of a typical VSC-HVDC system is shown in Fig. 2.8. VSC converters use semiconductor switching devices, such as IGBT with anti-parallel freewheeling diodes, which can be switched ON and OFF at any time in the waveform cycle. This means that the current can be made to lead or lag the AC voltage, and so the converter can control both, reactive power as well as active power [4].

A VSC-HVDC system has the following main components [4,56]:

- Transformers: Transformers are installed in order to raise the voltage to the required level of the transmission system.
- VSC converter based on IGBTs: It is a three-phase converter based on IGBTs operating at low switching frequencies. Multilevel converters can also be used in this application due to their high-voltage capacity, lower harmonic content and high efficiency. VSC-HVDC systems operating at 300 kV and with a nominal power of 1100 MW are feasible with state of the art technology [36].
- AC and DC filters: VSC converters generate lower harmonic content in comparison with LCC converters, so the AC and DC filters are smaller.
- DC current filtering reactance: Each DC cable needs a reactance to limit DC fault currents and reduce current harmonics in the cable.
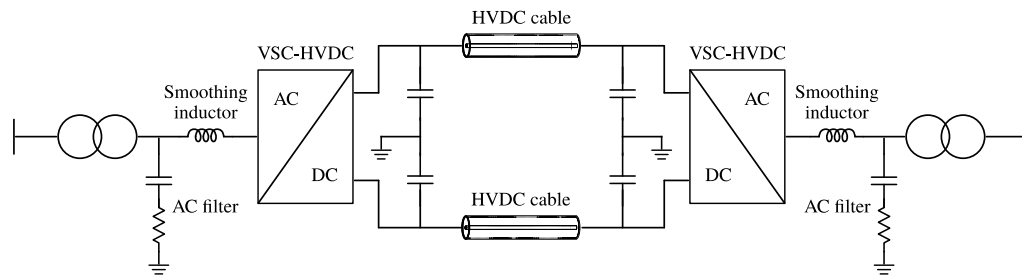
Fig. 2.8. Schematic of a typical VSC-HVDC system. Source [56].

Some advantages of the VSC technology are [57–59]:

- Power flow can be reversed without the need to reverse the polarity of the DC link voltage.
- Voltage support to the AC networks during faults. This support is limited to values lower or equal to the rated current.
- VSC-HVDC can be controlled to provide fast frequency and/or damping support to the AC networks through active power modulation.
- VSC-HVDC stations are smaller than LCC-HVDC stations. The offshore platform size can be smaller and less expensive [4].

2.5 Grounding in OWPPs

The topic of system grounding is extremely important in power systems, and hence in OWPP, due to the following reasons [60,61]:

- Provides protection to human life and equipment against high-voltages.
- Reduces switching transients overvoltages.
- Reduces earth fault currents (via the connection of the earth system through a limit impedance).
- Makes an abnormally large current such as a lightning strike to dissipate into the ground.
- Provides fast fault detection (e.g. in less than 150 ms) and the possibility of selectively clearing the fault.

There are six means of grounding. These are solidly grounded, inductance grounded, resistance grounded, resonant grounded, capacitance grounded and ungrounded. Details of the advantages and disadvantages of these types of grounding can be found in reference [61]. In general, the type of grounding affects the sequence impedances of the overall power system. For more information about grounding in OWPPs, the reader is suggested to review references [62,63]. Reference [63] presents a grounding study of Lillgrund OWPP.

A brief description of typical grounding configurations in OWPPs is addressed next.

2.5.1 Grounding of Transformers

In OWPPs, it is typical to have $Y - \Delta$ transformers of two- or three-windings. Generally, the Y-connected winding is solidly grounded [38] as shown in Fig. 2.9. It can be grounded through an impedance as well. The $\Delta -$ connected winding provides no path for zero-sequence currents to flow outside the winding of the transformer.
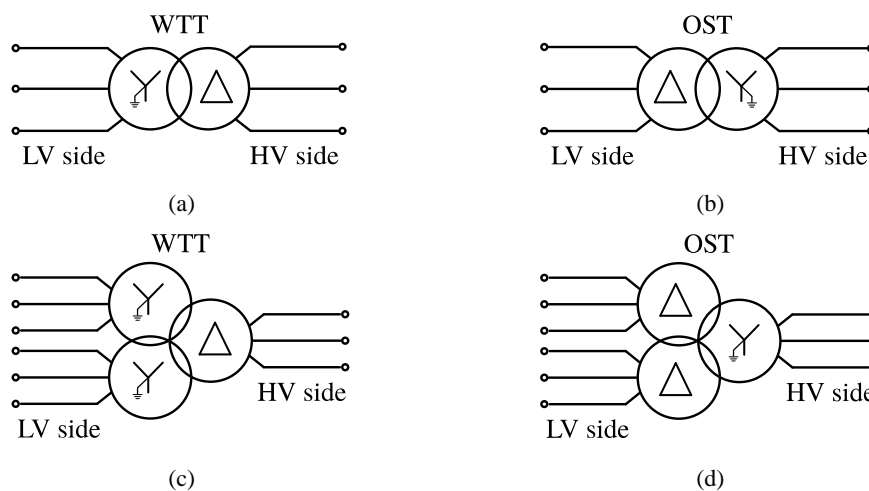
Fig. 2.9. Typical grounding of transformers in OWPP scenarios. (a) Two-winding wind turbine transformer. (b) Two-winding offshore substation transformer. (c) Three-winding wind turbine transformer. (d) Three-winding offshore substation transformer.

2.5.2 Grounding Transformers

As pointed out in previous subsection, wind tubine transformers (WTT) are generally $\Delta-$ connected on their high-voltage side. On the contrary, offshore substation transformers (OST) are $\Delta-$ connected on their low-voltage side. The necessary high level of reliability demands effective grounding in OWPPs [38]. In this sense, to appropriately account for effective grounding, grounding transformers are typically used to do the following [64]:

- Provide a relatively low impedance path to ground to either an ungrounded Y- or a $\Delta-$ connected system.
- Maintain the system neutral at or near ground potential.
- Limit the magnitude of transient overvoltages when re-striking ground faults occur.
- Provide a source of ground fault current during line-to-ground faults.
- Allow the connection of phase-to-neutral loads if required.

Grounding transformers are normally zigzag- or Ynd-connected winding, as shown in Fig. 2.10. For the Ynd-connected grounding transformer, the $\Delta-$ connected secondary may be used to supply auxiliary power (if required) as shown in Fig. 2.10(b).
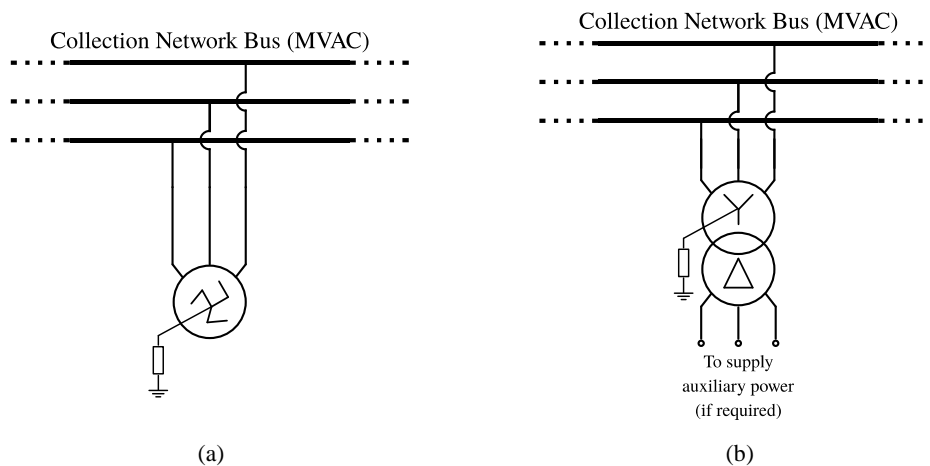
Fig. 2.10. Grounding transformers options for OWPPs. (a) Zigzag-connected grounding transformer (b) Ynd-connected grounding transformer.

2.5.3 Grounding of Submarine Cables

Submarine cable screens are normally installed in one of two grounding configurations, as shown in Fig. 2.11. These are single-end bonding and both-ends bonding.

Single-end bonding avoids the circulation of currents in the screen, as there is no closed loop. As effective as this technique is to reduce the circulating current losses, it has the big drawback of increasing the screen voltage (proportional to the length of the cable). As a result, this technique is limited to short cables, typically less than 3km, for which the voltage in the screen is still within tolerable values [45].

Both-ends bonding reduces the induced voltage in the screen to very low values (virtually zero at both ends). However, there is a closed path for the current in the screen, which

increases the losses. The screens and external armour of submarine cables are generally grounded at both ends [46].

The cross-bonding technique, generally used for underground cables, is not taken into account for submarine cables since it is unpractical to transpose the screens at sea [46].
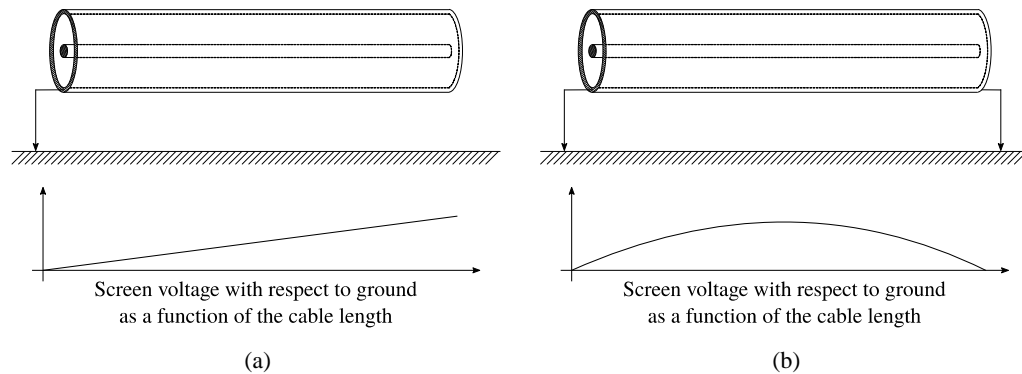
Fig. 2.11. Grounding configurations of submarine cables in OWPPs. (a) Single-end bonding. (b) Both-ends bonding.

2.6 Chapter Summary

This chapter has provided an overview of the electrical system of offshore wind power plants. The main power components of OWPPs, collection network topologies, transmission system options and grounding in OWPPs are the key points that have been addressed in this chapter. For each key point, the most important ideas are pointed out next.

Currently installed offshore wind turbines tend to be type-4. In this configuration, the generator is connected to the grid via a full-capacity converter. The two core control functions in a wind turbine are the pitch-angle and converter controls. A combination of the power converter and the two control functions enables variable speed operation over a wide range of wind speeds, which is essential for the efficiency of the energy conversion in WTs.

Power transformers are needed in OWPPs to step-up the voltage of the wind turbines (typically from 690-3.3 kV to 10-36 kV) and for transmission link levels, typically from 10-36 kV to 110-150 kV. The goal of increasing the voltage is to reduce power losses (because the currents become lower) and capital costs (since smaller cross-section cables are required).

Submarine cables play an important role in the transmission of energy in OWPPs. They connect each WT to the collection point and provides a link between the offshore substation and shore. Cross-Linked Polyethylene (XLPE) submarine cables are the most common type of cable used in OWPPs.

For AC systems, three-core submarine cables are installed to transmit a smaller amount of power with voltage levels up to 225 kV. Three-core designs are typically the preferred choice for the collection network (MVAC submarine cables). Three single-core submarine cables are installed to transmit large amounts of power with a voltage level up to 420 kV. Single-core submarine cables are generally installed for HVDC links.

The most relevant AC protection systems are circuit breakers, relays, fuses, meters and control switches. These elements need coordinated actions among them in order to ensure correct equipment operation, thus proper fault clearing. DC breakers are still an immature technology, thus in HVDC transmission systems, protection systems rely on circuit breakers on the AC side of the converters.

The overall function of the collection network is to gather the power coming from individual wind turbines. A collection network can be designed using different topologies (radial-, ring- and star- layouts). The design of the collection network depends mainly on the size of the OWPP and the desired level of reliability.

The transmission system is used to transfer power from the OWPP to shore. Most operational OWPPs are connected through an HVAC link. However, HVDC may be more cost-effective and have lower losses over longer distances. Key factors that influence the transmission technology are the distance between the OWPP to shore and the amount of power to be transmitted.

Grounding is extremely important in OWPPs. The reasons have been pointed out in section 2.5. In general, it provides protection to human life and equipment. The type of grounding affects the sequence impedances of the OWPP. Typical grounding practices of transformers and submarine cables have been presented. Additionally, the use of grounding transformers has been addressed to provide an effective grounding connection of the collection network.

Chapter 3

Wind Turbine Modeling

This chapter presents the development of a wind turbine model for harmonic analysis in power systems. For that purpose and based on generic wind turbine models, some changes and the implementation of additional structures are proposed to represent the harmonic emission of WTs for harmonics up to 5 kHz. The validation of the model is done via a comparison of the results obtained from the WT harmonic model implemented in Simulink® and an experimental platform. The harmonic emission is tested for two modulation strategies, the typical CB-PWM and a synchronous SHE-PWM modulation.

3.1 Introduction

There is an increasing requirement from wind power plant (WPP) developers to demand accurate information regarding the harmonics emitted by the WTs that they install. The reason behind this is the need to manage the harmonics correctly in order to fulfill the grid connection regulations and certify the compatibility of the internal grid of the WPP, onshore or offshore.

The evaluation of harmonics in power systems is halfway between electromagnetic transient (EMT) simulation and RMS simulation models [8]. Conventional EMT models of WTs are usually complex, highly detailed and generally confidential. The complexity of those models many times presents big constraints to analyze large power systems. Therefore, the use of Norton or Thevenin equivalents is typical.

In references [10] and [65], it is suggested that WT manufacturers share to wind power plant developers at least one Thevenin or Norton equivalent for several operation points in

order to describe the harmonic behavior of the WTs. Furthermore, a clear description of how to aggregate the different WT models in the wind power plant is necessary [65]. However, those models cannot analyze harmonic problems related to dynamical aspects of a wind power plant. For example, some modulation techniques are synchronous in comparison with typical asynchronous PWM modulations, and that aspect related to the phase angle and propagation issues of harmonics cannot be analyzed using models without dynamics.

A common way to analyze large power systems is by using generic WT models. These generic WT models are way less detailed than EMT models and are capable of representing all aspects related to grid integration. For example, the plant level controls (voltage control, frequency control, and others) are important aspects when the analyses are focused on power systems. The intended usage of the generic WT models is primarily for power system stability analysis and they do not include the harmonic emission of the converter. However, the capability to represent the dynamic behavior of a WT is well proven.

Based on the generic models, this chapter proposes a WECC type-4 algorithm controlled voltage source with a synthesized voltage waveform as the WT harmonic model. This way of representation allows flexibility and relative simplicity to perform harmonic analyses in large power systems, such as offshore wind power plants.

This chapter is structured as follows. Section 3.2 and section 3.3 give an overview of the generic wind turbine models and grid side converter (GSC) aspects, respectively. Section 3.4 presents the proposed WT harmonic model. This section details the way the model is built to represent the harmonic emission of WTs for harmonics up to 5 kHz. Section 3.5 treats the validation of the WT harmonic model. The validation is performed via a comparison of the harmonic evolution, in steady-state, of the proposed model with a real power converter (experimental platform). Additionally, this section gives the specification of the GSC, modulation strategies, and the GSC connection filter considered in this Ph.D. thesis. Finally, section 3.6 gives the chapter summary.

3.2 Overview of Generic Wind Turbine Models

Two groups developed generic WT models for the use in power system simulations. Those groups are the Western Electricity Coordinating Council (WECC) [66] and the International Electrotechnical Commission (IEC 61400-27-1:2015) [67].

From these two generic models, this Ph.D. thesis takes as reference the generic model proposed by the Western Electricity Coordinating Council (WECC). Fig. 3.1 shows the overall structure of the WECC type-4 wind turbine generic model. The model has four main blocks or modules. These are:

- Renewable energy generator/converter model (regc_a).
- Renewable energy electrical controls model (reec_a).
- Renewable energy plant controller (repc_a).
- Drive-train model (wtgt_a).

A brief description of these modules is addressed below. The reader is suggested to review reference [66] for details about the WECC type-4 WT generic model.
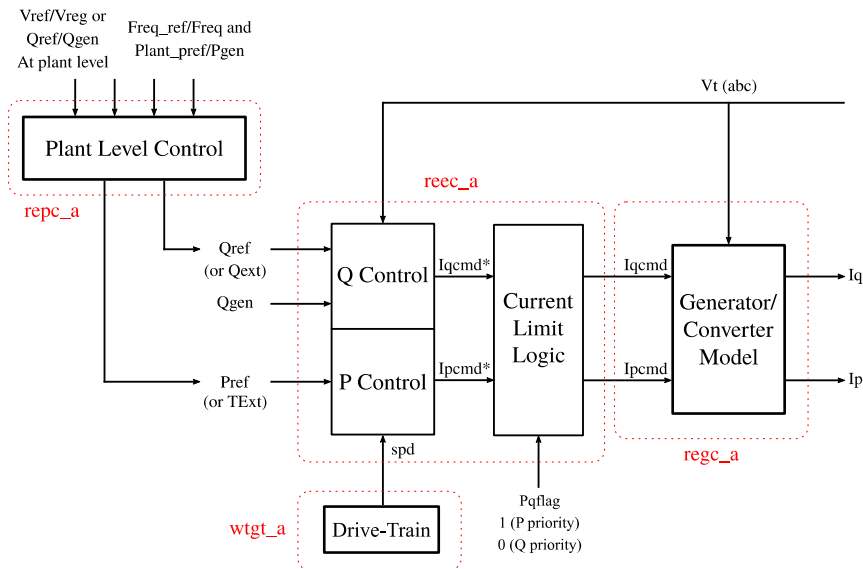
Fig. 3.1. WECC type-4 WT generic model. Source [66].

Renewable energy generator/converter model

The main function of this block is to generate the active (Ip) and reactive (Iq) currents injected to the grid (outputs of the model). The inputs of the module are the active current (Ipcmd) and reactive current (Iqcmd) setpoints from the control block (reec_a). Other parameters must be defined by the user (e.g lookup tables, filter time constants and rate limiters).

Renewable energy electrical controls model

The main function of this block is to define the active current (Ipcmd) and reactive current (Iqcmd) setpoints. These output variables are generated in accordance with specific logics and states. These states are executed as function of specific conditions, which are defined by several routines and user-defined variables. Some of the tasks that this module performs are:

- Detection of a voltage dip.
- Proper selection of injected reactive current scenario.
- Freezing of PI blocks.
- Current limit logic: This logic is implemented via a flowchart that allows the change in the P-Q priority and determines the maximum drive current.
- Filtering of waveform signals.

Renewable energy plant controller

The main function of this block is to generate the active and reactive power setpoints that are needed as inputs to the control model (reec_a).

Drive-train model

The drive-train module consists of a two-mass model. The purpose of this block is to emulate the behavior of torsional mode oscillations. This module can be neglected if it is not required to emulate this effect. The output of the model is speed and the user-defined parameters are the turbine inertia, generator inertia, damping coefficient and spring constant of the shaft.

3.3 Overview of Grid Side Converter Aspects

This section covers five main aspects regarding grid side converters. A brief description of the three-level neutral point clamped converter, PWM-based modulation methods, GSC current control strategies, grid synchronization, and GSC connection filters is given next.

3.3.1 Three-Level Neutral Point Clamped Converter

As pointed out in subsection 2.2.1, the Three-Level Neutral Point Clamped (3L-NPC) converter is the most common converter topology of offshore wind turbines to date [4]. Fig. 3.2 shows the simplified schematic of a 3L-NPC.
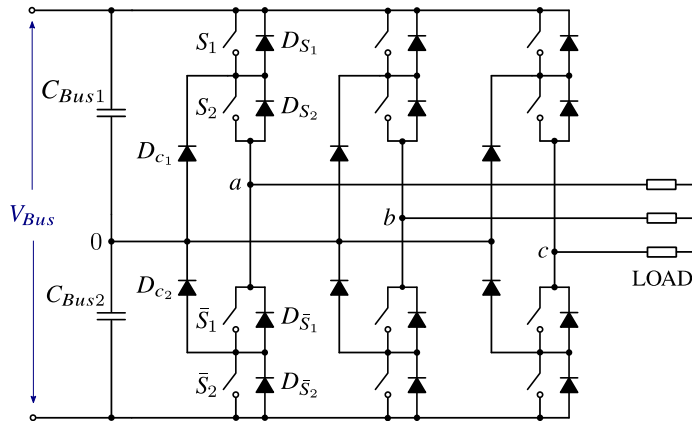
Fig. 3.2. Simplified schematic of the 3L-NPC converter. Source [68].

The converter leg "a" is composed of four active switches with four antiparallel diodes. The DC Bus voltage of this converter is split into two equal DC Bus capacitors, which provide a floating neutral point or midpoint (0). The diodes connected to the midpoint are known as clamping diodes.

The switching states shown in Table 3.1 represent the operating status of the switches in the 3L-NPC converter. A deeper explanation of this converter topology can be found in reference [68].

Table 3.1. Switching states of the 3L-NPC converter. Source [68].

Allowable Switching States for phase "a"				Output
S_1	S_2	$\bar{S}_1$	$\bar{S}_2$	v_{a0}
1	1	0	0	$V_{Bus}/2$
0	1	1	0	0
0	0	1	1	$-V_{Bus}/2$

3.3.2 PWM-Based Modulation Methods

The following subsection presents a brief description of Carrier-Based PWM and Optimal PWM techniques for multilevel converters, e.g. a 3L-NPC converter. The aim of this subsection is to provide a general background and identification of key references. For more details on PWM-based modulation methods, the reader is suggested to review references [68–70].

Carrier-Based PWM Techniques

The conventional sinusoidal PWM (SPWM) schemes for the two-level converters can be extended to modulate multilevel VSCs, e.g. a 3L-NPC converter, by using a multiple number of carrier waves. Depending on the arrangement of the carriers, the multicarrier SPWM methods are generally classified into phase-shifted modulation (PS-PWM) and level-shifted modulation (LS-PWM) [71].

Generally, a multilevel converter with m voltage levels requires $(m-1)$ triangular carriers. In the PS-PWM scheme, all the triangular carriers have the same frequency and the same peak-to-peak amplitude, but there is a phase shift between any two adjacent carriers. The phase displacement is given by equation (3.1).

$$\phi_{carrier} = 360 / (m-1) \tag{3.1}$$

The PS-PWM scheme is particularly suited for converter topologies such as the cascaded H-bridge (CHB), flying capacitor (FC), or modular multilevel converters (MMC) with limited number of power cells [72,73].

In contrast to the PS-PWM scheme, the LS-PWM vertically shifts the levels of the carriers. For any $m-$ level VSC, $m-1$ carriers are needed to compare with the sinusoidal reference. The multicarrier LS-PWM has several variations depending on the phase disposition of the carriers. These are:

- In Phase Disposition (IPD): where all carriers are in phase.
- Alternative Phase Opposite Disposition (APOD): where all carriers are alternatively in opposite disposition.
- Phase Opposite Disposition (POD): where all carriers above zero are in phase but in opposition with those below zero.

IPD provides the best harmonic profile of all the three schemes [68]. The LS-PWM can be applied to any multilevel topology such as 3L-NPC converter.

Optimal PWM Techniques

Optimal PWM techniques are typically used in high-power low-switching frequency applications such as HVDC transmission, OWPPs and motor drives. These techniques use a precalculated switching pattern, which is computed through the solution of a system of nonlinear trigonometrical equations with the aim of achieving certain harmonic requirements [70]. In its most common implementation, the switching waveforms possess quarter-wave symmetry. This assumption simplifies both the mathematical formulation and the acquisition of solutions at the cost of a restricted range of solutions.

Since optimal PWM methods allow for individual control of specific harmonics of the output voltage spectrum, the mathematical formulation can be expanded to achieve objectives other than complete elimination of harmonics. Examples of these objectives are the compliance of specific grid codes and the minimization of harmonic metrics such as the total harmonic distortion (THD) of the output voltage or current, as it is presented in chapter 9 of this document for the case of an OWPP. According to the previous idea, optimal PWM can be classified into three approaches [69]. These are:

- Selective Harmonic Elimination (SHE-PWM): It is the most common among all optimal PWM techniques. In this technique, the exact instant of the commutations within a fundamental period (or switching angle, α_m) is calculated so that the fundamental frequency is regulated to a certain amplitude while ($m-1$) harmonics (typically of low-order harmonic frequencies) are also eliminated from the output voltage spectrum.
  The main advantages of SHE-PWM lie in the tight control of the harmonic spectrum resulting in the elimination of low-order harmonics, reduction of the switching frequency, and relatively simple implementation based on precalculated switching angles and look-up tables.
- Selective Harmonic Minimization (SHM-PWM): SHM-PWM is well suited for grid-connected applications due to its inherent formulation to meet grid codes. SHM-PWM reduce the magnitude of a greater number of harmonics for a given number of transitions.
- Optimal Pulse Pattern (OPP-PWM): OPP-PWM provides optimal performance with regard to specific harmonic goals and is well suited for low-speed motor drive applications [69].

3.3.3 GSC Current Control

Different control structures are possible in type-4 wind turbines due to the use of full-size back-to-back converters [74]. The implementation of the control strategy can be achieved in different reference frames such as synchronous reference frame (dq), stationary reference frame (αβ), and natural reference frame (abc). Each of them has its advantages and

drawbacks. For the purposes of this Ph.D. thesis, a comprenhensive review is presented for some of the control strategies in the synchronous reference frame (dq). The reader is suggested to review references [5,39,69] for details on different current control strategies and outer loops.

The control structure of the positive-sequence current involving cross coupling and grid voltage feedforward in synchronous reference frame is shown in Fig. 3.3.
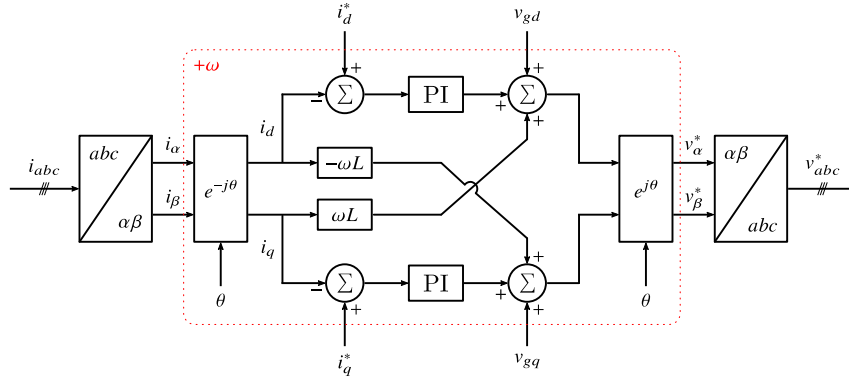
Fig. 3.3. Basic control structure of the current controller in synchronous reference frame. Source [5].

Fig. 3.4 illustrates the converter control of positive- and negative-sequence components in synchronous reference frame. This type of control structure is used to deal with converter operation under grid faults when negative-sequence current control is required [5].
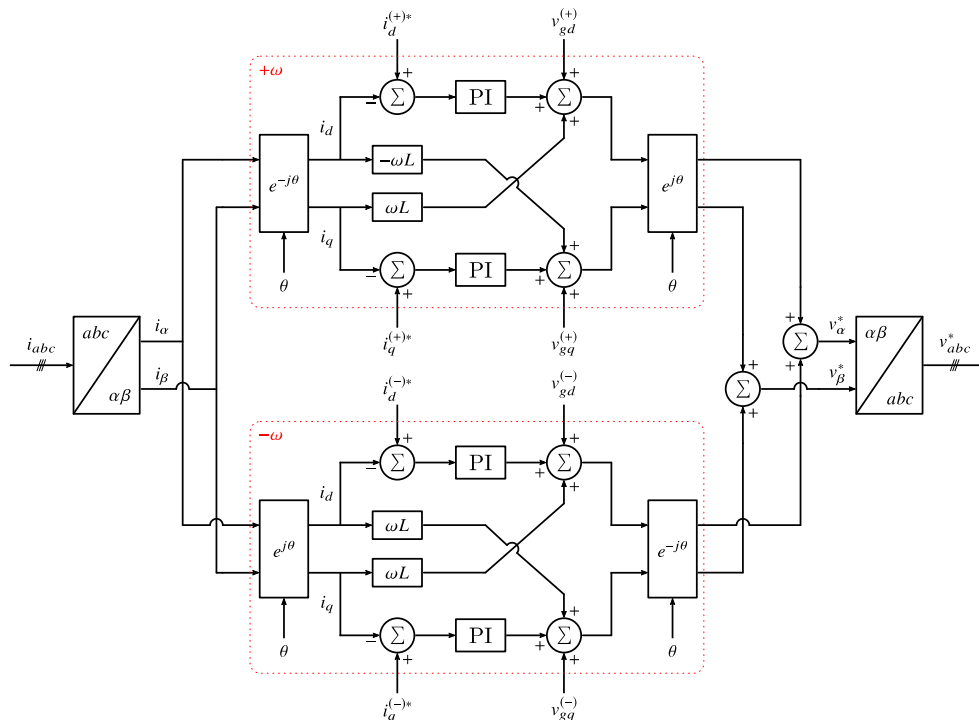
Fig. 3.4. Dual current (fundamental component) controller in synchronous reference frame for both positive- and negative-sequence components. Source [5].

Cross coupling exists between dq signals in both synchronous reference frames. Due to the coupling, second order harmonic oscillations are present. Such oscillations cannot be completely attenuated by PI controllers and therefore causes steady-state errors. In order to improve control performance, these oscillations should be cancelled to achieve full control of measured positive- and negative-sequence currents under unbalanced conditions. This can be obtained by application of notch filters only to attenuate the unwanted 2nd harmonic component [39]. A typical notch filter can be represented as given by equation (3.2) [5].

$$G_{NF}(s) = \frac{s^2 + \omega_n^2}{s^2 + \dfrac{\omega_n}{Q_d}s + \omega_n^2} \tag{3.2}$$

Double Harmonic Current Control

The voltage in real-life existing wind power systems is distorted and contains mainly low-order harmonics. To compensate unwanted harmonic current flow, additional harmonic current control loops are combined with the basic current control. Harmonic compensation can be applied by implementation of additional control to the basic one.

In order to control harmonic current, there is a need to implement a controller for each harmonic of interest. Therefore, if one would like to control typically observed harmonics in the network, e.g. 5th and 7th harmonics, integral controllers for both positive- and negative-sequence of the 6th harmonic component can be implemented [39] as shown in Fig. 3.5.
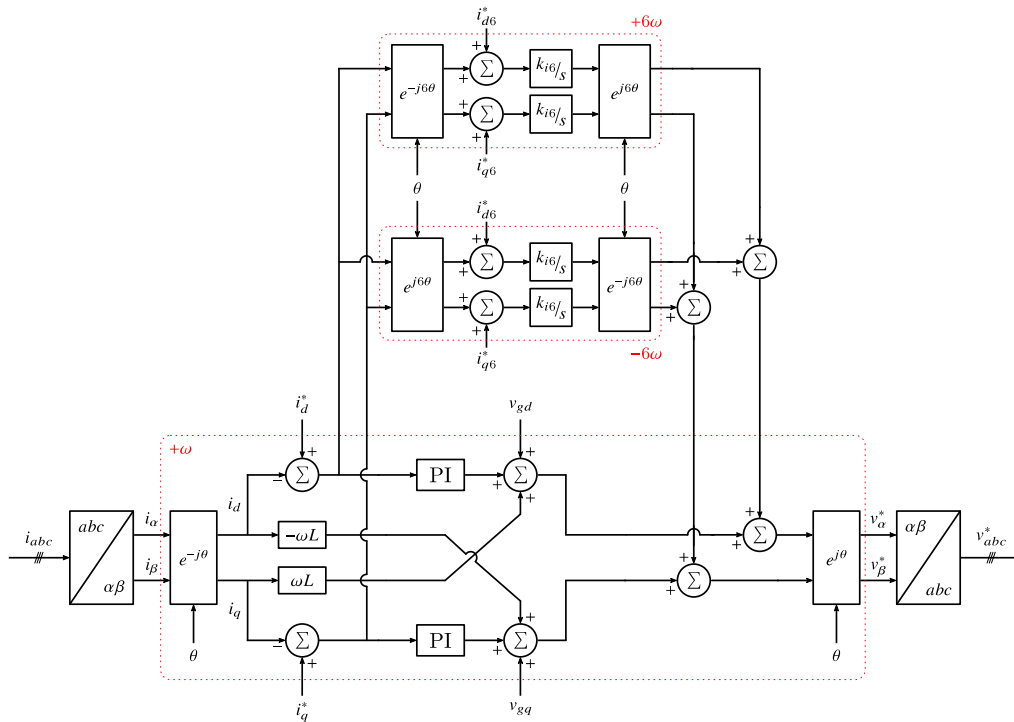
Fig. 3.5. Double harmonic current control in two nested rotating frames. Source [5].

Another possibility of implementing an equivalent solution is to implement two controllers in two frames rotating at -5ω and $+7\omega$. Of course, it is assumed that the 5th is a negative-sequence harmonic and the 7th is a positive-sequence harmonic. Normally, there is not intention to have any harmonics in the system, so the control is basically tuned to completely eliminate these harmonics (i.e. $i_{d5}^* = 0$, $i_{q5}^* = 0$, $i_{d7}^* = 0$, $i_{q7}^* = 0$).

Resonant Selective Controller

A resonant controller can be used to successfully compensate harmonics caused by the external network. The resonant controller ideally achieves an infinite gain at a certain tuned frequency of interest. Due to its selectivity, it is characterized by almost no attenuation outside the tuned frequency. Thus, it can be used as a notch filter in order to compensate the harmonics in a very selective way [75].

Instead of using two separated harmonic controllers in synchronous reference frame, one resonant controller can be used as shown in Fig. 3.6. One of the most important features of a resonant controller is that it is capable to track AC currents of different frequencies of interest and sufficiently eliminate steady-state error of controlled variables [76].
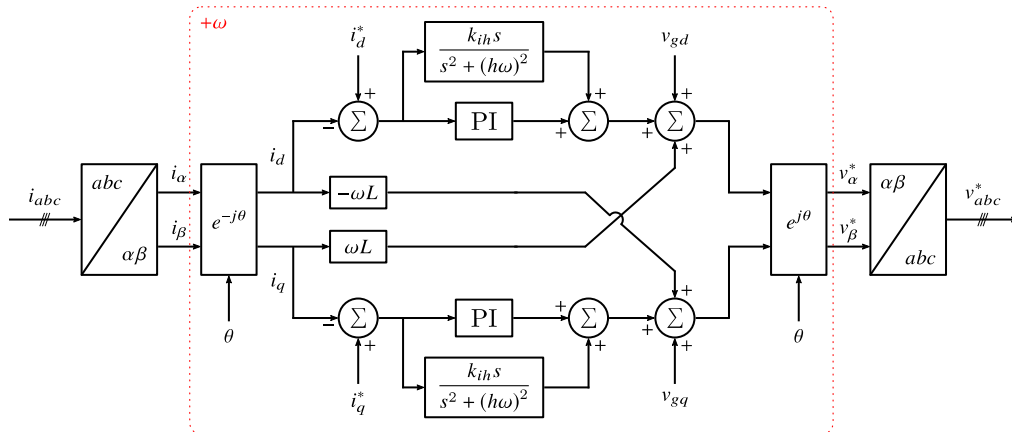
Fig. 3.6. Harmonic compensation based on resonant controller in synchronous reference frame. Source [5].

3.3.4   Grid Synchronization

Grid synchronization is one of the most important issues in the control of GSCs. The popular control strategies, presented in previous subsection, strongly rely on the phase angle of the grid voltage to implement the decoupled current control under the dq axis. In this subsection, a brief description of the most popular designs of three-phase PLLs is presented. The reader is suggested to review references [39,69,77,78] for more information about the different designs of three-phase PLLs.

Synchronous Reference Frame-Based PLL (SRF-PLL)

The basic scheme of a three-phase PLL is the synchronous reference frame PLL (SRF-PLL). The schematic of the SRF-PLL is depicted in Fig. 3.7 and it contains the following parts [77]:

- Phase Detector (PD).
- Low-Pass Filter (LPF).
- Voltage Controlled Oscillator (VCO).
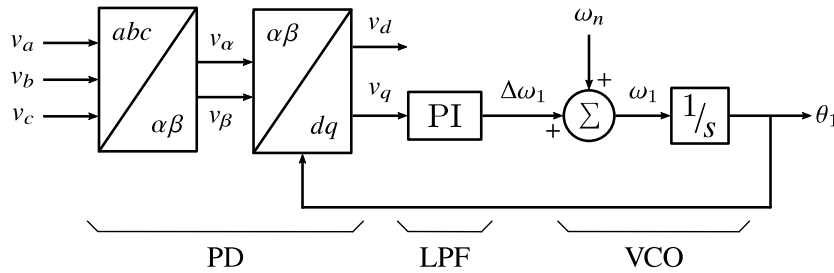
Fig. 3.7. Schematic diagram of the conventional SRF-PLL. Source [77].

The operation principle of the SRF-PLL can be summarized as follows. First, it transforms the three-phase grid voltage v_{abc} to the v_{dq} in the synchronous frame. Then, the PI controller is adopted to make the voltage v_q to zero, and consequently align the grid voltage to d-axis. The integration of the output of the PI controller produces the grid phase angle, which is delivered back to the Park transformation.

The tuning of the SRF-PLL is not a trivial task, particularly when considering power quality phenomena [78]. The required signal for phase-angle tracking is the DC component after the phase detector block. Any other harmonic content in the error signal should be canceled. The first action to cancel the presence of non-DC components in the error signal is the reduction of the PLL bandwidth, giving rise to a low-gain PLL. Low-gain PLLs are required when handling distorted voltages [78]. The main drawback is that the transient response of the system is reduced.

In general, the SRF-PLL performs well only under three-phase balanced and sinusoidal grid voltage, but unsatisfactory in the case of any nonideal grid voltage condition (e.g. three-phase unbalance, harmonic distorted, low voltage fault) [69].

PLLs with Enhanced Filtering Capability

In order to solve the aforementioned problems of the SRF-PLL under nonideal grid voltage conditions, many advanced PLLs with enhanced disturbance rejection capability have been designed by different researchers [77]. Almost all these PLLs can be understood as a conventional SRF-PLL with additional filters, which can be included inside the SRF-PLL control loop or before its input. Some of these PLLs are presented next.

- Moving Average Filter-Based PLL (MAF-PLL): The moving average filter (MAF) is a linear-phase filter that can be described in the Laplace domain as [79,80]:

$$G_{MAF}(s) = \frac{1 - e^{-T_\omega s}}{T_\omega s} \tag{3.3}$$

Where T_ω is the MAF window length. The MAF passes the DC component and completely blocks frequency components of integer multiples of $1/T_\omega$ [79]. Fig. 3.8 illustrates the schematic diagram of the MAF-PLL.
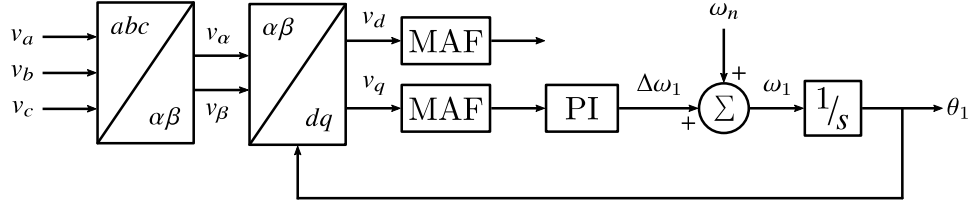
Fig. 3.8. Schematic diagram of the MAF-PLL. Source [77].

- Notch Filter-Based PLL (NF-PLL): The NF-PLL provides selective cancellation of the desired harmonic components in the PLL control loop [81][82]. Fig. 3.9 shows the structure of the NF-PLL. To achieve a satisfactory compromise, often using three NFs with notch frequencies at $2\omega_1$, $6\omega_1$, and $12\omega_1$ is recommended according to reference [77].
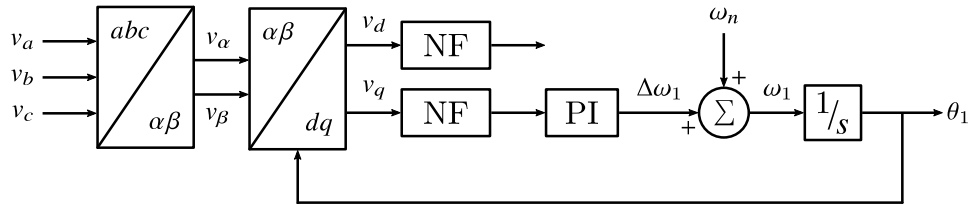
Fig. 3.9. Schematic diagram of the NF-PLL. Source [77].

- Dual Second-Order Generalized Integrator-Based PLL (DSOGI-PLL): One of the most popular improved PLL is the DSOGI-PLL [69]. To certain extent, the DSOGI-PLL can be regarded as the combination of both the DSOGI unit and the conventional SRF-PLL. Fig. 3.10 illustrates the schematic diagram of the DSOGI-PLL.

(a)

39

(b)
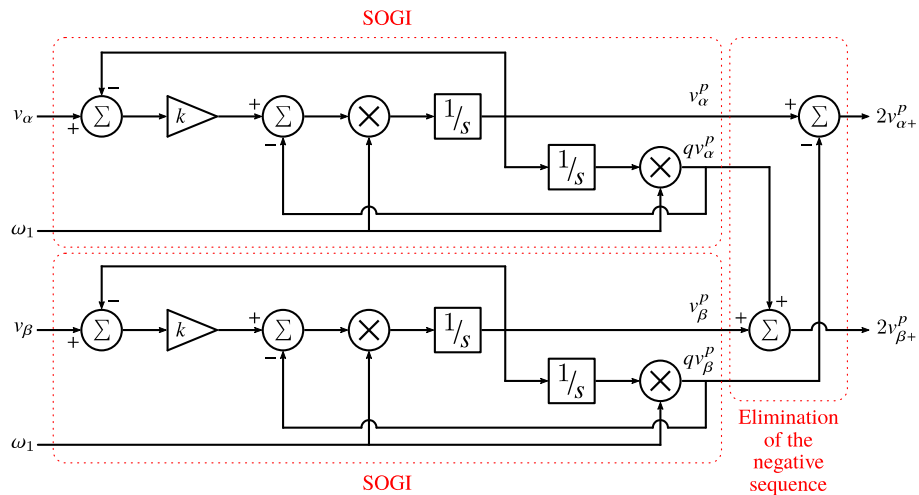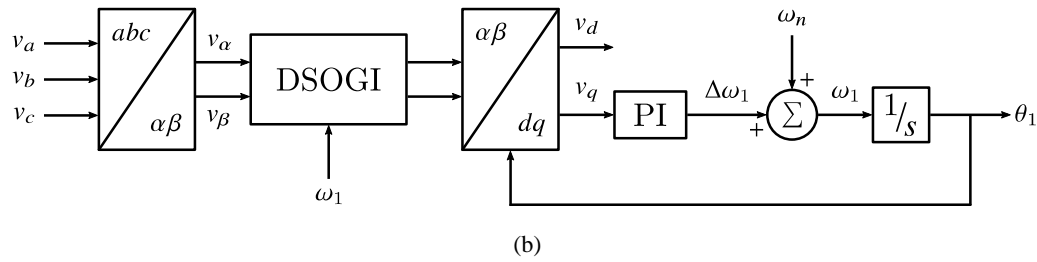
Fig. 3.10. Schematic diagram of the DSOGI-PLL. (a) DSOGI unit (b) DSOGI-PLL. Source [69].

The DSOGI-PLL is able to eliminate the negative and harmonic sequence in the v_α and v_β components. This indicates that the pure balanced and sinusoidal grid voltage is delivered into the conventional SRF-PLL. In general, the DSOGI-PLL is able to track precisely the grid voltage under nonideal grid voltage conditions [69].

3.3.5 GSC Connection Filter

Grid-connected power converters ideally supply sinusoidal currents. These converters employ either an inductor or an LCL filter to limit the current ripple [83]. The latter is widely used in today's applications because it results in lower inductance values and power losses [84]. Fig. 3.11 shows the simplified single-line schematic of an LCL filter.
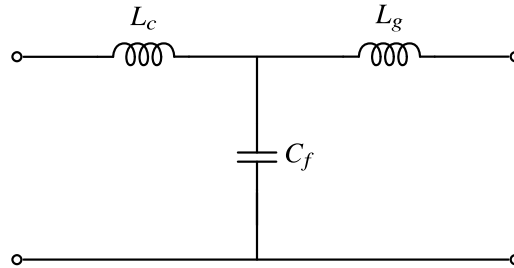
Fig. 3.11. Simplified single-line schematic of an LCL filter.

Despite the previous advantages, the current control in closed-loop may be unstable because of the LCL filter resonance [85]. Passive damping solutions solve this issue by inserting resistors at the expense of additional losses [86]. On the contrary, active damping solutions modify the control algorithm without using physical passive elements [39]. Thus, these solutions achieve a reduction in power losses.

Next, a brief description of passive- and active-damping solutions of LCL filter resonances is presented. The reader is suggested to review reference [87] for more details about these damping solutions. In reference [87], the frequency response of each solution is presented in detail.

Passive Damping Solution of LCL Filter Resonance

A direct way to damp the LCL filter resonance is to insert a resistor into the filter network. According to the location of the resistor, there are six ways to provide basic passive damping. These are (i) resistor in series with L_c, (ii) resistor in series with L_g, (iii) resistor

in series with C_f, (iv) resistor in parallel with L_c, (v) resistor in parallel with L_g, and (vi) resistor in parallel with C_f.

Based on the passive solution of adding a resistor in series with the capacitor C_f, several improvements have been proposed in references [88,89] to further reduce the power loss in this resistor. Fig. 3.12 shows four of the most representative passive-damping solutions.
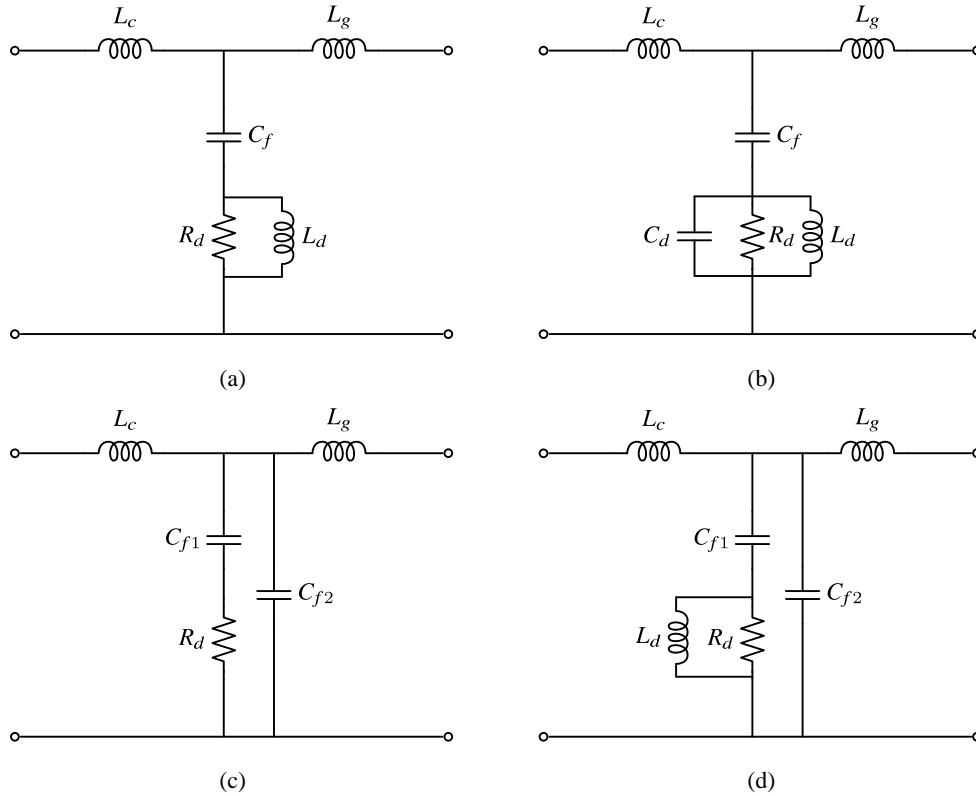
Fig. 3.12. Schematic diagram of the four improved passive damping solutions. (a) Adding a bypass inductor. (b) Adding a bypass inductor and capacitor. (c) Splitting the capacitor. (d) Splitting the capacitor and adding a bypass inductor. Source [87].

It can be pointed out that a lower power loss and a high harmonic attenuating ability is achieved when implementing the solutions shown in Fig. 3.12 in comparison with the original LCL filter (Fig. 3.11). However, it is worth to remark that the circuit complexity and the system volume and cost are also increased. Because of these aspects, it is typical to implement the solution depicted in Fig. 3.12(a) [90].

Active Damping Solution of LCL Filter Resonance

Active damping solutions can be classified into two types. These are:

- State-Variable-Feedback Active Damping: This method uses the feedback of proper state variable to mimic a virtual resistor (e.g. a resistor in parallel with the filter capacitance) in place of a physical one [87]. Several strategies of this kind of active solution have been proposed such as proportional feedback of the capacitor voltage [91], derivative feedback of the capacitor voltage [92], and second-

derivative feedback of the grid current [93]. These strategies can achieve a similar damping performance as a resistor in parallel with the filter capacitance C_f. From all these alternatives, the proportional feedback of the capacitor current has been widely used for its simple implementation and effectiveness [87].

- Notch-Filter-Based Active Damping: The main idea of this active solution is to place an antiresonance peak at the LCL filter resonance frequency f_{res} [87]. In that way, the antiresonance provided by the notch filter cancels out the LCL filter resonance. At low- and high-frequency ranges, the magnitude of the notch filter is 0 dB, thus it will not affect the magnitude-frequency characteristic of the LCL filter at these frequency ranges. One important point to consider for this kind of solution is that the LCL filter resonance frequency must be known exactly for appropriate implementation. However, in practice, due to tolerances and aging of the filter components, the LCL filter parameters will vary and deviate from the designed ones. Consequently, the performance of this strategy becomes poorer or even ineffective over time. To tackle this issue, the LCL filter resonance frequency can be detected online as proposed in reference [94]. In this sense, the resonant frequency of the notch filter is adjusted to be adaptive to the resonance frequency variation. However, this feature inherently increases hardware and control complexity.

3.4 Proposed Wind Turbine Harmonic Model

In this section, a generic type-4 WT model based on WECC standard is presented to perform harmonic analyses in large power systems such as an OWPP. The proposed model takes into account the phase angle of harmonics, so it can guarantee in a better way the harmonic assessment.

The main idea of this model is the use of simplified control structures to represent the dynamic behavior of the wind turbine (without a high computational burden) and the use of a voltage source with a synthesized voltage waveform. The main blocks of the WECC type-4 WT standard are used to represent the dynamic behavior of the WT, as depicted in Fig. 3.13.

The biggest change compared to the WECC standard comes in the generator/converter block. The proposed model consists of implementing a voltage source containing both, the fundamental component and the harmonics emitted by the converter. Fig. 3.14 shows the schematic of the proposed generator/converter block of the WT harmonic model. Remaining blocks are very similar in comparison with the WECC model, so they are not described in this document. The reader is suggested to review reference [66] for more details.
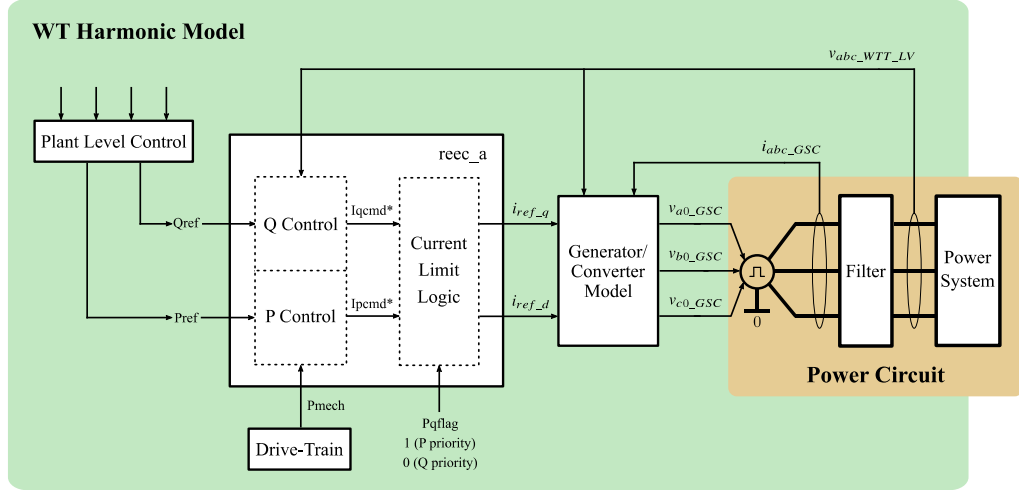
Fig. 3.13. Schematic diagram of the proposed WT harmonic model based on WECC type-4 WT standard.
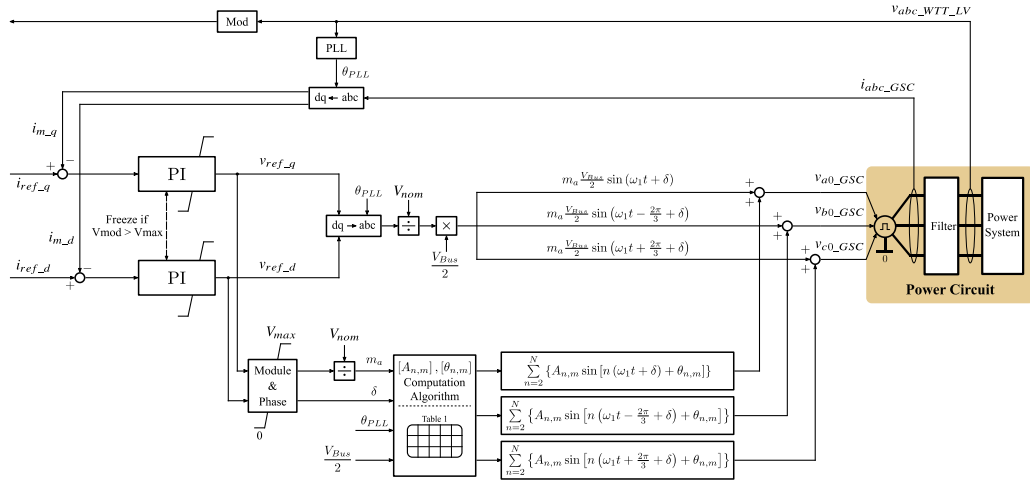
Fig. 3.14. Proposed schematic for the Generator/Converter model. Source [95].

The voltage commands are in dq reference frame. The voltage is limited once the output voltage module is calculated in order to not exceed the maximum voltage that can be generated by the implemented modulation strategy. This limited voltage is used to estimate the amplitude modulation index m_a, which is required by the harmonic synthesis block. It is computed according to equation (3.4).

$$m_a = \frac{2\sqrt{v_{ref\_d}^2 + v_{ref\_q}^2}}{V_{Bus}} \tag{3.4}$$

From Fourier transform theory [70], any time varying function $f(t)$ can be expressed as a sum of harmonic components, equation (3.5).

$$f(t) = \frac{a_0}{2} + \sum_{n=1}^{\infty}\left[a_n \cos(\omega_n t) + b_n \sin(\omega_n t)\right] \tag{3.5}$$

43

Where the first term represents the mean value of the signal, a_n and b_n are the Fourier coefficients, and ω_n is the angular frequency of the nth harmonic.

The time response of the converter output voltage can be synthesized using the Fourier series expansion. Assuming a null mean value and considering a finite number of harmonics, the converter output voltage for each phase with respect to the DC-link Bus midpoint can be approximated by equations (3.6), (3.7) and (3.8).

$$v_{a0\_GSC}(t) \approx m_a \frac{V_{Bus}}{2} \sin(\omega_1 t + \delta) + \sum_{n=2}^{N} \left\{ A_{n,m} \sin\left[n(\omega_1 t + \delta) + \theta_{n,m} \right] \right\} \tag{3.6}$$

$$v_{b0\_GSC}(t) \approx m_a \frac{V_{Bus}}{2} \sin\left(\omega_1 t - \frac{2\pi}{3} + \delta \right) + \sum_{n=2}^{N} \left\{ A_{n,m} \sin\left[n\left(\omega_1 t - \frac{2\pi}{3} + \delta \right) + \theta_{n,m} \right] \right\} \tag{3.7}$$

$$v_{c0\_GSC}(t) \approx m_a \frac{V_{Bus}}{2} \sin\left(\omega_1 t + \frac{2\pi}{3} + \delta \right) + \sum_{n=2}^{N} \left\{ A_{n,m} \sin\left[n\left(\omega_1 t + \frac{2\pi}{3} + \delta \right) + \theta_{n,m} \right] \right\} \tag{3.8}$$

Where ω_1 is the angular frequency of the fundamental component, $A_{n,m}$ is the magnitude of the nth harmonic for the mth amplitude modulation index, and $\theta_{n,m}$ corresponds to the phase of the nth harmonic for the mth amplitude modulation index. Furthermore, δ is the phase shift between the converter output voltage and grid voltage in order to control the power flow.

Therefore, for the representation of the harmonic emission of the GSC, a table with values of frequency, magnitude and phase is made for different amplitude modulation indexes. This table is obtained by the characterization of the converter including the main features that impact on the harmonic emission such as types of modulation and other factors (e.g. control loops, DC-link capacitor voltage balancing, dead-time compensation method, interleaving, etc.). Table 3.2 shows the general structure of this table of harmonics. Table 3.2 takes into account 99 members of Fourier series because the most representative harmonics are located around the considered frequency range (fundamental component up to 5 kHz). Furthermore, the requirements of some grid codes such as IEEE 519 [96] and the technical guideline from BDEW [97] generally define the lowest limits of the harmonics injected into the grid around this frequency range.

As depicted in Fig. 3.14, the model sets the fundamental component of the voltage from the voltage setpoints, which are mainly, dictated by the control logics and the converter control block. On the contrary, for harmonics greater than the fundamental component, the model searches the required amplitude modulation index in the table and synthesizes the remaining $N-1$ spectral components. When the required amplitude modulation index is not defined in the table, the $A_{n,m}$ and $\theta_{n,m}$ computation algorithm takes the upper and lower value that is defined in the table and performs a linear interpolation of the magnitude of the harmonic. For the phase, the nearest value is selected. The inherent error, as a result of

these simplifications, is reduced by considering a greater number of amplitude modulation indexes (M).

Table 3.2. Example of table of the converter harmonic content (per-phase). Phase angles are related to the fundamental phase angle.

Harmonics		Amplitude Modulation Index (m_a)							
		0.638	0.678	0.718	0.758	0.798	0.838	0.878	0.918
5th	$A_{5,m}$	0	0	0	0	0	0	0	0
	$\theta_{5,m}$	0	0	0	0	0	0	0	0
7th	$A_{7,m}$	0	0	0	0	0	0	0	0
	$\theta_{7,m}$	0	0	0	0	0	0	0	0
11th	$A_{11,m}$	0	0	0	0	0	0	0	0
	$\theta_{11,m}$	0	0	0	0	0	0	0	0
13th	$A_{13,m}$	0	0	0	0	0	0	0	0
	$\theta_{13,m}$	0	0	0	0	0	0	0	0
17th	$A_{17,m}$	0.093	0.066	0.035	0.0003	0.036	0.074	0.108	0.12
	$\theta_{17,m}$	0	0	0	0	180	180	180	0
19th	$A_{19,m}$	0.067	0.053	0.039	0.023	0.013	0.038	0.073	0.154
	$\theta_{19,m}$	0	0	0	0	180	180	180	180
23th	$A_{23,m}$	0.077	0.082	0.085	0.087	0.085	0.08	0.071	0.036
	$\theta_{23,m}$	0	0	0	0	0	0	0	0
25th	$A_{25,m}$	0.056	0.066	0.078	0.091	0.102	0.109	0.103	0.022
	$\theta_{25,m}$	0	0	0	0	0	0	0	0
29th	$A_{29,m}$	0.124	0.144	0.157	0.161	0.151	0.119	0.046	0.006
	$\theta_{29,m}$	180	180	180	180	180	180	180	180
31th	$A_{31,m}$	0.101	0.112	0.107	0.086	0.050	0.002	0.043	0.004
	$\theta_{31,m}$	180	180	180	180	180	180	0	0
⋮	⋮	⋮	⋮	⋮	⋮	⋮	⋮	⋮	⋮
99th	$A_{99,m}$	0.011	0.008	0.012	0.013	0.002	0.012	0.058	0.038
	$\theta_{99,m}$	180	180	180	180	0	0	0	0

The proposed model, depicted in Fig. 3.13 and Fig. 3.14, has three main related advantages. First, complexity is transferred from implementation and modeling of the modulation to analysis and measurement of the harmonics generated by the real converter. Second, the fact of implementing a simpler representation (compared to traditional electromagnetic transients models used in these analyses) results in a reduction in the computational burden of the model. This allows longer simulations (of the order of tens of seconds) and with several wind turbines. Last, it is possible from the manufacturer's point of view to disclose the simulation model to third parties. The model has a high level of abstraction, thus not infringing in confidentiality issues because the manufacturer is not sharing the details of its design.

3.5 Validation of the Proposed Wind Turbine Model

This section treats the validation of the WT harmonic model proposed previously (section 3.4). For the validation, it is required to define the remaining blocks of the WT harmonic model, a description of the grid side converter and the modulation strategies that are taken as a reference of study in this Ph.D. thesis, the GSC connection filter, and the characteristics

of the experimental platform (or test bench). Finally, the results from the comparison of the harmonic emission of both the real converter and the WT harmonic model are shown.

3.5.1   Simplified Definition of Remaining Blocks for Model Validation

This section is focused on the validation of the WT harmonic model. Thus, for practical reasons, the plant level control and the drive-train are simplified (only for validation purposes) as a constant input power. At the testing platform, the drive-train is simplified as a power generator and a drive.

The dynamic part of the presented model is not strictly the same compared to the WECC standard. Due to the fact that this model is oriented to EMT simulation environments (such as Matlab/Simulink Power System Toolbox), some changes have been performed on reec-a block (reec-a).

The main function of the reec-a block is to define the active- and reactive-current setpoints of the GSC. Fig. 3.15 shows the proposed simplified schematic of the reec-a block for model validation. As shown in Fig. 3.15, the active- and reactive-current setpoints are generated in accordance with logics, states and simplified transfer functions.
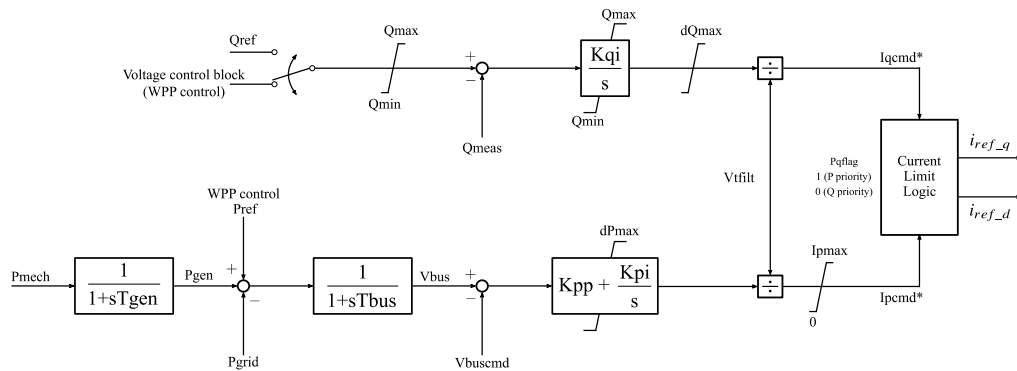
Fig. 3.15. Proposed simplified schematic of the converter control block.

Wind Turbine Harmonic Model Parameters

Once the algorithm and blocks have been disclosed, the values used to validate the model are presented. The proposed model is intended to be generic, the term "generic" refers to a model that is not specific to any manufacturer, but it can be parameterized to reasonably represent the dynamic behavior of a wide range of equipment. This way, the values shown in Table 3.3 are not related to any specific WT manufacturer, but they are intended to be some reference to set the dynamic behavior. The parameters are given in p.u. values because the proposed model has been validated in a scaled platform.

Table 3.3. Values of PQ control loops used for validation purposed.

Q control loop				P control loop			
Qmax	0.42 pu	Iqmax	1.1 pu	Tgen	0.25	Kip	0.19
Qmin	-0.42 pu	Iqmin	-1.1 pu	Tbus	0.015	Kiip	2.77
Kqi	40e3	Kiq	0.19	Kpp	1000	Ipmax	1.1 pu
dQmax	0.23 pu/s	Kiiq	2.77	Kpi	40e3	Ipmin	0 pu
Vmax	1.15 pu			dPmax	0.13 pu/s		

3.5.2 Description of the Grid Side Converter

The MV100 converter, manufactured by Ingeteam, is the equipment considered for the validation that is presented in this chapter and the studies presented in subsequent chapters (chapters 7 and 9). The MV100 converter is a 3L-NPC converter, in a back-to-back configuration, aimed to be used in full conversion stages in offshore wind turbines for ratings above 5 MVA. Table 3.4 shows the main parameters of this converter [98].

Table 3.4. INGECON WIND MV100 converter characteristics.

Parameter	Value
Line-to-Line Grid Voltage	3.3 kV
Power Rating	5-15 MW
Fundamental Frequency	50 Hz, or 60 Hz
Power Factor	±0.9
Switching Device	4.5 kV IGBTs
DC-Link Bus Voltage	5.6 kV

GSC connection Filter

The WT output filter can change in accordance with the type of wind turbine, the location of the wind farm and the grid codes that must fulfill [99]. In this Ph.D. thesis, a filter oriented to offshore multi-megawatt turbines, presented in reference [90], is considered for this stage.

Fig. 3.16 depicts the per-phase filter topology that is used at the output of the converter, designed mainly to meet grid code requirements related to current harmonics. It is an LCL filter with a damping circuit formed by a resistor (R_d) and an inductor (L_d) in parallel. This type of damping circuit reduces the losses in the damping resistor, because inductor L_d provides a new path without losses to the fundamental current component of the filter. Table 3.5 shows the per-unit LCL-RL filter parameter values.
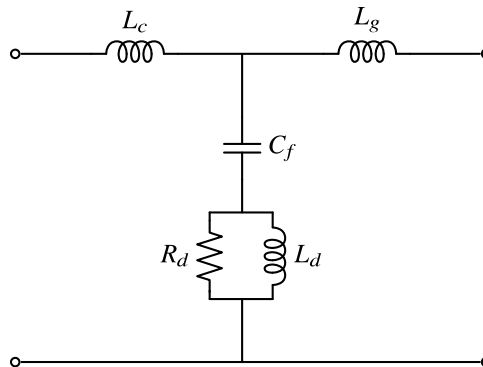
Fig. 3.16. Grid per-phase LCL filter with RL damping circuit.

Table 3.5. LCL-RL filter parameters values. Source [90].

L_c	L_g	C_f	R_d	L_d
0.11 pu	0.059 pu	0.16 pu	0.27 pu	0.031 pu

Modulation Strategies

Two modulation strategies are tested, the typical CB-PWM and a new synchronous SHE-PWM based modulation. The first one is intended to validate a classic modulation strategy, while the second one is intended to validate a special, advanced and not common modulation solution. Next, the harmonic spectrums are presented for both modulation strategies. For visual clearness, only magnitude information is presented. The angle information is not so well depicted in this kind of 3D plot. It is worth to point out, that these harmonic spectrums are also considered in subsequent chapters (chapters 7 to 9).

Carrier Based (CB-PWM):

Fig. 3.17 shows the harmonic spectrum, for phase "a", of the typical CB-PWM modulation as a function of the amplitude modulation index. On the contrary, Fig. 3.18 shows the line-to-line harmonic spectrum of this type of modulation.
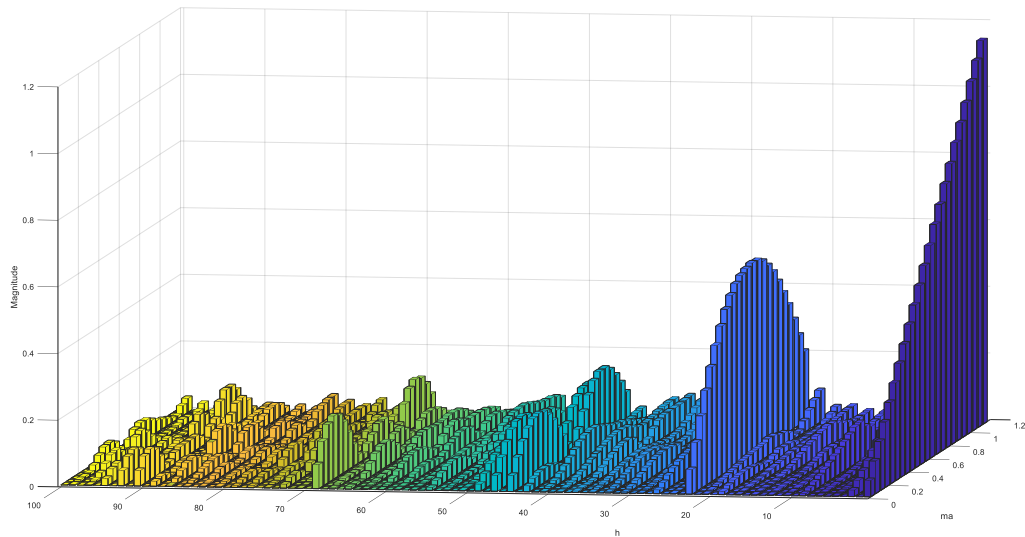
Fig. 3.17. Harmonic spectrum, for phase "a" with respect to the Bus midpoint (0), of CB-PWM modulation as a function of the amplitude modulation index.
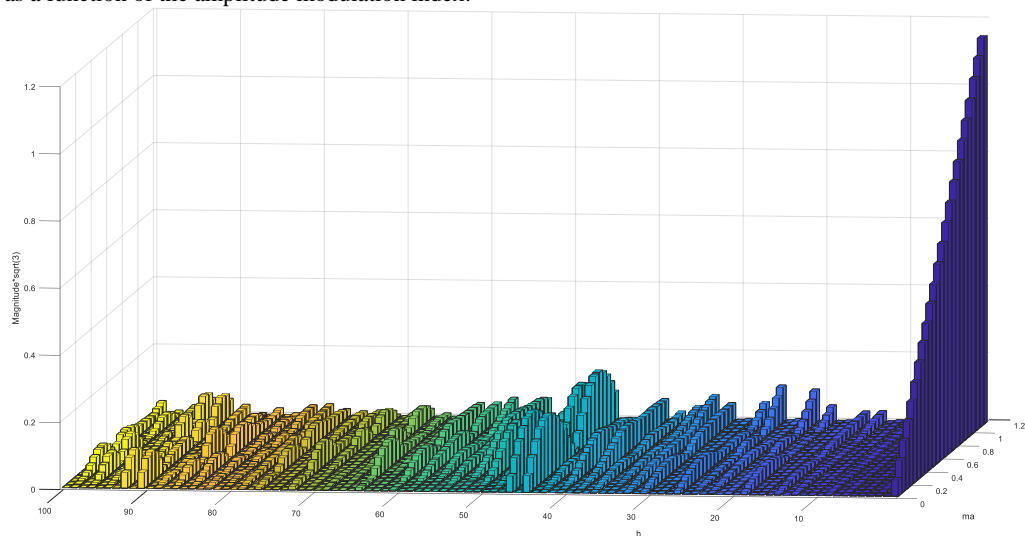
Fig. 3.18. Line-to-line harmonic spectrum of CB-PWM modulation as a function of the amplitude modulation index.

Selective Harmonic Elimination (SHE-PWM):

The following figures show the harmonic spectrum of a specific solution of a synchronous SHE-PWM modulation. Fig. 3.19 shows the harmonic spectrum, for phase "a", of the particular solution of SHE-PWM as a function of the amplitude modulation index. On the contrary, Fig. 3.20 shows the line-to-line harmonic spectrum of this particular solution of SHE-PWM.
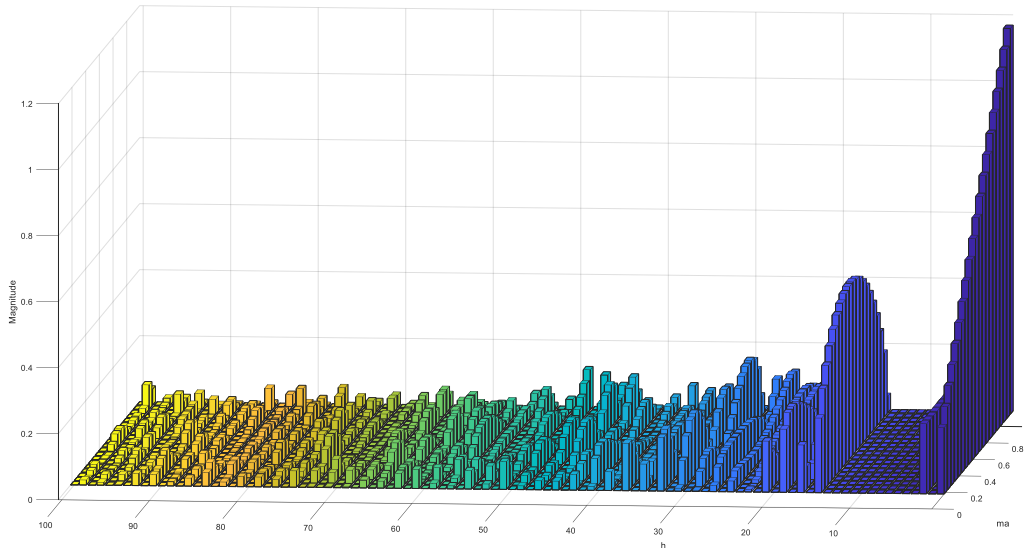
Fig. 3.19. Harmonic spectrum, for phase "a" with respect to the Bus midpoint (0), of SHE-PWM modulation as a function of the amplitude modulation index.
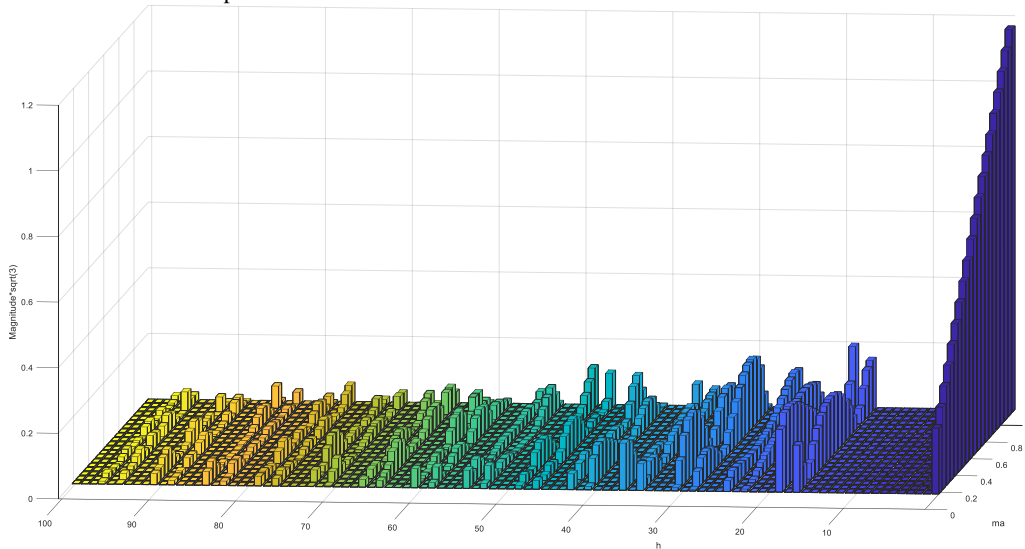
Fig. 3.20. Line-to-line harmonic spectrum of SHE-PWM modulation as a function of the amplitude modulation index.

3.5.3 Characteristics of the Test Bench

The tests required for the validation process are done in a scaled test bench, which is described with more detail in reference [100]. The test bench has three main parts: a grid emulator, a simple turbine environment (drive-generator + simple wind turbine control)

and a downscaled INGECON WIND MV100 replica. Table 3.6 gives the test bench parameters that are required to estimate the per-unit values.

Table 3.6. Test bench characteristics, parameters used to estimate the p.u. values.

Parameter	Value
Line-to-line grid voltage	690 V
Power rating	300 kVA
Fundamental frequency	50 Hz
DC-link voltage	1200 V

The main purpose for the configuration implemented in this test bench is to test a system as close as possible to the real one. For this purpose, the control hardware and the control code in the real equipment and the scaled one are the same, with the same control logics, auxiliary equipment and input/output signals. The components of the main power circuit are scaled maintaining the same p.u. value.

Additionally, the grid emulator allows the characterization of the converter at different grid frequency values and against voltage and frequency ramp variations. Moreover, the converter can be tested for a wide range of modulation indexes.

3.5.4 Validation Results

The validation process is done via the Sliding Discrete Fourier Transform (SDFT) in order to compare the harmonic emission of both the real equipment and the proposed WT harmonic model. The SDFT algorithm performs an *N*-point DFT on time samples within a sliding window. The window is shifted in time one sample and a new *N*-point DFT is computed. The incremental advance of the time window for each computation is what gives it the name of sliding DFT [101,102]. The measurement of time variation of harmonics is complex. Nevertheless, if the variation in module and/or phase of the measured harmonics does not vary with a high time variation rate, this method gives reasonably accurate results.

The validation is performed for two conditions: a ramp variation of only active power and the other one with only reactive power (Fig. 3.21). The comparison of the harmonic evolution is done in steady-state operation for both systems, real and model. To ensure a realistic comparison, both systems are settled to work at the same voltage and current operating points.

(a)   (b)
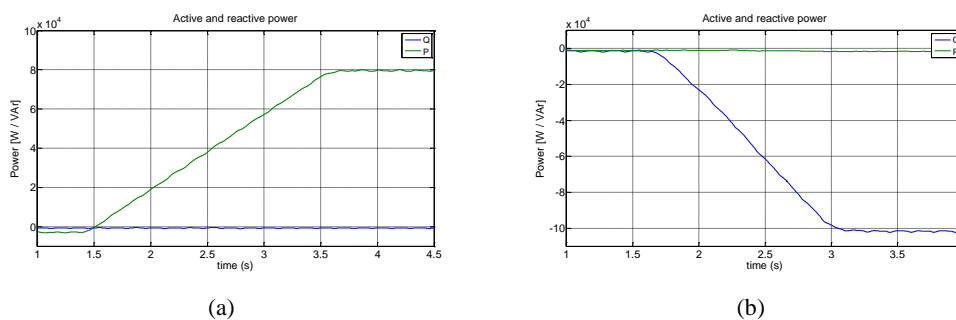
Fig. 3.21. Active and reactive ramp variations used to validate the WT harmonic model.

Validation over the classic CB-PWM modulation

The comparison between the results measured on the test bench and the simulation model are compared in Fig. 3.22 for a P-ramp variation and in Fig. 3.23 for a Q-ramp variation.
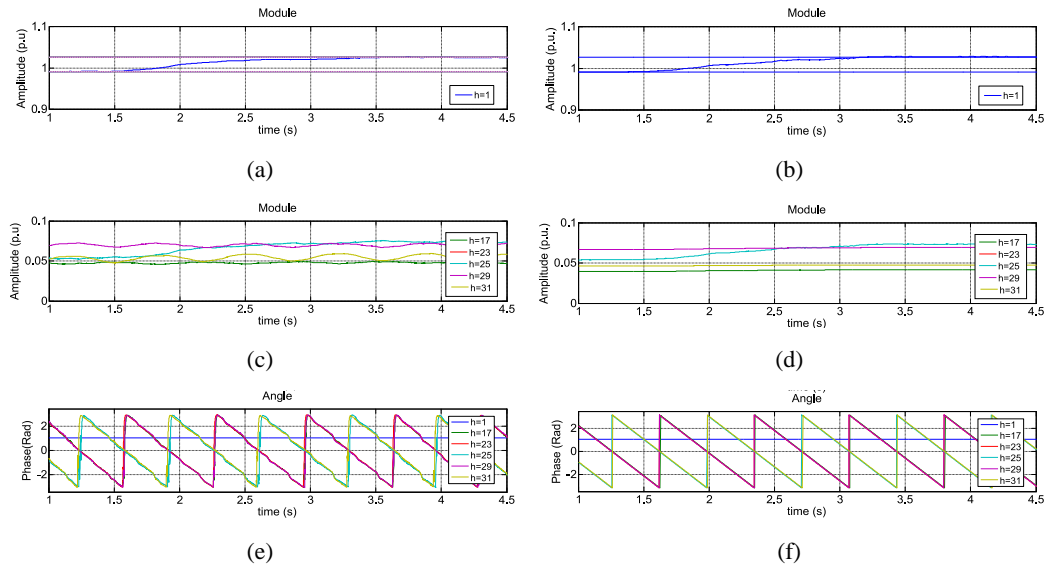
Fig. 3.22. Magnitude and phase of harmonics injected by the converter for a ramp variation of active power with CB-PWM modulation. Evolution of the modulation index of the real converter (a) and on the proposed model (b). Evolution of the magnitude of the harmonics of the real converter (c) and on the proposed model (d). Evolution of the phase of the harmonics of the real converter (e) and on the proposed model (f).
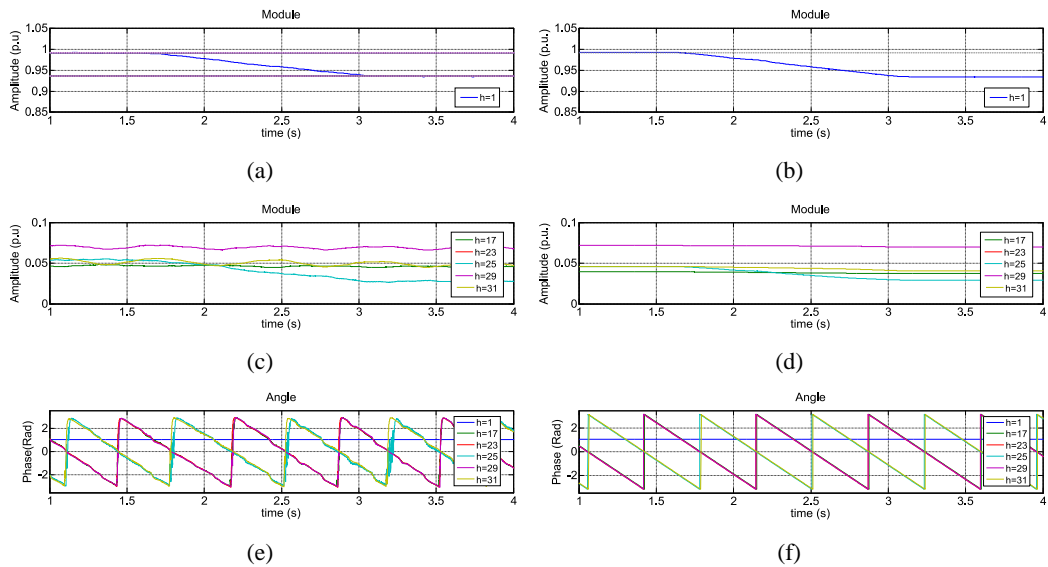
Fig. 3.23. Magnitude and phase of harmonics injected by the converter for a ramp variation of reactive power with CB-PWM modulation. Evolution of the modulation index of the real converter (a) and on the proposed model (b). Evolution of the magnitude of the harmonics of the real converter (c) and on the proposed model (d). Evolution of the phase of the harmonics of the real converter (e) and on the proposed model (f).

For simplicity of comparison and visualization due to several harmonics, the results for the real converter and the model are not depicted on the same graph. Instead, left graphs show the results of the real converter and right graphs show the ones with the model. Same axes scale is defined between left and right graphs in order to appropriately compare both results.

At normal operation (steady-state conditions), the harmonics generated by the converter are mostly determined by the modulation index. Other control structures, such as third harmonic injection or DC bus balancing control can also influence the harmonic emission, but with a smaller impact. So, the evolution of harmonics related to the modulation index is shown.

Looking at Fig. 3.23, it can be noticed that the phase angle is not constant. This effect is caused by the asynchrony between the fundamental frequency and the switching frequency (f_{sw}) of the CB-PWM. The carrier is not an exact multiple of the fundamental. All the harmonics depicted in Fig. 3.23 are from the first group ($f_{sw} \pm n \cdot f_n$), so all of them except the fundamental one have the same phase change rate. The phase angle is depicted normalized.

Validation over the synchronous SHE-PWM modulation

The comparison between the results measured on the test platform and the simulation model are compared in Fig. 3.24 for a P-ramp variation and in Fig. 3.25 for a Q-ramp variation.

Comparing Fig. 3.23 and Fig. 3.25, it can be seen that this type of modulation is synchronous. All the harmonics (depicted normalized) are in phase or in counter-phase with the fundamental. At the moment that the module of a harmonic crosses "zero-amplitude", the phase angle changes 180º. As the amplitude of the harmonic gets smaller, the more difficult is to determine its phase, but fortunately, small or close to zero harmonic amplitude does not affect significantly in power systems.
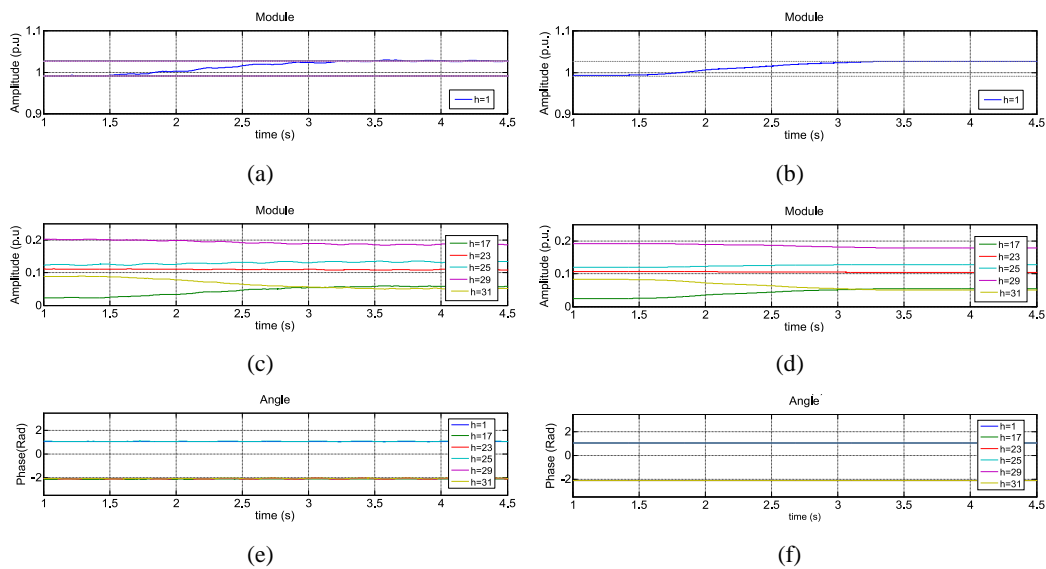
Fig. 3.24. Magnitude and phase of harmonics injected by the converter for a ramp variation of active power with SHE-PWM modulation. Evolution of the modulation index of the real converter (a) and on the proposed model (b). Evolution of the magnitude of the harmonics of the real converter (c) and on the proposed model (d). Evolution of the phase of the harmonics of the real converter (e) and on the proposed model (f).
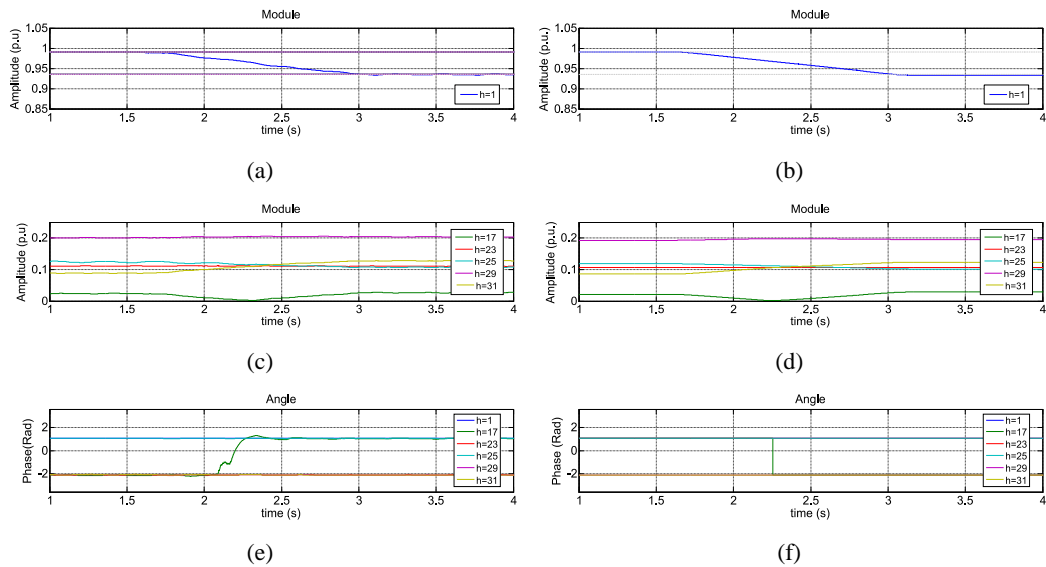
Fig. 3.25. Magnitude and phase of harmonics injected by the converter for a ramp variation of reactive power with SHE-PWM modulation. Evolution of the modulation index of the real converter (a) and on the proposed model (b). Evolution of the magnitude of the harmonics of the real converter (c) and on the proposed model (d). Evolution of the phase of the harmonics of the real converter (e) and on the proposed model (f).

3.6   Chapter Summary

This chapter has presented the development of a wind turbine model for harmonic analysis in power systems. For that purpose and based on the generic WT model from WECC, some changes and the implementation of additional structures are proposed to represent the harmonic emission of WTs for harmonics up to 5 kHz. The additional structure consists of implementing a voltage source containing both, the fundamental component and the harmonics emitted by the converter.

In order to validate the model at the dynamic performance, the validation has been carried out by comparing the evolution in phase and module of harmonics for active and reactive ramp variations. The results show good agreement between the model and the real converter. Therefore, this model can represent reasonably well the wind turbine in normal operation. This model cannot represent in an accurate way harmonics due to control interactions (undesired control oscillations). For those analyses that are beyond the normal stable operation, more precise models are needed such as manufacturer models, probably under non-disclosure agreement.

Wind plant level controls or voltage depended PQ charts can be implemented by simple blocks. Thus, the model can be integrated in a power system and reach a specific operation point related to its particular characteristics (position on the wind farm, incident wind, and other features). Even more, as the control is simple, instead of using an aggregated model, this WT harmonic model allows evaluation of the whole OWPP.

Furthermore, by only changing some parameters, the model can represent a wide range of wind turbines. The complexity is transferred from implementation and modeling of the control and modulation to analysis and measurement of the harmonics generated by the real converter.

Chapter 4

Wake Effect Modeling

This chapter briefly describes the best-known models of wind turbine wakes. Jensen's wake model is described in detail and the reasons for its selection are pointed according to the objectives of the Ph.D. thesis.

4.1 Introduction

Wind turbines extract part of the wind's kinetic energy to produce electricity. This transformation process leads to an energy loss, making the wind downstream of the WT to have a lower speed and to be turbulent [103]. This phenomenon is known as wake effect. As the wind flow proceeds further downstream of the wind turbine, the wake of the WT begins to spread and gradually the wind speed returns to free stream conditions.

The wake produced by a wind turbine, which affects wind turbines downstream, has two negative effects on a wind farm [103]. First, it reduces the lifetime of the wind turbines due to the increase in the mechanical stress on turbines blades, which is produced by an increase in wind turbulence. Appropriate turbine blade design has to be taken into account to minimize this effect. Second, a reduction in the energy production of the wind farm is obtained due to a reduction of incoming wind speed for WTs affected by the wake of wind turbines located upstream. For this second aspect, the spatial disposition of wind turbines should be optimized to improve energy yield.

In general, it is important to consider the wake effect in the design of a wind farm in order to maximize the energy output and lifetime of the wind turbines [104]. Regarding the scope of this Ph.D. thesis, it is of particular interest to model the wake of a wind turbine to

represent, as close to reality, the different operation points of the wind turbines in an OWPP scenario.

This chapter is structured as follows. Section 4.2 gives an overview of WT wake models. Section 4.3 describes in detail the Jensen's wake model. The reasons for its selection are pointed according to the scope of this Ph.D. thesis. Finally, section 4.4 gives the chapter summary.

4.2   Overview of Wind Turbine Wake Models

The wake of a wind turbine is typically divided into near- and far- wake [105]. The near wake is the region from the wind turbine to almost two to three rotor diameters downstream. For this region, the geometry of the turbine blades determines the shape of the downstream wind, thus determining the performance of the wind turbine [106]. On the contrary, the far wake is the region in which the shape of the rotor is less important. For this region, focus lies on wake modeling, wake interference among WTs, turbulence modeling and topographic effects [107]. In this Ph.D. thesis, emphasis is taken on the study of far wake models since the separation distance among wind turbines is typically higher than three rotor diameters [107].

Far wake models, from now on only wake models, can be classified into three main groups as shown in Fig. 4.1. These are kinematic models, field models and added turbulence models. A general description of the best-known models is done below.
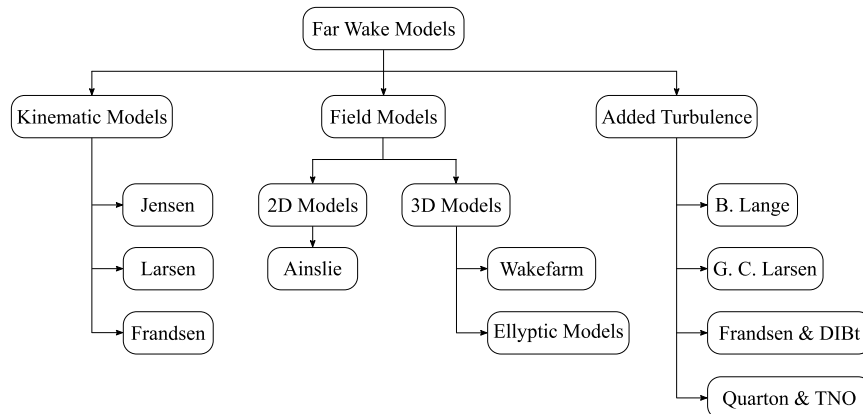
Fig. 4.1. General classification of far wake models.

4.2.1   Kinematic Models

The mathematical formulation of kinematic models is based on the law of momentum conservation [104]. Despite the simplicity of these models, accurate results can be obtained if the parameters of the model are chosen correctly [103]. The following is a general description of the best-known kinematic models.

Jensen-Katic Model

This model (hereafter referred to as Jensen's model) was initially proposed by N. O. Jensen in 1984 [108], and further developed to its current form by Katic in 1986 [109].

Jensen's model is based on global momentum conservation [110]. This model neglects the near wake and supposes that the far wake starts directly after the rotor of the wind turbine. Furthermore, the model assumes a linear expansion of the wake diameter and a constant velocity deficit across the wake. The input variables and the mathematical formulation of this model are presented in section 4.3.

Larsen's Model

Larsen initially proposed this model in 1988. The mathematical formulation of this model is based on Prandtl's turbulent boundary layer equations. In order to calculate the wake velocity profile, Larsen's model requires the following input variables: incoming wind speed, turbulence intensity, thrust coefficient, diameter and height of the wind turbine. Details of the mathematical formulation of this model can be found in reference [111].

Frandsen's Model

This wake model is mainly applied to wind farms with the following characteristics:

- A rectangular array geometry with straight rows of wind turbines.
- Equidistant spacing between units in each row and between rows.
- Parallel wind flow direction to the rows.

The governing equations of this model are based on the law of momentum conservation. This law is applied to the wind flow in a cylindrical control volume around the wind turbine rotor and in which acceleration, pressure, gravity and turbulent shear are neglected. Similar to Jensen's model, Frandsen's model also assumes a constant velocity profile across the wake. Details of the mathematical formulation of this model can be found in reference [112].

4.2.2 Field Models

Field models are developed based on approximations of the Navier-Stokes equations [103]. These models calculate the flow properties numerically at every point of the flow field using a specific mesh. Therefore, field models require substantially higher computation power than kinematic models. In this subsection, a brief description of the best-known field models is done.

Ainslie's Model

This model, also known as Eddy's viscosity model, is based on the simultaneous solution of the continuity equation and the simplified version of the Navier-Stokes equation in order to obtain the wind speed components in the field defined inside the wake.

Ainslie's model suggests that the solution obtained from the velocity components of the wake is valid from a distance equal to twice the diameter of the turbine. Besides, Ainslie's

model assumes that the velocity deficit in the cross-section of the wake obeys a Gaussian distribution. Details of this model can be found in reference [113].

Wakefarm

This model is developed by the Energy Research Centre of the Netherlands (ECN). Wakefarm is a 3D-parabolic Navier-Stokes code for the far wake using a $k - \varepsilon$ turbulence model. To model the near wake, momentum theory is used together with the use of empirical corrections. Details of this model can be found in reference [114].

Elliptical Models

Several elliptical models have been developed to study the wind flow of wind turbines and wind farms. These models are based on actuator disc theory. Despite these models are able to represent the near wake with a lot of detail, their computational load is high. Of particular interest are the contributions of Mikkelsen [115], Troldborg [116] and Ammara [117].

4.2.3   Added Turbulence Models

These models are combined with kinematic models for load calculations. The best-known added turbulence models are the B. Lange Model [118], G. C. Larsen Model [119], Frandsen & DIBt [120] and D. C. Quarton & TNO [119]. In addition, there are Computational Fluid Dynamics (CFD) models which are more accurate but demanding in terms of computational burden. The reader is suggested to review previous references for more detail.

4.3   Jensen's Model

The analysis that is carried out within the framework of this thesis focus on the electrical phenomena of the OWPP, not on the aerodynamic ones. Therefore, Jensen's model has been chosen since it is a simple and widely used model [121]. Its implementation represents a low computational load and its accuracy is similar to more complex models [122].

Jensen's model is adequate in order to estimate the mean wind speed at each wind turbine according to the spatial distribution of the OWPP and wind conditions, i.e. wind speed and wind direction. This allows the wind turbines to work at different operation points according to reality.

4.3.1   Jensen's Single Wake Model

According to Jensen's wake model, equation (4.1) describes the downstream wind speed of a single wind turbine [108].

$$V_{wind,x} = V_{wind,0} \left[1 - \frac{1 - \sqrt{1 - C_T}}{\left(1 + \frac{2k_{wdc}x}{D_{turbine}}\right)^2} \right] \tag{4.1}$$

Being,

$D_{turbine}$: diameter of the turbine rotor.

x : distance behind the turbine.

C_T : thrust coefficient.

k_{wdc} : wake decay constant.

$V_{wind,0}$: free stream wind.

$V_{wind,x}$: wind speed at distance x from the wind turbine.

The area affected by the wake is given by the distance behind the wind turbine and the wake decay constant as shown in Fig. 4.2. Jensen experimentally found approximated values for k_{wdc} of 0.075 and 0.04 for onshore and offshore applications, respectively [121].
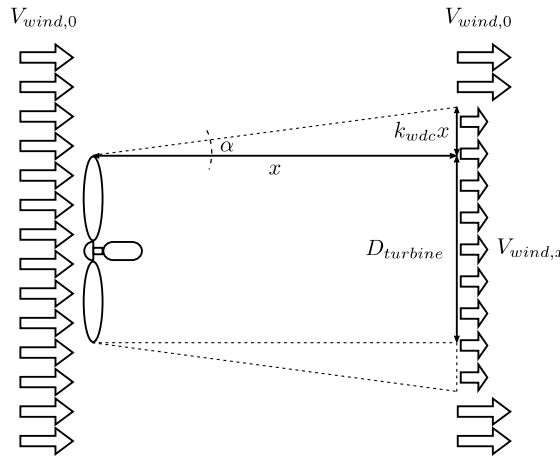
Fig. 4.2. Schematic view of Jensen's wake model. Source [108].

4.3.2 Jensen's Multiple Wake Model

The models described in section 4.2 are single wake models. However, in a wind farm with a large number of wind turbines, it is quite possible that one wind turbine is affected by the wakes of several wind turbines, either partially or completely. This situation is shown in Fig. 4.3. In cases, such as the one depicted in this figure, the multiple wake effect should be taken into account. This can be done by different empirical methods [123]. These methods are:

- Sum of squares of velocity deficits

- Energy balance
- Geometric sum
- Linear superposition
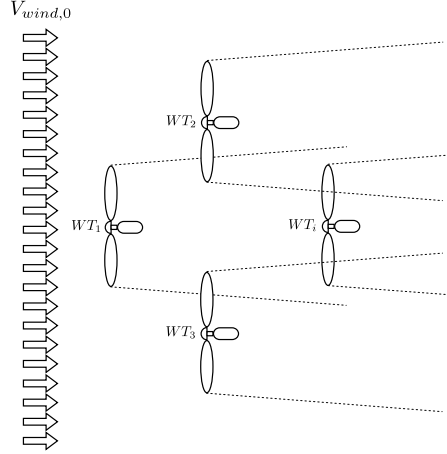
Fig. 4.3. Example of a WT affected by the wake effect of multiple wind turbines.

The sum of squares of velocity deficits is chosen according to Katic recommendations [109]. In this sense, the wind speed at WT_i, which is shadowed by the wake of wind turbines WT_j upstream, is given by equation (4.2) according to reference [123].

$$V_{wind,WT_i} = V_{wind,0} \left[1 - \sqrt{\sum_{j=1}^{N_{WTs,up}} \beta_{WT_{ij}} \left(1 - \frac{V_{wind,WT_{ij}}}{V_{wind,0}} \right)^2 } \right] \tag{4.2}$$

Being,

$N_{WTs,up}$: number of wind turbines upstream of WT_i.

$V_{wind,WT_{ij}}$: wind speed at WT_i due to the incidence of the wake of WT_j.

V_{wind,WT_i} : wind speed at WT_i.

The weighting factor $\beta_{WT_{ij}}$ is the ratio of the shadowed area by the wake in relation to the total rotor area. This ratio is given by equation (4.3) according to reference [124].

$$\beta_{WT_{ij}} = \frac{A_{shad}}{A_{WT_i}} \tag{4.3}$$

Being,

$$A_{WT_i} = \pi r_2^2 \tag{4.4}$$

$$A_{shad} = r_1^2 \cos^{-1}\left(\frac{r_1^2 + d^2 - r_2^2}{2 \cdot d \cdot r_1}\right) + r_2^2 \cos^{-1}\left(\frac{r_2^2 + d^2 - r_1^2}{2 \cdot d \cdot r_2}\right)$$
$$- d \cdot r_1 \sin\left[\cos^{-1}\left(\frac{r_1^2 + d^2 - r_2^2}{2 \cdot d \cdot r_1}\right)\right] \quad (4.5)$$

The parameters r_1, r_2 and d are shown in Fig. 4.4.
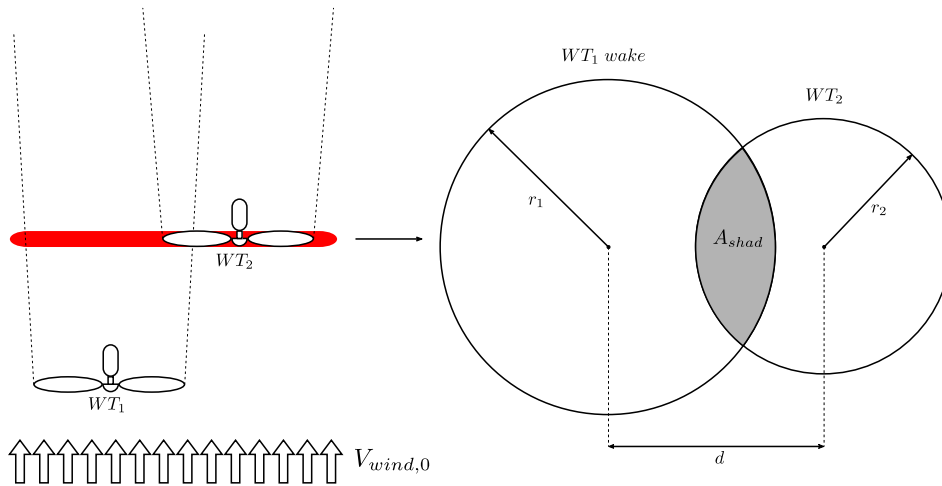
Fig. 4.4. Partial shadowing at WT_2 produced by the wake of WT_1.

4.3.3 Jensen's Model Implementation in Matlab®

Jensen's model has been implemented in a *.m-file in Matlab®. This script is added to the Simulink®-based model of the OWPP (presented in section 7.3), thus considering WT wake effect in power system simulations as presented in reference [125]. Fig. 4.5 shows the schematic diagram of this tool. The figure depicts the input- and output variables required by the Matlab® script.
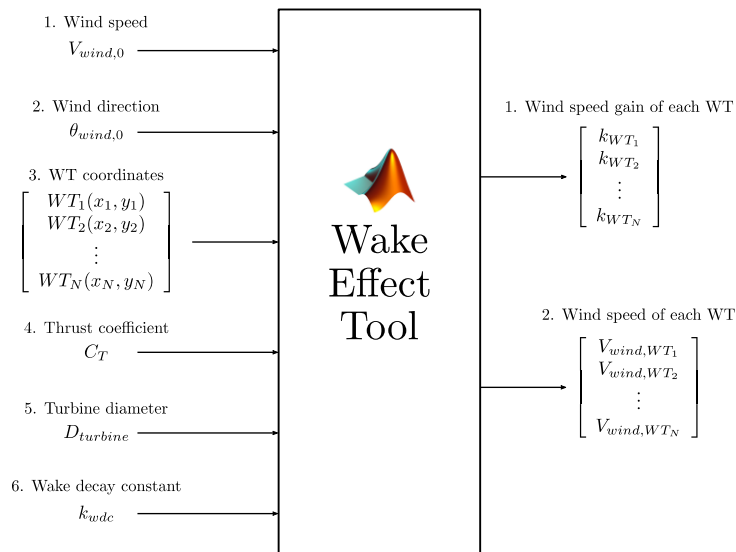
Fig. 4.5. Schematic diagram of the wake effect tool.

61

The following is a simplified pseudo-code of the Matlab® script.

1. Transform the coordinates of the wind turbines based on the direction of the free wind stream ($\theta_{wind,0}$).

2. Create an array of variables between wind turbines. The following variables are computed:

    2.1. Separation distance according to new coordinate system for each pair of wind turbines.

    2.2. Single wake of each WT, computed by equation (4.1).

    2.3. Weighting factor for each pair of wind turbine, equations (4.3) to (4.5).

        2.3.1. Complete shadowing $(\beta = 1)$.

        2.3.2. Partial shadowing $(0 < \beta < 1)$.

        2.3.3. Null shadowing $(\beta = 0)$.

3. Compute the wind speed gain of each WT, equation (4.6).

$$k_{WT_i} = \left[1 - \sqrt{\sum_{j=1}^{N_{WTs}-1} \beta_{WT_{ij}} \left(1 - \frac{V_{wind,WT_{ij}}}{V_{wind,0}} \right)^2} \right] \tag{4.6}$$

4. Compute the incident wind speed of each WT, equation (4.7).

$$V_{wind,WT_i} = V_{wind,0} k_{WT_i} \tag{4.7}$$

The results obtained with this tool are presented in subsection 7.3.2 for the OWPP base scenario.

4.4 Chapter Summary

This chapter has presented an overview of wind turbine wake models. Jensen´s model has been chosen to estimate the mean wind speed at each wind turbine according to the spatial distribution of the OWPP and wind conditions, i.e. wind speed and wind direction. Jensen's model has been implemented in a Matlab® script, which can be added to the Simulink®-based model of an OWPP. This way, wake effect is considered in power system simulations of an OWPP as presented in chapter 7 and chapter 9.

Chapter 5

Transformer Modeling

This chapter presents a Frequency-Dependent STC model of a three-phase two-winding transformer. The model is intended to be used for the representation of the power transformers in an OWPP scenario. For example, the Simulink®-based model of the OWPP base scenario that is presented in chapter 7. The transformer model includes four main parameters. These are the frequency-dependent behavior of the winding resistance, the impedance of the transformer core, stray capacitances and the zero-sequence impedance. Several approaches regarding the source of information have been identified and can be used to obtain the parameters of the transformer model. These approaches are manufacturer datasheets, parameter estimation, design information, and laboratory tests. Guidelines for transformer model parameterization are presented according to these approaches.

5.1 Introduction

Proper modeling of power transformers is important for performing harmonic analysis in offshore wind power plant scenarios. Accurate enough representation of a transformer can be very difficult due to two main factors. First, there are different core and winding designs. In this sense, the approach for modeling a specific type of transformer is not replicable to other designs. Second, transformer behavior is non-linear and frequency-dependent. Therefore, the behavior of the main physical features must be correctly represented. These features are:

- Self- and mutual inductances between coils.

- Skin effect and proximity effect in coils.
- Leakage fluxes.
- Magnetic core saturation.
- Hysteresis and Eddy current losses in the core.
- Capacitive effects.

The level of detail of a model is mainly determined by the available data for the determination of its parameters. An advanced model that requires confidential design data from the manufacturer or atypical measurements can rarely find application in practical studies. A less complex model based on commonly available data, e.g. standard nameplate and empirical parameters, is most suitable for the objectives and limitations of this Ph.D. thesis. Therefore, the selection of a model with these characteristics is performed in this chapter, together with some guidelines for the determination of the model parameters.

This chapter is structured as follows. Section 5.2 gives an overview of the most important transformer models to consider frequencies up to 10 kHz, which is a frequency range higher than the one required for the studies of this Ph.D. thesis. In this section, an overview of transformer core models and the modeling of frequency-dependent effects are presented as well. Section 5.3 presents the electrical schematic of the Frequency-Dependent STC model. The model aims to reproduce the behavior of a three-phase three-legged stacked core transformer. Section 5.4 provides guidelines for transformer model parameterization. Finally, section 5.5 gives the chapter summary.

5.2   Overview of Transformer Models

Transformer models for low- and mid-frequency range, as called in specialized references to consider frequencies up to 10 kHz, can be classified into three groups [126] as shown in Fig. 5.1. The first group uses either a branch impedance or an admittance matrix. The second group is an extension of the saturable transformer component model to a multi-phase transformer. Finally, the third group consists of topology-based models for which many approaches have been proposed. The more important ones are presented.
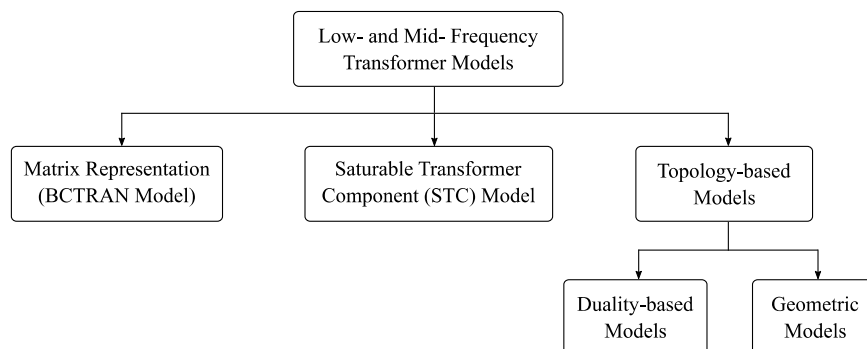
Fig. 5.1. Classification of low- and mid-frequency transformer models.

Even though some of the models in their original form are not valid for the entire frequency range of interest in this Ph.D. thesis, they can be extended in frequency by adding equivalent networks that account for the frequency dependence of the parameters. The following subsections present a summary of these models and the equivalent networks to extend their representation in frequency.

5.2.1 Matrix Representation

The matrix representation, also known as BCTRAN model in EMTP tools, of a three-phase two-winding transformer is depicted in Fig. 5.2(a). The mathematical representation of the BCTRAN model is given by equation (5.1). This model represents the resistance $[R]$ and inductance $[L]$ matrices of the transformer branch impedance. The dimension of these matrices is equal to the number of windings.

$$\frac{d}{dt}[i(t)] = [A][v(t)] - [A][R][i(t)] \tag{5.1}$$

Being,

$$[A] = [L]^{-1} \tag{5.2}$$

As inferred from the inductance matrix, BCTRAN model includes phase-to-phase couplings and terminal characteristics. However, it does not consider the representation of the core and differences in winding topology. BCTRAN model is linear and it is reasonably accurate for frequencies below 1 kHz [126].
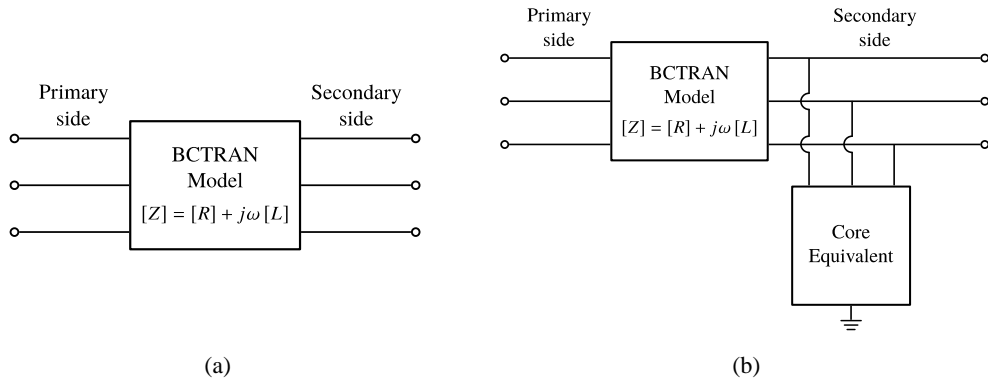
Fig. 5.2. BCTRAN model for a three-phase two-winding transformer. (a) Without an externally attached core. (b) With an externally attached core. Source [126].

For the simulation of saturable cores, a core equivalent can be attached to the model terminals, as shown in Fig. 5.2(b). The representation of the transformer core is not topologically correct, but it is good enough in many cases [126]. The mathematical formulation of the BCTRAN model can be found in reference [127].

5.2.2 Saturable Transformer Component (STC) Model

This model, also known as T-transformer model, is based on the star-circuit representation shown in Fig. 5.3. Coupling between windings is not considered in this model. Saturation and hysteresis effects are modeled by adding an extra non-linear inductor at the star point.
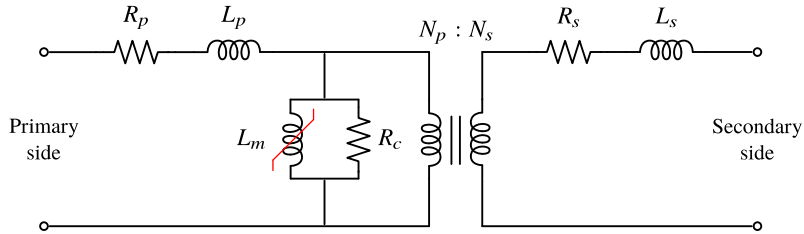
Fig. 5.3. STC model of a single-phase two-winding transformer. Source [128].

The STC model can be extended to three-phase units through the addition of a zero-sequence reluctance parameter. In a three-phase two-winding transformer, some part of the zero-sequence flux does not flow to the core. In this case, zero-sequence current-flux characteristics is linear (not saturable) [129]. The equivalent circuit is shown in Fig. 5.4.
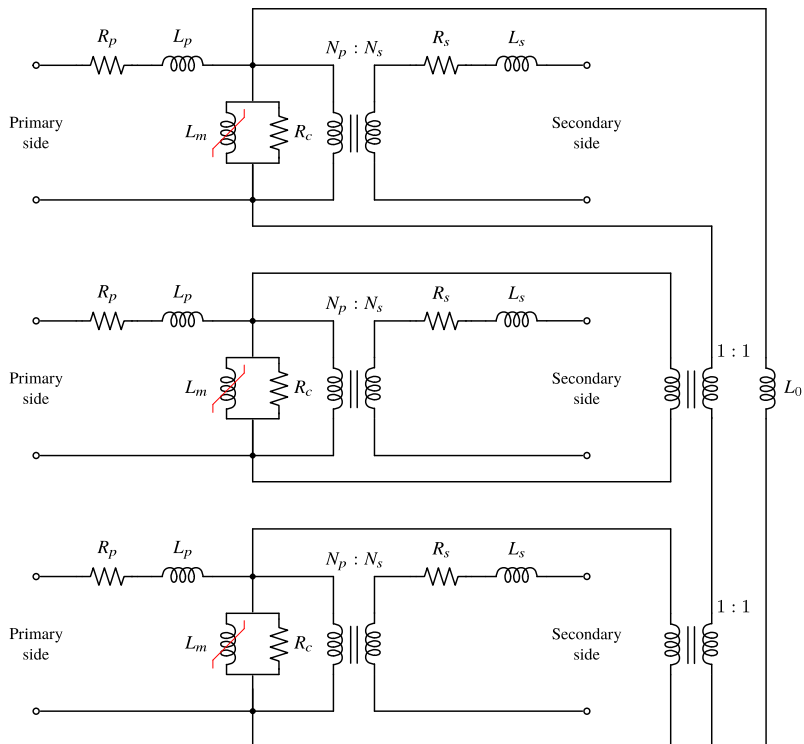
Fig. 5.4. STC model of a three-phase two-winding transformer. Source [129].

The input data of the model consists of R-L values of each star branch, the turn ratio, and the information of the magnetizing branch. This model presents some limitations, which are [126]:

- It cannot be used for more than three-windings.
- The magnetizing branch is connected to the star point, which is not always the correct topological connecting point.

- Numerical instability can be presented in time-domain simulations for three-winding transformers. Reference [130] points out that the negative value of one of the short-circuit reactances in the model is the reason of the numerical instability. Solutions for this issue are described in references [130,131].

5.2.3 Topology-based Models

According to the classification of Fig. 5.1, topology-based models are split into two subgroups. A brief description of these two subgroups is discussed below.

Duality-based Models

Topologically correct equivalent circuit models can be derived from a magnetic circuit model using the principle of duality, proposed by Colin Cherry in 1949. The principle is mainly based on the following two points:

- First, it is necessary to represent the magnetic network. With this representation, it is possible to recognize the leakage and common flux and the magnetomotive force (MMF).
- Second, the transformer electric equivalent circuit is obtained applying the basic rules of duality (Table 5.1). Winding resistances, core losses, and capacitive coupling effects are not obtained directly from the transformation but can be added to this equivalent electrical circuit.

Table 5.1. Duality transformations between magnetic and electric circuits.

Magnetic Circuit	Duality	Electric Circuit
MMF	⇔	Current Source
Reluctance	⇔	Susceptance
Meshes	⇔	Nodes
Nodes	⇔	Meshes

In general, these models are derived using a circuit-based approach without the use of a mathematical description. Duality-based models include the effects of saturation in each individual leg of the core, interphase magnetic coupling, and leakage effects.

The most important models that are derived based on the duality principle for three-phase stacked core transformers are mentioned below. The cited references provide useful information to reproduce the models. For the two last models, the magnetic and electrical circuits are presented.

- In 1981, Dick and Watson presented the derivation of the model of a three-phase three-legged stacked core transformer [132]. The main contributions of their work were the proposal of a new hysteresis model and the determination of transformer parameters from measurements.
- In 1994, de León and Semlyen proposed a three-phase transformer model for the calculation of electromagnetic transients. The transformer representation is derived from the combination of two approaches, leakage inductances and principle of duality. The model consists of a set of state equations solved with the trapezoidal

rule of integration in order to obtain an equivalent Norton circuit at the transformer terminals. Its main features are three. First, the basic elements for the winding model are the turns. Second, the model includes the losses due to eddy currents in windings and in the iron core. Third, the solution of the state equations is obtained in decoupled iterations. Details of this model can be found in reference [133].

- In 2007, Bruce Mork et al. developed a topologically correct hybrid transformer model for low- and mid-frequency transient simulations. The model is developed in a modular approach and is suitable for frequency values up to 5 kHz. The model represents a duality-based lumped-parameter saturable core. It also includes matrices accounting for leakage and capacitive effects. Furthermore, it represents the frequency-dependent coil resistance via a Foster equivalent network. The reader is suggested to review reference [134] for more details.

Fig. 5.5 shows the magnetic circuit for the derivation of the hybrid transformer model of a three-legged stacked core transformer. Shaded reluctances represent the flux paths of legs and yokes of the transformer core while unshaded reluctances represent leakage flux paths.
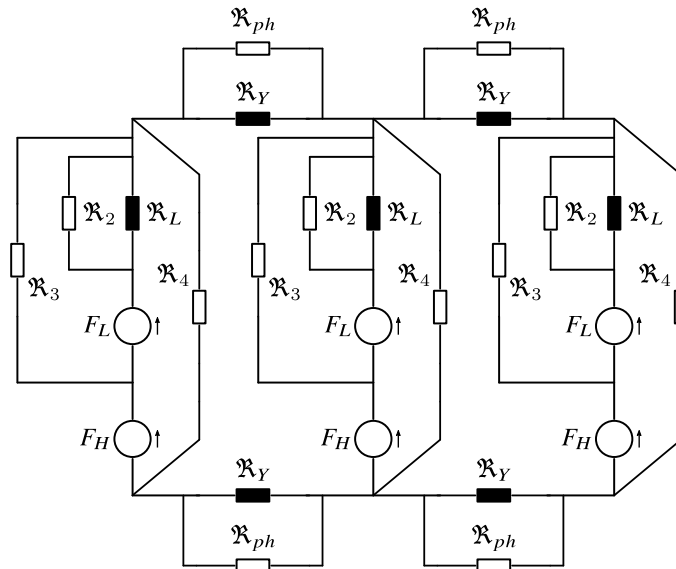
Fig. 5.5. Magnetic circuit of the hybrid transformer model proposed by Mork et al. for a three-phase three-legged stacked core transformer. Source [134].

Fig. 5.6 shows the electrical schematic of the hybrid model for a three-phase three-legged stacked core transformer.

The procedure for the determination of the electrical parameters of this model via laboratory measurements is presented in reference [135]. Implementation of this transformer model and some guidelines for parameter determination are explained in reference [136]. An important aspect to point out is that this model has been widely accepted due to its accurate results. The only problem is the difficulty, in some cases, to have all the available data for its implementation.
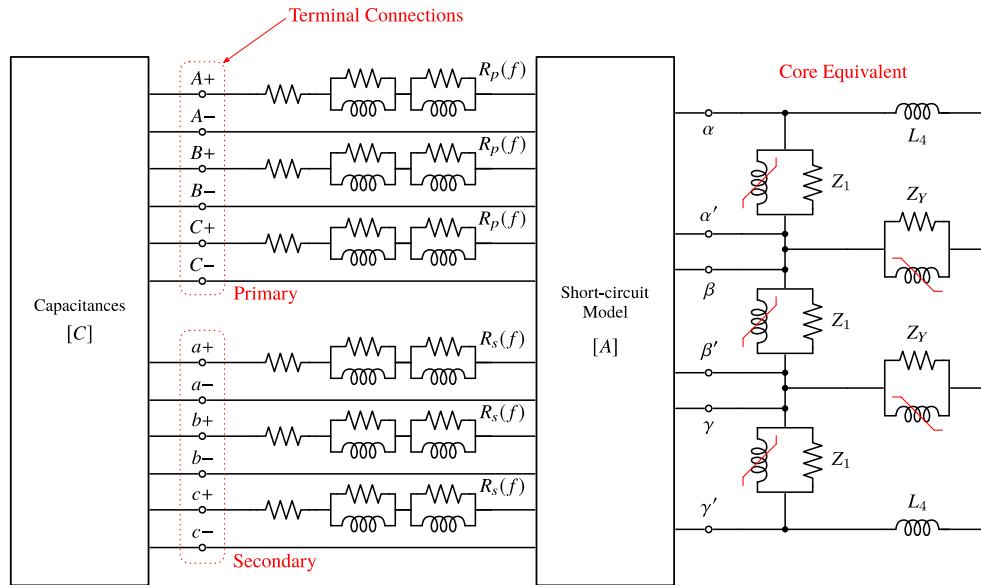
Fig. 5.6. Electrical equivalent circuit of the hybrid transformer model proposed by Mork et al. for a three-phase three-legged stacked core transformer. Source [134].

- In 2010, Chiesa et al. proposed a transformer model for low- and mid-frequency transient studies. The model focuses on the behavior in saturation and estimation of residual fluxes. It accurately represents energization (inrush currents) and de-energization transients of a three-phase three-legged stacked core transformer. Fig. 5.7 shows the magnetic circuit in order to derive the electrical equivalent by the principle of duality. On the other hand, Fig. 5.8 shows the electrical equivalent network of this transformer model. Details of this model can be found in reference [137].
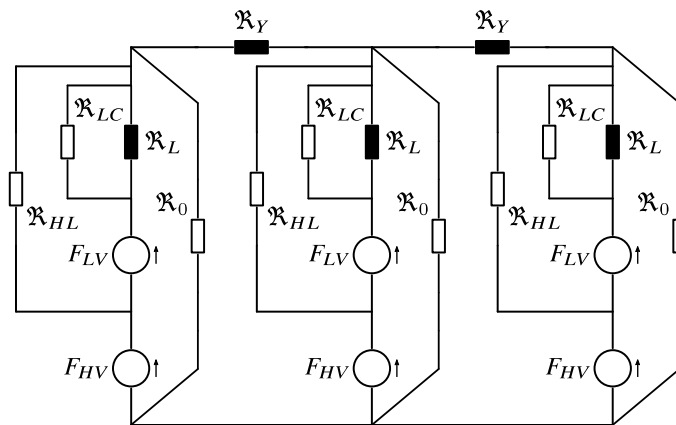
Fig. 5.7. Magnetic circuit of the transformer model proposed by Chiesa et al. for a three-phase three-legged stacked core. Source [137].
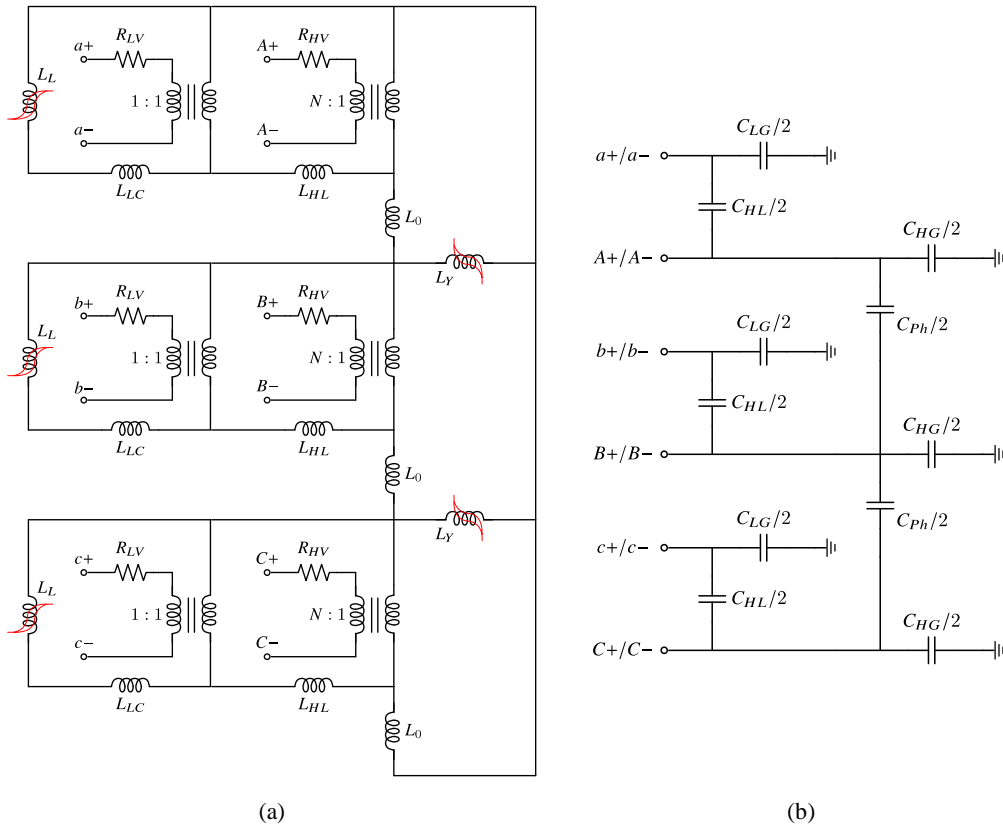
Fig. 5.8. Electrical equivalent circuit of the transformer model proposed by Chiesa et al. for a three-phase three-legged stacked core transformer. (a) Equivalent electric circuit. (b) Capacitances of the transformer model. Source [137].

Geometric Models

Topologically correct models can be based on the geometry of the transformer as well. These models use equation (5.3) for their formulation.

$$[v(t)] = [R][i(t)] + \frac{d}{dt}[\Psi(t)] \tag{5.3}$$

Being,

$$[\Psi(t)] = [L][i(t)] \tag{5.4}$$

The coupling between magnetic and electrical equations is made by taking into account the core topology. A short summary of the most representative models is presented below.

- In 1993, Hatziargyriou et al. developed a Generalized Transformer Model (GMTRAN) based on the analysis of its magnetic core circuit [138]. The most important contribution of this model was the derivation of the $[L]$ matrix from the core topology.

- In 1997, Arrillaga et al. proposed the Unified Magnetic Equivalent Circuit (UMEC) model. This model uses a normalized core for the derivation of the inductance matrix. Leakage permeances can be obtained from open and short-

circuit tests. UMEC model is widely used in EMT programs such as PSCAD/EMTDC. The reader is suggested to review references [139,140] for more details.

5.2.4 Overview of Core Models

Iron core behaviour is usually represented by a relationship between the magnetic flux density B and the magnetic field intensity H. A general difficulty in modeling the magnetization curves is the fact that each of the magnetic field values is related to an infinity of possible magnetization paths depending of the history of the core.

There are several models for the representation of the transformer core. Fig. 5.9 shows the most widely used models in EMTP simulation tools [141]. Below a brief description of these models.

- Type 98 (T98): This model consists of a non-linear inductance to which a parallel linear resistance is added to represent the Eddy losses. The non-linear inductance is normally represented by the Frolich equation or a modified version [142].

- Type 96 (T96): The Type 96 model consists of an inductive element that includes a hysteresis cycle including the hysteresis losses. A parallel resistive element is added to represent the remaining losses [143]. A constant width is added to the Frolich equation of the T98 model in order to represent a hysteresis loop.

- Jiles-Atherton (JA): This model is one of the best-known models of magnetic hysteresis. The main advantage of this model is the fact that allows the connection with physical parameters of the magnetic material (dual model). Jiles-Atherton model has two versions, static and dynamic. The reader is suggested to review reference [144] for more details.

- Dynamic Hysteresis Model (DHM): This model requires absolute core dimensions of the legs and yokes, number of turns and ferromagnetic material properties. The model represents the total core losses. Hysteresis losses, Eddy losses and stray losses are not split in the model. In many cases, it is unpractical to represent the transformer core impedance with this model due to lack of available information. Details of this model can be found in reference [141].
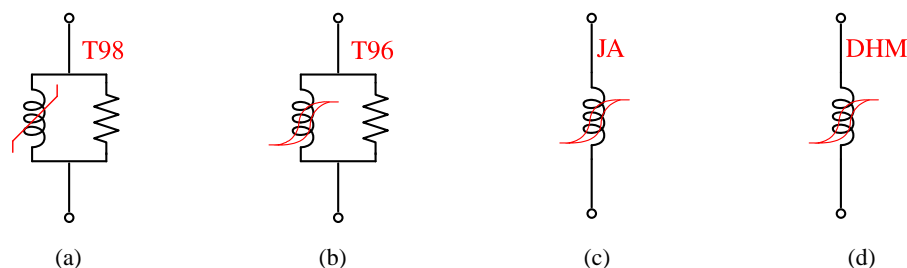
Fig. 5.9. Available models in EMTP for the representation of the transformer core. (a) T98 model. (b) T96 model. (c) JA model. (d) DHM model. Source [141].

Table 5.2 presents a qualitative comparison describing the magnetization model behavior for open-circuit test, ring-down and inrush current according to conclusions presented in reference [141].

Table 5.2. Qualitative comparison of the magnetization model behavior describing the open-circuit test, ring-down and inrush current. Source [141].

Core Model	Open-Circuit Test	Ring-down	Inrush Current
T98	Good. Low P_0 at E_0>rated.	Zero	Too low. Pattern is relatively different.
T96	Good. Low P_0 at E_0>rated.	Low	Ok. Pattern different at diagonal.
JA	Too low I_0 and P_0 at E_0>rated.	Ok	Ok. Pattern Ok.
DHM	Too low I_0 and P_0	Too high	Too high. Pattern Ok.

5.2.5 Modeling of Frequency-Dependent Effects

A brief description of the modeling of frequency-dependent effects in transformers is discussed next.

Frequency-Dependent Winding Resistance

Winding resistances vary widely depending on the frequency of the current flowing through it. The variation is due to skin effect and proximity effect. Skin effect is caused by the non-uniform distribution of current in the conductor; therefore, the effective resistance increases. On the contrary, proximity effect is caused by the external magnetic field generated from the flow of current in other conductors. In a transformer, a high number of layers in the coil lead to a great resistance variation due to this effect. Skin effect dominates the losses up to a certain frequency, then proximity effect becomes predominant.

The frequency-dependent variation of the winding resistances can be implemented in a transformer model by using equivalent networks. Foster equivalent networks, depicted in Fig. 5.10, are widely used to represent the frequency-dependent variation of the winding resistance. In general, the equivalent networks must be of infinite order to exactly reproduce the variation of the winding resistance at all frequencies. However, this fact is unpractical and a network of finite order must be defined to represent the variation of the winding resistance over the frequency range of interest.

Several fitting procedures have been developed to determine the circuit parameters of this equivalent network. The two most remarkable are Bode's asymptotic fitting and Vector Fitting (VF). These two fitting techniques are briefly described in Appendix A.

Reference [126] suggests that a series model of order 3 or less is adequate for practical studies. Such a model neglects displacement currents, so it is valid at frequencies below the first winding resonance (i.e. up to tens of kilohertz).

Details of the modeling of frequency-dependent winding resistance can be found in references [145,146].
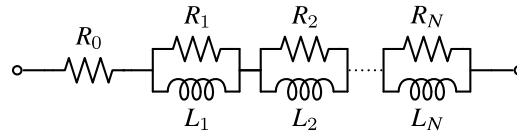
Fig. 5.10. Series Foster equivalent network for windings. Source [145].

Eddy Current Losses of the Core

As frequency changes, the flux distribution in the iron core lamination changes. At high frequencies, the flux will be confined to a thin layer close to the lamination surface, whose thickness decreases as the frequency increases. This indicates that inductances representing iron path magnetization and resistances representing Eddy current losses are frequency-dependent [44]. The circulation of these Eddy currents introduces additional losses. To limit their influence, a transformer core is built-up from a large number of parallel laminations.

Computationally efficient models have been derived by synthesizing a Foster or Cauer equivalent network to account for the Eddy current losses of the core. Cauer networks, depicted in Fig. 5.11, are the preferred choice because they have a physical meaning. In fact, Fig. 5.11(b) is the most common representation of the frequency-dependent behavior of the Eddy current losses in the transformer iron core due to its duality with the magnetic circuit.

In order to represent strictly the behavior of the iron core by this Cauer equivalent network, inductive components representing the magnetizing reactances must be non-linear to account for the hysteresis and saturation effects. However, since the high-frequency components do not contribute appreciably to the flux in the transformer core, it can be assumed that only low-frequency components are responsible for driving the core into saturation. It may, therefore, be justifiable to represent as non-linear only the first section of the model [44]. Details of the modeling of Eddy current losses in transformer cores can be studied with more detail in references [44,126,145,147].
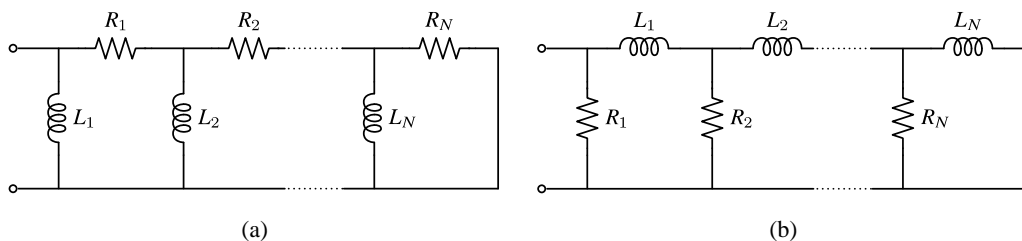
Fig. 5.11. Cauer equivalent circuits for representing the frequency-dependent variation of Eddy current losses. (a) Standard Cauer equivalent. (b) Dual Cauer equivalent. Source [145].

5.3   Frequency-Dependent STC Model

Fig. 5.12 shows the STC transformer model with its extension in frequency. The frequency-dependent STC model is adopted for the representation of the power transformers in an OWPP. The model includes the following parameters:

- Short-circuit impedance.
- Core impedance.
- Stray capacitances.
- Zero-sequence impedance.
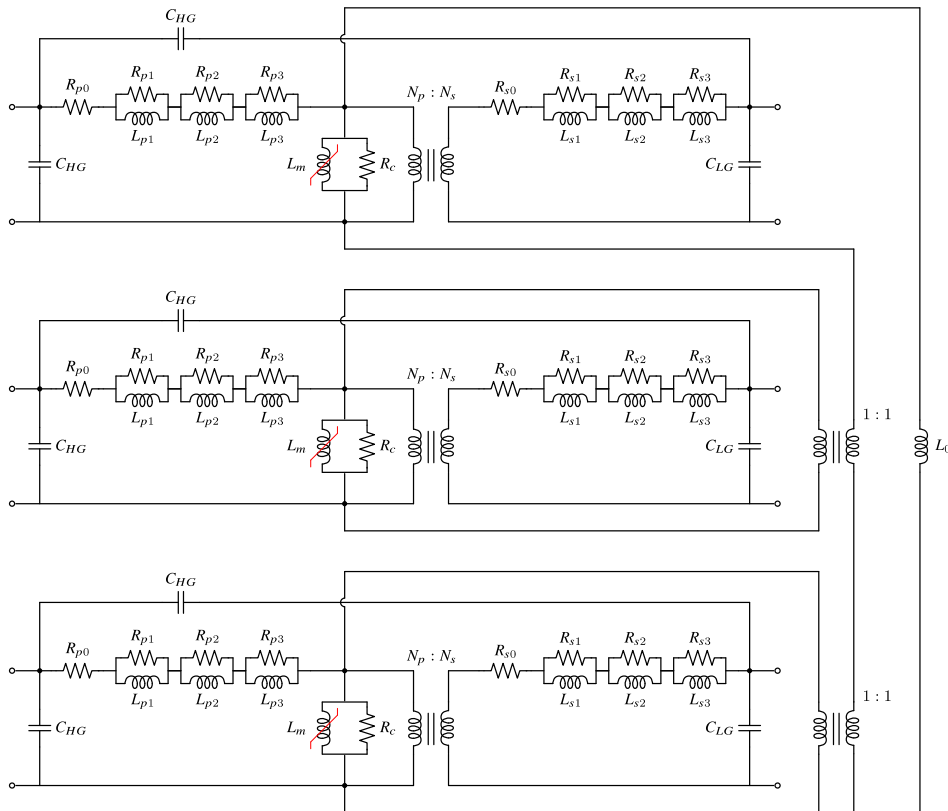
Fig. 5.12. Frequency-Dependent STC model for a two-winding three-legged stacked core transformer.

It is worth to point that some of these parameters are not reproduced for the OWPP base scenario presented in chapter 7.

Each parameter of the transformer model shown in Fig. 5.12 is briefly described below.

Short-circuit impedance

The frequency-dependent behaviour of the short-circuit impedance is represented by a Foster equivalent network of order three. According to reference [126], a Foster equivalent network of order two or three can be adequate for frequencies up to 10 kHz. This frequency range is higher in comparison with the frequency range of study in this Ph.D. thesis. This characteristic allows a good approximation of the frequency-dependent behavior of the winding resistance.

Vector fitting is used for the computation of the parameters of this equivalent network. As pointed out, a brief description of VF is addressed in Appendix A. The short-circuit impedance of the primary and the secondary side are expressed in the Lapace domain by equations (5.5) and (5.6), respectively.

$$Z_p = R_{p0} + \frac{R_{p1} \cdot sL_{p1}}{R_{p1} + sL_{p1}} + \frac{R_{p2} \cdot sL_{p2}}{R_{p2} + sL_{p2}} + \frac{R_{p3} \cdot sL_{p3}}{R_{p3} + sL_{p3}} \tag{5.5}$$

$$Z_s = R_{s0} + \frac{R_{s1} \cdot sL_{s1}}{R_{s1} + sL_{s1}} + \frac{R_{s2} \cdot sL_{s2}}{R_{s2} + sL_{s2}} + \frac{R_{s3} \cdot sL_{s3}}{R_{s3} + sL_{s3}} \tag{5.6}$$

Core impedance

A type 98 transformer core model, Fig. 5.9(a), has been chosen due to its relative simplicity and low computational cost in comparison with other models described in subsection 5.2.4.

The non-linear inductance L_m represents the magnetic saturation of the core. This non-linear inductance is represented by the Frolich equation, which is described in the next section.

The transformer core losses are represented by the parallel resistor R_C. Eddy current losses, hysteresis losses and stray load losses can be included in the resistance value. The resistor adds area to the anhysteretic curve.

The frequency-dependent behavior of Eddy current losses can be incorporated by replacing the T98 core representation to the one of Fig. 5.13. According to reference [44], a Cauer equivalent circuit of order two is enough for transients below 10 kHz. This representation is not incorporated in the model of Fig. 5.12 because the transformer models that were studied in section 5.2 (state of the art models) do not incorporate it.
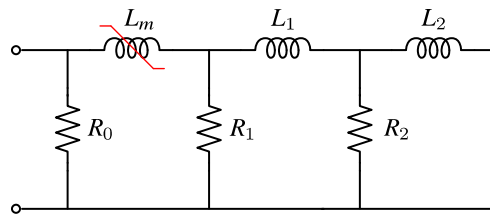
Fig. 5.13. Dual Cauer equivalent circuit to account for the frequency dependence behavior of the Eddy current losses of the transformer core.

Stray capacitances

The capacitances of windings to ground (C_{HG}, C_{LG}) and between windings of the same phase (C_{HL}) are included in the model. Capacitances between windings of different phase can be included as well. These capacitances are not included in the model due to lack of information mainly.

5.4 Guidelines for Transformer Model Parameterization

An exact procedure cannot be defined for the determination of the parameters of the transformer model. This is mainly because the available information for a specific transformer depends on several factors such as type of transformer, physical availability of the transformer, installation facilities for transformer testing, equipment, manufacturer, and many more.

In this sense, several approaches regarding the source of information can be identified and be used to obtain the parameters of the transformer model. These approaches are manufacturer datasheets, parameter estimation, design information, and laboratory tests. A combination of these approaches is usually performed, especially between the information provided by the manufacturer datasheet and estimations.

Fig. 5.14 depicts the approaches for parameterization of advanced transformer models. The aim of these models, e.g. the one presented in Fig. 5.12, is to reproduce the frequency-dependent and non-linear behavior of a transformer. As shown in Fig. 5.14, the selection of an approach or approaches depends on requirements such as availability and accuracy.
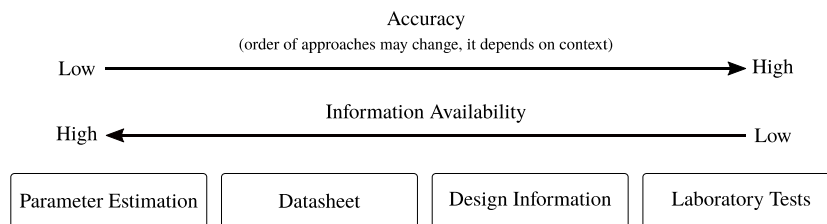
Fig. 5.14. Approaches for parameterization of advanced transformer models to reproduce the frequency-dependent and non-linear behavior of a transformer.

This section presents some key points for transformer model parameterization. As already mentioned in section 5.1, the information presented in this section applies to two-winding three-legged stacked core transformers. For more details on procedures and equations of this type and other types of transformers, the reader is suggested to review the references that are cited along this section.

5.4.1 Datasheet with Parameter Estimation

It is quite common for transformer model parameterization to combine information given in the transformer datasheet with estimation of parameters. This is done to include, for example, the frequency-dependent and non-linear behavior of the transformer. A description of this approach for each transformer parameter is presented below.

Short-circuit impedance

The short-circuit impedance at rated frequency can be determined with information provided by the manufacturer datasheet or nameplate (short-circuit impedance or losses, and base power). The manufacturer of the transformer does not provide information about the frequency-dependent behavior of the short-circuit impedance.

To include the frequency-dependency of transformer winding resistance, the approach presented in reference [148] can be used. This approach is based on typical curves of $R(\omega)/L$ ratios (CIGRE typical curves). From the resistance at rated frequency, the inductance component is calculated via Kramers-Kronig dispersion method. The resulting short-circuit impedance is subjected to low-order rational approximation and represented by means of a Foster equivalent circuit of order three. The per-unit R and L parameters of the Foster equivalent network of order three are given in Table 5.3.

Table 5.3. R and L parameters for the Foster equivalent network of order three. Source [148].

Parameter	20 MVA	100 MVA	500 MVA
R_0/R_{50Hz}	0.85	0.85	0.85
R_1/R_{50Hz}	21.0768	33.4367	31.3912
R_2/R_{50Hz}	2205.3118	2176.8834	2080.7688
R_3/R_{50Hz}	2311.709	2483.8188	1723.2928
L_1/R_{50Hz}	$5.1203 \cdot 10^{-3}$	$6.2436 \cdot 10^{-3}$	$6.0033 \cdot 10^{-3}$
L_2/R_{50Hz}	$25.0870 \cdot 10^{-3}$	$28.0169 \cdot 10^{-3}$	$27.9849 \cdot 10^{-3}$
L_3/R_{50Hz}	$0.9745 \cdot 10^{-3}$	$1.0237 \cdot 10^{-3}$	$1.1650 \cdot 10^{-3}$
$R_{eq(50Hz)}/R_{50Hz}$	1.0002	1.0003	1.0001
$L_{eq(50Hz)}/R_{50Hz}$	$31.1519 \cdot 10^{-3}$	$35.2625 \cdot 10^{-3}$	$35.1312 \cdot 10^{-3}$
$R_{eq(60Hz)}/R_{50Hz}$	1.0659	1.0661	1.0659
$L_{eq(60Hz)}/R_{50Hz}$	$31.1388 \cdot 10^{-3}$	$35.2529 \cdot 10^{-3}$	$35.1215 \cdot 10^{-3}$

This approach can be easily applied to any transformer in the range of 20-500 MVA by rescaling the given Foster circuit parameters by the 50 Hz winding resistance. The reader is suggested to review reference [148] for more details.

Core impedance

Transformer datasheet provides information about the open-circuit test, excitation current and no-load losses. From the information of these tests, the magnetizing inductance and the core losses can be determined as described below.

Magnetizing Inductance:

Depending on the number of points provided by the manufacturer, a linear or non-linear magnetizing inductance can be represented.

- One point: It is given at rated voltage (1 Vpu). A linear magnetizing inductance can be represented.
- Two points: If given, these points are typically provided at 1 Vpu and 1.1 Vpu. A non-linear representation of the magnetizing inductance can be modeled with the two-term Frolich equation [149], equation (5.7).

$$\Psi = \frac{i}{a + b \cdot |i|} \tag{5.7}$$

- Three points: If given, these points are typically provided at 0.9 Vpu, 1 Vpu and 1.1 Vpu. A non-linear representation of the magnetizing inductance can be modeled with the three-term Frolich equation [150], equation (5.8).

$$\Psi = \frac{i}{a + b \cdot |i| + c \cdot \sqrt{|i|}} \tag{5.8}$$

- More than three points: A better approach can be achieved by using a curve fitting procedure via least squares algorithm.

Variables a, b and c of equations (5.7) and (5.8) must be fitted for each transformer.

In the Frolich equation there is a horizontal asymptote indicating that, from a current value, the flux does not continue to increase [150]. This characteristic restricts the use of the Frolich equation for values of flux between zero and the obtained saturation value [150]. In case of currents that demand a flux greater than the saturation flux, the inductance value must be set to that of the vacuum L_∞. In this case, the two-term or three-term Frolich equation can be reformulated as given by equation (5.9) and equation (5.10) [149], respectively.

$$\Psi = \frac{i}{a + b \cdot |i|} + L_\infty \cdot i \tag{5.9}$$

$$\Psi = \frac{i}{a + b \cdot |i| + c \cdot \sqrt{|i|}} + L_\infty \cdot i \tag{5.10}$$

The L_∞ variable is given by equation (5.11) [150].

$$L_\infty = \mu_0 \cdot N_{turns}^2 \cdot \frac{A}{L} \tag{5.11}$$

Being,

μ_0 : permeability of the vacuum.

N_{turns} : number of turns of the winding.

A : cross-sectional area of the core.

In case the manufacturer does not provide enough information to represent a non-linear magnetizing inductance, the $B - H$ curve of the Armco M4 core material can be adopted. Table 5.4 gives several $B - H$ data points for this core material. This type of material is commonly used in power transformer cores [151].

Table 5.4. B-H data points for Armco M4 core material. Source [151].

B (T)	0	0.2	0.4	0.6	0.8	1.0	**1.2**	1.4	**1.6**	1.7	1.8
H (A/m)	0	2	4	6	8.4	11.1	**14.4**	23	**55**	130	416

The $B-H$ anhysteretic curve can be represented, for example, by the Frolich empirical expression. This is given by equation (5.12).

$$B = \frac{H}{a' + b' \cdot |H|} \tag{5.12}$$

If transformer dimensions are known, the parameters of the $B-H$ curve can be expressed to the equivalent $\Psi - i$ curve, equations (5.13) and (5.14).

$$\Psi = B \cdot A \cdot N_{turns} \tag{5.13}$$

$$i = \frac{H \cdot l}{N_{turns}} \tag{5.14}$$

Being,

A: core cross-sectional area.

l: mean length of the magnetic path.

N_{turns}: number of turns of the winding.

Where a, b and a', b' are related by equations (5.15) and (5.16).

$$a = a' \cdot \frac{l}{A \cdot N_{turns}^2} \tag{5.15}$$

$$b = \frac{b'}{A \cdot l} \tag{5.16}$$

If transformer dimensions are not known, the $\Psi - i$ curve of the Armco M4 core material can be obtained with the typical dimension ratios shown in Table 5.5.

Table 5.5. Typical dimension ratios of three-legged stacked core transformers. Source [151].

Dimension ratios	Cross-section area ratio	Length ratio
Leg	$A_{Leg1} = A_{Leg2} = A_{Leg3} = 1$	$l_{Leg1} = l_{Leg2} = l_{Leg3} = 1$
Yoke	$A_{Yoke1} = A_{Yoke2} = 1$	$l_{Yoke1} = l_{Yoke2} = 1.725$

Core losses:

The frequency-dependent core losses can be approximated by a straight line as shown in Fig. 5.15. The approximation can be expressed by equation (5.17) according to reference [152].

$$\frac{P_{loss}}{f} = W_{Hyst} + W_{Eddy} \cdot \frac{f}{f_r} \tag{5.17}$$

Being,

f: frequency at which the loss is measured or estimated.

f_r : rated frequency, 50 Hz or 60 Hz.

W_{Hyst} : Hysteresis loss per-cycle.

W_{Eddy} : Eddy loss per-cycle at rated frequency.

Taking equation (5.17) and writing the loss for the angular frequency, equation (5.18) is obtained.

$$P_{loss} = \frac{1}{2\pi}\left(W_{Hyst} \cdot \omega + W_{Eddy} \cdot \frac{\omega^2}{\omega_r} \right) \tag{5.18}$$

The resistance of the transformer core is given by equation (5.19).

$$R_C(\omega) = \frac{\Psi^2 \omega^2}{2 P_{loss}} \tag{5.19}$$

The hysteresis loss per-cycle and the Eddy loss per-cycle can be considered equal if there is no available information of the loss/cycle curve [152].
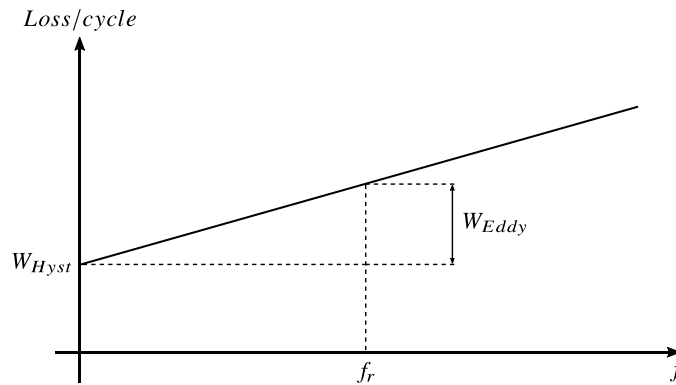
Fig. 5.15. Estimation of frequency-dependent transformer core losses. Source [152].

Capacitances

Transformer manufacturers usually do not provide information of the capacitance values in the datasheets. To include the capacitances of windings to ground and between windings, the values of Table 5.6 can be assumed. This table gives typical capacitance values of three-legged transformers for power ratings up to 75 MVA [153].

In reference [154], the values of this table have been compared with values of real wind turbine transformers and offshore substation transformers around these power ratings. The values of capacitances obtained in this reference are similar to the ones presented in Table 5.6.

Table 5.6. Typical stray capacitances of three-legged stacked core transformers. Source [153].

Nominal Power (MVA)	C_{HG} (nF)	C_{HL} (nF)	C_{LG} (nF)
1	1.2 – 14	1.2 – 17	3.1 – 16
2	1.2 – 16	1 – 18	3 – 16
5	1.2 – 14	1.1 – 20	5.5 – 17
10	4 – 7	4 – 11	8 – 18
25	2.8 – 4.2	2.5 – 18	5.2 – 20
50	4 – 6.8	3.4 – 11	3 – 24
75	3.5 – 7	5.5 – 13	2.8 – 13

5.4.2 Design Information

Manufacturers in general do not share information of the design of the transformer (e.g. transformer dimensions, $B - H$ curve of the core material, width of the laminations of the core, number of turns of each winding, and other variables). The design information is highly confidential.

There are two procedures that can be performed to determine the parameters of advanced transformer models with this type of information. These are Finite Element Method (FEM) simulations and analytical equations.

In general, FEM simulations provide accurate parameters. The main drawback of this method is to know with detail the design of the transformer under consideration. Furthermore, the computational time is high. FEM simulations are better suited for designing the transformer. The reader is suggested to review references [155,156] for more information about this method and its application to determine transformer parameters.

On the other hand, analytical equations provide a simpler and faster method for model parameterization of transformers. However, the accuracy is lower when compared with the accuracy of the FEM approach or laboratory tests. This is mainly due to simplifications. Below a brief description of some of the analytical equations that can be used to determine the parameters of a more advanced transformer model, e.g. the transformer model of Fig. 5.12. More details can be found in references [44,128,157]

Short-circuit impedance

The frequency-dependent winding resistance can be approximated according to equation (5.20) [158].

$$R_{sc}(\omega) = real\left\{ R_{DC} \cdot u\left[\coth(u) - \frac{2}{3}\tanh(u) + \frac{2}{3}n_{layers}^2 \cdot \tanh\left(\frac{u}{2}\right) \right] \right\} \tag{5.20}$$

$$u = (1 + j)\frac{a}{\delta_{skin}} \tag{5.21}$$

$$\delta_{skin} = \sqrt{\frac{1}{\pi f \sigma_{Cu}\mu_0}} \tag{5.22}$$

Being,

a : coil diameter.

δ_{skin} : skin depth.

σ_{Cu} : copper conductance.

μ_0 : vacuum permeability.

n_{layers} : number of layers.

The previous equation only takes into account skin effect. It does not take into account the proximity effect.

Core impedance

The effect of Eddy currents due to flux penetration in the core can be described by means of equation (5.23) [145,147].

$$Z_{core}(\omega) = x \cdot \tanh(x) \cdot \frac{4N_{turns}^2 A \rho_{core}}{l_{mag} d_{lam}^2} \qquad (5.23)$$

$$x = \frac{d_{lam}}{2} \sqrt{\frac{j\omega\mu_{core}}{\rho_{core}}} \qquad (5.24)$$

Being,

l_{mag} : length of the magnetic element (leg or yoke).

d_{lam} : thickness of the lamination.

N_{turns} : number of turns.

A : total cross-sectional area of the core (all laminations).

μ_{core} : permeability of the core material.

ρ_{core} : resistivity of the core material.

Equation (5.23) approximates the core impedance and account for Eddy current losses as a function of frequency. Hysteresis and stray losses are not taken into account with this expression. To consider these losses, information about the iron core material must be known.

Capacitances

The inner and outer sides of the windings can be considered as parallel plates of a capacitor [151]. The parallel plates of this capacitor are separated by a dielectric. In this sense, equation (5.25) is generally valid for calculating the capacitance between windings.

$$C_{HL} = \frac{2\pi \cdot \varepsilon \cdot h}{\ln\left(\dfrac{d_2}{d_1}\right)}$$

(5.25)

Being,

h: height of the windings.

d_1: Inner diameter of the HV side winding.

d_2: outer diameter of the LV side winding.

ε: permittivity of the dielectric.

Equation (5.25) can be used as well for computing C_{HG} and C_{LG} [151]. Variable d_2 now indicates the diameter of the leg of the transformer core. Variable d_1 is now, depending on the case, the inner diameter of the LV side or HV side winding.

5.4.3 Laboratory Tests

Laboratory tests can be done to determine the parameters of the model, e.g. the transformer model of Fig. 5.12, in case of having the transformer physically. Furthermore, appropriate equipment (e.g. measurement equipment) and adequate facilities must be required to obtain accurate results and be able to perform a variety of tests.

A description of the laboratory test approach is presented below for each parameter.

Short-circuit impedance

Short-circuit test must be performed at different frequency values to compute the frequency variation of this parameter. The determination of the short-circuit impedance can be based on:

- True RMS Wattmeter (TRMS): The procedure of the measurements and the determination of the parameters is detailed in references [44,152].
- Oscilloscope measurements: post-processing of voltage- and current waveforms at different values of frequency and magnitude. The procedure of the measurement campaign and the determination of the parameters is detailed in references [157,159,160]. A brief description of how to compute the parameters of the short-circuit impedance with this approach is presented below.

Fig. 5.16 shows the short-circuit test recommended in references [159,160] for the determination of the short-circuit impedance of a three-legged stacked core transformer. The test is performed for each phase.
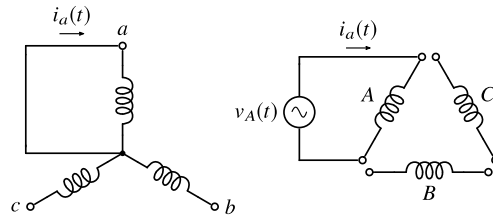
Fig. 5.16. Short-circuit test on phase A (HV side). Source [159].

For this test, the equivalent circuit can be reduced to a resistance R_{sc} in series with an inductance L_{sc}, as shown in Fig. 5.17. The equivalent circuit for the test of Fig. 5.16 can be simplified to that of Fig. 5.17 by neglecting the influence of the core impedance, which is very big compared to short-circuit impedance.
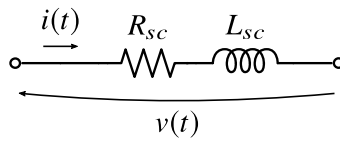
Fig. 5.17. Simplified equivalent circuit for the short-circuit test. Source [160].

The values of resistance and inductance can be computed by equations (5.26) and (5.27), respectively.

$$R_{sc} = \left. \frac{v(t)}{i(t)} \right|_{\frac{d}{dt}i(t)=0} \tag{5.26}$$

$$L_{sc} = \left. \frac{\frac{v(t)}{1}}{\frac{d}{dt}i(t)} \right|_{i(t)=0} \tag{5.27}$$

Core impedance

Open-circuit test must be performed at rated frequency and at different voltage levels. If it is possible from 0.3 Vpu to 1.5 Vpu with increments of 0.1 Vpu. The determination of the parameters of the core can be based on:

- True RMS Wattmeter (TRMS): The procedure of the measurements and the determination of the model parameters is detailed in references [44,152].
- Oscilloscope measurements: post-processing of voltage- and current waveforms at different values of frequency and magnitude. The procedure of the measurement campaign and the determination of the parameters is detailed in references [157,159,160]. A brief description of how to compute the parameters of the transformer core with this approach is presented below.

Fig. 5.18 shows the open-circuit test recommended in references [159,160] for the determination of the core parameters of a three-legged stacked core transformer. The test

configuration of Fig. 5.18(a) allows the determination of the center leg of the transformer core, while the test configuration of Fig. 5.18(b) allows the determination of the outer leg.
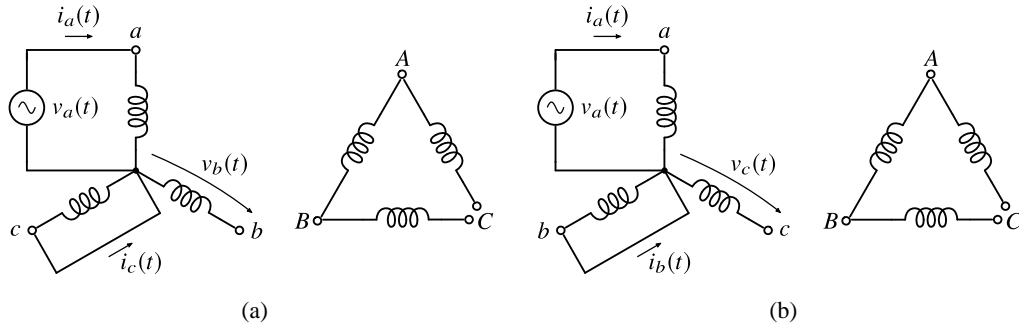
Fig. 5.18. Circuit configuration for open-circuit test. (a) Center leg. (b) Outer leg. Source [159].

The equivalent circuit for the test of Fig. 5.18(a) can be simplified to that of Fig. 5.19 by neglecting the influence of the short-circuit impedance, which is very small compared to the core impedance.
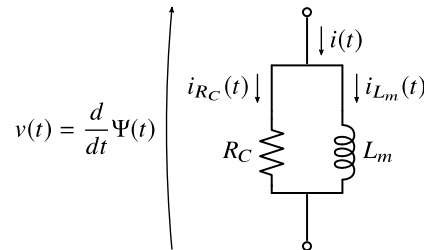
Fig. 5.19. Simplified equivalent circuit for the open-circuit test. Source [160].

The determination of the parameters of the transformer core, for the legs and yokes, follows a similar procedure. For example, the values of resistance and inductance can be computed by equations (5.28) and (5.29), respectively.

$$R_C = \frac{v(t)}{i(t)}\bigg|_{\Psi(t)=0} \tag{5.28}$$

$$L_m = \frac{\Psi(t)}{i(t)}\bigg|_{v(t)=0} \tag{5.29}$$

The flux linkage is computed by equation (5.30).

$$\Psi(t) = \int v(t)\,dt \tag{5.30}$$

Capacitances

For the determination of the capacitances via laboratory tests, the transient recovery voltage (TRV) of each winding must be measured and the frequency of oscillation of these voltages must be determined. With this information, the effective terminal capacitance can be determined by using equation (5.31) [151].

$$C_{eff} = \frac{1}{\left(2\pi f_{TRV}\right)^2 L_{leakage}} \qquad (5.31)$$

Being,

f_{TRV} : TRV frequency of each winding.

$L_{leakage}$: transformer leakage inductance.

The capacitances of the windings can be computed with equations (5.32)-(5.34) and the effective capacitance value obtained previously.

$$C_{eff} = C_{HG} + C_{HL} \qquad (5.32)$$

$$C_{eff} = C_{LG} + C_{HL} \qquad (5.33)$$

$$\frac{C_{HL}}{C_{HL} + C_{LG}} < 0.4 \qquad (5.34)$$

Details of the measurement procedure and capacitance determination can be found in reference [151]. This reference shows representative frequencies for power transformers and suggests values lower than 0.4 for the capacitive coupling ratio, equation (5.34).

5.5   Chapter Summary

In this chapter, a Frequency-Dependent STC model has been developed for the representation of the power transformers in an OWPP scenario. The transformer model includes four main parameters. These are the frequency-dependent behavior of the winding resistance, the impedance of the transformer core, stray capacitances and the zero-sequence impedance.

The main reason for adopting the general structure of the STC model is the availability of data to determine the parameters of the model. Other models, especially the hybrid model of Fig. 5.6, were taken into account because of its accuracy. The main problem of using this type of model is the available data and the lack of clear and valid assumptions for the determination of some of its parameters.

Guidelines for transformer model parameterization have been described briefly. These approaches are manufacturer datasheets, parameter estimation, design information, and laboratory tests. A combination of these approaches is usually performed, especially between the information provided by the manufacturer datasheet and estimations. Emphasis has been paid to this approach mainly because of the lack of information, the no availability of this type of transformer (wind turbine transformer and offshore substation

transformer) and the limitations in measurement equipment and installation conditions to perform laboratory tests to these transformers.

Chapter 6

Submarine Cable Modeling

This chapter presents a Frequency-Dependent Pi (FDPi) model of a three-core submarine cable. The model is intended to be used for the representation of submarine cables in an OWPP scenario. For example, the Simulink®-based model of the OWPP base scenario that is presented in chapter 7. The frequency-dependent variation of each conductive layer is modeled by a Foster equivalent network whose parameters are tuned by means of Vector Fitting (VF) algorithm. The formulation for the parameterization of the model is presented in detail, which allows an easy reproduction of the presented model. The validation of the model is performed via a comparison with a well-established reference model, the Universal Line Model (ULM) from PSCAD/EMTDC software. Two cable system case studies are presented. The first case study shows the response of the FDPi model for a three-core submarine cable. On the other hand, the second case study depicts the response of three single-core underground cables laying in trefoil formation. This last case shows the applicability of the FDPi model to other types of cable systems and indirectly validates the response of the aforementioned model with experimental results.

6.1 Introduction

Increasing construction of Offshore Wind Power Plants (OWPPs) has been accompanied by a progressive installation of submarine cables in the power system [2]. Since these type of cable networks are affected by many transient phenomena (frequent load changes,

switching operations, etc.) and harmonics that can be amplified by cable resonances, proper modeling of submarine cables is crucial in order to perform an adequate analysis of their behaviour and their effects on the power system.

State of the art time-domain models of power cables take into account the frequency-dependent behaviour of the electrical parameters in order to enable accurate transient simulations [161]. Due to their formulation, these models cannot be directly converted into the Laplace domain or in a state-space form in order to analyze the frequency response and stability of the power system under study.

On the other hand, cascaded traditional Pi sections, which can be directly converted to Laplace domain or state-space form, can be used to represent submarine cables. The main problem with this type of model is that it neglects the frequency-dependent effects of the cable [32]. Thus, this type of model is unable to accurately represent the behavior of the cable and it will lead to incorrect results and incorrect analysis of the harmonic evaluation of an OWPP [162]. Regarding this issue, several contributions have been done in order to improve the damping characteristic of the traditional Pi model. These contributions, referred in this document as enhanced Pi models, are addressed in subsection 6.2.1.

This chapter presents an alternative Frequency-Dependent Pi (FDPi) model that represents the steady-state and transients comprising frequencies up to 5 kHz (frequency range of study of this Ph.D. thesis). The model consists of cascaded FDPi sections, which incorporate both inductive coupling and the frequency-dependent characteristic of some series impedance terms of the conductive layers. If it is required, the model can be extended to represent a higher frequency range but its accuracy will be diminished due to previous characteristic.

The strengths of the presented model in comparison to other published model contributions lie in the following points:

- The model represents each cable conductive layer, thus not assuming the elimination of the cable screens and external wire armour. This feature allows the visualization of the voltages and currents of these conductors and the representation of different grounding configurations. Furthermore, it is possible to account for the frequency dependency of the earth-related terms by explicitly representing the earth as another conductor [163,164].
- The model is explicitly represented in the phase-domain, thus avoiding the transformation between phase-domain to modal-domain and vice versa.
- The model can be directly formulated in the Laplace domain or in a state-space representation. In this sense, both time- and frequency-domain analysis can be performed. Backward Euler method, or other methods presented in reference [165], can be used in order to compute the voltages and currents along the cable in the time-domain.
- The model can be easily implemented in Matlab/Simulink® or any other circuit simulation tool by means of discrete RLC components. Coupled resistances and

inductances are directly implemented by means of a generalized mutual inductance component.

- The modeling approach is not only applicable to three-core submarine cables. It can be extended to other types of cable systems, such as single-core underground and submarine cables or a set of single-core cables arranged in flat- or trefoil formation.

In this sense, the FDPi model is intended to be used for the representation of submarine cables in an OWPP scenario and for the studies addressed in this Ph.D. thesis (i.e. frequency analysis and harmonic assessment). However, it is important to mention that other potential applications can be carried out with this model, as stated in reference [166].

The chapter is structured as follows. Section 6.2 gives an overview of the most important cable models up to date. Section 6.3 presents the electrical schematic and the general equations that describe the behavior of the FDPi model. Section 6.4 presents a detailed description of the parameterization of the model. Section 6.5 treats the validation of two cable systems, a three-core submarine cable and three single-core underground cables laying in trefoil formation. The validation of the FDPi model is performed via a comparison of the proposed model with the well-established Universal Line Model (ULM) from PSCAD/EMTDC software. The validation is done for frequencies up to 10 kHz, which is a frequency range higher than the one required for the studies of this Ph.D. thesis. Section 6.6 provides a methodology for the determination of a suitable order of the FDPi model. The order of the FDPi model is highly dependent on accuracy and frequency range requirements, and the particular characteristics of the cable system. Finally, section 6.7 gives the chapter summary.

6.2   Overview of Cable Models

Cable models can be classified into two main groups [27], lumped- and distributed parameters, as depicted in Fig. 6.1.
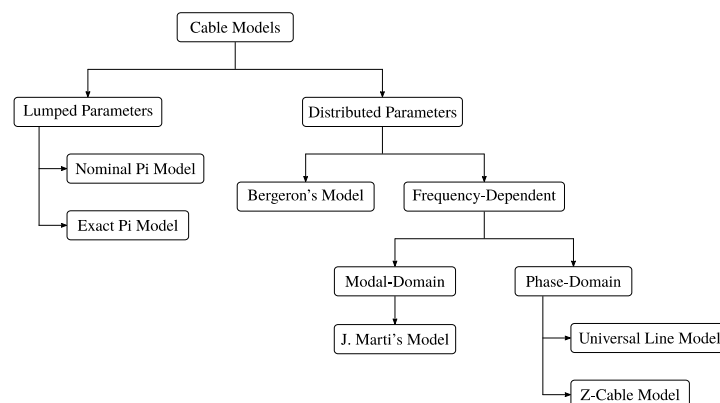
Fig. 6.1. Cable models classification. Source [27].

A brief description of the models is presented in the following subsections. For simplicity, the figures presented in this section represent the models of a single-conductor cable but they can be extended to represent multiconductor cables.

6.2.1   Pi-based Models

A brief description of Pi-based models is performed below.

Nominal Pi Model

The nominal Pi model is one of the simplest representations of a cable. The model is based on lumped *R, L, G* and *C* parameters. The conductance *G* is usually not taken into account [167]. Fig. 6.2 shows the schematic of the nominal Pi model.
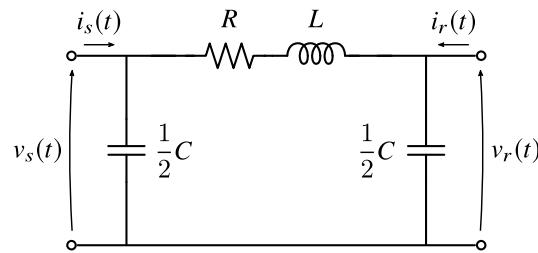
Fig. 6.2. Nominal Pi model of a cable. Source [167].

The lumped parameters are multiplied by the length of the cable section that they represent, hence the distributed nature of these parameters is not considered. Due to this characteristic, the model is only valid for short distances as the errors in the electrical parameters become more noticeable when the cable length increases [168]. The error can be reduced by cascading several Pi sections.

In general, this model should be used for performing simple analyses or studies. It is not appropriate to be used for harmonic evaluation since the model does not provide an accurate frequency spectrum. Furthermore, the model presents resonances that are not real at higher frequencies [168].

Exact Pi Model

The exact Pi model considers the distributed nature of the impedance and admittance terms and can be used to represent long cables. The impedance and admittance are corrected by means of hyperbolic functions for the cable length that the model represents [169].

One important aspect to mention about this model is its accuracy when used in the frequency domain for a single-frequency. Hence, it is normally used to validate other models [167,170]. The schematic of Fig. 6.2 is also valid for this model.

Enhanced Pi Models

In the last years, several contributions have been done in order to improve the representation of the nominal Pi model. The main contributions are presented in references [162,163,171]. In general terms, enhanced Pi models consist of including the inductive

coupling between the cable layers (core and screen) and by including equivalent networks that represent the variation in frequency of the cable parameters.

The model proposed in reference [162] includes an equivalent network to represent the variation in frequency of the cable parameters. This model eliminates the contribution of the cable screens by assuming them to be at ground potential (even though they might not be grounded at both ends).

On the contrary, reference [171] represents a cable system with a Pi equivalent circuit including the frequency dependence of the cable longitudinal impedance in the modal-domain. For this approach, transformations between both domains (phase and modal) are required, as shown in Fig. 6.3.

(a)

(b)
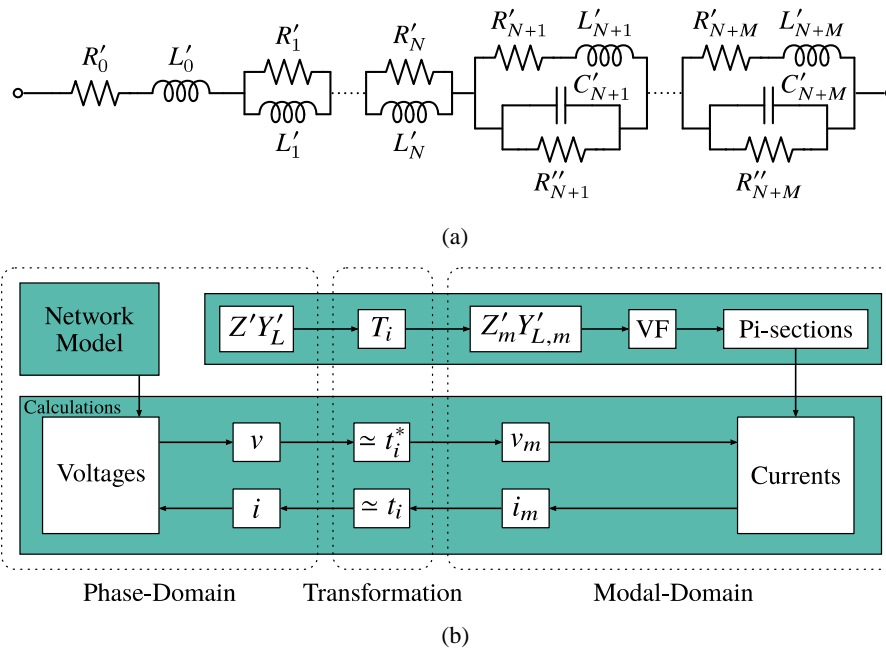
Fig. 6.3. Schematic of the frequency-dependent cable model (enhanced Pi model) proposed in reference [171]. (a) Representation of the frequency dependence of the cable longitudinal impedance. (b) Principle of the three-phase cable model.

6.2.2 Bergeron-based Models

A brief description of Bergeron-based models is done next.

Bergeron's Model

Fig. 6.4 shows the Bergeron's model of a cable. Bergeron's model is based on traveling wave theory and it is represented by a Norton equivalent [161]. The model approximates system losses by including its distributed series resistance in a lumped form. The lumped resistances can be included throughout the cable by dividing its total length into several sections. Typically, the model is divided into two sections [161].

Bergeron's model is a single-frequency model whose parameters are usually calculated at either 50 Hz or 60 Hz. It is therefore not suited for transient- or frequency studies [140].
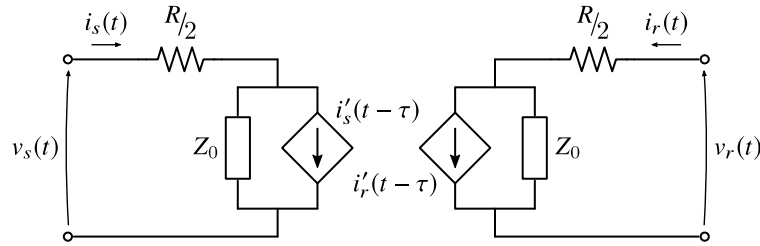
Fig. 6.4. Bergeron's model of a cable. Source [161].

Frequency-Dependent Bergeron's Model

In 2015, Pablo Torrez et.al. proposed a frequency-dependent multiconductor line model based on the Bergeron's method. The frequency-dependent Bergeron's model is shown in Fig. 6.5. The inclusion of the frequency effect in the Bergeron circuit consists in replacing the constant resistances that represent the line losses by a Foster equivalent circuit, which allows a direct representation in the time-domain.

The number of RL blocks depends on the type of electromagnetic transient to be analyzed. For example, no more than three or four RL-circuits are required for representing input signals composed of low-frequencies (e.g. switching operation) [172]. The reader is suggested to review reference [172] for a detail description of this model.
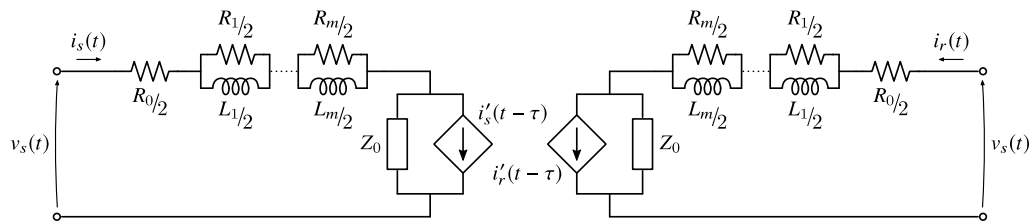
Fig. 6.5. Frequency-Dependent Bergeron's model of a cable. Source [172].

6.2.3   Frequency-Dependent Models

Frequency-Dependent (FD) models are models that include the frequency dependence behavior of the cable parameters [161]. These models are based on traveling wave theory, hence all parameters are distributed. For these models, all calculations are done in the frequency-domain and the solutions converted to time-domain by means of the Fourier transform or Z-transform [170]. A brief description of the best-known FD models is presented next. The reader is suggested to review reference [170] for an outline of the historical evolution of the different FD models.

J. Marti's Model

J. Marti's model is one of the most widely used models for overhead lines and cables. This model includes the full frequency dependence of the cable parameters in the propagation matrix and the characteristic admittance. These parameters are approximated by using rational functions obtained through Bode asymptotic fitting technique. This fitting technique is briefly described in Appendix A.2.

A constant modal transformation matrix is used to decouple a multiconductor cable into separate, mutually exclusive modes. Each mode is then treated as a single-phase circuit. The benefit of assuming a constant transformation matrix is to gain high computational efficiency, but it leads to erroneous results in the cases of strongly asymmetrical cables because in these cases the elements of the matrix highly depend on frequency [173]. A detailed description of Marti's model can be found in reference [174].

Universal Line Model (ULM)

ULM represents the full frequency dependence of a cable in a similar way to J. Marti's model. The difference lies in the domain of representation and the way the fitting process is performed. The parameters of the model are fitted directly in the phase-domain by using Vector Fitting (VF) algorithm [170,175]. VF is briefly described in Appendix A.2.

Once the cable parameters have been fitted, the cable terminal conditions (voltages and currents) can be calculated in time-domain and interfaced to the electric network by means of a Norton equivalent circuit, as shown in Fig. 6.6.

ULM presents two main advantages in comparison with J. Marti's model. First, it avoids the problems associated with the modal transformation matrix in terms of conversion between domains and the assumption of considering this matrix constant. The second advantage is the high accuracy that this model presents for asymmetrical cable geometries. A detailed description of this model can be found in reference [176].

Finally, it is important to mention that this model is highly used for transient and harmonic studies of cable systems in specialized software such as PSCAD, EMTP-RV, and others.
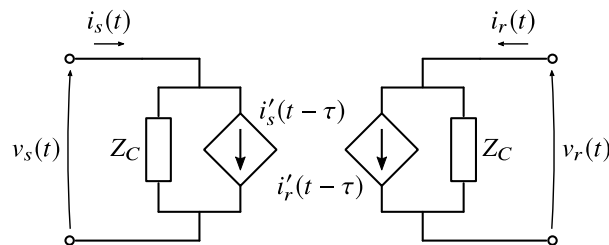
Fig. 6.6. Time-domain implementation of the Universal Line Model. Source [44].

Z-Cable Model

The Z-Cable model splits the representation of the propagation phenomena into two parts, as shown in Fig. 6.7. The first part represents the electric and magnetic fields outside the conductors, which depend mainly on the electrical properties and geometry of the cable. This part is represented in modal-domain, therefore phase-to-modal and modal-to-phase transformations are necessary. The second part is a loss section with frequency-dependent parameters in the phase-domain. This section takes into account losses associated with skin effect of the conductors and dielectric losses. A detailed description of this model is presented in references [177,178].

95
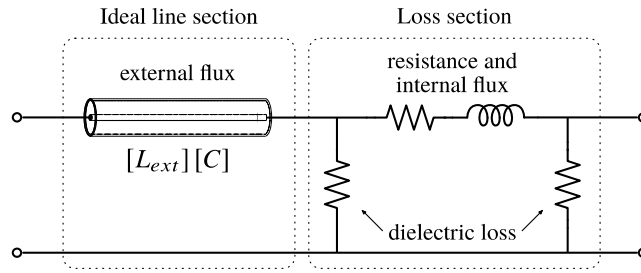
Fig. 6.7. Representation of the propagation phenomena in the Z-Cable model. Source [177].

6.3 Frequency-Dependent Pi Model

Fig. 6.8 shows the electrical schematic of the Frequency-Dependent Pi (FDPi) model. The model physically represents the seven conductors of a three-core submarine cable system. These are three-core conductors, three-screen conductors and a pipe representing the external wire armour of the cable.

As depicted in Fig. 6.8(a), the model consists of N cascaded FDPi sections. Each FDPi section consists of a resistance- and inductance matrix computed at nominal frequency, 50 Hz or 60 Hz. The capacitive coupling between conductors is computed at nominal frequency as well.

The frequency-dependent behaviour of the series impedance terms of each conductive layer is represented by means of a Foster equivalent network as depicted in Fig. 6.8(b).

The order of the FDPi model is given by the number of cascaded sections (N) together with the order of the Foster equivalent networks (M). The order of the model is chosen depending on the cable length, accuracy, and frequency range requirements.

The general equations that describe the behaviour of the model are expressed in the Laplace domain $(s = j\omega)$. The terminal voltages and currents of the FDPi model are given by equation (6.1). Being $[I]$, the identity matrix of order seven.

$$\begin{bmatrix} [V_s] \\ [I_s] \end{bmatrix} = \begin{bmatrix} [I] + \dfrac{[Z][Y]}{2} & [Z] \\ [Y] + \dfrac{[Y][Z][Y]}{4} & [I] + \dfrac{[Y][Z]}{2} \end{bmatrix}^N \begin{bmatrix} [V_r] \\ [I_r] \end{bmatrix} \tag{6.1}$$

The voltages and currents at the sending- and receiving ends are vectors defined by equation (6.2). Each voltage is referenced to ground potential as depicted in Fig. 6.8.

(a)

(b)
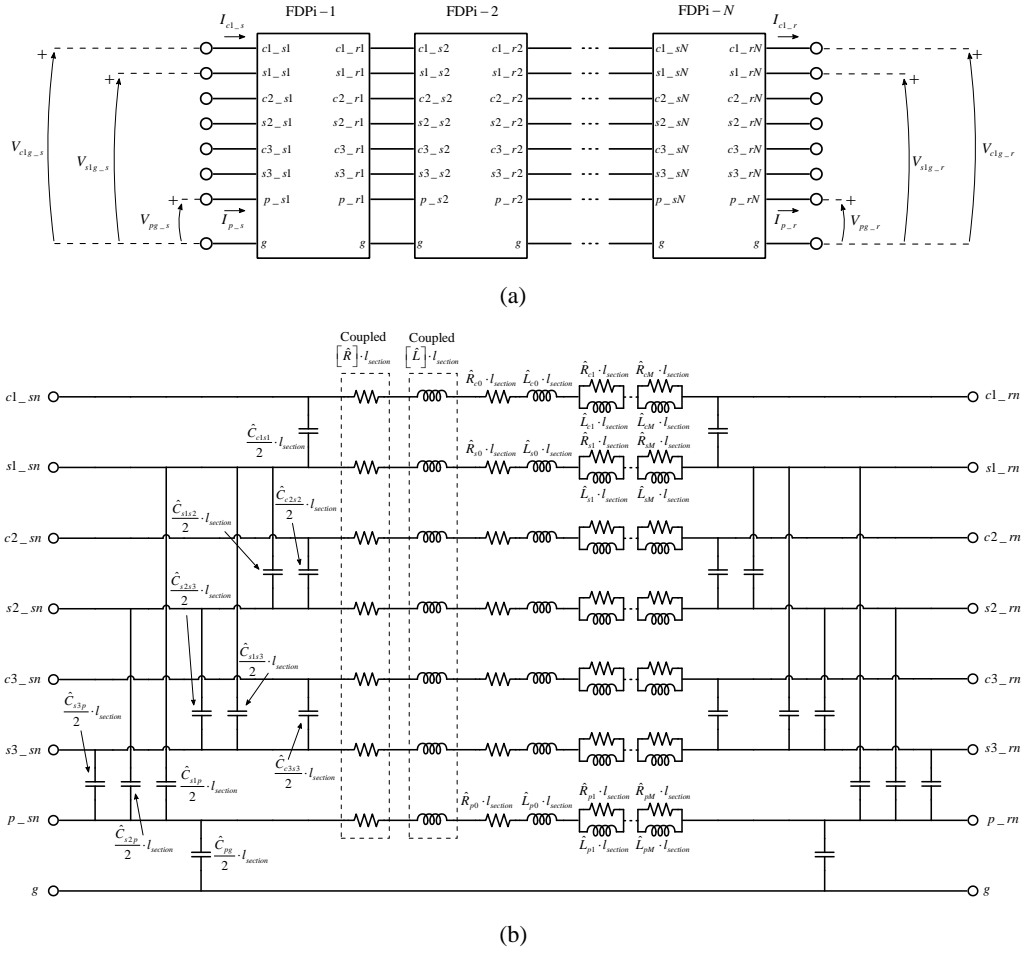
Fig. 6.8. Electrical schematic of the Frequency-Dependent Pi (FDPi) Model. (a) Cascaded FDPi sections. (b) Detailed schematic of an FDPi section (Capacitances at the right hand side are equal to the left hand side, but their names are omitted for simplicity).

$$
[V_s] = \begin{bmatrix} V_{c1g\_s} \\ V_{s1g\_s} \\ V_{c2g\_s} \\ V_{s2g\_s} \\ V_{c3g\_s} \\ V_{s3g\_s} \\ V_{pg\_s} \end{bmatrix} \quad ; \quad [V_r] = \begin{bmatrix} V_{c1g\_r} \\ V_{s1g\_r} \\ V_{c2g\_r} \\ V_{s2g\_r} \\ V_{c3g\_r} \\ V_{s3g\_r} \\ V_{pg\_r} \end{bmatrix} \quad ; \quad [I_s] = \begin{bmatrix} I_{c1\_s} \\ I_{s1\_s} \\ I_{c2\_s} \\ I_{s2\_s} \\ I_{c3\_s} \\ I_{s3\_s} \\ I_{p\_s} \end{bmatrix} \quad ; \quad [I_r] = \begin{bmatrix} I_{c1\_r} \\ I_{s1\_r} \\ I_{c2\_r} \\ I_{s2\_r} \\ I_{c3\_r} \\ I_{s3\_r} \\ I_{p\_r} \end{bmatrix} \quad (6.2)
$$

The series impedance matrix $[Z]$ and the shunt admittance matrix $[Y]$ are given by equations (6.3) and (6.4), respectively.

$$
[Z] = \left[\hat{Z} \right] \cdot l_{section} \tag{6.3}
$$

$$
[Y] = \left[\hat{Y} \right] \cdot l_{section} \tag{6.4}
$$

The length of an FDPi section is given by equation (6.5), where l_{cable} is the total length of the cable.

$$l_{section} = \frac{l_{cable}}{N_{FDPi}} \tag{6.5}$$

The per-length series impedance matrix $\left[\hat{Z} \right]$ is given by equation (6.6).

$$\left[\hat{Z} \right] = \left[\hat{Z}_{Fn} \right] + \left[\hat{Z}_{Foster} \right] \tag{6.6}$$

Being $\left[\hat{Z}_{Fn} \right]$ matrix defined by equation (6.7).

$$\left[\hat{Z}_{Fn} \right] = \left[\hat{R} \right] + s \left[\hat{L} \right] \tag{6.7}$$

$$\left[\hat{R} \right] = \begin{bmatrix} \hat{R}_{11} & \hat{R}_{12} & \cdots & \hat{R}_{17} \\ \hat{R}_{21} & \hat{R}_{22} & \cdots & \hat{R}_{27} \\ \vdots & \vdots & \ddots & \vdots \\ \hat{R}_{71} & \hat{R}_{72} & \cdots & \hat{R}_{77} \end{bmatrix} \quad ; \quad \left[\hat{L} \right] = \begin{bmatrix} \hat{L}_{11} & \hat{L}_{12} & \cdots & \hat{L}_{17} \\ \hat{L}_{21} & \hat{L}_{22} & \cdots & \hat{L}_{27} \\ \vdots & \vdots & \ddots & \vdots \\ \hat{L}_{71} & \hat{L}_{72} & \cdots & \hat{L}_{77} \end{bmatrix} \tag{6.8}$$

The $\left[\hat{Z}_{Foster} \right]$ matrix includes the contribution of the Foster equivalent networks of each conductive layer (cores, screens and armour) and is given by equations (6.9)-(6.13).

$$\left[\hat{Z}_{Foster} \right] = \begin{bmatrix} \left[\hat{Z}_{F1} \right] & \left[0 \right]_2 & \left[0 \right]_2 & \left[0 \right]_{2\times 1} \\ \left[0 \right]_2 & \left[\hat{Z}_{F2} \right] & \left[0 \right]_2 & \left[0 \right]_{2\times 1} \\ \left[0 \right]_2 & \left[0 \right]_2 & \left[\hat{Z}_{F3} \right] & \left[0 \right]_{2\times 1} \\ \left[0 \right]_{1\times 2} & \left[0 \right]_{1\times 2} & \left[0 \right]_{1\times 2} & \hat{Z}_{Fp} \end{bmatrix} \tag{6.9}$$

$$\left[\hat{Z}_{Fj} \right] = \begin{bmatrix} \hat{Z}_{Fc} & 0 \\ 0 & \hat{Z}_{Fs} \end{bmatrix} \tag{6.10}$$

$$\hat{Z}_{Fc} = \hat{R}_{c0} + s\hat{L}_{c0} + \sum_{m=1}^{M} \frac{s\hat{R}_{cm}\hat{L}_{cm}}{\hat{R}_{cm} + s\hat{L}_{cm}} \tag{6.11}$$

$$\hat{Z}_{Fs} = \hat{R}_{s0} + s\hat{L}_{s0} + \sum_{m=1}^{M} \frac{s\hat{R}_{sm}\hat{L}_{sm}}{\hat{R}_{sm} + s\hat{L}_{sm}} \tag{6.12}$$

$$\hat{Z}_{Fp} = \hat{R}_{p0} + s\hat{L}_{p0} + \sum_{m=1}^{M} \frac{s\hat{R}_{pm}\hat{L}_{pm}}{\hat{R}_{pm} + s\hat{L}_{pm}} \tag{6.13}$$

The per-length shunt admittance matrix $\left[\hat{Y} \right]$ is defined by equation (6.14).

$$\left[\hat{Y} \right] = s \left[\hat{C} \right] \tag{6.14}$$

Being,

$$\left[\hat{C} \right] = \begin{bmatrix} \hat{C}_{11} & \hat{C}_{12} & \cdots & \hat{C}_{17} \\ \hat{C}_{21} & \hat{C}_{22} & \cdots & \hat{C}_{27} \\ \vdots & \vdots & \ddots & \vdots \\ \hat{C}_{71} & \hat{C}_{72} & \cdots & \hat{C}_{77} \end{bmatrix} \tag{6.15}$$

The per-length capacitances between conductors, depicted in Fig. 6.8(b), are given by the following equations.

$$\hat{C}_{c1s1} = -\hat{C}_{21} = -\hat{C}_{12} \quad ; \quad \hat{C}_{c2s2} = -\hat{C}_{43} = -\hat{C}_{34} \quad ; \quad \hat{C}_{c3s3} = -\hat{C}_{65} = -\hat{C}_{56} \tag{6.16}$$

$$\hat{C}_{s1s2} = -\hat{C}_{42} = -\hat{C}_{24} \quad ; \quad \hat{C}_{s1s3} = -\hat{C}_{62} = -\hat{C}_{26} \quad ; \quad \hat{C}_{s2s3} = -\hat{C}_{64} = -\hat{C}_{46} \tag{6.17}$$

$$\hat{C}_{s1p} = -\hat{C}_{72} = -\hat{C}_{27} \quad ; \quad \hat{C}_{s2p} = -\hat{C}_{74} = -\hat{C}_{47} \quad ; \quad \hat{C}_{s3p} = -\hat{C}_{76} = -\hat{C}_{67} \tag{6.18}$$

The capacitances to ground for each cable conductor (cores, screens and armour) are computed according to the following equations.

$$\hat{C}_{c1g} = \hat{C}_{11} + \hat{C}_{12} \quad ; \quad \hat{C}_{c2g} = \hat{C}_{33} + \hat{C}_{34} \quad ; \quad \hat{C}_{c3g} = \hat{C}_{55} + \hat{C}_{56} \tag{6.19}$$

$$\hat{C}_{s1g} = \hat{C}_{22} + \hat{C}_{21} + \hat{C}_{24} + \hat{C}_{26} + \hat{C}_{27} \quad ; \quad \hat{C}_{s2g} = \hat{C}_{44} + \hat{C}_{42} + \hat{C}_{43} + \hat{C}_{46} + \hat{C}_{47} \tag{6.20}$$

$$\hat{C}_{s3g} = \hat{C}_{66} + \hat{C}_{62} + \hat{C}_{64} + \hat{C}_{65} + \hat{C}_{67} \tag{6.21}$$

$$\hat{C}_{pg} = \hat{C}_{77} + \hat{C}_{72} + \hat{C}_{74} + \hat{C}_{76} \tag{6.22}$$

The capacitances of equations (6.19)-(6.21) are zero because of the physical structure of the cable. Therefore, they are not represented in the schematic of Fig. 6.8(b). The rest of the capacitance elements presented in equation (6.15) and not named previously are zero as well. Supporting information about the capacitance matrix $\left[\hat{C} \right]$ is presented in reference [179].

6.4 Model Parameterization

There are several methods proposed in the technical literature for determining the electrical parameters of a cable system and their variations with frequency, which are mainly due to skin effect and proximity effect. The most remarkable techniques are based on analytical formulas [180–182], numerical tools based on Finite Element Method (FEM) [183,184], conductor partitioning [185,186] and the Method of Moments (MoM-SO) proposed in

references [187–189]. Each technique has its advantages and disadvantages in terms of complexity, accuracy, computational time, phenomena that represent and other aspects.

In this Ph.D. thesis, the analytical equations (presented in reference [180]) are used for the parameterization of the model. The main reason for its selection is that most Electromagnetic Transient (EMT) tools use this formulation to compute the electrical parameters of the cable. Therefore, this way of parameterization is followed in order to compare the behaviour of the FDPi model with a reference model, the Universal Line Model (ULM) from PSCAD/EMTDC software. It is worth to mention, that the analytical equations, presented in reference [180], only take into account the skin effect and do not consider the proximity effect. If it is required to consider the proximity effect, the methodology presented in reference [181] and other special methods already mentioned above can be used for model parameterization.

In order to perform the cable parameterization according to the analytical equations, it is necessary to perform a data conversion of the original cable parameters into a new set of parameters. This new set of parameters consists in the simplification of the cable layers and in the correction of the materials properties. Details of the conversion procedure can be found in references [167,190]. Fig. 6.9 shows the simplified cross-section of a three-core submarine cable (cable under study). Table 6.1 gives information about the required set of parameters for this type of cable.
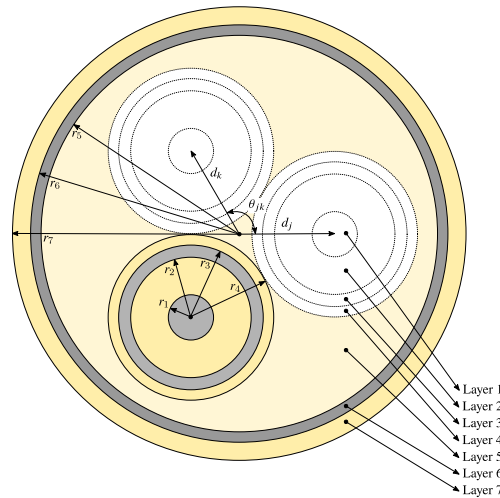
Fig. 6.9. Simplified cross-section of a three-core submarine cable.

Table 6.1. Simplified layers of a three-core submarine cable.

Layer Number	Layer Name	Parameters
1	Core Conductor	r_1 , ρ_c , μ_{rc}
2	Core Insulation	r_2 , μ_{rins1} , ε_{rins1}
3	Screen Conductor	r_3 , ρ_s , μ_{rs}
4	Screen Insulation	r_4 , μ_{rins2} , ε_{rins2}
5	Armour Inner Insulation	r_5 , μ_{rins3} , ε_{rins3}
6	Armour Conductor	r_6 , ρ_p , μ_{rp}
7	Armour Outer Insulation	r_7 , μ_{rins4} , ε_{rins4}

The determination of the electrical parameters of the FDPi model involves three steps, which are described in the next subsections in order to allow an easy reproduction of the model.

6.4.1 Computation of per-length Resistance- and Inductance Matrices

For the determination of the resistance- and inductance matrices, the per-length series impedance matrix $\left[\hat{Z}_{Fn} \right]$ is computed at nominal frequency and it is given by equation (6.23).

$$\left[\hat{Z}_{Fn} \right] = [Z_i] + \left[Z_p \right] + [Z_c] + [Z_e] \tag{6.23}$$

The cable internal impedance $[Z_i]$ matrix is given by equation (6.24).

$$[Z_i] = \begin{bmatrix} [Z_{i1}] & [0]_2 & [0]_2 & [0]_{2\times1} \\ [0]_2 & [Z_{i2}] & [0]_2 & [0]_{2\times1} \\ [0]_2 & [0]_2 & [Z_{i3}] & [0]_{2\times1} \\ [0]_{1\times2} & [0]_{1\times2} & [0]_{1\times2} & 0 \end{bmatrix} \tag{6.24}$$

Being,

$$\left[Z_{ij} \right] = \begin{bmatrix} Z_{ccj} & Z_{csj} \\ Z_{csj} & Z_{ssj} \end{bmatrix} \tag{6.25}$$

$$Z_{ccj} = Z_{CSins} + Z_{Sinner} + Z_{Souter} + Z_{Sins} - 2Z_{Smutual} \tag{6.26}$$

$$Z_{csj} = Z_{Souter} + Z_{Sins} - Z_{Smutual} \quad ; \quad Z_{ssj} = Z_{Sins} \tag{6.27}$$

The series impedance of the core insulation is given by equation (6.28).

$$Z_{CSins} = \frac{s\mu_{ins1}}{2\pi} \ln\left(\frac{r_2}{r_1} \right) \tag{6.28}$$

The screen inner and outer series impedances are given by equations (6.29) and (6.30), respectively.

$$Z_{Sinner} = \frac{\rho_s m_s}{2\pi r_2} \cdot \frac{J_0\left(x_2\right)K_1\left(x_3\right) + K_0\left(x_2\right)J_1\left(x_3\right)}{J_1\left(x_3\right)K_1\left(x_2\right) - J_1\left(x_2\right)K_1\left(x_3\right)} \tag{6.29}$$

$$Z_{Souter} = \frac{\rho_s m_s}{2\pi r_3} \cdot \frac{J_0\left(x_3\right)K_1\left(x_2\right) + K_0\left(x_3\right)J_1\left(x_2\right)}{J_1\left(x_3\right)K_1\left(x_2\right) - J_1\left(x_2\right)K_1\left(x_3\right)} \tag{6.30}$$

Being,

$$x_2 = m_s r_2 \quad ; \quad x_3 = m_s r_3 \quad ; \quad m_s = \sqrt{\frac{s\mu_s}{\rho_s}} \tag{6.31}$$

$J_n(x)$: Bessel function of x, of first kind and order n.

$K_n(x)$: Bessel function of x, of second kind and order n.

The series impedance of the screen insulation is given by equation (6.32).

$$Z_{Sins} = \frac{s\mu_{ins2}}{2\pi} \ln\left(\frac{r_4}{r_3}\right) \tag{6.32}$$

The screen mutual series impedance is given by equation (6.33).

$$Z_{Smutual} = \frac{\rho_s}{2\pi r_2 r_3} \cdot \frac{1}{J_1(x_3)K_1(x_2) - J_1(x_2)K_1(x_3)} \tag{6.33}$$

The pipe internal impedance matrix $\left[Z_p\right]$ is defined by equation (6.34).

$$\left[Z_p\right] = \begin{bmatrix} \left[Z_{p11}\right] & \left[Z_{p12}\right] & \left[Z_{p13}\right] & \left[0\right]_{2\times1} \\ \left[Z_{p21}\right] & \left[Z_{p22}\right] & \left[Z_{p23}\right] & \left[0\right]_{2\times1} \\ \left[Z_{p31}\right] & \left[Z_{p32}\right] & \left[Z_{p33}\right] & \left[0\right]_{2\times1} \\ \left[0\right]_{1\times2} & \left[0\right]_{1\times2} & \left[0\right]_{1\times2} & 0 \end{bmatrix} \tag{6.34}$$

Being,

$$\left[Z_{pjj}\right] = \begin{bmatrix} Z_{pjj} & Z_{pjj} \\ Z_{pjj} & Z_{pjj} \end{bmatrix} \quad ; \quad \left[Z_{pjk}\right] = \begin{bmatrix} Z_{pjk} & Z_{pjk} \\ Z_{pjk} & Z_{pjk} \end{bmatrix} \tag{6.35}$$

$$Z_{pjj} = \frac{s\mu_0}{2\pi}\left[\frac{\mu_{rp}}{x_5} \cdot \frac{D_{pnum}}{D_{pden}} + Q_{jj} + 2\mu_{rp}y_{jj}\right] \tag{6.36}$$

$$Z_{pjk} = \frac{s\mu_0}{2\pi}\left[\frac{\mu_{rp}}{x_5} \cdot \frac{D_{pnum}}{D_{pden}} + Q_{jk} + 2\mu_{rp}y_{jk}\right] \tag{6.37}$$

$$D_{pnum} = J_0(x_5)K_1(x_6) + K_0(x_5)J_1(x_6) \tag{6.38}$$

$$D_{pden} = K_1(x_5)J_1(x_6) - J_1(x_5)K_1(x_6) \tag{6.39}$$

$$Q_{jj} = \ln\left\{\left(\frac{r_5}{r_4}\right)\left[1-\left(\frac{d_j}{r_5}\right)^2\right]\right\} \tag{6.40}$$

$$Q_{jk} = \ln\left[\frac{r_5}{\sqrt{d_j^2 + d_k^2 - 2d_j d_k \cos\theta_{jk}}}\right] - \sum_{n=1}^{\infty}\frac{c_n}{n} \tag{6.41}$$

$$y_{jj} = \sum_{n=1}^{\infty}\left(\frac{d_j d_k}{r_5^2}\right)^n \frac{1}{n(1+\mu_{rp}) + \dfrac{x_5 K_{n-1}(x_5)}{K_n(x_5)}} \tag{6.42}$$

$$y_{jk} = \sum_{n=1}^{\infty} \frac{c_n}{n(1+\mu_{rp}) + \dfrac{x_5 K_{n-1}(x_5)}{K_n(x_5)}} \tag{6.43}$$

$$\left[Z_{pjj} \right] = \begin{bmatrix} Z_{pjj} & Z_{pjj} \\ Z_{pjj} & Z_{pjj} \end{bmatrix} \quad ; \quad \left[Z_{pjk} \right] = \begin{bmatrix} Z_{pjk} & Z_{pjk} \\ Z_{pjk} & Z_{pjk} \end{bmatrix} \tag{6.44}$$

$$c_n = \left(\frac{d_j d_k}{r_5^2} \right)^n \cos(n\theta_{jk}) \quad ; \quad x_5 = m_p r_5 \quad ; \quad x_6 = m_p r_6 \quad ; \quad m_p = \sqrt{\frac{s\mu_p}{\rho_p}} \tag{6.45}$$

The mutual impedance matrix $[Z_c]$ between pipe inner and outer surfaces is given by equation (6.46).

$$[Z_c] = \begin{bmatrix} [Z_{c1}]_2 & [Z_{c1}]_2 & [Z_{c1}]_2 & [Z_{c2}]_{2\times1} \\ [Z_{c1}]_2 & [Z_{c1}]_2 & [Z_{c1}]_2 & [Z_{c2}]_{2\times1} \\ [Z_{c1}]_2 & [Z_{c1}]_2 & [Z_{c1}]_2 & [Z_{c2}]_{2\times1} \\ [Z_{c2}]_{1\times2} & [Z_{c2}]_{1\times2} & [Z_{c2}]_{1\times2} & Z_{c3} \end{bmatrix} \tag{6.46}$$

Being,

$$Z_{c1} = Z_{Pouter} + Z_{PGinsul} - 2Z_{Pmutual} \quad ; \quad Z_{c2} = Z_{Pouter} + Z_{PGinsul} - Z_{Pmutual} \tag{6.47}$$

$$Z_{c3} = Z_{PGinsul} \tag{6.48}$$

The pipe outer series impedance is given by equation (6.49).

$$Z_{Pouter} = \frac{\rho_p m_p}{2\pi r_6} \cdot \frac{J_0(x_6) K_1(x_5) + K_0(x_6) J_1(x_5)}{J_1(x_6) K_1(x_5) - J_1(x_5) K_1(x_6)} \tag{6.49}$$

The series impedance of the pipe outer insulation is given by equation (6.50).

$$Z_{PGins} = \frac{s\mu_{ins4}}{2\pi} \ln\left(\frac{r_7}{r_6} \right) \tag{6.50}$$

The pipe mutual series impedance is given by equation (6.51).

$$Z_{Pmutual} = \frac{\rho_p}{2\pi r_5 r_6} \cdot \frac{1}{K_1(x_5) J_1(x_6) - J_1(x_5) K_1(x_6)} \tag{6.51}$$

Finally, $[Z_e]$ is a square matrix of order seven that represents the earth return impedance. This impedance term can be defined by Saad's approximation, equation (6.52).

$$Z_e = \frac{\rho_{seabed} m_e^2}{2\pi} \left[K_0(x_7) + \frac{2e^{-2hm_e}}{4 + m_e^2 r_7^2} \right] \tag{6.52}$$

Being,

$$x_7 = m_e r_7 \quad ; \quad m_e = \sqrt{\frac{s\mu_{seabed}}{\rho_{seabed}}} \tag{6.53}$$

Once all previous terms are calculated, the $\left[\hat{Z}_{Fn}\right]$ matrix is computed at nominal frequency and the $\left[\hat{R}\right]$ and $\left[\hat{L}\right]$ matrices can be obtained by splitting real and imaginary parts, as given by equations (6.7) and (6.8).

6.4.2   Computation of per-length Foster Equivalent Networks

For the computation of the Foster equivalent networks shown in Fig. 6.8(b), a frequency sweep is done to Z_{Couter}, Z_{Souter} and Z_{Pouter} terms. The series impedance of the core conductor Z_{Couter} is given by equation (6.54).

$$Z_{Couter} = \frac{\rho_c m_c}{2\pi r_1} \frac{J_0(x_1)}{J_1(x_1)} \tag{6.54}$$

Being,

$$x_1 = m_c r_1 \quad ; \quad m_c = \sqrt{\frac{s\mu_c}{\rho_c}} \tag{6.55}$$

Z_{Souter} and Z_{Pouter} terms are defined in equations (6.30) and (6.49), respectively. Table 6.2 shows the general data that is needed to obtain the Forster equivalent networks. The frequency vector is mainly defined in dependence of the frequency range of interest.

Table 6.2. Required general data for the determination of the Foster equivalent networks.

ω_1	ω_2	ω_3	$\cdots$	ω_t
$Z_{Couter}(\omega_1)$	$Z_{Couter}(\omega_2)$	$Z_{Couter}(\omega_3)$	$\cdots$	$Z_{Couter}(\omega_t)$
$Z_{Souter}(\omega_1)$	$Z_{Souter}(\omega_2)$	$Z_{Souter}(\omega_3)$	$\cdots$	$Z_{Souter}(\omega_t)$
$Z_{Pouter}(\omega_1)$	$Z_{Pouter}(\omega_2)$	$Z_{Pouter}(\omega_3)$	$\cdots$	$Z_{Pouter}(\omega_t)$

The frequency-dependent behaviour for each series impedance term is approximated by means of Vector Fitting (VF) algorithm [191,192]. VF provides an adequate representation of the series elements in the frequency-domain by means of a rational function on pole residue form, as given by equation (6.56).

$$f(s) = \sum_{m=1}^{M} \frac{c_m}{s - p_m} + d + se \tag{6.56}$$

The rational function, obtained from the fitting process, is represented by a Foster equivalent network of order M, as depicted in Fig. 6.10.
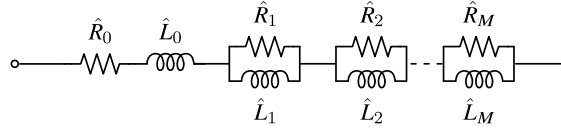
Fig. 6.10. Foster equivalent network of order *M*.

The order of the equivalent network depends mainly on the frequency range and accuracy requirements. The electrical parameters of the Foster equivalent network are given by equation (6.57).

$$\hat{R}_0 = d - \sum_{m=1}^{M} \frac{c_m}{p_m} \quad ; \quad \hat{L}_0 = e \quad ; \quad \hat{R}_m = \frac{c_m}{p_m} \quad ; \quad \hat{L}_m = -\frac{\hat{R}_m}{p_m} \tag{6.57}$$

6.4.3 Computation of per-length Capacitance Matrix

The per-length capacitance matrix $\left[\hat{C}\right]$ is computed at nominal frequency from the potential coefficient matrix $[P]$, as given by equations (6.58) and (6.59).

$$\left[\hat{C}\right] = [P]^{-1} \tag{6.58}$$

$$[P] = [P_i] + [P_p] + [P_c] \tag{6.59}$$

The cable internal coefficient matrix $[P_i]$ is given by equation (6.60).

$$[P_i] = \begin{bmatrix} [P_{i1}] & [0]_2 & [0]_2 & [0]_{2\times1} \\ [0]_2 & [P_{i2}] & [0]_2 & [0]_{2\times1} \\ [0]_2 & [0]_2 & [P_{i3}] & [0]_{2\times1} \\ [0]_{1\times2} & [0]_{1\times2} & [0]_{1\times2} & 0 \end{bmatrix} \tag{6.60}$$

Being,

$$[P_{ij}] = \begin{bmatrix} P_{cj} + P_{sj} & P_{sj} \\ P_{sj} & P_{sj} \end{bmatrix} \tag{6.61}$$

$$P_{cj} = \frac{1}{2\pi\varepsilon_{ins1}} \ln\left(\frac{r_2}{r_1}\right) \quad ; \quad P_{sj} = \frac{1}{2\pi\varepsilon_{ins2}} \ln\left(\frac{r_4}{r_3}\right) \tag{6.62}$$

The pipe internal coefficient matrix $[P_p]$ is given by equation (6.63).

$$[P_p] = \begin{bmatrix} [P_{pjj}] & [P_{pjk}] & [P_{pjk}] & [0]_{2\times1} \\ [P_{pjk}] & [P_{pjj}] & [P_{pjk}] & [0]_{2\times1} \\ [P_{pjk}] & [P_{pjk}] & [P_{pjj}] & [0]_{2\times1} \\ [0]_{1\times2} & [0]_{1\times2} & [0]_{1\times2} & 0 \end{bmatrix} \tag{6.63}$$

Being,

$$\left[P_{pij} \right] = \begin{bmatrix} P_{pij} & P_{pij} \\ P_{pij} & P_{pij} \end{bmatrix} \quad ; \quad \left[P_{pjk} \right] = \begin{bmatrix} P_{pjk} & P_{pjk} \\ P_{pjk} & P_{pjk} \end{bmatrix} \tag{6.64}$$

$$P_{pij} = \frac{Q_{jj}}{2\pi\varepsilon_{ins3}} \quad ; \quad P_{pjk} = \frac{Q_{jk}}{2\pi\varepsilon_{ins3}} \tag{6.65}$$

The potential coefficient matrix between pipe inner and outer surfaces $\left[P_c \right]$ is a square matrix of order seven with all its elements given by equation (6.66).

$$P_c = \frac{1}{2\pi\varepsilon_{ins4}} \ln\left(\frac{r_7}{r_6} \right) \tag{6.66}$$

As already shown, the above procedure details the steps and the formulation required for model parameterization.

6.5 Validation Case Studies

This section introduces two numerical case studies in order to validate the model of Fig. 6.8. The FDPi model is directly implemented in Simscape Electrical (Matlab/Simulink) and the Backward Euler technique is chosen as solver method for time-domain computations.

6.5.1 Case Study 6.1: Three-Core Submarine Cable

This case study consists of a buried three-core submarine cable. Fig. 6.11 shows the simplified cross-section of the submarine cable under study and gives information about the surrounding medium properties and burial depth of the cable. The required geometrical and material properties of the cable are listed in Table 6.3. The information presented in Fig. 6.11 and Table 6.3 is taken from reference [189,193].

The requirement of the validation is to represent the steady-state and transients comprising frequencies up to 10 kHz, which is a frequency range higher than the one required for the studies of this Ph.D. thesis. To fulfill this objective, the FDPi model is built with 32 cascaded FDPi sections (*N*=32), each one with Foster equivalent networks of order three (*M*=3) for each conductive layer term. The series impedance terms were fitted for a frequency range from 0.1 Hz up to 10 kHz by means of VF algorithm.

In order to validate the FDPi model in the time-domain, the test configuration of Fig. 6.12 has been used considering a cable length of 50 km. The test is as proposed in references [27,194]. The test consists of energizing one-phase of the cable with an AC voltage source at its sending end and with the receiving ends open. The input source signal is a cosine

function with a nominal voltage of 100 kVrms. The energization takes place at the peak voltage of the input source in order to produce the highest transient current.
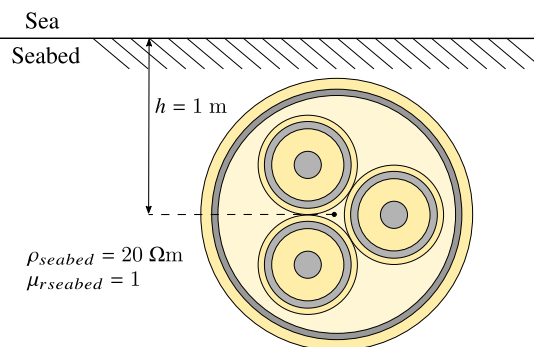
Fig. 6.11. Cable cross-section for case study 6.1 and installation conditions (laying depth and surrounding medium properties).

Table 6.3. Geometrical and material parameters for case study 6.1.

Layer	Parameters
1	$r_1 = 11.6 \text{ mm}$, $\rho_c = 1.7241 \cdot 10^{-8} \, \Omega\text{m}$, $\mu_{rc} = 1$
2	$r_2 = 26.6 \text{ mm}$, $\mu_{rins1} = 1$, $\varepsilon_{rins1} = 2.3$
3	$r_3 = 26.82 \text{ mm}$, $\rho_s = 2.20 \cdot 10^{-7} \, \Omega\text{m}$, $\mu_{rs} = 1$
4	$r_4 = 30.82 \text{ mm}$, $\mu_{rins2} = 1$, $\varepsilon_{rins2} = 2.3$
5	$r_5 = 72 \text{ mm}$, $\mu_{rins3} = 1$, $\varepsilon_{rins3} = 2.3$
6	$r_6 = 80 \text{ mm}$, $\rho_p = 2.86 \cdot 10^{-8} \, \Omega\text{m}$, $\mu_{rp} = 1$
7	$r_7 = 83 \text{ mm}$, $\mu_{rins4} = 1$, $\varepsilon_{rins4} = 2.3$

Fig. 6.12. Setup for time response validation – case study 6.1.

Fig. 6.13 shows the time response of the receiving end signals depicted in Fig. 6.12. Each graphic shows information about the steady-state and transient-state (top one) and a zoom in for the first 10 ms (down one) in order to show the transient response in detail.

As depicted in Fig. 6.13, the results of the FDPi model show a very good agreement with the ones obtained from the reference model. The shape and amplitude of the time signals are very similar and a good representation of the wave travel time is performed by the FDPi model.

Fig. 6.14 shows the magnitude and phase of the cable admittance. As indicated for the signals in the time-domain, the admittance of the cable (magnitude and phase) is very similar for both models up to a frequency value of 10 kHz.

(a)

(b)

(c)
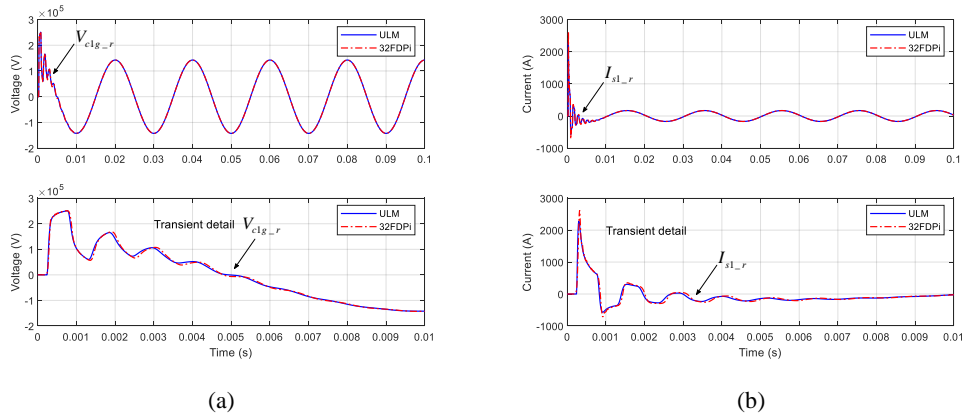
Fig. 6.13. Time response for case study 6.1. (a) V_{c1g_r}. (b) I_{s1_r}. (c) I_{p_r}.
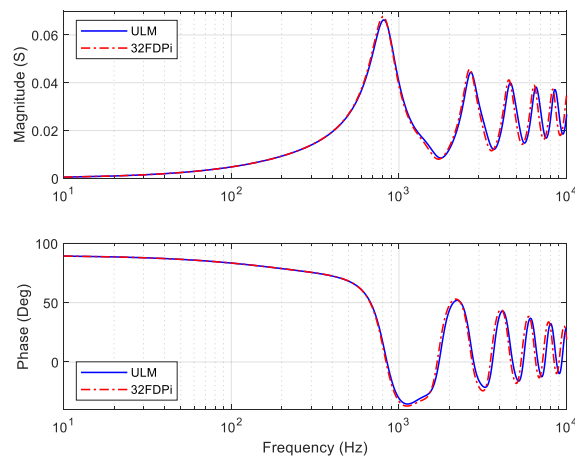
Fig. 6.14. Cable admittance comparison for case study 6.1.

The short deviation of the FDPi model with respect to the reference model is due to four main reasons. First, the parameterization that is performed by the ULM model from PSCAD/EMTDC software is not exactly the same as in reference [180]. Therefore, the comparison of both models is performed with slightly different parameter values.

Second, the representation of the FDPi model is built in order to consider frequencies up to 10 kHz. The error of the model can be reduced by considering a higher frequency range. In order to do this, the order of the model has to be increased but at the expense of increasing the computational cost.

Third, the FDPi model only takes into account the frequency dependency of the series impedance terms Z_{Couter}, Z_{Souter} and Z_{Pouter}. The frequency-dependent behaviour of other terms is not taken into account.

Finally, an additional oscillation is presented in the results of the FDPi model due to the nature that lumped parameters models introduce an unreal resonance, as explained in references [168,170]. Is in fact, a resonance that is not present in the real cable but that appears because of the characteristics of the model. In order to show this unreal resonance, Fig. 6.15 depicts the cable admittance for a frequency range of 100 kHz. It can be seen that for the FDPi model order (M=3 and N=32) considered previously, the unreal resonance is located around 40 kHz and with a magnitude of 0.01 Siemens.

Fig. 6.15 also performs an evaluation of different number (N) of cascaded FDPi sections while keeping the same order of Foster equivalent networks (M=3). Two important aspects can be inferred from Fig. 6.15. The first aspect is that an increase of the model order allows extending the frequency range of the model, which gives a lower deviation in time- and frequency-domain results. The second one is that the unreal resonance is shifted to the right in frequency and decreased in magnitude by increasing the model order.
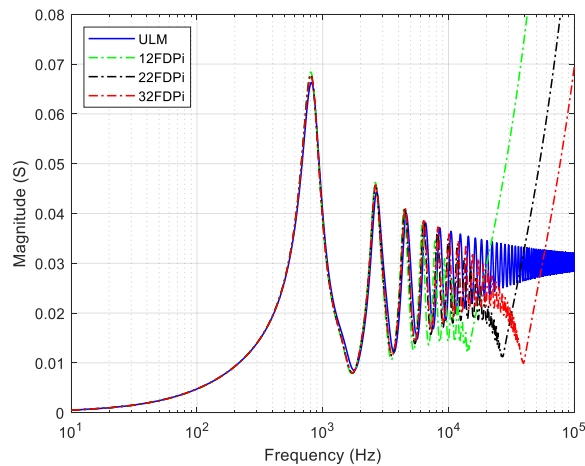
Fig. 6.15. Cable admittance comparison for case study 6.1 with different number (N) of cascaded FDPi sections.

Fig. 6.16 shows the impact of the model order on time signals. It can be seen that for lower model orders there is a higher oscillation magnitude.
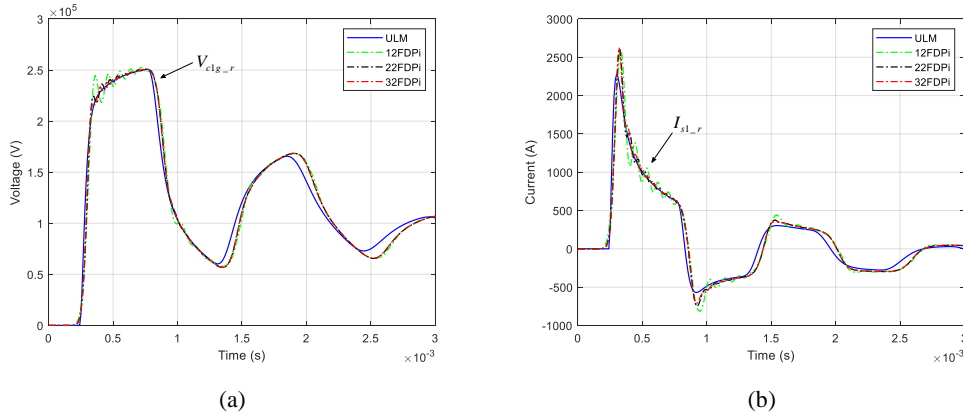
Fig. 6.16. Time response comparison with different number (*N*) of cascaded FDPi sections for case study 6.1. (a) V_{c1g_r}. (b) I_{s1_r}.

6.5.2 Case Study 6.2: Three Single-Core Underground Cables

The cable system for this second case study consists of three single-core cables, one for each phase, as shown in Fig. 6.17. This figure shows the simplified cross-section of each single-core cable and gives information about the surrounding medium properties, burial depth and laying formation of the cable system.

Each single-core underground cable operates with a nominal voltage of 150 kV. The cable has a core cross-section of 1200 mm² and its insulation material is XLPE (cross-linked polyethylene).

The required geometrical and material properties of the cable are listed in Table 6.4. The information presented in Fig. 6.17 and Table 6.4 is adopted from reference [170].
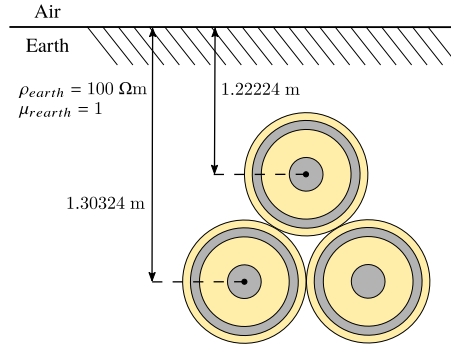
Fig. 6.17. Cable cross-section for case study 6.2 and installation conditions (laying depth and surrounding medium properties). Source [170].

Table 6.4. Geometrical and material parameters for case study 6.2. Source [170].

Layer	Parameters
1	$r_1 = 20.75$ mm , $\rho_c = 3.19 \cdot 10^{-8}$ Ωm , $\mu_{rc} = 1$
2	$r_2 = 40.25$ mm , $\mu_{rins1} = 1.08$, $\varepsilon_{rins1} = 2.68$
3	$r_3 = 42.76$ mm , $\rho_s = 1.19 \cdot 10^{-7}$ Ωm , $\mu_{rs} = 1$
4	$r_4 = 46.76$ mm , $\mu_{rins2} = 1$, $\varepsilon_{rins2} = 2.5$

As in the previous case, the requirement of the validation is to represent the steady-state and transients comprising frequencies up to 10 kHz, which is a frequency range higher than the one required for the studies of this Ph.D. thesis. To fulfill the objective, the FDPi model is built with 35 cascaded FDPi sections (*N*=35), each one with Foster equivalent networks of order three (*M*=3) for each conductive layer term. The series impedance terms were fitted for a frequency range from 0.1 Hz up to 10 kHz by means of VF algorithm.

In order to validate the response of the FDPi model in the time-domain, the test configuration of Fig. 6.18 has been used considering a cable length of 50 km. Similar to the previous case, the test consists of energizing one-phase of the cable with an AC voltage source at its sending end and with the receiving ends open. The input source signal is a cosine function with a voltage magnitude of 150 kVrms (nominal voltage given by the cable manufacturer). The energization takes place at the peak voltage of the input source in order to produce the highest transient current.
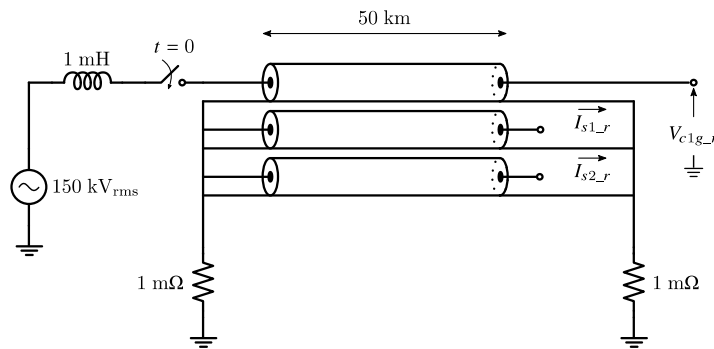
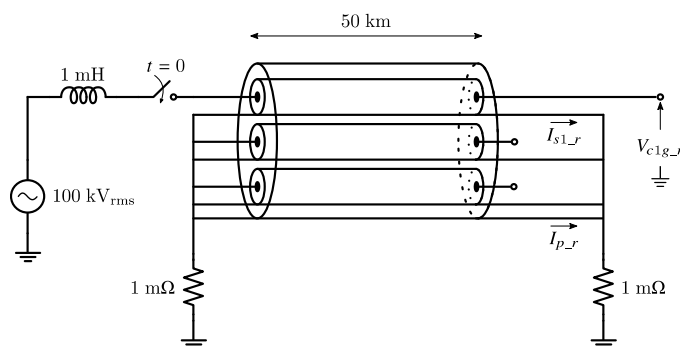Fig. 6.18. Setup for time response validation – case study 6.2.

Fig. 6.19 shows the time domain response of the receiving end signals depicted in Fig. 6.18. As in the previous case, each plot shows information about the steady- and transient-state (top one) and a zoom in for the first 10 ms (down one) in order to show the transient response in detail.

Fig. 6.20 shows the magnitude and phase of the cable admittance for a frequency value up to 10 kHz.

As depicted in previous figures, time- and frequency-domain results obtained from the FDPi model show a very good agreement with the ones obtained from the reference model. The shape and amplitude of the time signals are very similar and a good representation of the wave travel time is obtained by the FDPi model. Furthermore, it can be seen that the results obtained for this case study present a lower deviation in comparison with the previous one.

This lower deviation is mainly because the formulation used for cable parameterization (single-core cables) is the same as the one by the ULM model from PSCAD/EMTDC software. Therefore, the same values for the series impedance terms and shunt admittance terms are obtained and the differences in the results are mainly due to the characteristics of both models.
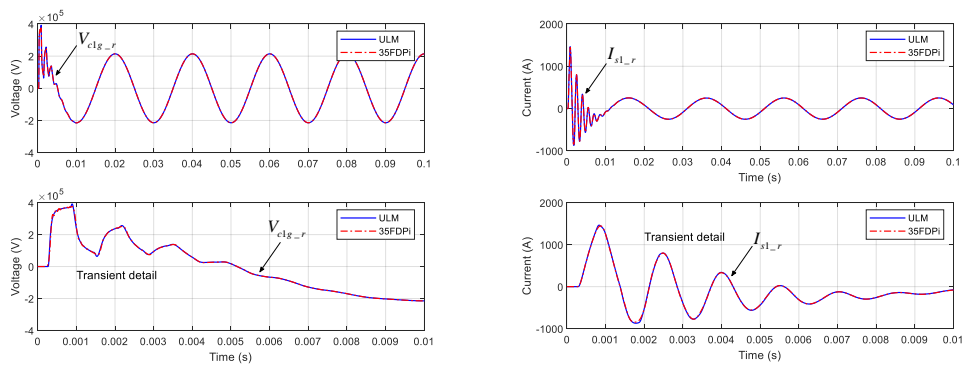
(a)

(b)
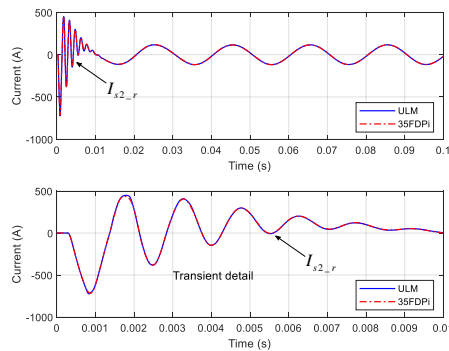
(c)

Fig. 6.19. Time response for case study 6.2. (a) V_{c1g_r}. (b) I_{s1_r}. (c) I_{s2_r}.
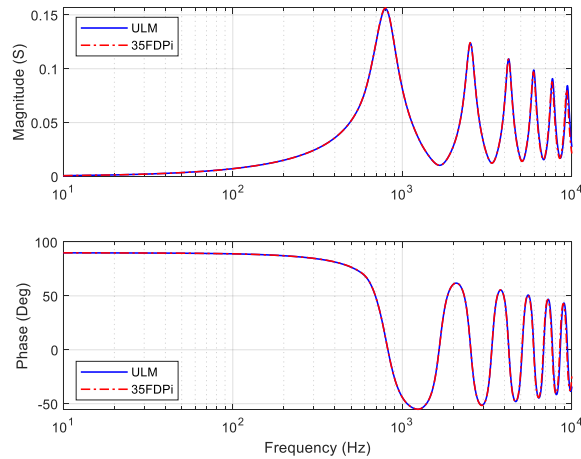
Fig. 6.20. Cable admittance comparison for case study 6.2.

As presented in the previous case study, some changes are done to the number (N) of cascaded FDPi sections in order to show its effects on the frequency range and unreal resonance of the cable (Fig. 6.21). Similar conclusions are obtained as in the previous example.
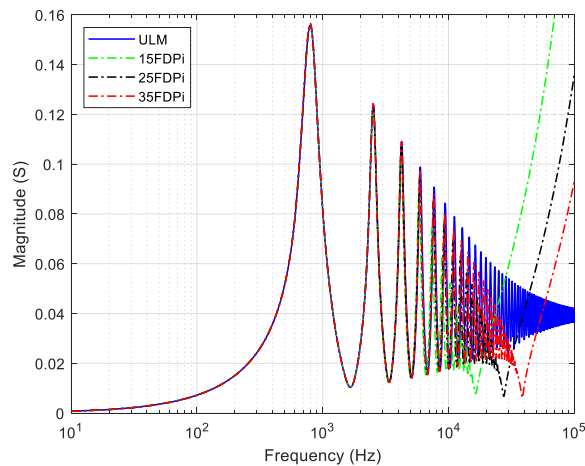
Fig. 6.21. Cable admittance comparison for case study 6.2 with different number (*N*) of cascaded FDPi sections.

As last point, it is worth to emphasize that all the parameters information for this cable is taken from reference [170]. In this reference, field measurements were done to a single section of a 150 kV underground cable and the results were compared with the Universal Line Model (ULM) from PSCAD/EMTDC software. The conclusions obtained in reference [170] describes a good agreement between measurements and ULM model for the coaxial mode of the real cable. In this sense, it can be stated that the results presented in this example indirectly validate the response of the FDPi model with experimental measurements.

6.6 Methodology for the Selection of the FDPi Model Order

As it can be inferred from the results shown in the previous section, the choice of an optimal model order, selection of *M* and *N*, does not obey deterministic rules and is highly dependent on several factors. This characteristic difficults the possibility of presenting guidelines that are valid for all the scenarios.

This section is intended to serve as a basis for creating a software tool that is capable of selecting a suitable model order for representing a given cable under specific performance requirements. Fig. 6.22 shows the general procedure that should be implemented in the software tool for the determination of the optimal order of the FDPi model.
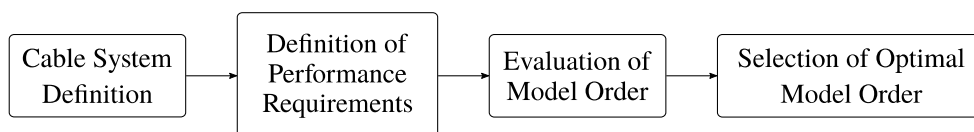
Fig. 6.22. General procedure for the determination of the optimal order of the FDPi model.

The first point to take into account is the definition of the cable system under study. This definition comes from the characteristics of the cable system, which are mentioned next.

- Type of cable: Submarine or underground cable. Three-core or single-core cables.
- Cable length.
- Cable disposition: Tight or spaced disposition in flat or trefoil formation.
- Surrounding medium properties: resistivity and relative permeability of the surrounding medium.
- Burial depth.
- Grounding configuration: Single-end bonding, both-ends bonding or cross bonding.
- Load connected to the cable system: The cable impedance depends on the termination of the cable. This impedance can vary continuously (infinite possibilities). Extreme cases can be considered for the cable system, short-circuited cable and open-ended cable.
- Couplings between other cable systems.

All these aspects change the time response and frequency response of the cable. Therefore, they need to be evaluated in order to select an optimal model order.

The second step consists of defining the performance requirements that the FDPi model must fulfill. The most relevant requirements are:

- Frequency range: The definition of the frequency range is crucial for the intended application of the model. An adequate value should be assigned in order to include all the relevant dynamics that can have an effect on the studies that are going to be performed.
- Accuracy: It is necessary to define a minimum accuracy limit and quantify the accuracy. In order to quantify the accuracy, a measure of the error associated with the FDPi model must be defined. Several criteria can be used for the quantification of the error such as averaged error, weighted error and absolute error. Additionally, the error can be computed in the time-domain, frequency-domain or taking into account both domains. In reference [166], the authors suggest assessing the accuracy of the FDPi model in the frequency-domain by computing the absolute error point-by-point over the frequency range of interest. Absolute error is chosen over other methods mainly to avoid a high error in a single-frequency (for example in a resonance frequency). Furthermore, the accuracy of the FDPi model should be performed by evaluating the amplitude and phase error by separately. ULM model can be considered as the reference model if measurements are not available.

The third block of Fig. 6.22 consists of evaluating the order of the FDPi model. A sweep of M and N values should be performed for the cable system under study. Accuracy and computational time must be recorded for each M and N combination.

The last step is to select the optimal model. The selection of the optimal model order is a balanced trade-off between the following two conditions:

- Accuracy level within the allowable limit.
- The lowest computational time.

In general, higher values of M and N will lead to a better accuracy. However, beyond a certain model order, the improvements in accuracy with further increase of the model order tend to become almost negligible.

Another important aspect to take into account for the accuracy of the FDPi model is the way VF algorithm performs the approximation of the frequency-dependent variation of the electrical parameters of the cable system. VF algorithm may be fine-tuned by applying a weighting function [191]. This weighting function can improve the accuracy in a specific frequency region.

6.7 Chapter Summary

In this chapter, an FDPi model has been developed in order to reproduce the behavior of a three-core submarine cable. The model consists of N cascaded FDPi sections. Each FDPi section incorporates the following (i) the magnetic coupling which is represented by an inductance matrix, (ii) the electrical coupling between conductors and represented by means of capacitances, (iii) the frequency-dependent variation of the conductive layers by means of Foster equivalent networks, and (iv) the loss mechanism of the cable represented with each resistive element. All these four points allow an easy implementation of the model by means of discrete RLC components.

Parameterization of the model is described in detail and is performed according to analytical equations. However, other parameterization methods can be used to account for proximity effect and other medium characteristics.

Regarding the validation of the FDPi model, two case studies are presented and a comparison is performed with a reference model, the ULM model from PSCAD/EMTDC software. The first case presents the results of the FDPi model for the cable under study, a three-core submarine cable. The second case study presents the results of three-single core underground cables laid in trefoil formation. This last case confirms two important points in order to give more weight to the validity of the FDPi model. The first point is the model applicability to other types of cable systems and the second point is an indirect validation with experimental measurements that were performed on a real cable system for the coaxial mode.

The results for both case studies show a very good agreement of the FDPi model in representing the behaviour of a power cable, submarine and underground cable, for

frequencies up to 10 kHz. This frequency range is higher than the one required for the studies of this Ph.D. thesis, 50 Hz to 5 kHz. Additionally, the effects of model order on the time response and the unreal resonance of the cable model are presented for a different number of cascaded FDPi sections.

Finally, it is important to emphasize that the choice of a suitable FDPi model order does not obey deterministic rules. It is highly dependent on requirements such as desired accuracy and frequency range of interest on the one hand and characteristic of the cable under study such as type of cable, cable configuration and cable length on the other hand.

Chapter 7

Offshore Wind Power Plant Modeling

This chapter presents two complementary approaches to model an offshore wind power plant, the Simulink®-based model and an analytical sequence network model in state-space form. A description of the model development, model parameterization and an initial analysis of two case studies are some of the aspects carried out for both modeling approaches. The development of both modeling approaches is based on the models presented in previous chapters and in the definition of an OWPP base scenario. This last is defined taking into account information of a real OWPP. The parameterization procedure is briefly explained for each power component model. The results shown for the two case studies are based on specific characteristics such as power factor, wind conditions, type of modulation of grid side converters and other features that are set for the OWPP base scenario.

7.1 Introduction

Harmonics are a special concern in the offshore wind industry due to the high penetration of power converters in type-4 wind turbines [5]. Some of the many advantages of installing type-4 wind turbines are presented in subsection 2.2.1. As a side effect, this type of WT can be considered as a source of harmonics, which significantly contributes to the overall harmonic emission at the point of common coupling of the OWPP. Furthermore, this contribution can be worsened due to the presence of resonances that may increase a given

voltage or current harmonic component. These resonances can be classified into series and parallel resonances and they occur due to capacitive- and inductive behavior of installed power components in combination with the impedance of the grid. Submarine cables exhibit a predominant capacitive behavior while transformers behave predominantly as inductors for the frequency range of study of this document, 50 Hz to 5 kHz.

This scenario constitutes a power quality problem since voltage and current waveforms can be highly distorted leading to the infringement of grid codes in terms of harmonics. In this sense and with the aim of achieving the objective of this Ph.D. thesis, it is required to consider three important factors. First, an accurate representation of the harmonics injected by the wind turbines, which clearly depend on modulation strategy and control loops of the GSCs. Second, the frequency-dependent characteristic of installed passive components, e.g. submarine cables and transformers. The third factor to consider is the evaluation of different operation points for each wind turbine, not only for the rated condition. These operation points depend on power factor requirements, wind conditions, and location of each wind turbine.

According to the previous ideas and the main objective of this Ph.D. thesis, two modeling approaches are performed for the studies presented in subsequent chapters. The first modeling approach consists of a Simulink®-based model of an OWPP by implementing and connecting the models described from chapter 3 to chapter 6. The aim of the Simulink®-based model is to determine voltage and current distortion at different points along the OWPP, the BDEW grid code compliance in terms of harmonics, and the design and evaluation of technical solutions to potential problems. Even though this Ph.D. thesis addresses the aforementioned aspects, it is important to emphasize that studies such as the fulfillment of grid codes in terms of LVRT, HVRT, and others can be performed. For these studies, the addition of certain power components, control strategies, and other functionalities or blocks that are not covered in this Ph.D. thesis can be required. A better description of these aspects is addressed in future work.

The second modeling approach addressed in this project is the development of a sequence network model of the passive components of the OWPP, hereafter only called sequence network model. The sequence network model is developed by means of a state-space representation of the OWPP and it is implemented in a *.m-file in Matlab®. The purpose of the sequence network model is to perform a series of studies whose computation is not an easy task to be performed by the Simulink®-based model in terms of post-processing and time consumption. Among the studies that can be performed and are addressed in chapter 8 are the frequency response and parameter sensitivity studies of the OWPP.

This chapter is structured as follows. Section 7.2 defines an OWPP base scenario where all the required parameters, for the modeling of the main power components, are known. The base scenario is defined taking into account information of a real OWPP. Section 7.3 carries out the Simulink®-based model of the OWPP base scenario. The parameterization of the Simulink®-based model, the wake effect for the OWPP base scenario, and the results of two case studies are presented for this section. The results shown for both case studies are

based on characteristics such as power factor, wind conditions, type of modulation of GSCs and other features that are set for the OWPP base scenario. The aim of both case studies is to provide initial insight into the steady-state harmonic evaluation of an OWPP by means of the Simulink®-based model. A deeper study of this aspect is addressed in chapter 9. Section 7.4 presents the second modeling approach, the sequence network based model. Two main aspects are carried out in this section. First, a general- and a simplified-approach of the sequence network model of the OWPP base scenario is presented. Second, the sequence network model of each passive component is provided together with its state-space formulation. Finally, section 7.5 gives the chapter summary.

7.2 Definition of an OWPP Base Scenario

Before starting with the development of both modeling approaches, it is necessary to define an OWPP base scenario where all the required parameters, for the modeling of the main power components, are known.

The base scenario is defined taking into account information of a real OWPP. The real OWPP, taken as reference, is Alpha Ventus offshore wind farm [195]. There are two main reasons for its selection among other real OWPPs. The first one and more important is that general information regarding voltage levels at different points of the OWPP, wind farm layout, grounding scheme, and main electrical components are known. The last one is that the number of power components (such as WTs, transformers and submarine cables) is not too high, so the computational burden of the Simulink®-based model is not high too. All the information and references that support the definition of the OWPP base scenario are given in Appendix B. The reader is suggested to review this Appendix.

It is important to emphasize that even though the OWPP base scenario is defined based on Alpha Ventus, it is not an exact reproduction of this offshore wind farm. It is also worthy to point out that certain parameters, required for the modeling of the main power components, have been assumed due to a lack of information. The assumptions were made according to supporting references and the datasheets of other components, as it is presented in subsection 7.3.1. A brief description of the OWPP is given next.

Fig. 7.1 depicts the simplified single-line diagram of the OWPP base scenario. The OWPP base scenario has a total capacity of 60 MW. This amount of power is generated from 12 type-4 WTs, each one with a power rating of 5 MW. The MV100 converter, as pointed out and presented in subsection 3.5.2, is the GSC considered to be installed at each WT for subsequent studies. The GSC connection filter described in subsection 3.5.2 is considered too. It is an LCL-rl filter designed mainly to meet grid code requirements related to current harmonics.

The step-up transformer installed inside the WTs, hereafter called Wind Turbine Transformer (WTT), increases the converter voltage level from 3.3 kV to 30 kV, which is the voltage level of the collection network. The windings of the wind turbine transformer are Dyg1 connected.

(a)

(b)
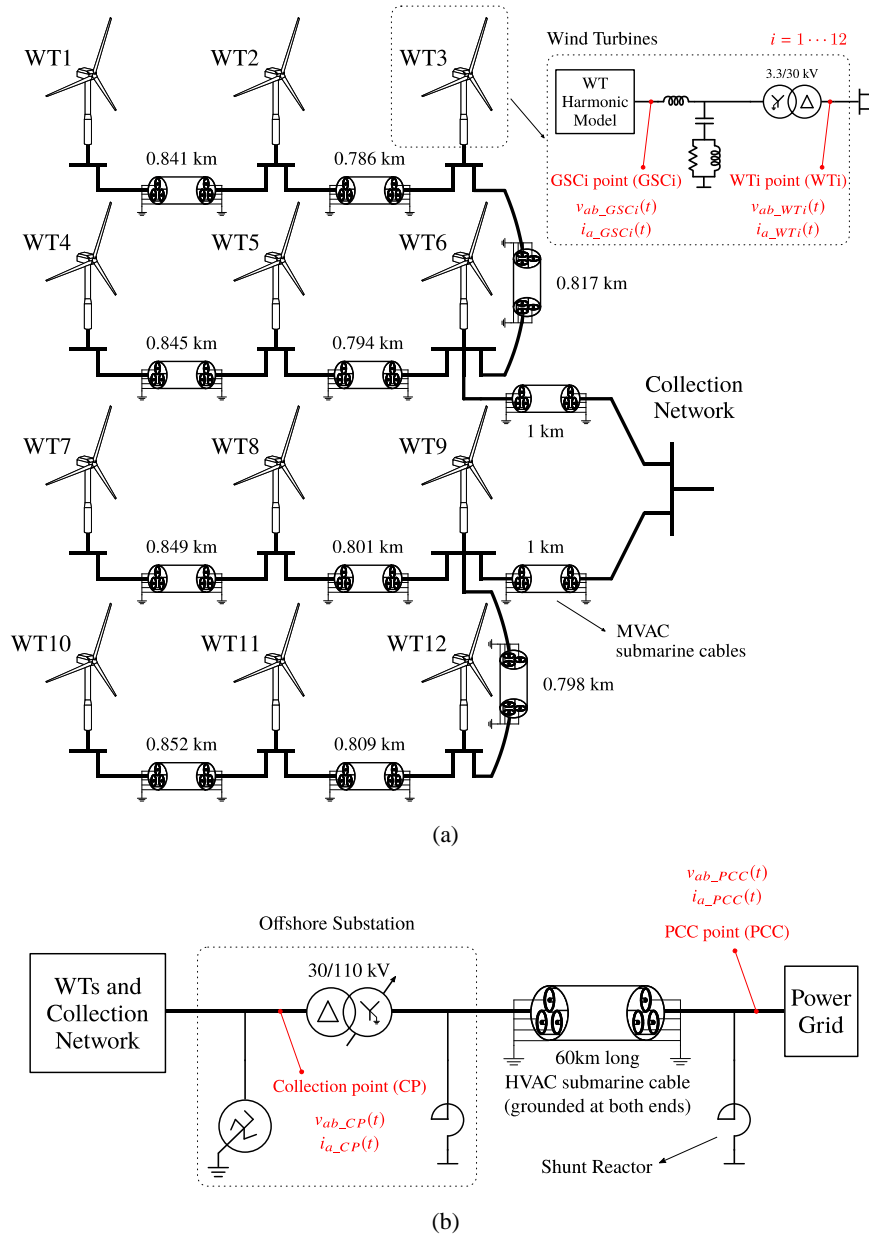
Fig. 7.1. Simplified single-line diagram of the OWPP base scenario. (a) Wind turbines and collection network. (b) Transmission system.

The WTs are clustered into groups of three forming a collection network with a rectangular shape. As already mentioned, the voltage level of the collection network is 30 kV. Information about the wind farm layout and the distance of each submarine cable of the collector network is depicted in Fig. 7.1(a). Redundant connections are not implemented for this base scenario. The collector network then links all the WTs to an offshore platform.

The offshore platform has a step-up transformer and a grounding transformer. The step-up transformer, hereafter called Offshore Substation Transformer (OST), increases the voltage of the collection network to 110 kV, which is the voltage level of the transmission system. The OST has a rated power of 75 MVA and the windings are Ygd1 connected. The grounding transformer provides a neutral in the three-phase, three-wire system of the collection network. The grounding transformer consists of three two-winding transformers connected in zigzag.

The link between the offshore substation to onshore is done by a single three-core submarine cable of 60 km long. The screens and armour of the submarine cables of the collection network and transmission system are grounded at both ends as depicted in Fig. 7.1. Shunt reactors are installed at both ends of the transmission system. The purpose of those reactors is the management of the reactive power through the 60 km long submarine cable [27]. The energy transmission of the OWPP is improved since these shunt reactors reduce the required rated current of the cable and the active power losses.

Finally, the OWPP is connected to the main power grid of 110 kV, 50 Hz and representing a grid with a Short-Circuit Ratio (SCR) equal to 20 [27].

In subsequent chapters and in this chapter, voltage- and current signals at different points along the OWPP and Bode plots of transfer functions relating different voltage- and current variables are presented. In this sense, it is important to define certain points of study. These points are highlighted in red and are depicted in Fig. 7.1.

The GSCi point refers to voltages and currents of the ith converter whereas the WTi point indicates the voltages and currents of the ith wind turbine. This last point refers to the voltages and currents at the high voltage (HV) side of the WTT as depicted in Fig. 7.1(a).

The collection point (CP) is the point where the energy generated by all the WTs is collected. On the other hand, the Point of Common Coupling (PCC) is considered the point where the transmission system of the OWPP meets the main grid. At this point, the OWPP has to fulfill the grid code requirements such as harmonic limits (e.g. the ones described by the BDEW), THD, power factor, and others. Fig. 7.1(b) shows the location of both points, Collection- and PCC point.

7.3 Simulink®-based Model of the OWPP Base Scenario

Once the definition of the OWPP base scenario is performed, each Simulink®-based component model, described in previous chapters, is implemented. The models are defined as library components in order to use them according to the characteristics of the OWPP scenario to represent. The definition of each power component as a library component allows the possibility to scale or make changes to the Simulink®-based model in a faster way. The wake effect of a WT is considered by means of adding the tool shown in Fig. 4.5.

While the Simulink® model is running, it stores several variables in a *.mat-file in order to perform future post-processing, visualization, and comparison of such variables. These tasks are executed by running additional scripts. One additional aspect to point out is that having several scopes is not required anymore due to the storage of signals. Specific scopes in order to visualize certain variables, the ones with higher interest, can be included according to the user criterion. The reduction of scopes allows an additional decrease of the total simulation time, which is a positive aspect when analyzing several cases and scenarios with a high number of power components.

Fig. 7.2 shows the Simulink®-based model of the OWPP base scenario. Fig. 7.3 depicts the schematic of the implemented WT model. The WT model considers some simplifications, which are described in the following subsection.
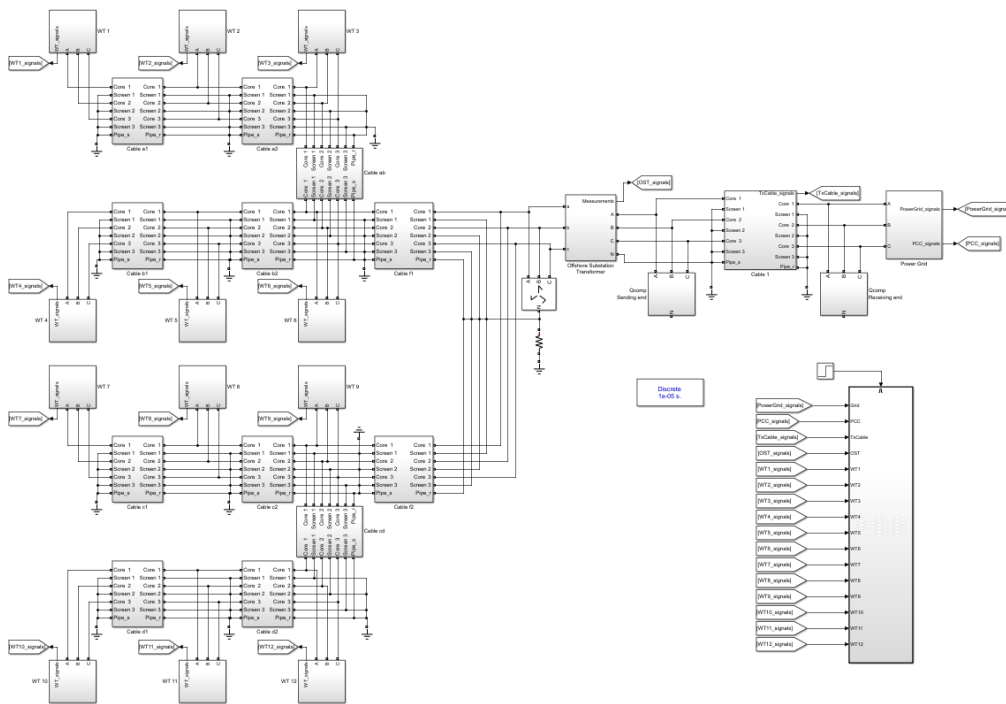
Fig. 7.2. Simulink®-based model of the OWPP base scenario.
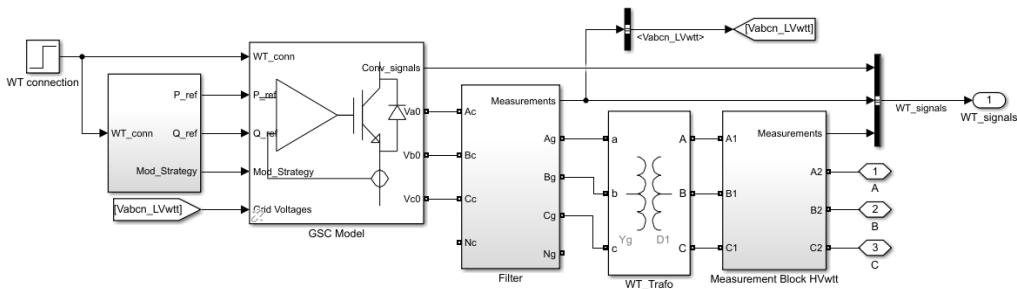
Fig. 7.3. Simplified WT harmonic model for the representation of the OWPP base scenario.

The parameterization of each model, the wake effect in the OWPP base scenario and the results of a specific case considering certain wind conditions and the two types of

modulation schemes, CB-PWM and SHE-PWM, are addressed in the following subsections.

7.3.1   Parameters of the Simulink®-based model of the OWPP Base Scenario

The following information provides the parameters of the models presented from chapter 3 to chapter 6 with the aim of representing the Simulink®-based model of the OWPP of Fig. 7.2.

Grid Side Converter (GSC) of Wind Turbines

The studies presented in chapter 9 focus on the steady-state current-harmonic evaluation of an OWPP. This harmonic evaluation is performed by means of computing the spectrum of current signals, THDi values and the fulfillment of the BDEW grid code. Taking into consideration these target studies, certain blocks of the WT harmonic model presented in section 3.4 can be simplified or not represented as suggested in reference [27].

The grid side converter and the machine side converter are considered decoupled. In this sense and according to the target studies addressed in this Ph.D. thesis, only the GSC is considered. The drive-train block of the WT harmonic model is not taken into account for the reasons described previously.

The reec_a block of the WT harmonic model of Fig. 3.13 is simplified. The estimated active- and reactive power generation are inputs of this block. The PQ-priority logic at fault conditions, depicted in Fig. 3.13, is not taken into account as well. The current limit logic is set to 1.15 pu.

The estimated active power generation of each WT is defined according to the wake effect and is addressed in subsection 7.3.2. The reactive power reference of each WT is defined in order to make the WTs operate with a unity power factor.

Table 7.1 gives the general parameters of the GSC of each wind turbine.

Table 7.1. General parameters of the GSC of each wind turbine.

General parameters of the GSC	
Rated active power	5 MW
Grid voltage	3.3 kV
DC-link voltage	$V_{Bus} = 5700$ V
Modulation strategy	CB-PWM
Switching frequency	$f_{sw} = 1150$ Hz

Fig. 7.4 shows the schematic of the current control strategy of the GSC. As depicted in this figure, Proportional-Integral (PI) controllers in the synchronous reference frame are implemented for the positive-sequence only. Cancellation of cross-coupling terms is included in order to improve the time response to reach the steady-state due to a change in the current setpoints. Table 7.2 gives the parameters of the current control loop of the GSC model.
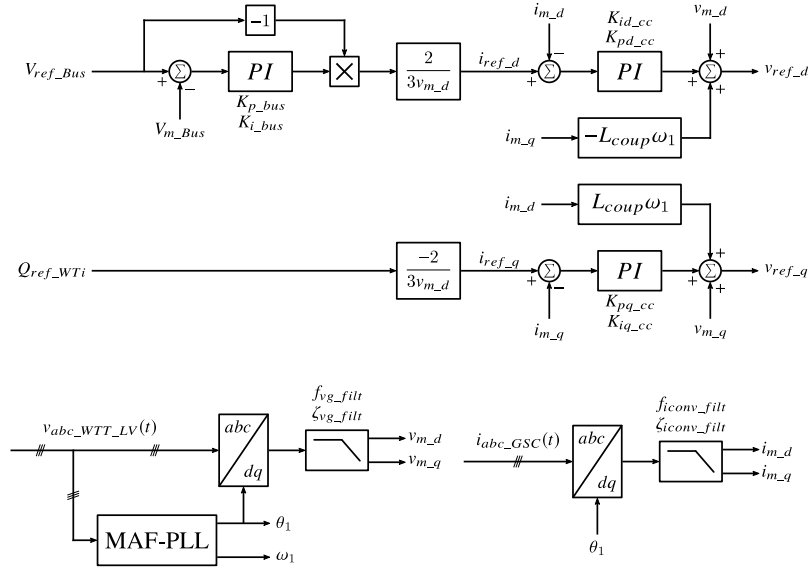
Fig. 7.4. Schematic of the current control strategy of the GSC.

Table 7.2. Parameters of the GSC current control loop.

Current control loop	
Proportional gain d-axis	$K_{pd\_cc} = 0.1426$
Integral gain d-axis	$K_{id\_cc} = 4.8652$
Proportional gain q-axis	$K_{pq\_cc} = 0.1426$
Integral gain q-axis	$K_{iq\_cc} = 4.8652$
Coupling term inductance	$L_{coup} = 675\ \mu H$

The voltage generated by the GSC has to be synchronized with the phase angle of the grid. To achieve this synchronization, the MAF-PLL of Fig. 3.8 is implemented. According to the guidelines presented in subsection 3.3.4, the bandwidth of the PLL is designed to be lower than the system fundamental frequency in order not to bring in any harmonic frequency oscillations. Additionally, the MAF-filter implemented in this type of PLL aids in this task. Table 7.3 provides the parameters of the MAF-PLL.

Table 7.3. Parameters of the MAF-PLL.

MAF-PLL	
Proportional gain	$K_{p\_pll} = 20$
Integral gain	$K_{i\_pll} = 70$
Maximum rate of change of frequency	$f_{max\_rate} = 12\ Hz/s$
Filter cut-off frequency for frequency measurement	$f_{fmeas\_filt} = 25\ Hz$

As pointed out in previous paragraph, it is desired not to bring in any harmonic frequency oscillation or at least reduce the magnitude of them. One common practice to reduce the pollution that affects the current control scheme is to filter the signals that are inputs of the control scheme. In this sense, Low Pass Filters (LPFs) are added to the current control scheme in order to filter the converter current and grid voltage dq signals. Table 7.4 shows the parameters of these measurement filters.

Table 7.4. Parameters of the measurement filters for the GSC model.

Measurement filters		
GSC Current	Filter type	Second-order LPF
	Cut-off frequency	$f_{iconv\_filt} = 200$ Hz
	Damping	$\zeta_{iconv\_filt} = 1$
Grid Voltage	Filter type	Second-order LPF
	Cut-off frequency	$f_{vg\_filt} = 200$ Hz
	Damping	$\zeta_{vg\_filt} = 1$

GSC connection Filter

Table 7.5 gives the parameters of the LCL-rl filter that is taken into account as the connection filter of the GSCs. This filter is designed considering a type-4 WT, the harmonic spectrum of the typical CB-PWM modulation (presented in subsection 3.5.2) and the grid code that must fulfill. For this last, the BDEW grid code in terms of harmonics is considered.

The value of the grid side inductor is not given since this value is defined by the short-circuit inductance of the WT transformer. This value is given in the parameterization of the wind turbine transformer, the next component.

Table 7.5. Parameters of the CB-PWM modulation oriented filter. Source [90].

LCL-rl filter			
$L_{c\_wt} = 675\,\mu H$	$C_{f\_wt} = 270\,\mu F$	$L_{d\_wt} = 190\,\mu H$	$R_{d\_wt} = 0.52\,\Omega$

Wind Turbine Transformer

The parameterization of the Wind Turbine Transformer (WTT) is performed by considering the datasheet of a 2.35 MVA ABB transformer and by performing assumptions for the unknown information. The assumptions are based on the guidelines presented in section 5.4. Appendix B.2 presents the datasheet of the ABB transformer.

In order to determine the parameter values of the WTT, the ABB transformer data is scaled up to 5 MVA considering the same per-unit values. The frequency-dependent behavior of the short-circuit impedance is assumed due to the lack of information about the real transformer. The assumption is based on the per-unit values of the third-order Foster equivalent network given in Table 5.3 for a typical transformer of 20 MVA, closest information available to the required 5 MVA WTT.

The representation of the core is made by considering a linear core resistance and a magnetic linear inductance. The non-linear magnetic inductance presented in the adopted model of Fig. 5.12 cannot be reproduced due to a lack of supporting information.

The values of the stray capacitances are assumed according to the information given in Table 5.6 for a 5 MVA transformer. The influence of the stray capacitances can be neglected for the studied frequency range, frequencies up to 5 kHz. These capacitances cannot be neglected if considering frequencies higher than 10 kHz according to reference [154].

Taking into account the previous procedure and the schematic of the transformer model presented in Fig. 5.12, Table 7.6 shows the parameters of the WT transformer model.

Table 7.6. Model parameters of the wind turbine transformers.

Basic nameplate information			
Rated Power	5 MVA	Rated Voltage (LV side)	3.3 kV
Rated Voltage (HV side)	30 kV	Transformer Connection	Dyg1
Short-circuit impedance of the HV-side winding			
$R_{p0\_wtt} = 0.6426\,\Omega$	$R_{p1\_wtt} = 15.9341\,\Omega$	$R_{p2\_wtt} = 1.6672\,\text{k}\Omega$	$R_{p3\_wtt} = 1.7477\,\text{k}\Omega$
	$L_{p1\_wtt} = 3.8709\,\text{mH}$	$L_{p2\_wtt} = 18.9658\,\text{mH}$	$L_{p3\_wtt} = 0.7367\,\text{mH}$
Short-circuit impedance of the LV-side winding			
$R_{s0\_wtt} = 0.0078\,\Omega$	$R_{s1\_wtt} = 0.1928\,\Omega$	$R_{s2\_wtt} = 20.1733\,\Omega$	$R_{s3\_wtt} = 21.1466\,\Omega$
	$L_{s1\_wtt} = 46.8\,\mu\text{H}$	$L_{s2\_wtt} = 229.5\,\mu\text{H}$	$L_{s3\_wtt} = 8.9143\,\mu\text{H}$
Core impedance (referred to the HV-side)			
$R_{C\_wtt} = 90\,\text{k}\Omega$		$L_{M\_wtt} = 125.03\,\text{H}$	
Stray capacitances			
$C_{HG\_wtt} = 1.2\,\text{nF}$	$C_{HL\_wtt} = 1.1\,\text{nF}$		$C_{LG\_wtt} = 5.5\,\text{nF}$
Zero-sequence inductance (referred to the HV-side)			
$L_{0\_wtt} = 0.2865\,\text{H}$			

Submarine Cable of the Collection Network

For the parameterization, it is required to have constructional data of a real cable in order to represent the FDPi model presented in section 6.3. In this sense, the 2XS2YRAA 18/30(36) kV three-core submarine cable from Nexans manufacturer is chosen. There are two reasons for its selection. The first one is that technical data such as voltage, current ratings and cross-sectional area of the core conductor are very similar to the ones defined by the real OWPP that is taken as reference for the definition of the OWPP base scenario, see Table B.3 in Appendix B.1.

The other reason is that information about constructional data is known. Table B.7 and Table B.8 give information about Nexans 2XS2YRAA 18/30(36) kV submarine cable. The simplified geometrical and material parameters of this submarine cable together with considered surrounding medium properties and burial depth are described in Appendix B.3.

Once having the constructional data and the installation conditions of the cable, the parameterization of the submarine cable is performed according to the procedure detailed in section 6.4. Taking into account the previous procedure and the schematic of the FDPi model presented in Fig. 6.8, Table 7.7 shows the model parameters of the collection network cable.

Now, each submarine cable of the collection network can be represented by multiplying the parameters given in per-length with the distance of each submarine cable, shown in Fig. 7.1(a). The number of FDPi sections is equal to one in order to represent frequencies up to 5 kHz, frequency range of interest for the studies presented in this Ph.D. thesis as explained in chapter 1.

Table 7.7. Model parameters of the collection network cable.

Resistance matrix						

$$
\left[\hat{R}_{cc}\right] = \begin{bmatrix}
131.0867 & 55.5535 & 46.5393 & 46.5393 & 46.5393 & 46.5393 & 49.4799 \\
55.5535 & 785.4892 & 46.5393 & 46.5393 & 46.5393 & 46.5393 & 49.4799 \\
46.5393 & 46.5393 & 132.4423 & 55.5535 & 46.5393 & 46.5393 & 49.4799 \\
46.5393 & 46.5393 & 55.5535 & 785.4892 & 46.5393 & 46.5393 & 49.4799 \\
46.5393 & 46.5393 & 46.5393 & 46.5393 & 132.4423 & 55.5535 & 49.4799 \\
46.5393 & 46.5393 & 46.5393 & 46.5393 & 55.5535 & 785.4892 & 49.4799 \\
49.4799 & 49.4799 & 49.4799 & 49.4799 & 49.4799 & 49.4799 & 162.9230
\end{bmatrix} \; \text{m}\Omega/\text{km}
$$

Inductance matrix						

$$
\left[\hat{L}_{cc}\right] = \begin{bmatrix}
2.1283 & 1.9817 & 1.8445 & 1.8445 & 1.8445 & 1.8445 & 1.8032 \\
1.9817 & 1.9807 & 1.8445 & 1.8445 & 1.8445 & 1.8445 & 1.8032 \\
1.8445 & 1.8445 & 2.1452 & 1.9817 & 1.8445 & 1.8445 & 1.8032 \\
1.8445 & 1.8445 & 1.9817 & 1.9807 & 1.8445 & 1.8445 & 1.8032 \\
1.8445 & 1.8445 & 1.8445 & 1.8445 & 2.1452 & 1.9817 & 1.8032 \\
1.8445 & 1.8445 & 1.8445 & 1.8445 & 1.9817 & 1.9807 & 1.8032 \\
1.8032 & 1.8032 & 1.8032 & 1.8032 & 1.8032 & 1.8032 & 1.7945
\end{bmatrix} \; \text{mH/km}
$$

Capacitance matrix						

$$
\left[\hat{C}_{cc}\right] = \begin{bmatrix}
0.230 & -0.230 & 0 & 0 & 0 & 0 & 0 \\
-0.230 & 0.5051 & 0 & -0.0808 & 0 & -0.0808 & -0.1134 \\
0 & 0 & 0.230 & -0.230 & 0 & 0 & 0 \\
0 & -0.0808 & -0.230 & 0.5051 & 0 & -0.0808 & -0.1134 \\
0 & 0 & 0 & 0 & 0.230 & -0.230 & 0 \\
0 & -0.0808 & 0 & -0.0808 & -0.230 & 0.5051 & -0.1134 \\
0 & -0.1134 & 0 & -0.1134 & 0 & -0.1134 & 1.9462
\end{bmatrix} \; \mu\text{F/km}
$$

Foster equivalent network of the core conductor		
$\hat{R}_{c0\_cc} = 75.6999 \; \text{m}\Omega/\text{km}$	$\hat{R}_{c1\_cc} = 289.6160 \; \text{m}\Omega/\text{km}$	$\hat{R}_{c2\_cc} = 103.6979 \; \text{m}\Omega/\text{km}$
$\hat{L}_{c0\_cc} = 5.8834 \; \mu\text{H/km}$	$\hat{L}_{c1\_cc} = 12.0161 \; \mu\text{H/km}$	$\hat{L}_{c2\_cc} = 31.7205 \; \mu\text{H/km}$
Foster equivalent network of the screen conductor		
$\hat{R}_{s0\_cc} = 0.7299 \; \Omega/\text{km}$	$\hat{R}_{s1\_cc} = 2.4367 \; \Omega/\text{km}$	$\hat{R}_{s2\_cc} = 1.4400 \; \Omega/\text{km}$
$\hat{L}_{s0\_cc} = 0.1212 \; \mu\text{H/km}$	$\hat{L}_{s1\_cc} = 0.1712 \; \mu\text{H/km}$	$\hat{L}_{s2\_cc} = 0.4464 \; \mu\text{H/km}$
Foster equivalent network of the pipe conductor		
$\hat{R}_{p0\_cc} = 113.4570 \; \text{m}\Omega/\text{km}$	$\hat{R}_{p1\_cc} = 448.6083 \; \text{m}\Omega/\text{km}$	$\hat{R}_{p2\_cc} = 216.9205 \; \text{m}\Omega/\text{km}$
$\hat{L}_{p0\_cc} = 0.8968 \; \mu\text{H/km}$	$\hat{L}_{p1\_cc} = 1.5562 \; \mu\text{H/km}$	$\hat{L}_{p2\_cc} = 3.8302 \; \mu\text{H/km}$
Number of cascaded FDPi sections		
$N_{FDPi\_cc} = 1$		

Offshore Substation Transformer

The parameterization of the Offshore Substation Transformer (OST) is performed with a similar procedure as the one presented previously for WTTs. Similar to the WTT, the ABB transformer data of Appendix B.2 is scaled up to 75 MVA considering the same per-unit values. The frequency-dependent behavior of the short-circuit impedance is assumed based on the per-unit values of the third-order Foster equivalent network presented in Table 5.3 for a typical transformer of 100 MVA, closest information available to the required 75 MVA transformer.

The values of the stray capacitances are assumed according to the information presented in Table 5.6 for a 75 MVA transformer. Similar to the explanation given for the WTT, the stray capacitances can be neglected for the studied frequency range, frequency values up to 5 kHz.

Taking into account the previous procedure and the schematic of the transformer model presented in Fig. 5.12, Table 7.8 shows the parameters of the offshore substation transformer.

Table 7.8. Model parameters of the offshore substation transformer.

Basic nameplate information			
Rated Power	75 MVA	Rated Voltage (LV side)	30 kV
Rated Voltage (HV side)	110 kV	Transformer Connection	Ygd1
Short-circuit impedance of the HV-side winding			
$R_{p0\_ost} = 0.5760 \; \Omega$	$R_{p1\_ost} = 22.6567 \; \Omega$	$R_{p2\_ost} = 1.4751 \; \text{k}\Omega$	$R_{p3\_ost} = 1.6830 \; \text{k}\Omega$
	$L_{p1\_ost} = 4.2307 \; \text{mH}$	$L_{p2\_ost} = 18.9843 \; \text{mH}$	$L_{p3\_ost} = 0.6936 \; \text{mH}$
Short-circuit impedance of the LV-side winding			
$R_{s0\_ost} = 0.0428 \; \Omega$	$R_{s1\_ost} = 1.6852 \; \Omega$	$R_{s2\_ost} = 109.7149 \; \Omega$	$R_{s3\_ost} = 125.1845 \; \Omega$
	$L_{s1\_ost} = 0.3146 \; \text{mH}$	$L_{s2\_ost} = 1.4121 \; \text{mH}$	$L_{s3\_ost} = 51.594 \; \mu\text{H}$
Core impedance (referred to the HV-side)			
$R_{c\_ost} = 80.667 \; \text{k}\Omega$		$L_{m\_ost} = 112.0639 \; \text{H}$	
Stray capacitances			
$C_{HG\_ost} = 3.5 \; \text{nF}$	$C_{HL\_ost} = 5.5 \; \text{nF}$		$C_{LG\_ost} = 2.8 \; \text{nF}$
Zero-sequence inductance (referred to the HV-side)			
$L_{0\_ost} = 0.2568 \; \text{H}$			

Submarine Cable of the Transmission System

For this case, as described for the collection network cable, it is also required to have constructional data of a real cable in order to represent the FDPi model presented in section 6.3. Table B.11 and Table B.12, in Appendix B.4, present information about ABB HVAC three-core submarine cable. The simplified geometrical and material parameters of this submarine cable together with considered surrounding medium properties and burial depth are described in Appendix B.4. Once having this information, the parameterization of the submarine cable is performed according to the procedure detailed in section 6.4.

Taking into account the previous procedure and the schematic of the FDPi model presented in Fig. 6.8, Table 7.9 shows the model parameters of the submarine cable for the transmission system of the OWPP base scenario.

The number of cascaded FDPi sections is equal to 20 in order to represent frequencies up to 5 kHz, frequency range of interest for the studies presented in this Ph.D. thesis.

The cable length is 60 km long for the OWPP base scenario, as depicted in Fig. 7.1(b). Therefore, the parameters given in Table 7.9 are multiplied by 3, which corresponds to the length of each FDPi-section.

Table 7.9. Model parameters of the transmission system cable.

Resistance matrix						
$$\left[\hat{R}_{tc}\right] = \begin{bmatrix} 127.6481 & 55.6833 & 46.5123 & 46.5123 & 46.5123 & 46.5123 & 49.4761 \\ 55.6833 & 693.4614 & 46.5123 & 46.5123 & 46.5123 & 46.5123 & 49.4761 \\ 46.5123 & 46.5123 & 129.0656 & 55.6833 & 46.5123 & 46.5123 & 49.4761 \\ 46.5123 & 46.5123 & 55.6833 & 693.4614 & 46.5123 & 46.5123 & 49.4761 \\ 46.5123 & 46.5123 & 46.5123 & 46.5123 & 129.0656 & 55.6833 & 49.4761 \\ 46.5123 & 46.5123 & 46.5123 & 46.5123 & 55.6833 & 693.4614 & 49.4761 \\ 49.4761 & 49.4761 & 49.4761 & 49.4761 & 49.4761 & 49.4761 & 131.6694 \end{bmatrix} \text{m}\Omega/\text{km}$$						

Inductance matrix						
$$\left[\hat{L}_{tc}\right] = \begin{bmatrix} 2.1227 & 1.8960 & 1.7815 & 1.7815 & 1.7815 & 1.7815 & 1.7388 \\ 1.8960 & 1.8895 & 1.7815 & 1.7815 & 1.7815 & 1.7815 & 1.7388 \\ 1.7815 & 1.7815 & 2.1395 & 1.8960 & 1.7815 & 1.7815 & 1.7388 \\ 1.7815 & 1.7815 & 1.8960 & 1.8895 & 1.7815 & 1.7815 & 1.7388 \\ 1.7815 & 1.7815 & 1.7815 & 1.7815 & 2.1395 & 1.8960 & 1.7388 \\ 1.7815 & 1.7815 & 1.7815 & 1.7815 & 1.8960 & 1.8895 & 1.7388 \\ 1.7388 & 1.7388 & 1.7388 & 1.7388 & 1.7388 & 1.7388 & 1.7324 \end{bmatrix} \text{mH/km}$$						

Capacitance matrix						
$$\left[\hat{C}_{tc}\right] = \begin{bmatrix} 0.150 & -0.150 & 0 & 0 & 0 & 0 & 0 \\ -0.150 & 0.4827 & 0 & -0.1054 & 0 & -0.1054 & -0.1219 \\ 0 & 0 & 0.150 & -0.150 & 0 & 0 & 0 \\ 0 & -0.1054 & -0.150 & 0.4827 & 0 & -0.1054 & -0.1219 \\ 0 & 0 & 0 & 0 & 0.150 & -0.150 & 0 \\ 0 & -0.1054 & 0 & -0.1054 & -0.150 & 0.4827 & -0.1219 \\ 0 & -0.1219 & 0 & -0.1219 & 0 & -0.1219 & 1.7623 \end{bmatrix} \mu\text{F/km}$$						

Foster equivalent network of the core conductor		
$\hat{R}_{c0\_tc} = 72.1379 \text{ m}\Omega/\text{km}$	$\hat{R}_{c1\_tc} = 281.5491 \text{ m}\Omega/\text{km}$	$\hat{R}_{c2\_tc} = 100.2902 \text{ m}\Omega/\text{km}$
$\hat{L}_{c0\_tc} = 5.7901 \mu\text{H/km}$	$\hat{L}_{c1\_tc} = 11.9054 \mu\text{H/km}$	$\hat{L}_{c2\_tc} = 31.8845 \mu\text{H/km}$
Foster equivalent network of the screen conductor		
$\hat{R}_{s0\_tc} = 0.6377 \Omega/\text{km}$	$\hat{R}_{s1\_tc} = 2.5455 \Omega/\text{km}$	$\hat{R}_{s2\_tc} = 1.2343 \Omega/\text{km}$
$\hat{L}_{s0\_tc} = 0.6694 \mu\text{H/km}$	$\hat{L}_{s1\_tc} = 1.1601 \mu\text{H/km}$	$\hat{L}_{s2\_tc} = 2.8547 \mu\text{H/km}$
Foster equivalent network of the pipe conductor		
$\hat{R}_{p0\_tc} = 82.2034 \text{ m}\Omega/\text{km}$	$\hat{R}_{p1\_tc} = 329.2978 \text{ m}\Omega/\text{km}$	$\hat{R}_{p2\_tc} = 159.2872 \text{ m}\Omega/\text{km}$
$\hat{L}_{p0\_tc} = 0.6584 \mu\text{H/km}$	$\hat{L}_{p1\_tc} = 1.1425 \mu\text{H/km}$	$\hat{L}_{p2\_tc} = 2.8135 \mu\text{H/km}$
Number of cascaded FDPi sections		
$N_{FDPi\_tc} = 20$		

Shunt Reactors for Reactive Power Compensation of the Transmission Link

As pointed out in section 7.2, shunt reactors are installed at both ends of the transmission system. The purpose of those reactors is the management of the reactive power through the 60 km long submarine cable [27]. The energy transmission of the OWPP is improved since these shunt reactors reduce the required rated current of the cable and the active power losses.

Shunt reactors are modeled as ideal inductors. The inductance value is adjusted to the conditions where the cable is transmitting the rated power, resulting in a power factor at the PCC equal to one. Table 7.10 gives the parameter values of these phase inductances.

Table 7.10. Model parameters of the shunt reactors of the transmission system.

Shunt reactors of the transmission system	
Shunt reactor at sending end (offshore substation side)	$L_{Qcomp\_s} = 4\,\text{H}$
Shunt reactor at receiving end (power grid side)	$L_{Qcomp\_r} = 4\,\text{H}$

Power Grid

The power grid is modeled as an ideal voltage source and a short-circuit impedance [27]. The short-circuit impedance is considered an inductor as a simplification [27]. Fig. 7.5 shows the schematic of the power grid model.
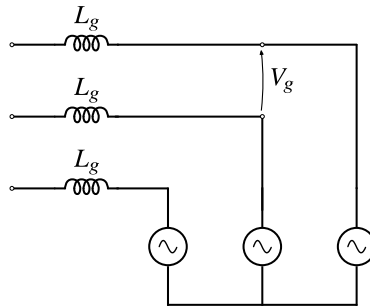
Fig. 7.5. Schematic of the power grid model.

The value of the impedance is calculated considering the Point of Common Coupling (PCC) a strong point with a short-circuit power 20 times the rated power of the OWPP [27]. Table 7.11 gives the values of the parameters of the power grid model for the representation of the OWPP base scenario.

Table 7.11. Model parameters of the power grid equivalent.

Parameters of the power grid	
Grid voltage	$V_g = 110\,\text{kV}$
Short-circuit ratio	$SCR = 20\quad (Z_{sc} = 5\%)$
Series inductance	$L_g = 32.09\,\text{mH}$

7.3.2 Wake Effect in OWPP Base Scenario

As already pointed out in chapter 4, it is of particular interest to consider the wake effect of a wind turbine to represent, according to the spatial distribution of the WTs and wind conditions (speed and direction), the mean wind speed of each WT and hence their estimated active power generation. In this sense, different operation points (i.e. m_a and δ) among WTs can be considered and the evaluation of harmonics can be addressed according to reality for several conditions and not just for the rated one, as evaluated in chapter 9.

The tool developed in subsection 4.3.3 is added to the Simulink®-based model of the OWPP base scenario. The input parameters required by the tool, depicted in Fig. 4.5, are presented in Table 7.12. The turbine diameter is given by the manufacturer, see Table B.1 and the value corresponding to wind turbine M5000. The values for the wake decay constant and thrust coefficient are assumed according to recommendations presented in reference [121]. The WT coordinates are defined taking into account the spatial disposition of the wind turbines, see Fig. 7.1(a).

Table 7.12. Input parameters of the tool presented in subsection 4.3.3.

Parameters of the wake effect tool			
Turbine diameter	$D_{turbine} = 116\,\text{m}$	Thrust coefficient	$C_T = 0.75$
Wake decay constant	$k_{wdc} = 0.038$	WT coordinates	Defined according to Fig. 7.1(a).

Wind conditions are defined according to the wind rose presented in Fig. 7.6 with the aim of taking into account wind conditions with high, medium and low occurrence or percentage of time. Three different wind directions are considered for the studies and the results presented in chapter 9. These are West, NorthWest and North wind direction. It is important to mention that the tool described in subsection 4.3.3 can evaluate other wind conditions.
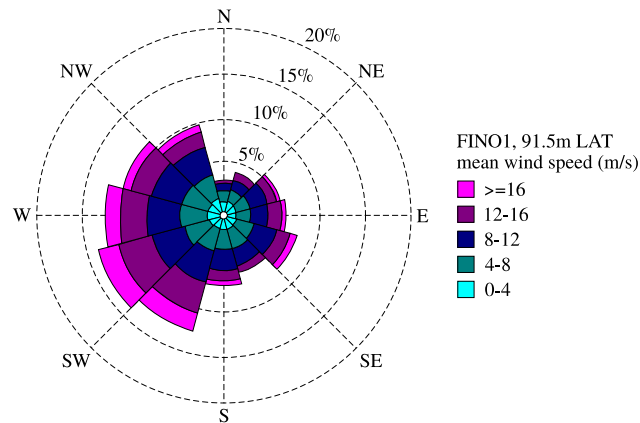
Fig. 7.6. Wind rose at Alpha Ventus OWPP during 2010-07-01 to 2012-06-30 and taken as reference for the definition of the evaluated wind conditions. Source [196,197].

The wind speed gains k_{WTi} for each WT and for the aforementioned wind directions are depicted in Fig. 7.7.
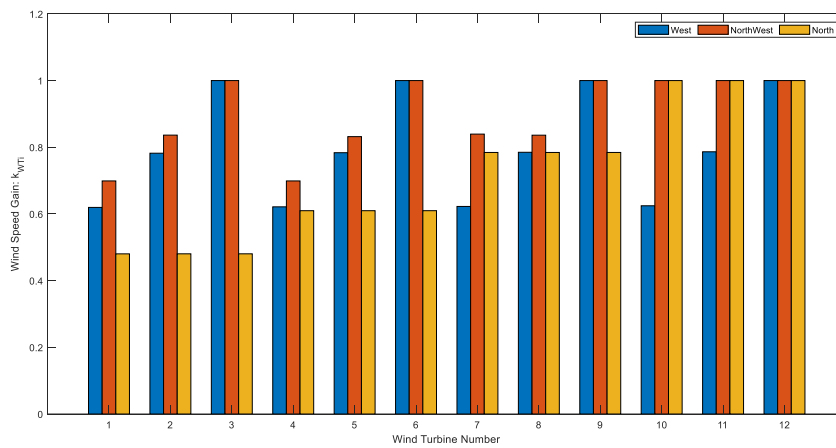
Fig. 7.7. Wind speed gains of each WT for three different wind directions: West, NorthWest and North.

The Multibrid M5000 power curve is obtained from the manufacturer datasheet and is depicted in Fig. 7.8.
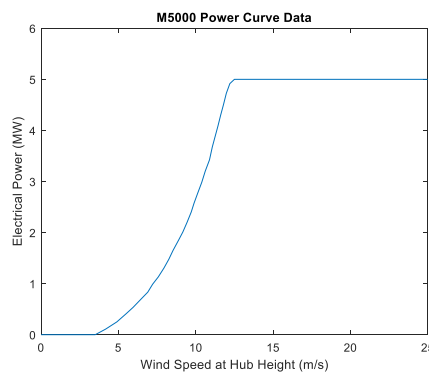
Fig. 7.8. Power Curve AREVA Multibrid M5000. Source [198].

The power curve is used to compute the active power setpoints of each WT as depicted in Fig. 7.9. Note that this is a simplified model, in reality, the wind turbines implement a Maximum Power Point Tracking (MPPT) strategy.
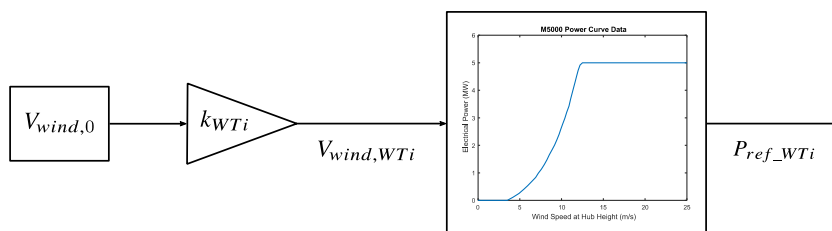
Fig. 7.9. Computation of the active power setpoint of each WT.

The active power setpoints of each WT, for the aforementioned wind directions and for different wind speeds, are depicted in Fig. 7.10. The active power setpoints of the entire OWPP, for the evaluated wind directions and wind speeds, are depicted in Fig. 7.11. In chapter 9, the study of the BDEW grid code compliance is presented by evaluating the estimated active power generation depicted in these figures.
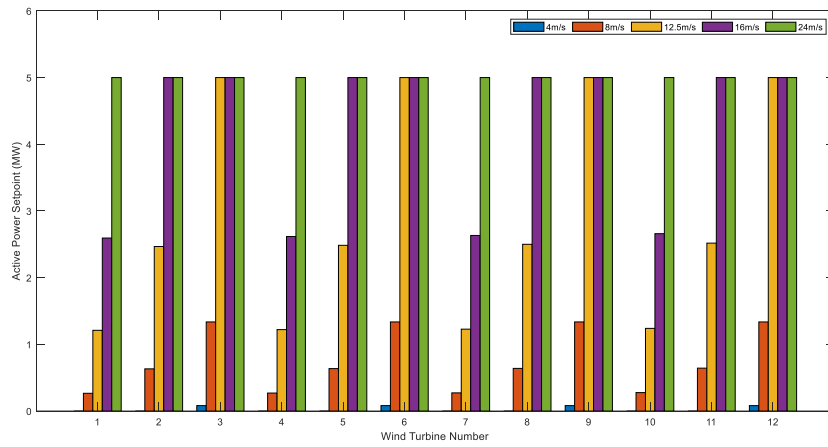
(a)
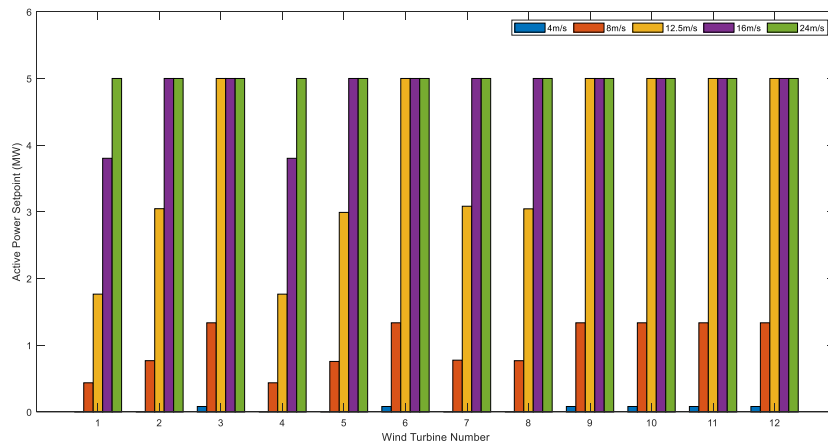
(b)
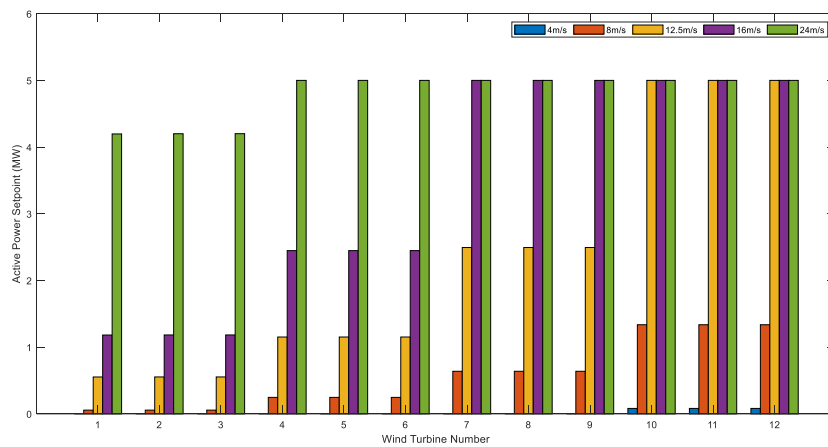
(c)

Fig. 7.10. Estimated active power generation of each WT for different wind conditions. (a) West. (b) NorthWest. (c) North.
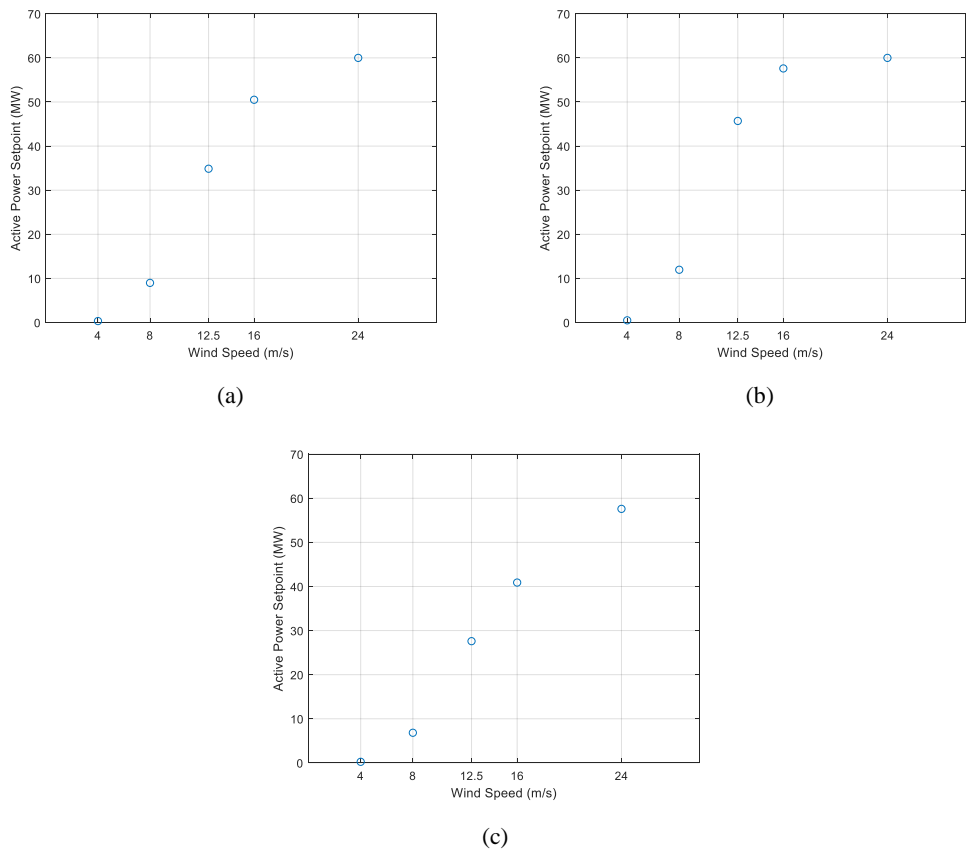
Fig. 7.11. Estimated active power generation of the entire OWPP for different wind conditions. (a) West. (b) NorthWest. (c) North.

7.3.3 Case Study 7.1: CB-PWM at steady-state

Once the Simulink®-based model is built, it is important to perform analysis based on case studies among the infinite possible cases that can be represented. The idea is to categorize the case studies according to different conditions and in that way be able to perform a comparison between cases. The comparison among different case studies can result, as an example, in the determination of the "better conditions", e.g. parameter values, configurations, control strategies, and other aspects for obtaining a specific voltage and/or current distortion value (THD) at the PCC and other points along the OWPP. This method of study is addressed in subsequent chapters.

It is important to emphasize that the aim of this case study and case study 7.2 is to provide initial insight into the steady-state harmonic evaluation of the OWPP by means of the Simulink®-based model. A deeper study of this aspect is addressed in chapter 9.

According to the previous ideas, case study 7.1 considers the following conditions for the OWPP base scenario. The wind blows from east to west, i.e. westerly direction. Wind speed is 16 m/s. Taking into account these wind conditions, the estimated active power generation of each WT is defined according to Fig. 7.10(a).

The reactive power reference is defined so each WT operates with a unity power factor, at WTT terminals. The modulation strategy of the grid side converter of each WT is the typical CB-PWM modulation, already presented in chapter 3. All wind turbines are connected and the grid side converters are enabled.

The operation point of a WT is defined by the amplitude modulation signal and the phase angle. Fig. 7.12 depicts the amplitude modulation index and the phase angle of the twelve wind turbines. Steady-state has been reached for the analyzed time window. The time window is equal to 10 cycles of the fundamental component as recommended by the BDEW grid code and the IEC 61400-21 standard. For visual clearness, Fig. 7.12(a) and Fig. 7.12(b) only show the last cycle of the analyzed time window.
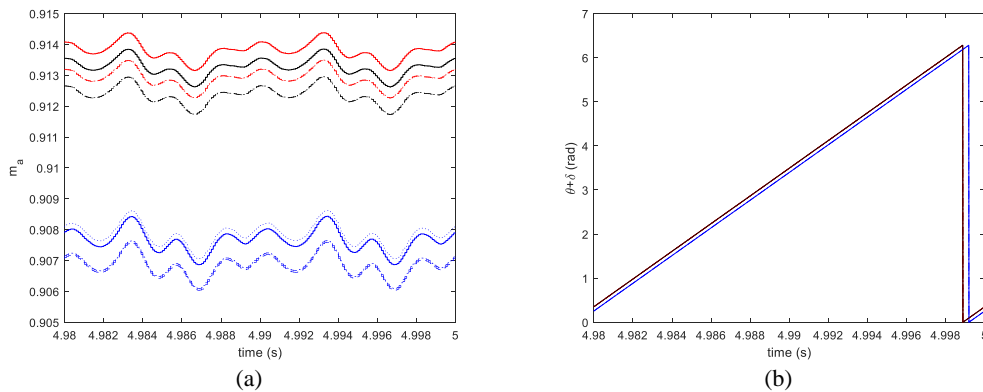
Fig. 7.12. Amplitude modulation index (m_a) and phase angle $(\theta + \delta)$ of each WT for case study 7.1. Grid voltage value 0.95 pu. (a) Amplitude modulation index. (b) Phase angle.

Fig. 7.12(a) shows the presence of low-frequency oscillations for the amplitude modulation index of each WT. As a first impression, the variation of the amplitude modulation index is small (fourth decimal) and by looking to Fig. 7.13, one can notice that this variation does not affect the grid side converter voltage, at least highly.

Ideally, it is required that the amplitude modulation index remains constant over one period of the fundamental frequency. In most of the cases and when having a scenario with a high penetration of power converters, such as OWPPs, the measured voltages and currents that are fed back to the control strategy of the GSCs are distorted. Furthermore, when implementing standard control schemes, such as the one implemented for this case study, some harmonics are filtered to a certain degree, not completely. Thus, they provoke oscillations to the amplitude modulation index.

One way of reducing these oscillations is by means of implementing additional filtering capabilities or by means of advanced control strategies that reduce these unwanted oscillations. As presented in subsection 3.3.3, a possible solution to further reduce these unwanted oscillations is to use notch filters. This is to implement NFs to the measured signals in dq-frame that are fed back to the current controller.

An important aspect to point out is that the oscillations that can be noticed in the amplitude modulation index are not noticed in the angle obtained by the PLL. This is mainly due to

the implementation of the MAF-PLL and its tuning criteria, as described in subsection 7.3.1.

The following figures show the results of voltage and current signals at different points of the OWPP base scenario for this case study. These signals are shown for the last cycle of the analyzed time window with the aim of showing only integer harmonics. It is important to mention that the results presented in chapter 9 considers a time window of 10 cycles. This with the goal of computing any signal of a frequency that is not an integer multiple of the fundamental frequency, i.e. interharmonics.

Fig. 7.13 shows the spectrum of the voltage signal $v_{ab\_GSC1}(t)$, generated by the GSC1, which employs a typical CB-PWM modulation. This variable denotes the line-to-line voltage between phases "a" and "b".

The synthesized waveform of the grid side converter is not a perfect chopped signal since the reconstruction is performed with a finite number of harmonics as it is explained by the Gibbs phenomenon [70]. For this case, harmonics up to a frequency value of 5 kHz are used for signal reconstruction.

For simplification, the voltages $v_{ab\_GSCi}(t)$ of remaining wind turbines are not presented because the synthesized waveforms are very similar in shape and just having their particular differences in amplitude and phase.
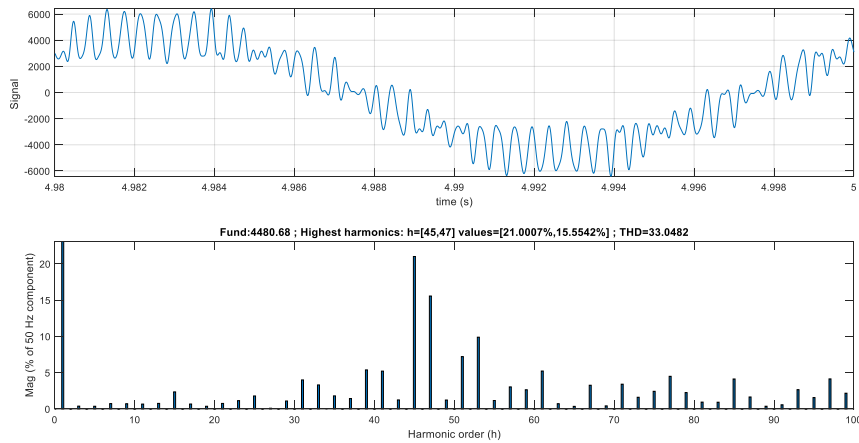
Fig. 7.13. Spectrum of voltage signal $v_{ab\_GSC1}(t)$ for case study 7.1. Grid voltage value 0.95 pu.

Fig. 7.14 and Fig. 7.15 show the voltage signal $v_{ab\_PCC}(t)$ and the current signal $i_{a\_PCC}(t)$ for this case study, respectively. The voltage signal $v_{ab\_PCC}(t)$ indicates the line-to-line voltage, between phases "a" and "b", at the PCC point of the OWPP. On the other hand, the current signal $i_{a\_PCC}(t)$ denotes the current at line "a" at the PCC point of the OWPP.

A priori and from the spectrums depicted in Fig. 7.14 and Fig. 7.15, it is highly possible that the OWPP does not fulfill the grid code in terms of harmonics at the PCC point and

for this case study. The possible reason behind the previous statement is the presence of a resonance that amplifies the values of the low order harmonics (e.g. 5th, 7th and 9th) injected by the GSCs of the wind turbines, apart from the way of how harmonics are added. These previous aspects are further studied in chapter 8 by means of computing the transfer functions, relating the current and voltage variables at the PCC with the injected voltage variable at each GSC point, and displaying the Bode plots for each of them.

Fig. 7.14. Spectrum of voltage signal $v_{ab\_PCC}(t)$ for case study 7.1. Grid voltage value 0.95 pu.
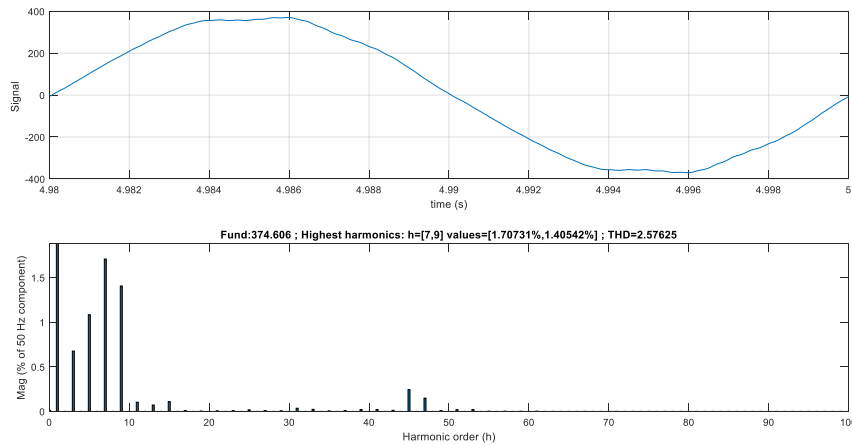
Fig. 7.15. Spectrum of current signal $i_{a\_PCC}(t)$ for case study 7.1. Grid voltage value 0.95 pu.

Table 7.13, presented in the next subsection, gives information about the total harmonic distortion values (THDs) of the previous signals. These values are not discussed in this subsection because a comparison of the THD values obtained for both modulation strategies is performed in next subsection.

Additionally, these values are indicative and they do not determine if the voltage and current limits imposed by the grid codes are fulfilled. A deeper study of this aspect is performed in chapter 9. The time signals and spectrums, previously shown, represent one of the many conditions that are studied and that cannot be depicted for each case due to space constraints.

7.3.4 Case Study 7.2: SHE-PWM at steady-state

Looking at the spectrums of the previous figures, it is clearly seen that the harmonic content at the PCC point of the OWPP can be improved if the grid side converters of the WTs eliminate or highly reduce the amplitude of low order harmonics. In this sense, the implementation of a particular solution of SHE-PWM modulation, e.g. the one proposed in chapter 3, is more suitable in order to reduce the harmonic content at the PCC point for this OWPP base scenario and be able to fulfill the grid code. As commented previously, the aim of presenting this case study is to give an introductory understanding of what is studied in chapter 9.

Case study 7.2 considers the same conditions described for case study 7.1 with the difference of implementing a particular solution of SHE-PWM modulation. Fig. 7.16 depicts the amplitude modulation index and the phase angle of the twelve WTs. As depicted in Fig. 7.16(a), steady-state has been reached for the analyzed time window.

If comparing Fig. 7.12(a) with Fig. 7.16(a), one can notice two important aspects. The first one is that the amplitude modulation index of each WT does not vary, at least in its mean value, when comparing the same wind turbine for both cases. The previous statement can be inferred because the conditions that define the operation points of the WTs have not changed. The second aspect is the magnitude of the oscillations that are shown for the m_a values of each WT. These oscillations are lower for this case study when comparing with the ones obtained for the previous case.
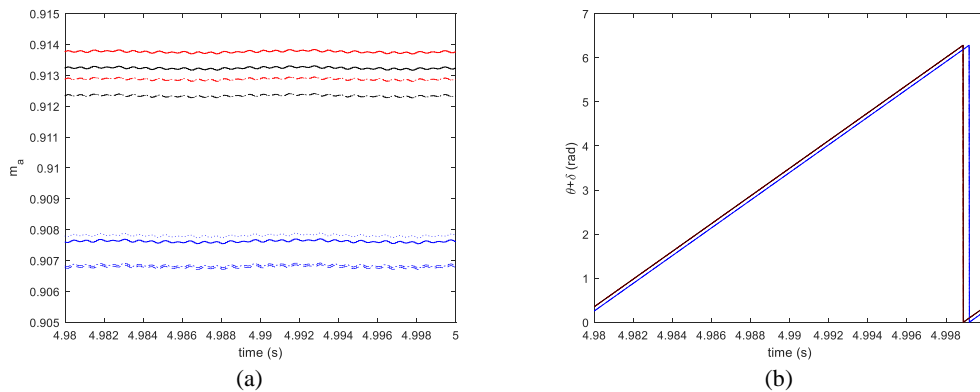
Fig. 7.16. Amplitude modulation index (m_a) and phase angle $(\theta + \delta)$ of each WT for case study 7.2. Grid voltage value 0.95 pu. (a) Amplitude modulation index. (b) Phase angle.

As pointed out, further reduction of these oscillations can be achieved if implementing notch filters to the measured signals in dq-frame or by means of active damping loops. For this case study, the anti-resonance introduced by the notch filters can be tuned at the 6th harmonic in the dq-frame.

The following figures show the results of voltage and current signals at different points of the OWPP base scenario. Similar to the previous case, these signals are shown for the last

cycle of the analyzed time window. Fig. 7.17 shows the spectrum of the voltage signal $v_{ab\_GSC1}(t)$ for this case study.
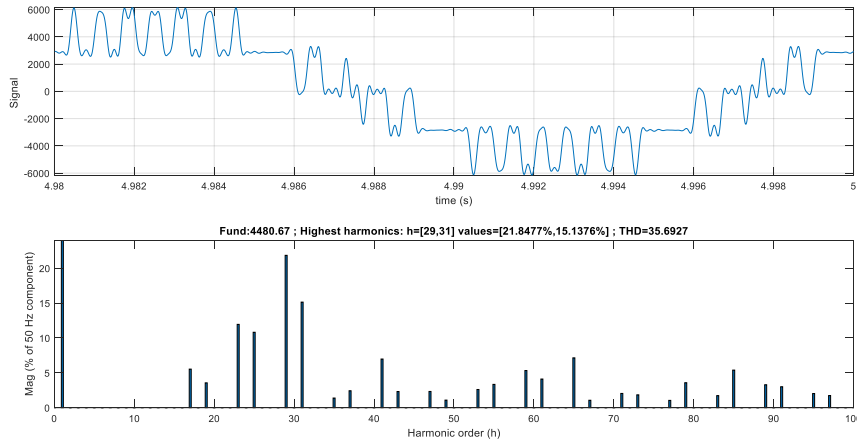
Fig. 7.17. Spectrum of voltage signal $v_{ab\_GSC1}(t)$ for case study 7.2. Grid voltage value 0.95 pu.

From the spectrum of Fig. 7.17, one can notice that harmonics of order 5th, 7th, 11th, and 13th are almost null.

Fig. 7.18 and Fig. 7.19 show the voltage $v_{ab\_PCC}(t)$ and current signal $i_{a\_PCC}(t)$, respectively. Comparing the results for this case study with the ones obtained for the previous one, a significant reduction of low order harmonics is achieved at the PCC. To give an example, the magnitude of harmonic of order 7th is reduced from 0.6% to a magnitude below 0.02% for the voltage signal $v_{ab\_PCC}(t)$. For current signal $i_{a\_PCC}(t)$, on the other hand, the magnitude of the same harmonic is reduced from 1.7% to a value lower than 0.05%.

As depicted in the previous two figures, the voltage and current at the PCC point are less distorted in comparison with the results obtained for case study 7.1. A comparison of the level of distortion for both case studies can be performed by computing the THD value of each signal. Table 7.13 gives the total harmonic distortion values (THDs) of the signals presented for both case studies.

Even though the THD value of the $v_{ab\_GSC1}(t)$ signal is higher for case study 7.2, it results in a lower harmonic distortion of the voltage and current signals at the PCC point. To give an example, the THD of the signal $i_{a\_PCC}(t)$ is reduced from a value of 2.5762, when employing CB-PWM, to a value of 0.2049 when implementing SHE-PWM. This implies a reduction of approximately 92%. A similar situation occurs for the case of the voltage signal $v_{ab\_PCC}(t)$. As discussed at the beginning of this subsection, the main reason for the improvement is that low order harmonics are highly reduced when implementing the particular solution of SHE-PWM.
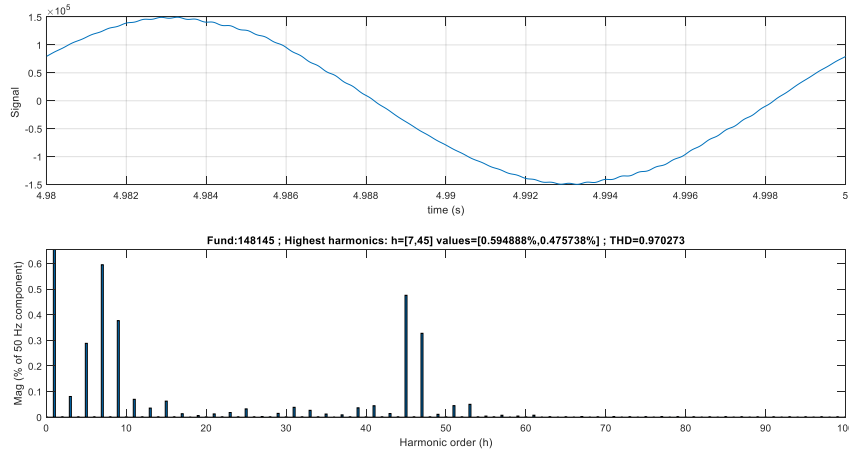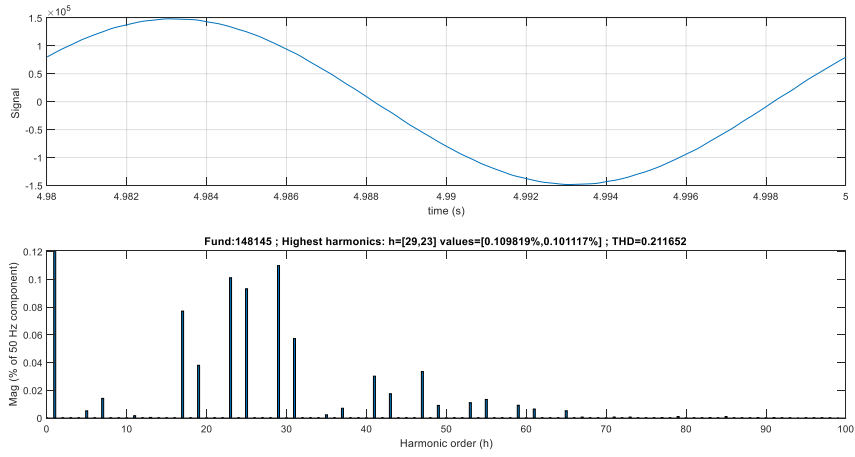
Fig. 7.18. Spectrum of voltage signal $v_{ab\_PCC}(t)$ for case study 7.2. Grid voltage value 0.95 pu.
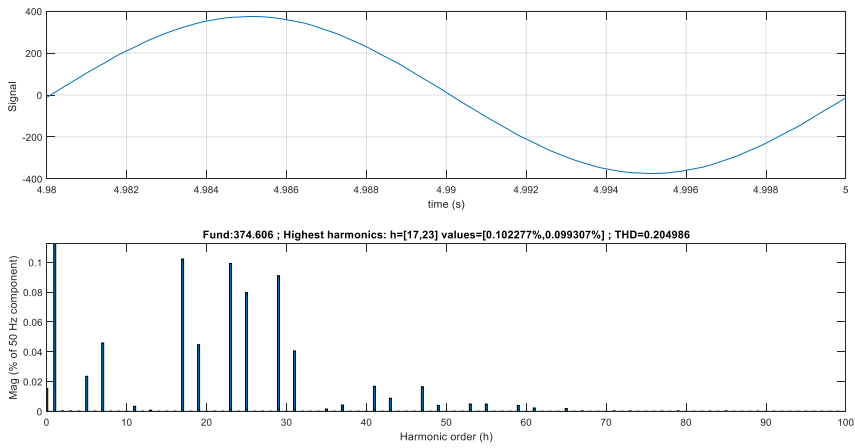
Fig. 7.19. Spectrum of current signal $i_{a\_PCC}(t)$ for case study 7.2. Grid voltage value 0.95 pu.

Table 7.13. Total harmonic distortion of voltage (THDv) and current (THDi) signals for case study 7.1 and case study 7.2.

Case study	$v_{ab\_GSC1}(t)$		$v_{ab\_PCC}(t)$		$i_{a\_PCC}(t)$	
	Fund. (V) peak value	THDv	Fund. (V) peak value	THDv	Fund. (A) peak value	THDi
7.1	4480.68	33.0482	148145	0.9702	374.606	2.5762
7.2	4480.67	35.6927	148145	0.2116	374.606	0.2049

7.4 Sequence Network based Model of the OWPP Base Scenario

This section presents the second modeling approach, the sequence network based model. Two main aspects are addressed in this section. First, a general- and a simplified-approach of the sequence network model of the OWPP base scenario is presented. Second, the sequence network model of each passive component of the OWPP is presented together with the state-space formulation of each passive component and block, understanding this last term as the association of two or more passive components.

7.4.1 Sequence Network Model of the OWPP Base Scenario

The sequence network model of the OWPP base scenario can be represented by means of equation (7.1).

$$\left[Y_{OWPP}^{+-0}(s)\right]_{120\times1} = \left[G_{OWPP}^{+-0}(s)\right]_{120\times39}\left[U_{OWPP}^{+-0}(s)\right]_{39\times1} \tag{7.1}$$

The matrices $\left[Y_{OWPP}^{+-0}(s)\right]_{120\times1}$ and $\left[U_{OWPP}^{+-0}(s)\right]_{39\times1}$ represent the output and input variables of the model, respectively. These variables contain the sequence components of voltages and current signals at different points of the OWPP, as given by equation (7.2), for phase "a". The following approach is done for phase "a" but it applies for phases "b" and "c" as well.

$$\left[Y_{OWPP}^{+-0}(s)\right]_{120\times1} = \begin{bmatrix} \left[I_{a\_GSC1}^{+-0}(s)\right]_{3\times1} \\ \vdots \\ \left[I_{a\_GSC12}^{+-0}(s)\right]_{3\times1} \\ \left[I_{a\_WT1}^{+-0}(s)\right]_{3\times1} \\ \vdots \\ \left[I_{a\_WT12}^{+-0}(s)\right]_{3\times1} \\ \left[V_{an\_WT1}^{+-0}(s)\right]_{3\times1} \\ \vdots \\ \left[V_{an\_WT12}^{+-0}(s)\right]_{3\times1} \\ \left[I_{a\_CP}^{+-0}(s)\right]_{3\times1} \\ \left[V_{an\_CP}^{+-0}(s)\right]_{3\times1} \\ \left[I_{a\_PCC}^{+-0}(s)\right]_{3\times1} \\ \left[V_{an\_PCC}^{+-0}(s)\right]_{3\times1} \end{bmatrix} \quad ; \quad \left[U_{OWPP}^{+-0}(s)\right]_{39\times1} = \begin{bmatrix} \left[V_{an\_GSC1}^{+-0}(s)\right]_{3\times1} \\ \left[V_{an\_GSC2}^{+-0}(s)\right]_{3\times1} \\ \vdots \\ \left[V_{an\_GSC12}^{+-0}(s)\right]_{3\times1} \\ \left[V_{an\_g}^{+-0}(s)\right]_{3\times1} \end{bmatrix} \tag{7.2}$$

The matrix of transfer functions $\left[G_{OWPP}^{+-0}(s)\right]_{120\times39}$ describes the behavior of the OWPP by relating the input- and output variables of the OWPP. Since the sequence components of the input- and output variables are given, the matrix $\left[G_{OWPP}^{+-0}(s)\right]_{120\times39}$ represents the transfer

functions of the sequence components too. Fig. 7.20 shows the general schematic of the sequence network model of the OWPP base scenario, which illustrates the mathematical expression given by equation (7.1). Furthermore, the definition and location of the input- and certain output variables are depicted in this figure. The location of remaining output variables, given by equation (7.2), can be inferred with the aid of Fig. 7.1.
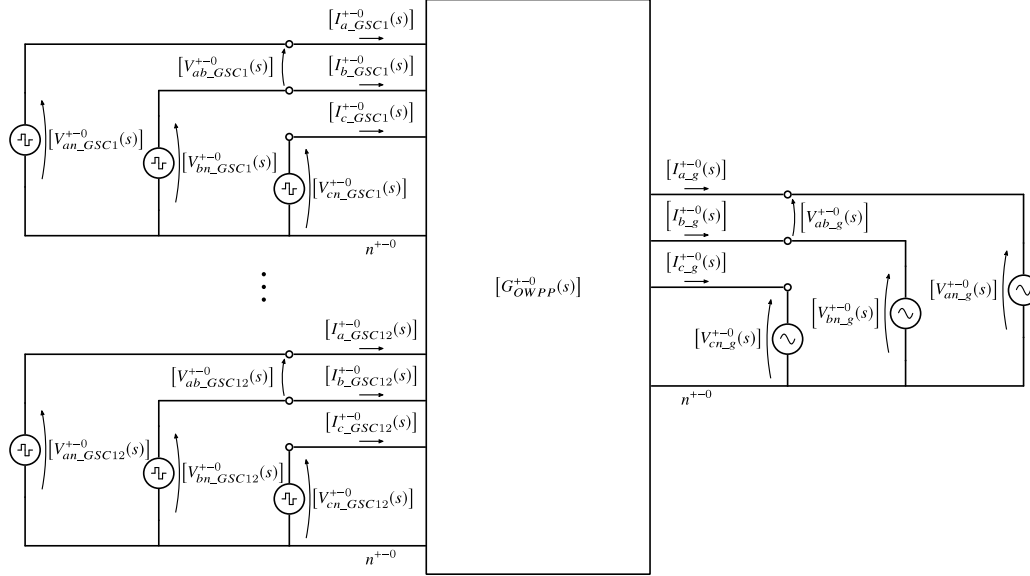
Fig. 7.20. General schematic of the sequence network model of the OWPP base scenario.

As seen from previous equations and figure, each voltage and current variable contains a positive-, negative-, and zero-sequence component. Equation (7.3) shows an example of the definition of the matrices $\left[V_{an\_GSCi}^{+-0}(s)\right]_{3\times1}$ and $\left[I_{a\_GSCi}^{+-0}(s)\right]_{3\times1}$ of the ith GSC.

$$\left[V_{an\_GSCi}^{+-0}(s)\right] = \begin{bmatrix} V_{an\_GSCi}^{+}(s) \\ V_{an\_GSCi}^{-}(s) \\ V_{an\_GSCi}^{0}(s) \end{bmatrix} \quad ; \quad \left[I_{a\_GSCi}^{+-0}(s)\right] = \begin{bmatrix} I_{a\_GSCi}^{+}(s) \\ I_{a\_GSCi}^{-}(s) \\ I_{a\_GSCi}^{0}(s) \end{bmatrix} \quad ; \quad 1 \le i \le 12 \tag{7.3}$$

If it is required to determine an output variable, the matrix product of equation (7.1) must be carried out. For example, the output $\left[I_{a\_PCC}^{+-0}(s)\right]_{3\times1}$ is computed by equation (7.4).

$$\left[I_{a\_PCC}^{+-0}(s)\right]_{3\times1} = \sum_{i=1}^{12}\left\{\left[G_{OWPP(39,i)}^{+-0}(s)\right]_{3}\left[V_{an\_GSCi}^{+-0}(s)\right]_{3\times1}\right\} +$$
$$\left[G_{OWPP(39,13)}^{+-0}(s)\right]_{3}\left[V_{an\_g}^{+-0}(s)\right]_{3\times1} \tag{7.4}$$

The contribution of the input $\left[V_{an\_GSC1}^{+-0}(s)\right]_{3\times1}$ to the output $\left[I_{a\_PCC}^{+-0}(s)\right]_{3\times1}$ is given by equation (7.5), which is fully detailed by equation (7.6).

$$\left[I_{a\_PCC}^{+-0}(s)\right]_{3\times1} = \left[G_{OWPP(39,1)}^{+-0}(s)\right]_{3}\left[V_{an\_GSC1}^{+-0}(s)\right]_{3\times1} \tag{7.5}$$

$$\begin{bmatrix} I_{a\_PCC}^+(s) \\ I_{a\_PCC}^-(s) \\ I_{a\_PCC}^0(s) \end{bmatrix} = \begin{bmatrix} G_{OWPP(39,1)}^{++}(s) & G_{OWPP(39,1)}^{+-}(s) & G_{OWPP(39,1)}^{+0}(s) \\ G_{OWPP(39,1)}^{-+}(s) & G_{OWPP(39,1)}^{--}(s) & G_{OWPP(39,1)}^{-0}(s) \\ G_{OWPP(39,1)}^{0+}(s) & G_{OWPP(39,1)}^{0-}(s) & G_{OWPP(39,1)}^{00}(s) \end{bmatrix} \begin{bmatrix} V_{an\_GSC1}^+(s) \\ V_{an\_GSC1}^-(s) \\ V_{an\_GSC1}^0(s) \end{bmatrix} \qquad (7.6)$$

Each matrix $\left[G_{OWPP(y,u)}^{+-0}(s) \right]_3$ is full, non-diagonal and non-symmetric. A non-diagonal matrix means that mutual coupling between the sequence circuits exists. On the other hand, a non-symmetric matrix is exemplified by the different mutual coupling terms. These previous conditions are identified when having a three-phase system or a power component that is not perfectly balanced, such as three single-core submarine cables laid in flat disposition.

The application of the symmetrical component theory in practical power system analysis requires the sequence circuits to be separate and decoupled. This is achieved by the removal of the off-diagonal mutual elements in each sequence matrix so that the matrix becomes diagonal. This can be accomplished if the physical phase impedances of the system under study are assumed to be balanced, i.e. the self-impedances and mutual impedances are assumed to be equal.

However, the creation of three decoupled single-phase sequence circuits is based on the assumption that the original three-phase system is perfectly balanced. In real-life scenarios, this is not the case. Nonetheless, reasonable assumptions of balance can be made to allow the use of the symmetrical component theory.

Based on the assumption that the original three-phase system is perfectly balanced, equation (7.6) can be simplified to equation (7.7).

$$\begin{bmatrix} I_{a\_PCC}^+(s) \\ I_{a\_PCC}^-(s) \\ I_{a\_PCC}^0(s) \end{bmatrix} = \begin{bmatrix} G_{OWPP(39,1)}^{++}(s) & 0 & 0 \\ 0 & G_{OWPP(39,1)}^{--}(s) & 0 \\ 0 & 0 & G_{OWPP(39,1)}^{00}(s) \end{bmatrix} \begin{bmatrix} V_{an\_GSC1}^+(s) \\ V_{an\_GSC1}^-(s) \\ V_{an\_GSC1}^0(s) \end{bmatrix} \qquad (7.7)$$

Based on the same assumption, the previous simplification can be extended to the sequence networks representing each matrix of $\left[G_{OWPP}^{+-0}(s) \right]_{120\times39}$ in equation (7.1). In this sense, the sequence circuits of the entire OWPP can be considered to be decoupled, equations (7.8) to (7.10). This means, for example, that a specific sequence (positive-sequence voltage or current) only produces the same sequence (positive-sequence voltage or current).

$$\left[Y_{OWPP}^+(s) \right]_{40\times1} = \left[G_{OWPP}^{++}(s) \right]_{40\times13} \left[U_{OWPP}^+(s) \right]_{13\times1} \qquad (7.8)$$

$$\left[Y_{OWPP}^-(s) \right]_{40\times1} = \left[G_{OWPP}^{--}(s) \right]_{40\times13} \left[U_{OWPP}^-(s) \right]_{13\times1} \qquad (7.9)$$

$$\left[Y_{OWPP}^0(s) \right]_{40\times1} = \left[G_{OWPP}^{00}(s) \right]_{40\times13} \left[U_{OWPP}^0(s) \right]_{13\times1} \qquad (7.10)$$

Fig. 7.21 shows the decoupled shematic of the sequence network model of the OWPP base scenario based on the previous assumption.

143
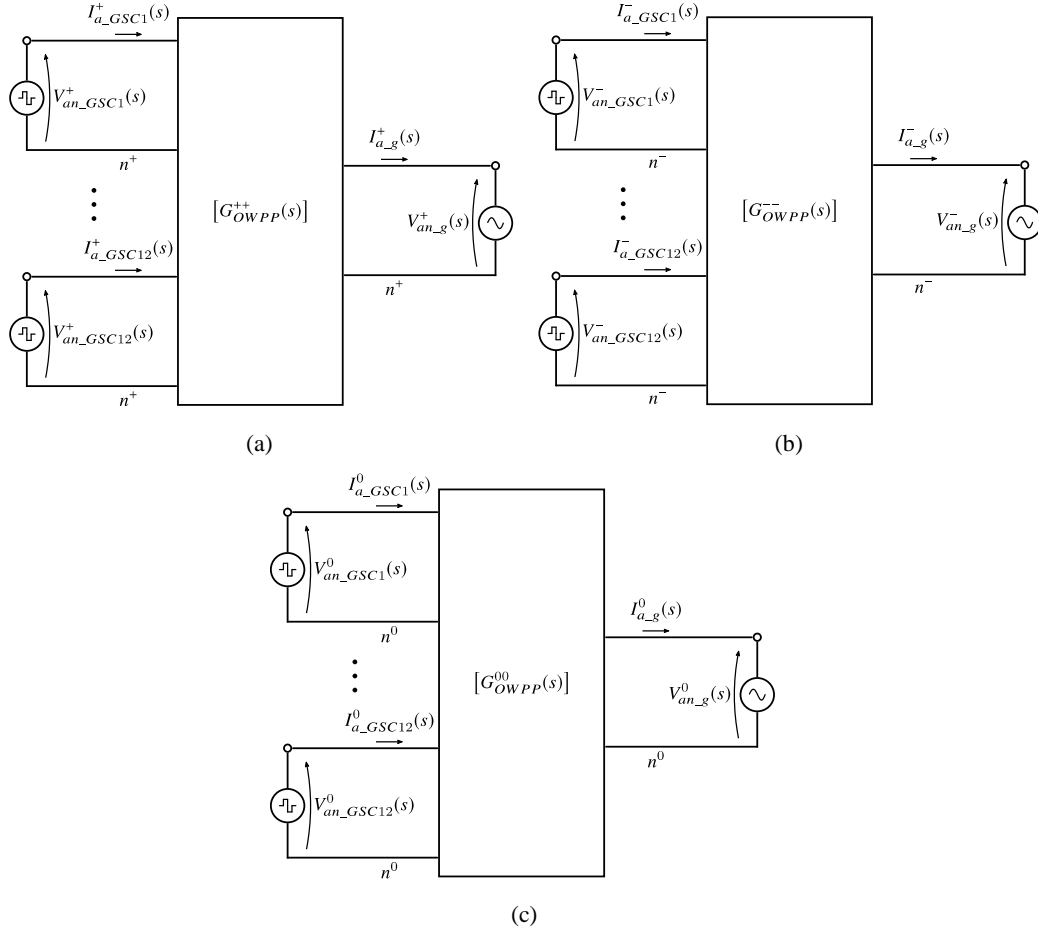
Fig. 7.21. Decoupled schematic of the sequence network model of the OWPP base scenario for phase "a". (a) Positive-sequence. (b) Negative-sequence. (c) Zero-sequence.

As pointed out in section 7.1 and in the introductory part of this section, the sequence network model of the OWPP is represented in state-space form for each sequence circuit. For example, the state-space representation of the positive-sequence circuit is given by equation (7.11).

$$
\frac{d}{dt}\left[x_{OWPP}^{+}(t) \right] = \left[A_{OWPP}^{++} \right]\left[x_{OWPP}^{+}(t) \right] + \left[B_{OWPP}^{++} \right]\left[u_{OWPP}^{+}(t) \right]
$$
$$
\left[y_{OWPP}^{+}(t) \right] = \left[C_{OWPP}^{++} \right]\left[x_{OWPP}^{+}(t) \right] + \left[D_{OWPP}^{++} \right]\left[u_{OWPP}^{+}(t) \right]
$$

$$(7.11)$$

There are two reasons for representing the sequence network model of the OWPP in state-space form. First, this definition is suitable for the implementation of the model in a *.m-file in the Matlab® (Matrix laboratory) programming language. Second, this kind of modeling approach allows performing modal analysis, specifically the participation factor technique that aids in the identification of how each state variable affects a given eigenvalue or system pole. This last technique is convenient for the analysis of systems with several power components, e.g. the OWPP under study. This way, it is possible to determine the influence each power component has, to give an example, on a given resonance as addressed in next chapter.

In order to obtain the state-space representation of equation (7.11), the Component Connection Method (CCM) is applied. With the CCM approach, the OWPP is decomposed into multiple components (e.g. filters, transformers, submarine cables, etc.) that are interconnected by linear algebraic relationships defined by their interfaces. For a description of the CCM approach, the reader is suggested to review the information presented in Appendix C.

Compared with the conventional state-space modeling approach, there are two main advantages of the component connection method. The first advantage is the convenience to perform extension for a system with multiple subsystems by modular modeling procedure; thereby it provides plug-and-play flexibility for connecting several subsystems [199]. The second advantage is the capability to simplify the modeling procedure and to reduce the computational burden due to simplicity and modularity.

The state-space representation of the OWPP base scenario is performed with the parameters defined in per-unit values. This is done to avoid referring all the impedances and admittances of each passive component to the primary- or secondary-side of the transformers, e.g. refer all the impedances of the OWPP to the HV-side of the offshore substation transformer.

Table 7.14 gives the system base values for the state-space representation of the passive components of the OWPP base scenario.

Table 7.14. System base values for the state-space representation of the passive components of the OWPP base scenario.

System Base			
$S_{base} = 60\,\mathrm{MVA}$		$f_{base} = 50\,\mathrm{Hz}$	
Grid side converter (GSC) zone			
$V_{base\_GSC} = 3.3\,\mathrm{kV}$	$Z_{base\_GSC} = 0.1815\,\Omega$	$L_{base\_GSC} = 577.73\,\mathrm{\mu H}$	$C_{base\_GSC} = 17.5\,\mathrm{mF}$
Collection network (CP) zone			
$V_{base\_CP} = 30\,\mathrm{kV}$	$Z_{base\_CP} = 15\,\Omega$	$L_{base\_CP} = 47.7\,\mathrm{mH}$	$C_{base\_CP} = 212.21\,\mathrm{\mu F}$
Point of common coupling (PCC) zone			
$V_{base\_PCC} = 110\,\mathrm{kV}$	$Z_{base\_PCC} = 201.6667\,\Omega$	$L_{base\_PCC} = 641.9\,\mathrm{mH}$	$C_{base\_PCC} = 15.784\,\mathrm{\mu F}$

The conversion to the matrix of transfer functions $\left[G_{OWPP}^{++}(s) \right]$ is given by equation (7.12).

$$\left[G_{OWPP}^{++}(s) \right] = \left[C_{OWPP}^{++} \right] \left\{ s[I] - \left[A_{OWPP}^{++} \right] \right\}^{-1} \left[B_{OWPP}^{++} \right] + \left[D_{OWPP}^{++} \right] \tag{7.12}$$

Before starting the next subsection, it is worth to mention that the positive- and negative-sequence circuits are equal for the case when the three-phase system is perfectly balanced, aforementioned assumption. In this sense and with the aim of not being repetitive, only the state-space representation of the positive-sequence circuits of each passive component or block are detailed in the next subsection.

The zero-sequence circuit of each power component is displayed too. Nonetheless, the state-space representation of the zero-sequence circuit of each power component is not

presented because the studies are focused on positive- and negative-sequence only. This is valid since the winding connections of the transformers, for the OWPP base scenario, do not allow the circulation of zero-sequence currents outside certain zones (e.g. outside the grid side converter zone, collection network zone, and the PCC zone). This is further detailed in the next subsection.

From the perspective of performing a steady-state harmonic evaluation of the OWPP in normal operation, it is not required to study the zero-sequence circuit due to the reason stated in the previous paragraph. Even though this sequence circuit is not considered in this Ph.D thesis, it is possible to model the zero-sequence circuit to perform studies, such as fault conditions, design of protections, and others.

7.4.2   Sequence Network Model of each Passive Component and Block

As stated before, this subsection presents the sequence circuits of each passive component or block. The state-space representation of each component or block is addressed for the positive-sequence circuit. With the equations presented in this subsection and the CCM approach, it is possible to obtain the state-space representation of the positive- and negative-sequence of the OWPP base scenario, Fig. 7.21(a) and Fig. 7.21(b).

Submarine Cables

Two main parts are detailed for this power component. First, the determination of the sequence circuits of a three-core submarine cable is addressed according to the theory presented in chapter 6. Second, the state-space representation of the positive-sequence circuit is presented for the submarine cables of the OWPP base scenario.

Equation (7.13) gives the voltage and current relationship that define the per-length series impedance matrix $\left[\hat{Z}_{series.sc}(\omega) \right]_7$. The elements of this matrix, given by equation (7.14), are equal to the ones presented in chapter 6 with the only difference of having a different arrangement.

$$
\begin{bmatrix}
V_{c1g\_s}(\omega) - V_{c1g\_r}(\omega) \\
V_{c2g\_s}(\omega) - V_{c2g\_r}(\omega) \\
V_{c3g\_s}(\omega) - V_{c3g\_r}(\omega) \\
V_{s1g\_s}(\omega) - V_{s1g\_r}(\omega) \\
V_{s2g\_s}(\omega) - V_{s2g\_r}(\omega) \\
V_{s3g\_s}(\omega) - V_{s3g\_r}(\omega) \\
V_{pg\_s}(\omega) - V_{pg\_r}(\omega)
\end{bmatrix}
= \left[\hat{Z}_{series.sc}(\omega) \right]_7
\begin{bmatrix}
I_{c1}(\omega) \\
I_{c2}(\omega) \\
I_{c3}(\omega) \\
I_{s1}(\omega) \\
I_{s2}(\omega) \\
I_{s3}(\omega) \\
I_p(\omega)
\end{bmatrix}
\tag{7.13}
$$

$$\left[\hat{Z}_{series.sc}(\omega)\right]=\begin{bmatrix} \hat{Z}_{c1,c1}(\omega) & \hat{Z}_{c1,c2}(\omega) & \hat{Z}_{c1,c3}(\omega) & \hat{Z}_{c1,s1}(\omega) & \hat{Z}_{c1,s2}(\omega) & \hat{Z}_{c1,s3}(\omega) & \hat{Z}_{c1,p}(\omega) \\ \hat{Z}_{c2,c1}(\omega) & \hat{Z}_{c2,c2}(\omega) & \hat{Z}_{c2,c3}(\omega) & \hat{Z}_{c2,s1}(\omega) & \hat{Z}_{c2,s2}(\omega) & \hat{Z}_{c2,s3}(\omega) & \hat{Z}_{c2,p}(\omega) \\ \hat{Z}_{c3,c1}(\omega) & \hat{Z}_{c3,c2}(\omega) & \hat{Z}_{c3,c3}(\omega) & \hat{Z}_{c3,s1}(\omega) & \hat{Z}_{c3,s2}(\omega) & \hat{Z}_{c3,s3}(\omega) & \hat{Z}_{c3,p}(\omega) \\ \hat{Z}_{s1,c1}(\omega) & \hat{Z}_{s1,c2}(\omega) & \hat{Z}_{s1,c3}(\omega) & \hat{Z}_{s1,s1}(\omega) & \hat{Z}_{s1,s2}(\omega) & \hat{Z}_{s1,s3}(\omega) & \hat{Z}_{s1,p}(\omega) \\ \hat{Z}_{s2,c1}(\omega) & \hat{Z}_{s2,c2}(\omega) & \hat{Z}_{s2,c3}(\omega) & \hat{Z}_{s2,s1}(\omega) & \hat{Z}_{s2,s2}(\omega) & \hat{Z}_{s2,s3}(\omega) & \hat{Z}_{s2,p}(\omega) \\ \hat{Z}_{s3,c1}(\omega) & \hat{Z}_{s3,c2}(\omega) & \hat{Z}_{s3,c3}(\omega) & \hat{Z}_{s3,s1}(\omega) & \hat{Z}_{s3,s2}(\omega) & \hat{Z}_{s3,s3}(\omega) & \hat{Z}_{s3,p}(\omega) \\ \hat{Z}_{p,c1}(\omega) & \hat{Z}_{p,c2}(\omega) & \hat{Z}_{p,c3}(\omega) & \hat{Z}_{p,s1}(\omega) & \hat{Z}_{p,s2}(\omega) & \hat{Z}_{p,s3}(\omega) & \hat{Z}_{p,p}(\omega) \end{bmatrix} \quad (7.14)$$

Voltages, currents and impedance terms of equations (7.13) and (7.14) can be grouped according to equation (7.15).

$$\begin{bmatrix} \left[V_{cg}(\omega)\right]_{3\times1} \\ \left[V_{sg}(\omega)\right]_{3\times1} \\ V_{pg}(\omega) \end{bmatrix} = \begin{bmatrix} \left[\hat{Z}_{c,c}(\omega)\right]_3 & \left[\hat{Z}_{c,s}(\omega)\right]_3 & \left[\hat{Z}_{c,p}(\omega)\right]_{3\times1} \\ \left[\hat{Z}_{s,c}(\omega)\right]_3 & \left[\hat{Z}_{s,s}(\omega)\right]_3 & \left[\hat{Z}_{s,p}(\omega)\right]_{3\times1} \\ \left[\hat{Z}_{p,c}(\omega)\right]_{1\times3} & \left[\hat{Z}_{p,s}(\omega)\right]_{1\times3} & \hat{Z}_{p,p}(\omega) \end{bmatrix} \begin{bmatrix} \left[I_c(\omega)\right]_{3\times1} \\ \left[I_s(\omega)\right]_{3\times1} \\ I_p(\omega) \end{bmatrix} \quad (7.15)$$

Equation (7.15) can be further simplified to obtain equation (7.16).

$$\begin{bmatrix} \left[V_{cg}(\omega)\right]_{3\times1} \\ \left[V_{sg-pg}(\omega)\right]_{4\times1} \end{bmatrix} = \begin{bmatrix} \left[\hat{Z}_{c,c}(\omega)\right]_3 & \left[\hat{Z}_{c,s-c,p}(\omega)\right]_{3\times4} \\ \left[\hat{Z}_{s,c-p,c}(\omega)\right]_{4\times3} & \left[\hat{Z}_{s,s-s,p-p,s-p,p}(\omega)\right]_4 \end{bmatrix} \begin{bmatrix} \left[I_c(\omega)\right]_{3\times1} \\ \left[I_{s-p}(\omega)\right]_{4\times1} \end{bmatrix} \quad (7.16)$$

Fig. 7.1 shows that the submarine cables of the OWPP base scenario are grounded at both ends. In this sense, it can be assumed that the voltages of the screens and pipe (or armour) with respect to ground are equal to zero, $\left[V_{sg-pg}(\omega)\right]_{4\times1}=0$. It should be noted that this assumption implies zero potential not only at both ends of the cable but also alongside the cable length. Based on this assumption, a simplified series impedance matrix can be obtained according to equation (7.17).

$$\begin{aligned} \left[\hat{Z}_{series.sc}^{abc}(\omega)\right]_3 = &\left[\hat{Z}_{c,c}(\omega)\right]_3 - \\ &\left[\hat{Z}_{c,s-c,p}(\omega)\right]_{3\times4}\left[\hat{Z}_{s,s-s,p-p,s-p,p}(\omega)\right]_4^{-1}\left[\hat{Z}_{s,c-p,c}(\omega)\right]_{4\times3} \end{aligned} \quad (7.17)$$

Applying the Fortescue transformation matrix $\left[T\right]$ to matrix $\left[\hat{Z}_{series.sc}^{abc}(\omega)\right]$, the sequence-series impedance is computed by means of equation (7.18).

$$\left[\hat{Z}_{series.sc}^{+-0}(\omega)\right]_3 = \left[T\right]^{-1}\left[\hat{Z}_{series.sc}^{abc}(\omega)\right]_3\left[T\right] \quad ; \quad \left[T\right]=\begin{bmatrix} 1 & 1 & 1 \\ a^2 & a & 1 \\ a & a^2 & 1 \end{bmatrix} \quad ; \quad a=e^{j\frac{2\pi}{3}} \quad (7.18)$$

The general representation of the sequence- series impedance is given by equation (7.19). A similar procedure is performed to obtain the sequence- shunt admittance of the submarine cable. The sequence- shunt admittance matrix is given by equation (7.20). As pointed out

in the previous subsection, this matrix is full, non-diagonal and non-symmetric if the cable system is not perfectly balanced. In other words, cable systems with a geometrical configuration in tight- or spaced flat formation.

$$
\left[\hat{Z}_{series.sc}^{+-0}(\omega) \right] = \begin{bmatrix} \hat{Z}_{series.sc}^{++}(\omega) & \hat{Z}_{series.sc}^{+-}(\omega) & \hat{Z}_{series.sc}^{+0}(\omega) \\ \hat{Z}_{series.sc}^{-+}(\omega) & \hat{Z}_{series.sc}^{--}(\omega) & \hat{Z}_{series.sc}^{-0}(\omega) \\ \hat{Z}_{series.sc}^{0+}(\omega) & \hat{Z}_{series.sc}^{0-}(\omega) & \hat{Z}_{series.sc}^{00}(\omega) \end{bmatrix} \tag{7.19}
$$

$$
\left[\hat{Y}_{shunt.sc}^{+-0}(\omega) \right] = \begin{bmatrix} \hat{Y}_{shunt.sc}^{++}(\omega) & \hat{Y}_{shunt.sc}^{+-}(\omega) & \hat{Y}_{shunt.sc}^{+0}(\omega) \\ \hat{Y}_{shunt.sc}^{-+}(\omega) & \hat{Y}_{shunt.sc}^{--}(\omega) & \hat{Y}_{shunt.sc}^{-0}(\omega) \\ \hat{Y}_{shunt.sc}^{0+}(\omega) & \hat{Y}_{shunt.sc}^{0-}(\omega) & \hat{Y}_{shunt.sc}^{00}(\omega) \end{bmatrix} \tag{7.20}
$$

Fig. 7.22 shows the per-length sequence-Pi model of a submarine cable for a specific frequency value according to equations (7.19) and (7.20). The general case that shows the coupling between different sequences.
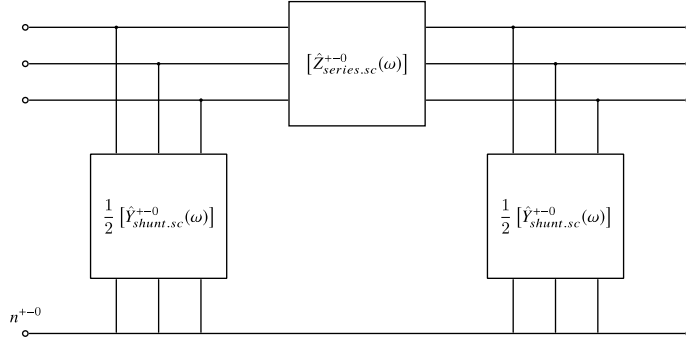
Fig. 7.22. General per-length sequence- Pi model of a submarine cable.

Due to the geometrical configuration of the submarine cables installed for the OWPP base scenario, the equivalent series impedance and shunt admittance matrices are symmetrical and the coupling terms are equal. Thus, the sequence- series impedance and sequence-shunt admittance matrix are given by equations (7.21) and (7.22), respectively.

$$
\left[\hat{Z}_{series.sc}^{+-0}(\omega) \right] = \begin{bmatrix} \hat{Z}_{series.sc}^{++}(\omega) & 0 & 0 \\ 0 & \hat{Z}_{series.sc}^{--}(\omega) & 0 \\ 0 & 0 & \hat{Z}_{series.sc}^{00}(\omega) \end{bmatrix} \tag{7.21}
$$

$$
\left[\hat{Y}_{shunt.sc}^{+-0}(\omega) \right] = \begin{bmatrix} \hat{Y}_{shunt.sc}^{++}(\omega) & 0 & 0 \\ 0 & \hat{Y}_{shunt.sc}^{--}(\omega) & 0 \\ 0 & 0 & \hat{Y}_{shunt.sc}^{00}(\omega) \end{bmatrix} \tag{7.22}
$$

As inferred from previous equations, the sequence circuits for this type of submarine cable are decoupled as shown in Fig. 7.23.
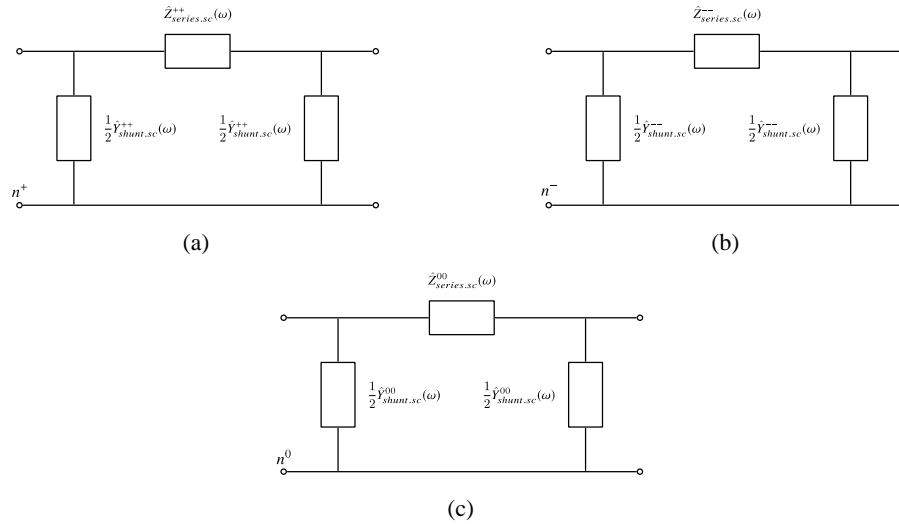
Fig. 7.23. Decoupled per-length sequence-Pi model of a submarine cable. (a) Positive-sequence. (b) Negative-sequence. (c) Zero-sequence.

For simplification purposes and with the aim of not being repetitive, the previous procedure is detailed only for this power component. For the rest of the power components, the starting point is to consider decoupled sequence circuits.

The schematic that is shown in Fig. 7.23 is valid for a given frequency value. Now with the aim of representing the frequency-dependent behavior of the sequence- series impedance into a unique model, a Foster equivalent network must be implemented. For the computation of the Foster equivalent network, a frequency sweep is done to each sequence-series impedance. Table 7.15 shows the general data that is needed to obtain the Foster equivalent network. The frequency vector is mainly defined in dependence of the frequency range of interest, 50 Hz to 5 kHz for this study.

Similar to the case addressed in chapter 6, the frequency-dependent behavior for each sequence- series impedance is approximated by means of VF algorithm. The rational function, obtained from the fitting process, is represented by a Foster equivalent network of order two. As pointed out in chapter 6, the order of the equivalent network depends mainly on the frequency range to study and accuracy requirements.

Table 7.15. Required general data for the determination of the Foster equivalent networks of the sequence-series impedances.

$\omega_{50\,Hz}$	$\cdots$	$\omega_{5\,kHz}$
$Z_{series.sc}^{++}(\omega_{50\,Hz})$	$\cdots$	$Z_{series.sc}^{++}(\omega_{5\,kHz})$
$Z_{series.sc}^{--}(\omega_{50\,Hz})$	$\cdots$	$Z_{series.sc}^{--}(\omega_{5\,kHz})$
$Z_{series.sc}^{00}(\omega_{50\,Hz})$	$\cdots$	$Z_{series.sc}^{00}(\omega_{5\,kHz})$

The decoupled per-length sequence-FDPi model, abbreviated from now on as sFDPi model, is depicted in Fig. 7.24.

149
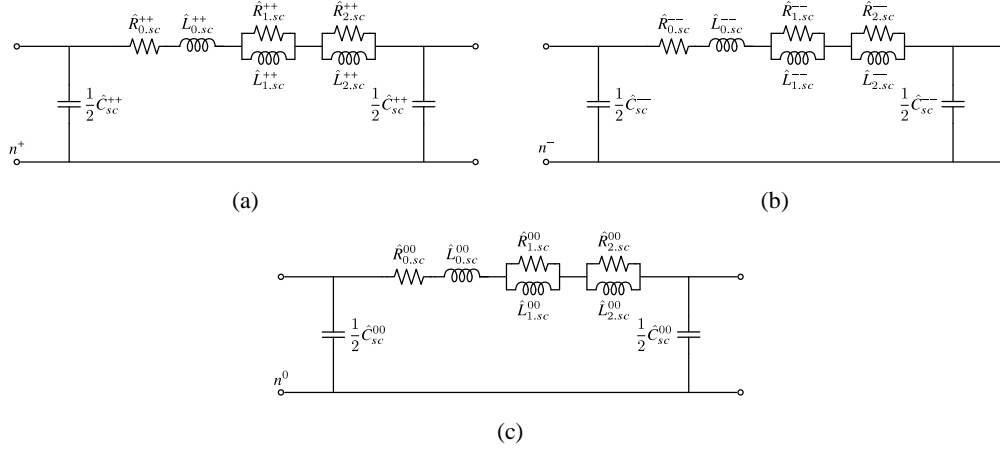
Fig. 7.24. Decoupled per-length sFDPi model of a submarine cable. (a) Positive-sequence. (b) Negative-sequence. (c) Zero-sequence.

Fig. 7.25 shows the schematic of the positive-sequence circuit of a submarine cable for a given number of sFDPi sections in cascade.
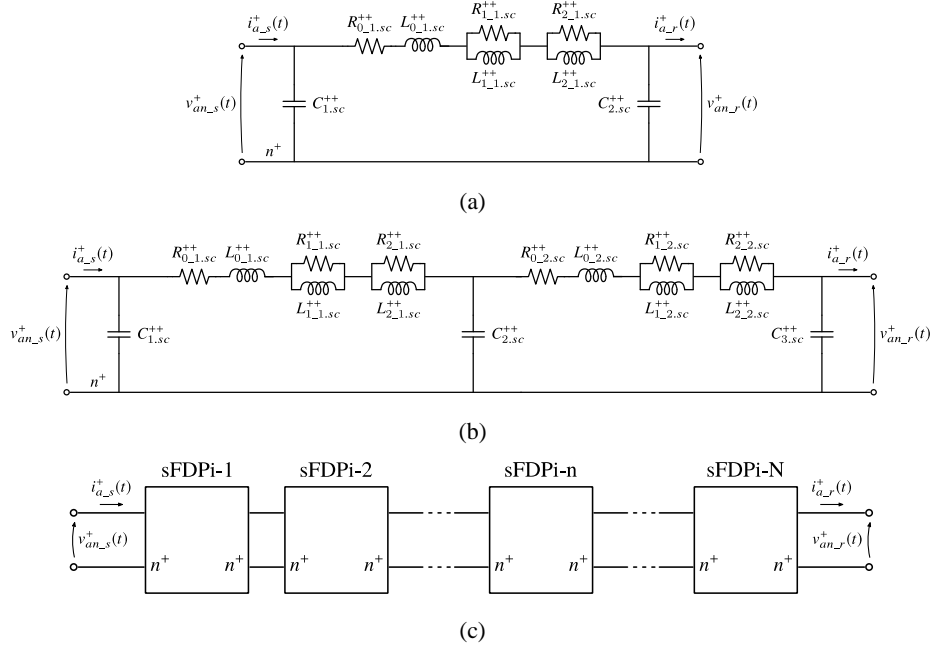
Fig. 7.25. Per-unit equivalent of the positive-sequence circuit of a submarine cable, sFDPi model. (a) One-section. (b) Two-sections in cascade. (c) N-sections in cascade.

The variables that are shown in Fig. 7.25 are given by equations (7.23) to (7.26) according to the number of sFDPi sections in cascade.

$$R_{m\_n.sc}^{++} = R_{m.sc}^{++} \quad ; \quad L_{m\_n.sc}^{++} = L_{m.sc}^{++} \quad ; \quad 0 \le m \le 2 \quad ; \quad 1 \le n \le N \quad (7.23)$$

$$N = 1 \quad \rightarrow \quad C_{1.sc}^{++} = \frac{1}{2}C_{sc}^{++} \quad ; \quad C_{2.sc}^{++} = \frac{1}{2}C_{sc}^{++} \quad (7.24)$$

$$N = 2 \quad \rightarrow \quad C_{1.sc}^{++} = \frac{1}{2}C_{sc}^{++} \quad ; \quad C_{2.sc}^{++} = C_{sc}^{++} \quad ; \quad C_{3.sc}^{++} = \frac{1}{2}C_{sc}^{++} \quad (7.25)$$

$$N > 2 \quad \rightarrow \quad C_{1.sc}^{++} = \frac{1}{2} C_{sc}^{++} \quad ; \quad C_{n.sc}^{++} = C_{sc}^{++} \quad ; \quad C_{(N+1).sc}^{++} = \frac{1}{2} C_{sc}^{++} \quad (7.26)$$

Being,

$$R_{m.sc}^{++} = \hat{R}_{m.sc}^{++} \cdot l_{section} \quad ; \quad L_{m.sc}^{++} = \hat{L}_{m.sc}^{++} \cdot l_{section} \quad ; \quad C_{sc}^{++} = \hat{C}_{sc}^{++} \cdot l_{section} \quad (7.27)$$

Table 7.16 and Table 7.17 provide the positive- and negative-sequence parameters of the collection network and transmission system cables. The parametes are given in pu-values. For clarity, the subscript "sc" that appears in the previous equations stands for submarine cable. It is a generic subscript and it is changed according to the type of submarine cable, collection cable (cc) or transmission cable (tc) as it is defined in the following tables.

Table 7.16. Positive- and negative-sequence parameters of the collection network submarine cables, given in pu-values.

Parameters	Base value
$\hat{R}_{0.cc}^{++} = \hat{R}_{0.cc}^{--} = 0.0050\ \mathrm{pu/km}$	
$\hat{R}_{1.cc}^{++} = \hat{R}_{1.cc}^{--} = 0.0590\ \mathrm{pu/km}$	$S_{base} = 60\ \mathrm{MVA}$
$\hat{R}_{2.cc}^{++} = \hat{R}_{2.cc}^{--} = 0.0068\ \mathrm{pu/km}$	$f_{base} = 50\ \mathrm{Hz}$
$\hat{L}_{0.cc}^{++} = \hat{L}_{0.cc}^{--} = 0.0031\ \mathrm{pu/km}$	$V_{base\_CP} = 30\ \mathrm{kV}$
$\hat{L}_{1.cc}^{++} = \hat{L}_{1.cc}^{--} = 0.0020\ \mathrm{pu/km}$	$Z_{base\_CP} = 15\ \Omega$
$\hat{L}_{2.cc}^{++} = \hat{L}_{2.cc}^{--} = 0.0024\ \mathrm{pu/km}$	$L_{base\_CP} = 47.7\ \mathrm{mH}$
$\hat{C}_{cc}^{++} = \hat{C}_{cc}^{--} = 0.0011\ \mathrm{pu/km}$	$C_{base\_CP} = 212.21\ \mu\mathrm{F}$
$N_{cc} = 1$	

Table 7.17. Positive- and negative-sequence parameters of the transmission system submarine cable, given in pu-values.

Parameters	Base value
$\hat{R}_{0.tc}^{++} = \hat{R}_{0.tc}^{--} = 3.5702 \cdot 10^{-4}\ \mathrm{pu/km}$	
$\hat{R}_{1.tc}^{++} = \hat{R}_{1.tc}^{--} = 0.0043\ \mathrm{pu/km}$	$S_{base} = 60\ \mathrm{MVA}$
$\hat{R}_{2.tc}^{++} = \hat{R}_{2.tc}^{--} = 3.4314 \cdot 10^{-4}\ \mathrm{pu/km}$	$f_{base} = 50\ \mathrm{Hz}$
$\hat{L}_{0.tc}^{++} = \hat{L}_{0.tc}^{--} = 3.5515 \cdot 10^{-4}\ \mathrm{pu/km}$	$V_{base\_PCC} = 110\ \mathrm{kV}$
$\hat{L}_{1.tc}^{++} = \hat{L}_{1.tc}^{--} = 1.4740 \cdot 10^{-4}\ \mathrm{pu/km}$	$Z_{base\_PCC} = 201.6667\ \Omega$
$\hat{L}_{2.tc}^{++} = \hat{L}_{2.tc}^{--} = 1.6253 \cdot 10^{-4}\ \mathrm{pu/km}$	$L_{base\_PCC} = 641.9\ \mathrm{mH}$
$\hat{C}_{tc}^{++} = \hat{C}_{tc}^{--} = 0.0095\ \mathrm{pu/km}$	$C_{base\_PCC} = 15.784\ \mu\mathrm{F}$
$N_{tc} = 20$	

The state-space representation of the schematic that is depicted in Fig. 7.25 is given by equation (7.28).

$$\frac{d}{dt}\left[x_{sc}^{+}(t) \right] = \left[F_{sc}^{++} \right]\left[x_{sc}^{+}(t) \right] + \left[G_{sc}^{++} \right]\left[a_{sc}^{+}(t) \right]$$

$$\left[b_{sc}^{+}(t) \right] = \left[H_{sc}^{++} \right]\left[x_{sc}^{+}(t) \right] + \left[J_{sc}^{++} \right]\left[a_{sc}^{+}(t) \right] \quad (7.28)$$

The input-, output-, and state-variable vector are given by equation (7.29).

$$
\left[a_{sc}^+(t) \right] = \begin{bmatrix} i_{a\_s}^+(t) \\ i_{a\_r}^+(t) \end{bmatrix} \quad ; \quad \left[b_{sc}^+(t) \right] = \begin{bmatrix} v_{an\_s}^+(t) \\ v_{an\_r}^+(t) \end{bmatrix} \quad ; \quad \left[x_{sc}^+(t) \right] = \begin{bmatrix} \left[i_{L_{0.sc}}^+(t) \right]_{N\times1} \\ \left[i_{L_{4.sc}}^+(t) \right]_{N\times1} \\ \left[i_{L_{2.sc}}^+(t) \right]_{N\times1} \\ \left[v_{C_{sc}}^+(t) \right]_{(N+1)\times1} \end{bmatrix} \tag{7.29}
$$

The vectors of $\left[x_{sc}^+(t) \right]$ are given by equations (7.30) and (7.31).

$$
\left[i_{L_{0.sc}}^+(t) \right]_{N\times1} = \begin{bmatrix} i_{L_{0\_1.sc}}^+(t) \\ i_{L_{0\_2.sc}}^+(t) \\ \vdots \\ i_{L_{0\_N.sc}}^+(t) \end{bmatrix} \quad ; \quad \left[i_{L_{4.sc}}^+(t) \right]_{N\times1} = \begin{bmatrix} i_{L_{1\_1.sc}}^+(t) \\ i_{L_{1\_2.sc}}^+(t) \\ \vdots \\ i_{L_{1\_N.sc}}^+(t) \end{bmatrix} \tag{7.30}
$$

$$
\left[i_{L_{2.sc}}^+(t) \right]_{N\times1} = \begin{bmatrix} i_{L_{2\_1.sc}}^+(t) \\ i_{L_{2\_2.sc}}^+(t) \\ \vdots \\ i_{L_{2\_N.sc}}^+(t) \end{bmatrix} \quad ; \quad \left[v_{C_{sc}}^+(t) \right]_{(N+1)\times1} = \begin{bmatrix} v_{C_{1.sc}}^+(t) \\ v_{C_{2.sc}}^+(t) \\ \vdots \\ v_{C_{N.sc}}^+(t) \\ v_{C_{(N+1).sc}}^+(t) \end{bmatrix} \tag{7.31}
$$

The matrix $\left[F_{sc}^{++} \right]$ is given by equation (7.32).

$$
\left[F_{sc}^{++} \right] = \begin{bmatrix} \left[F_{sc(1,1)}^{++} \right]_N & \left[F_{sc(1,2)}^{++} \right]_N & \left[F_{sc(1,3)}^{++} \right]_N & \left[F_{sc(1,4)}^{++} \right]_{N\times(N+1)} \\ \left[F_{sc(2,1)}^{++} \right]_N & \left[F_{sc(2,2)}^{++} \right]_N & \left[F_{sc(2,3)}^{++} \right]_N & \left[F_{sc(2,4)}^{++} \right]_{N\times(N+1)} \\ \left[F_{sc(3,1)}^{++} \right]_N & \left[F_{sc(3,2)}^{++} \right]_N & \left[F_{sc(3,3)}^{++} \right]_N & \left[F_{sc(3,4)}^{++} \right]_{N\times(N+1)} \\ \left[F_{sc(4,1)}^{++} \right]_{(N+1)\times N} & \left[F_{sc(4,2)}^{++} \right]_{(N+1)\times N} & \left[F_{sc(4,3)}^{++} \right]_{(N+1)\times N} & \left[F_{sc(4,4)}^{++} \right]_{(N+1)} \end{bmatrix} \tag{7.32}
$$

The matrices of $\left[F_{sc}^{++} \right]$ are given by equations (7.33) to (7.45).

$$
\left[F_{sc(1,1)}^{++} \right]_N = \frac{-\sum_{m=0}^{2} R_{m.sc}^{++}}{L_{0.sc}^{++}} \cdot [I]_N \quad ; \quad \left[F_{sc(1,2)}^{++} \right]_N = \frac{R_{1.sc}^{++}}{L_{0.sc}^{++}} \cdot [I]_N \tag{7.33}
$$

$$
\left[F_{sc(1,3)}^{++} \right]_N = \frac{R_{2.sc}^{++}}{L_{0.sc}^{++}} \cdot [I]_N \tag{7.34}
$$

The matrix $\left[F_{sc(1,4)}^{++} \right]$ is a special case and it is given by equations (7.35) to (7.37) for a different number of sFDPi sections in cascade.

$$N = 1 \quad \rightarrow \quad \left[F_{sc(1,4)}^{++} \right]_{1 \times 2} = \begin{bmatrix} \dfrac{1}{L_{0.sc}^{++}} & \dfrac{-1}{L_{0.sc}^{++}} \end{bmatrix} \tag{7.35}$$

$$N = 2 \quad \rightarrow \quad \left[F_{sc(1,4)}^{++} \right]_{2 \times 3} = \begin{bmatrix} \dfrac{1}{L_{0.sc}^{++}} & \dfrac{-1}{L_{0.sc}^{++}} & 0 \\ 0 & \dfrac{1}{L_{0.sc}^{++}} & \dfrac{-1}{L_{0.sc}^{++}} \end{bmatrix} \tag{7.36}$$

$$N > 2 \quad \rightarrow \quad \left[F_{sc(1,4)}^{++} \right]_{N \times (N+1)} = \begin{bmatrix} \dfrac{1}{L_{0.sc}^{++}} & \dfrac{-1}{L_{0.sc}^{++}} & 0 & \cdots & 0 \\ 0 & \dfrac{1}{L_{0.sc}^{++}} & \dfrac{-1}{L_{0.sc}^{++}} & \ddots & \vdots \\ \vdots & \ddots & \ddots & \ddots & 0 \\ 0 & \cdots & 0 & \dfrac{1}{L_{0.sc}^{++}} & \dfrac{-1}{L_{0.sc}^{++}} \end{bmatrix} \tag{7.37}$$

$$\left[F_{sc(2,1)}^{++} \right]_N = \frac{R_{1.sc}^{++}}{L_{1.sc}^{++}} \cdot [I]_N \quad ; \quad \left[F_{sc(2,2)}^{++} \right]_N = \frac{-R_{1.sc}^{++}}{L_{1.sc}^{++}} \cdot [I]_N \quad ; \quad \left[F_{sc(2,3)}^{++} \right]_N = [0]_N \tag{7.38}$$

$$\left[F_{sc(2,4)}^{++} \right]_{N \times (N+1)} = [0]_{N \times (N+1)} \quad ; \quad \left[F_{sc(3,1)}^{++} \right]_N = \frac{R_{2.sc}^{++}}{L_{2.sc}^{++}} \cdot [I]_N \quad ; \quad \left[F_{sc(3,2)}^{++} \right]_N = [0]_N \tag{7.39}$$

$$\left[F_{sc(3,3)}^{++} \right]_N = \frac{-R_{2.sc}^{++}}{L_{2.sc}^{++}} \cdot [I]_N \quad ; \quad \left[F_{sc(3,4)}^{++} \right]_{N \times (N+1)} = [0]_{N \times (N+1)} \tag{7.40}$$

Similar to the previous case, the matrix $\left[F_{sc(4,1)}^{++} \right]$ is given by equations (7.41) to (7.43) for a different number of sFDPi sections in cascade.

$$N = 1 \quad \rightarrow \quad \left[F_{sc(4,1)}^{++} \right]_{2 \times 1} = \begin{bmatrix} \dfrac{-2}{C_{sc}^{++}} \\ \dfrac{2}{C_{sc}^{++}} \end{bmatrix} \tag{7.41}$$

$$N = 2 \quad \rightarrow \quad \left[F_{sc(4,1)}^{++} \right]_{3 \times 2} = \begin{bmatrix} \dfrac{-2}{C_{sc}^{++}} & 0 \\ \dfrac{1}{C_{sc}^{++}} & \dfrac{-1}{C_{sc}^{++}} \\ 0 & \dfrac{2}{C_{sc}^{++}} \end{bmatrix} \tag{7.42}$$

153

$$N > 2 \quad \rightarrow \quad \left[F_{sc(4,1)}^{++} \right]_{(N+1)\times N} = \begin{bmatrix} \dfrac{-2}{C_{sc}^{++}} & 0 & \cdots & 0 \\[2mm] \dfrac{1}{C_{sc}^{++}} & \dfrac{-1}{C_{sc}^{++}} & \ddots & \vdots \\[2mm] 0 & \ddots & \ddots & 0 \\[2mm] \vdots & \ddots & \dfrac{1}{C_{sc}^{++}} & \dfrac{-1}{C_{sc}^{++}} \\[2mm] 0 & \cdots & 0 & \dfrac{2}{C_{sc}^{++}} \end{bmatrix} \tag{7.43}$$

$$\left[F_{sc(4,2)}^{++} \right]_{(N+1)\times N} = \left[0 \right]_{(N+1)\times N} \quad ; \quad \left[F_{sc(4,3)}^{++} \right]_{(N+1)\times N} = \left[0 \right]_{(N+1)\times N} \tag{7.44}$$

$$\left[F_{sc(4,4)}^{++} \right]_{(N+1)} = \left[0 \right]_{(N+1)} \tag{7.45}$$

The matrix $\left[G_{sc}^{++} \right]$ is given by equation (7.46).

$$\left[G_{sc}^{++} \right] = \begin{bmatrix} \left[G_{sc(1,1)}^{++} \right]_{3N \times 2} \\[2mm] \left[G_{sc(2,1)}^{++} \right]_{(N+1)\times 2} \end{bmatrix} \tag{7.46}$$

The matrices of $\left[G_{sc}^{++} \right]$ are given by equations (7.47) to (7.50). The matrix $\left[G_{sc(2,1)}^{++} \right]$ is given by equations (7.48) to (7.50) for a different number of sFDPi sections in cascade.

$$\left[G_{sc(1,1)}^{++} \right]_{3N \times 2} = \left[0 \right]_{3N \times 2} \tag{7.47}$$

$$N = 1 \quad \rightarrow \quad \left[G_{sc(2,1)}^{++} \right]_2 = \begin{bmatrix} \dfrac{2}{C_{sc}^{++}} & 0 \\[3mm] 0 & \dfrac{-2}{C_{sc}^{++}} \end{bmatrix} \tag{7.48}$$

$$N = 2 \quad \rightarrow \quad \left[G_{sc(2,1)}^{++} \right]_{3\times 2} = \begin{bmatrix} \dfrac{2}{C_{sc}^{++}} & 0 \\[3mm] 0 & 0 \\[3mm] 0 & \dfrac{-2}{C_{sc}^{++}} \end{bmatrix} \tag{7.49}$$

$$N > 2 \quad \rightarrow \quad \left[G_{sc(2,1)}^{++} \right]_{(N+1)\times 2} = \begin{bmatrix} \dfrac{2}{C_{sc}^{++}} & 0 \\[3mm] 0 & \vdots \\[3mm] \vdots & 0 \\[3mm] 0 & \dfrac{-2}{C_{sc}^{++}} \end{bmatrix} \tag{7.50}$$

The matrix $\left[H_{sc}^{++} \right]$ is given by equation (7.51).

$$\left[H_{sc}^{++} \right] = \left[\left[H_{sc(1,1)}^{++} \right]_{2 \times 3N} \quad \left[H_{sc(1,2)}^{++} \right]_{2 \times (N+1)} \right] \tag{7.51}$$

The matrices of $\left[H_{sc}^{++} \right]$ are given by equations (7.52) to (7.55). The matrix $\left[H_{sc(1,2)}^{++} \right]$ is given by equations (7.53) to (7.55) for a different number of sFDPi sections in cascade.

$$\left[H_{sc(1,1)}^{++} \right]_{2 \times 3N} = \left[0 \right]_{2 \times 3N} \tag{7.52}$$

$$N = 1 \quad \rightarrow \quad \left[H_{sc(1,2)}^{++} \right]_{2} = \begin{bmatrix} 1 & 0 \\ 0 & 1 \end{bmatrix} \tag{7.53}$$

$$N = 2 \quad \rightarrow \quad \left[H_{sc(1,2)}^{++} \right]_{2 \times 3} = \begin{bmatrix} 1 & 0 & 0 \\ 0 & 0 & 1 \end{bmatrix} \tag{7.54}$$

$$N > 2 \quad \rightarrow \quad \left[H_{sc(1,2)}^{++} \right]_{2 \times (N+1)} = \begin{bmatrix} 1 & 0 & \cdots & 0 \\ 0 & \cdots & 0 & 1 \end{bmatrix} \tag{7.55}$$

Finally, the matrix $\left[J_{sc}^{++} \right]$ is given by equation (7.56).

$$\left[J_{sc}^{++} \right] = \left[0 \right]_{2} \tag{7.56}$$

Transformers

The per-unit equivalents of the positive- and negative-sequence circuits of a three-phase two-winding power transformer are shown in Fig. 7.26. As shown in this figure, the voltages and currents at the primary and secondary sides depend on windings connection.
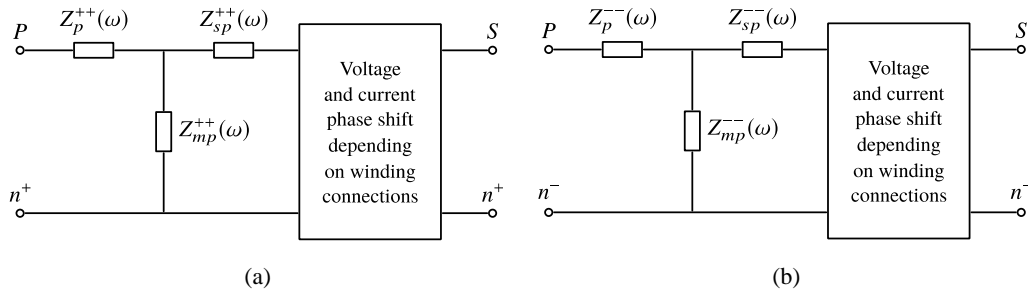
Fig. 7.26. Per-unit equivalents of the positive- and negative-sequence circuits of a three-phase two-winding power transformer. (a) Positive-sequence. (b) Negative-sequence.
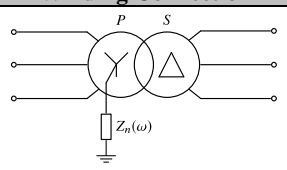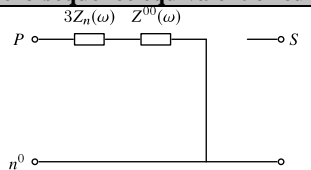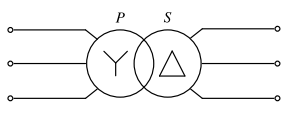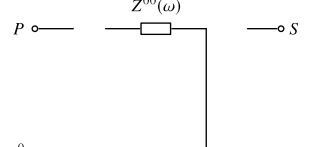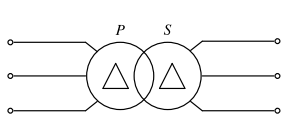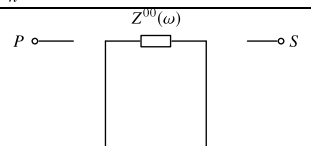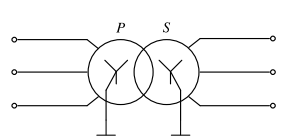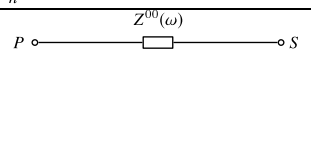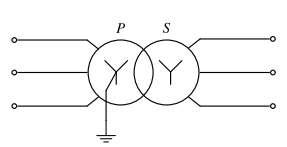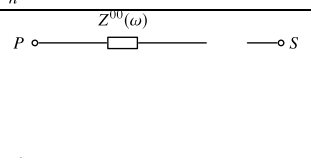
The impedance offered by a transformer to the flow of zero-sequence currents depends on windings connection. Table 7.18 gives the zero-sequence circuits for different windings connections, only applicable to two-winding transformers.

For zero-sequence currents to flow through windings on one side of the transformer and into the connected lines, a physical connection must exist. This physical connection provides a return path allowing the circulation of zero-sequence currents. Additionally, there must be a path for these sequence currents in the coupled windings on the other side of the transformer.

For illustration, let us consider the windings connection for case 1 of Table 7.18. The $Y-$ connected primary windings with the neutral grounded provide a path to ground. The $\Delta-$ connected secondary windings provide a path for the zero-sequence currents, which circulate within the Δ. This serves to balance the currents in the primary windings; however, the zero-sequence currents circulating within the secondary windings cannot flow in the lines connected to them. In other words, a $\Delta-$connected circuit provides no path for zero-sequence currents flowing outside the winding, which means that the impedance as seen from the secondary side is infinite.

If the windings on one side are $Y-$connected with neutral ungrounded, zero-sequence currents cannot flow in the windings on either side. Viewed from either the primary side or the secondary side, the zero-sequence impedance is infinite.

Table 7.18. Zero-sequence circuit of three-phase two-winding transformers. Source [200].

Case	Winding Connection	Zero-sequence equivalent circuit
1	P — S ; Y–Δ ; $Z_n(\omega)$	$3Z_n(\omega)$ $Z^{00}(\omega)$; P —▭—▭— S ; n^0
2	P — S ; Y–Δ	$Z^{00}(\omega)$; P ——▭— S ; n^0
3	P — S ; Δ–Δ	$Z^{00}(\omega)$; P ——▭— S ; n^0
4	P — S ; Y–Y	$Z^{00}(\omega)$; P ——▭—— S ; n^0
5	P — S ; Y–Y	$Z^{00}(\omega)$; P —▭— S ; n^0

The positive- and negative-sequence circuits, presented in Fig. 7.26, are only valid for a given frequency value. Now with the aim of representing the frequency-dependent behavior of the short circuit impedance of the transformers (sequence impedances) into a unique model, a Foster equivalent network must be implemented. Following a similar procedure as in the case of the submarine cable, a Foster equivalent network of order two is implemented.

The per-unit equivalent of the positive-sequence circuit of the offshore substation transformer is depicted in Fig. 7.27. For this transformer and the WTT, the impedance of the transformer core is very large compared to the series impedance and can be neglected [200]. For special studies requiring the representation of the transformer saturation, the magnetizing reactance may be approximated according to the models presented in chapter 5. Stray capacitances may be added too.
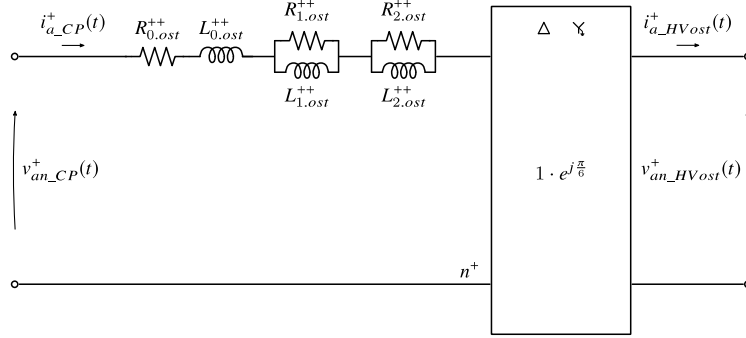
Fig. 7.27. Per-unit equivalent of the positive-sequence circuit of the offshore substation transformer.

Table 7.19 provides the positive- and negative-sequence parameters of the offshore substation transformer. The parameters are given in pu-values.

Table 7.19. Positive- and negative-sequence parameters of the offshore substation transformer, given in pu-values.

Parameters	Base value
$R_{0.ost}^{++} = R_{0.ost}^{--} = 0.85 \text{ pu}$	$S_{base} = 60 \text{ MVA}$
$R_{1.ost}^{++} = R_{1.ost}^{--} = 21.07 \text{ pu}$	$f_{base} = 50 \text{ Hz}$
$R_{2.ost}^{++} = R_{2.ost}^{--} = 2205.318 \text{ pu}$	$V_{base\_PCC} = 110 \text{ kV}$
$L_{0.ost}^{++} = L_{0.ost}^{--} = 5.1203 \cdot 10^{-3} \text{ pu}$	$Z_{base\_PCC} = 201.6667 \ \Omega$
$L_{1.ost}^{++} = L_{1.ost}^{--} = 25.0870 \cdot 10^{-3} \text{ pu}$	$L_{base\_PCC} = 641.9 \text{ mH}$
$L_{2.ost}^{++} = L_{2.ost}^{--} = 0.9745 \cdot 10^{-3} \text{ pu}$	

The state-space representation of the schematic that is depicted in Fig. 7.27 is given by equation (7.57).

$$\frac{d}{dt}\left[x_{ost}^{+}(t) \right] = \left[F_{ost}^{++} \right]\left[x_{ost}^{+}(t) \right] + \left[G_{ost}^{++} \right]\left[a_{ost}^{+}(t) \right]$$

$$\left[b_{ost}^{+}(t) \right] = \left[H_{ost}^{++} \right]\left[x_{ost}^{+}(t) \right] + \left[J_{ost}^{++} \right]\left[a_{ost}^{+}(t) \right] \tag{7.57}$$

The input-, output-, and state-variable vector are given by equation (7.58).

$$\left[a_{ost}^{+}(t) \right] = \begin{bmatrix} v_{an\_CP}^{+}(t) \\ v_{an\_HVost}^{+}(t) \end{bmatrix} \quad ; \quad \left[b_{ost}^{+}(t) \right] = \begin{bmatrix} i_{a\_CP}^{+}(t) \\ i_{a\_HVost}^{+}(t) \end{bmatrix} \quad ; \quad \left[x_{ost}^{+}(t) \right] = \begin{bmatrix} i_{L_{0.ost}}^{+}(t) \\ i_{L_{1.ost}}^{+}(t) \\ i_{L_{2.ost}}^{+}(t) \end{bmatrix} \tag{7.58}$$

The matrices $\left[F_{ost}^{++} \right]$ and $\left[G_{ost}^{++} \right]$ are given by equation (7.59).

$$
\left[F_{ost}^{++} \right] =
\begin{bmatrix}
\dfrac{-\sum\limits_{m=0}^{2} R_{m.ost}^{++}}{L_{0.ost}^{++}} & \dfrac{R_{1.ost}^{++}}{L_{0.ost}^{++}} & \dfrac{R_{2.ost}^{++}}{L_{0.ost}^{++}} \\[2em]
\dfrac{R_{1.ost}^{++}}{L_{1.ost}^{++}} & \dfrac{-R_{1.ost}^{++}}{L_{1.ost}^{++}} & 0 \\[2em]
\dfrac{R_{2.ost}^{++}}{L_{2.ost}^{++}} & 0 & \dfrac{-R_{2.ost}^{++}}{L_{2.ost}^{++}}
\end{bmatrix}
\quad ; \quad
\left[G_{ost}^{++} \right] =
\begin{bmatrix}
\dfrac{1}{L_{0.ost}^{++}} & \dfrac{-1}{L_{0.ost}^{++}} \\[2em]
0 & 0 \\[2em]
0 & 0
\end{bmatrix}
\tag{7.59}
$$

Finally, the matrices $\left[H_{ost}^{++} \right]$ and $\left[J_{ost}^{++} \right]$ are given by equation (7.60).

$$
\left[H_{ost}^{++} \right] =
\begin{bmatrix}
1 & 0 & 0 \\
1 & 0 & 0
\end{bmatrix}
\quad ; \quad
\left[J_{ost}^{++} \right] = [0]_2
\tag{7.60}
$$

The state-space model of the wind turbine transformer is represented together with the grid side connection filter. Both power components are grouped into one block, named WTi block. This is addressed next.

GSC connection filter and WTT block

The per-unit equivalents of the sequence circuits of the grid side connection filter are shown in Fig. 7.28. Since there is no physical connection to ground or connection between the neutral of the filter and the neutral point of the converter, a zero-sequence current cannot flow. The zero-sequence impedance is infinite.

Fig. 7.28. Per-unit equivalents of the sequence circuits of the grid side connection filter. (a) Positive-sequence. (b) Negative-sequence. (c) Zero-sequence.

Fig. 7.29 shows the positive-sequence circuit of the block grouping the GSC connection filter and the wind turbine transformer.

The variables that are shown in the schematic of Fig. 7.29 are given by equations (7.61) and (7.62) for the GSC connection filter and wind turbine transformer, respectively.

$$
L_{c.wti}^{++} = L_c^{++} \quad ; \quad C_{f.wti}^{++} = C_f^{++} \quad ; \quad L_{d.wti}^{++} = L_d^{++} \quad ; \quad R_{d.wti}^{++} = R_d^{++}
\tag{7.61}
$$

$$
R_{m.wtti}^{++} = R_{m.wtt}^{++} \quad ; \quad L_{m.wtti}^{++} = L_{m.wtt}^{++} \quad ; \quad 0 \le m \le 2
\tag{7.62}
$$
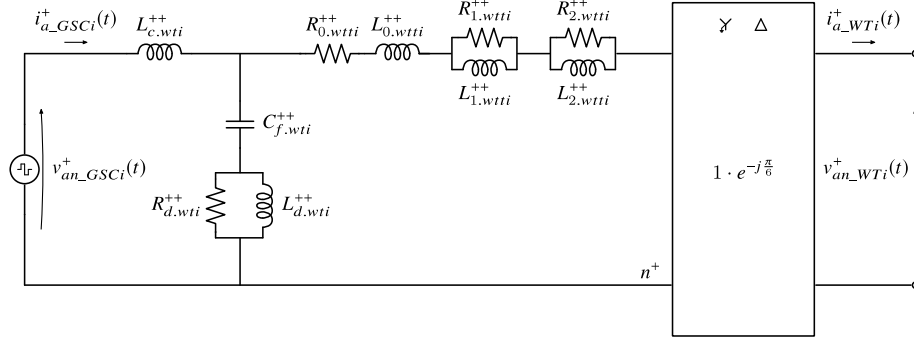
Fig. 7.29. Per-unit equivalent of the positive-sequence circuit of the grid side connection filter and wind turbine transformer block.

Table 7.20 and Table 7.21 provide the parameters of the grid side connection filter and wind turbine transformer for the positive- and negative-sequence circuits.

Table 7.20. Positive- and negative-sequence parameters of the grid side connection filter, given in pu-values.

Parameters	Base value
$L_c^{++} = L_c^{--} = 1.1684$ pu	$S_{base} = 60$ MVA
	$f_{base} = 50$ Hz
$C_f^{++} = C_f^{--} = 0.0154$ pu	$V_{base\_GSC} = 3.3$ kV
	$Z_{base\_GSC} = 0.1815\ \Omega$
$L_d^{++} = L_d^{--} = 0.3288$ pu	$L_{base\_GSC} = 577.73\ \mu H$
$R_d^{++} = R_d^{--} = 2.8650$ pu	$C_{base\_GSC} = 17.5$ mF

Table 7.21. Positive- and negative-sequence parameters of the wind turbine transformer, given in pu-values.

Parameters	Base value
$R_{0.wtt}^{++} = R_{0.wtt}^{--} = 0.85$ pu	
$R_{1.wtt}^{++} = R_{1.wtt}^{--} = 21.07$ pu	$S_{base} = 60$ MVA
$R_{2.wtt}^{++} = R_{2.wtt}^{--} = 2205.318$ pu	$f_{base} = 50$ Hz
$L_{0.wtt}^{++} = L_{0.wtt}^{--} = 5.1203 \cdot 10^{-3}$ pu	$V_{base\_GSC} = 3.3$ kV
$L_{1.wtt}^{++} = L_{1.wtt}^{--} = 25.0870 \cdot 10^{-3}$ pu	$Z_{base\_GSC} = 0.1815\ \Omega$
$L_{2.wtt}^{++} = L_{2.wtt}^{--} = 0.9745 \cdot 10^{-3}$ pu	$L_{base\_GSC} = 577.73\ \mu H$

The state-space representation of the schematic that is depicted in Fig. 7.29 is given by equation (7.63).

$$\frac{d}{dt}\left[x_{WTi}^+(t) \right] = \left[F_{WTi}^{++} \right]\left[x_{WTi}^+(t) \right] + \left[G_{WTi}^{++} \right]\left[a_{WTi}^+(t) \right]$$

$$\left[b_{WTi}^+(t) \right] = \left[H_{WTi}^{++} \right]\left[x_{WTi}^+(t) \right] + \left[J_{WTi}^{++} \right]\left[a_{WTi}^+(t) \right]$$

(7.63)

The input-, output-, and state-variable vector are given by equation (7.64).

159

$$
\left[a_{WTi}^+(t)\right]=\begin{bmatrix} v_{an\_GSCi}^+(t) \\ v_{an\_WTi}^+(t) \end{bmatrix} \quad ; \quad \left[b_{WTi}^+(t)\right]=\begin{bmatrix} i_{a\_GSCi}^+(t) \\ i_{a\_WTi}^+(t) \end{bmatrix} \quad ; \quad \left[x_{WTi}^+(t)\right]=\begin{bmatrix} i_{L_{c.wti}}^+(t) \\ i_{L_{0.wtti}}^+(t) \\ i_{L_{1.wtti}}^+(t) \\ i_{L_{2.wtti}}^+(t) \\ i_{L_{d.wti}}^+(t) \\ v_{C_{f.wti}}^+(t) \end{bmatrix} \tag{7.64}
$$

Finally, the matrices $\left[F_{WTi}^{++}\right]$, $\left[G_{WTi}^{++}\right]$, $\left[H_{WTi}^{++}\right]$ and $\left[J_{WTi}^{++}\right]$ are given by equations (7.65) to (7.67).

$$
\left[F_{WTi}^{++}\right]=\begin{bmatrix}
\dfrac{-R_d^{++}}{L_c^{++}} & \dfrac{R_d^{++}}{L_c^{++}} & 0 & 0 & \dfrac{R_d^{++}}{L_c^{++}} & \dfrac{-1}{L_c^{++}} \\[2mm]
\dfrac{R_d^{++}}{L_{0.wtt}^{++}} & \dfrac{-\left(R_d^{++}+\displaystyle\sum_{m=0}^{2}R_{m.wtt}^{++}\right)}{L_{0.wtt}^{++}} & \dfrac{R_{1.wtt}^{++}}{L_{0.wtt}^{++}} & \dfrac{R_{2.wtt}^{++}}{L_{0.wtt}^{++}} & \dfrac{-R_d^{++}}{L_{0.wtt}^{++}} & \dfrac{1}{L_{0.wtt}^{++}} \\[2mm]
0 & \dfrac{R_{1.wtt}^{++}}{L_{1.wtt}^{++}} & \dfrac{-R_{1.wtt}^{++}}{L_{1.wtt}^{++}} & 0 & 0 & 0 \\[2mm]
0 & \dfrac{R_{2.wtt}^{++}}{L_{2.wtt}^{++}} & 0 & \dfrac{-R_{2.wtt}^{++}}{L_{2.wtt}^{++}} & 0 & 0 \\[2mm]
\dfrac{R_d^{++}}{L_d^{++}} & \dfrac{-R_d^{++}}{L_d^{++}} & 0 & 0 & \dfrac{-R_d^{++}}{L_d^{++}} & 0 \\[2mm]
\dfrac{1}{C_f^{++}} & \dfrac{-1}{C_f^{++}} & 0 & 0 & 0 & 0
\end{bmatrix} \tag{7.65}
$$

$$
\left[G_{WTi}^{++}\right]=\begin{bmatrix} \dfrac{1}{L_c^{++}} & 0 \\[2mm] 0 & \dfrac{-1}{L_{0.wtt}^{++}} \\[2mm] 0 & 0 \\ 0 & 0 \\ 0 & 0 \\ 0 & 0 \end{bmatrix} \quad ; \quad \left[H_{WTi}^{++}\right]=\begin{bmatrix} 1 & 0 & 0 & 0 & 0 & 0 \\ 0 & 1 & 0 & 0 & 0 & 0 \end{bmatrix} \tag{7.66}
$$

$$
\left[J_{WTi}^{++}\right]=\left[0\right]_2 \tag{7.67}
$$

Shunt Reactors for Reactive Power Compensation of the Transmission Link

The per-unit equivalents of the sequence circuits of the shunt reactors are shown in Fig. 7.30. Since the shunt reactors are $Y-$connected and there is no physical connection to ground, a zero-sequence current cannot flow. The zero-sequence impedance is infinite.
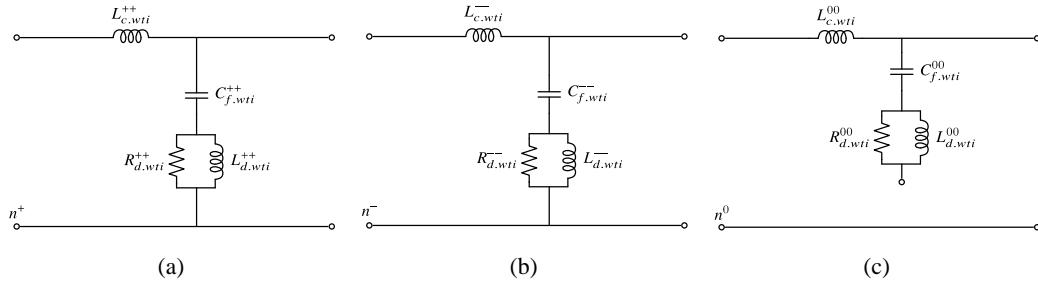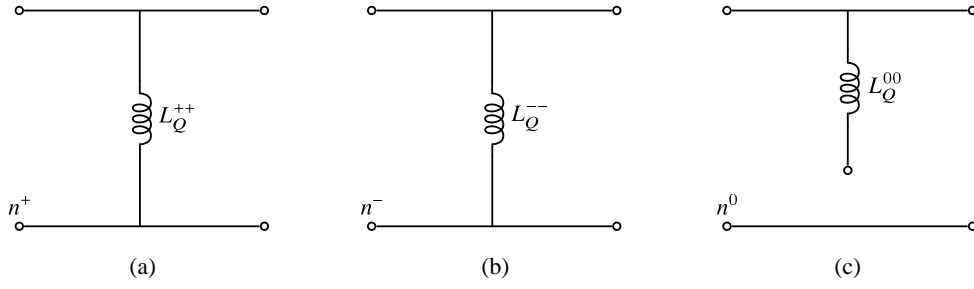
Fig. 7.30. Per-unit equivalents of the sequence circuits of the shunt reactors. (a) Positive-sequence. (b) Negative-sequence. (c) Zero-sequence.

Fig. 7.31 shows the positive-sequence circuit of the shunt reactor placed at the sending end of the transmission system.
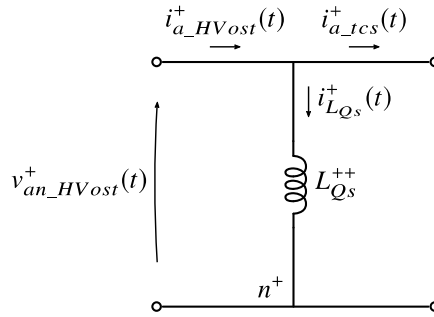
Fig. 7.31. Per-unit equivalent of the positive-sequence circuit of the shunt reactor placed at the sending end of the transmission system.

Table 7.22 provides the positive- and negative-sequence parameters of the shunt reactors at both ends of the transmission system, the sending- and receiving-end.

Table 7.22. Positive- and negative-sequence parameters of the shunt reactors of the transmission system, given in pu-values.

Parameters	Base value
$L_{Qs}^{++} = L_{Qs}^{--} = 6.2315$ pu	$S_{base} = 60$ MVA $f_{base} = 50$ Hz $V_{base\_PCC} = 110$ kV
$L_{Qr}^{++} = L_{Qr}^{--} = 6.2315$ pu	$Z_{base\_PCC} = 201.6667\ \Omega$ $L_{base\_PCC} = 641.9$ mH

The state-space representation of the schematic that is depicted in Fig. 7.31 is given by equation (7.68).

$$\frac{d}{dt}\left[x_{Qs}^+(t)\right] = \left[F_{Qs}^{++}\right]\left[x_{Qs}^+(t)\right] + \left[G_{Qs}^{++}\right]\left[a_{Qs}^+(t)\right]$$
$$\left[b_{Qs}^+(t)\right] = \left[H_{Qs}^{++}\right]\left[x_{Qs}^+(t)\right] + \left[J_{Qs}^{++}\right]\left[a_{Qs}^+(t)\right]$$

(7.68)

The input-, output-, and state-variable vector are given by equation (7.69).

$$\left[a_{Qs}^+(t)\right] = \begin{bmatrix} i_{a\_HVost}^+(t) \\ v_{an\_HVost}^+(t) \end{bmatrix} \quad ; \quad \left[b_{Qs}^+(t)\right] = \left[i_{a\_tcs}^+(t)\right] \quad ; \quad \left[x_{Qs}^+(t)\right] = \left[i_{L_{Qs}}^+(t)\right]$$

(7.69)

161

The matrices $\left[F_{Qs}^{++} \right]$ and $\left[G_{Qs}^{++} \right]$ are given by equation (7.70).

$$\left[F_{Qs}^{++} \right] = \begin{bmatrix} 0 \end{bmatrix} \quad ; \quad \left[G_{Qs}^{++} \right] = \begin{bmatrix} 0 & \dfrac{1}{L_{Qs}^{++}} \end{bmatrix} \tag{7.70}$$

Finally, the matrices $\left[H_{Qs}^{++} \right]$ and $\left[J_{Qs}^{++} \right]$ are given by equation (7.71).

$$\left[H_{Qs}^{++} \right] = \begin{bmatrix} -1 \end{bmatrix} \quad ; \quad \left[J_{Qs}^{++} \right] = \begin{bmatrix} 1 & 0 \end{bmatrix} \tag{7.71}$$

Power Grid and Shunt Reactor block

The per-unit equivalents of the sequence circuits of the power grid are shown in Fig. 7.32. It is common practice to consider the power grid as an ideal voltage source, generating only the fundamental component, with a short-circuit inductance in series. The short-circuit inductance is given by the grid strength or SCR. Ideally, negative- and zero-sequence voltages are not injected by the grid. However, there are some scenarios where harmonics are injected by the grid. For example, it is possible to have upstream the OWPP a HVDC-LCC transmission system operating with a 12-pulse thyristor configuration. For this scenario, harmonics of order 11th (negative-sequence) and 13th (positive-sequence) are injected. The reader is suggested to see reference [201] for a description of a real-life scenario addressing this situation.

Regarding the zero-sequence circuit, the electrical configuration of OWPPs does not provide a path to the circulation of zero-sequence currents coming from the grid due to the windings connection of the onshore substation transformer. The zero-sequence impedance is infinite.
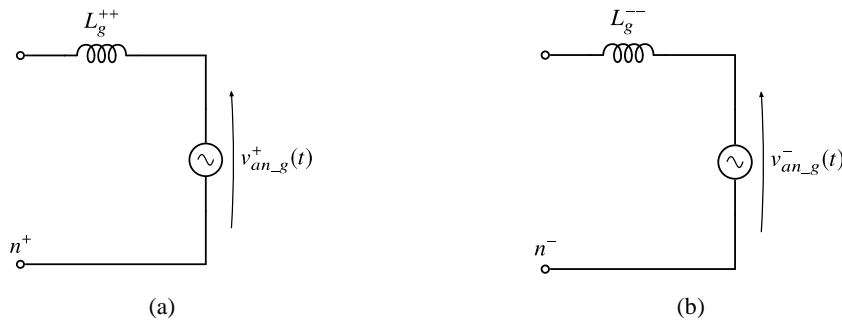
Fig. 7.32. Per-unit equivalent of the positive- and negative-sequence circuits of the power grid. (a) Positive-sequence. (b) Negative-sequence.

Fig. 7.33 shows the positive-sequence circuit of the power grid and the shunt reactor placed at the receiving end of the transmission system.

Table 7.22 provides the positive- and negative-sequence parameters of the shunt reactor placed at the receiving end of the transmission system. On the other hand, Table 7.23 provides the positive- and negative-sequence parameters of the short-circuit inductance of the power grid.
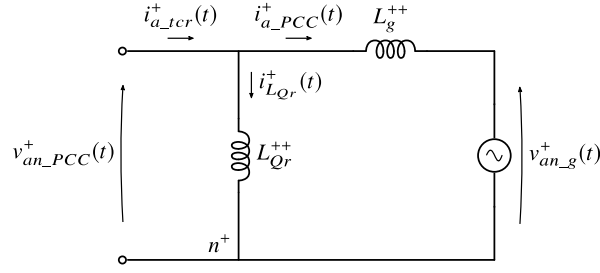
Fig. 7.33. Per-unit equivalent of the positive-sequence circuit of the power grid and the shunt reactor placed at the receiving end of the transmission system.

Table 7.23. Positive- and negative-sequence parameters of the short-circuit inductance of the power grid, given in pu-values.

Parameters	Base value
$L_g^{++} = L_g^{--} = 0.05\,\text{pu}$ (SCR = 20)	$S_{base} = 60\,\text{MVA}$ $f_{base} = 50\,\text{Hz}$ $V_{base\_PCC} = 110\,\text{kV}$ $Z_{base\_PCC} = 201.6667\,\Omega$ $L_{base\_PCC} = 641.9\,\text{mH}$

The state-space representation of the schematic that is depicted in Fig. 7.33 is given by equation (7.72).

$$\frac{d}{dt}\left[x_g^+(t)\right] = \left[F_g^{++}\right]\left[x_g^+(t)\right] + \left[G_g^{++}\right]\left[a_g^+(t)\right]$$
$$\left[b_g^+(t)\right] = \left[H_g^{++}\right]\left[x_g^+(t)\right] + \left[J_g^{++}\right]\left[a_g^+(t)\right] \tag{7.72}$$

The input-, output-, and state-variable vector are given by equation (7.73).

$$\left[a_g^+(t)\right] = \begin{bmatrix} v_{an\_PCC}^+(t) \\ v_{an\_g}^+(t) \end{bmatrix} \quad ; \quad \left[b_g^+(t)\right] = \begin{bmatrix} i_{a\_tcr}^+(t) \\ i_{a\_PCC}^+(t) \end{bmatrix} \quad ; \quad \left[x_g^+(t)\right] = \begin{bmatrix} i_{L_{Qr}}^+(t) \\ i_{L_g}^+(t) \end{bmatrix} \tag{7.73}$$

The matrices $\left[F_g^{++}\right]$ and $\left[G_g^{++}\right]$ are given by equation (7.74).

$$\left[F_g^{++}\right] = [0]_2 \quad ; \quad \left[G_g^{++}\right] = \begin{bmatrix} \dfrac{1}{L_{Qr}^{++}} & 0 \\ \dfrac{1}{L_g^{++}} & \dfrac{-1}{L_g^{++}} \end{bmatrix} \tag{7.74}$$

Finally, the matrices $\left[H_g^{++}\right]$ and $\left[J_g^{++}\right]$ are given by equation (7.75).

$$\left[H_g^{++}\right] = \begin{bmatrix} 1 & 1 \\ 0 & 1 \end{bmatrix} \quad ; \quad \left[J_g^{++}\right] = [0]_2 \tag{7.75}$$

7.5   Chapter Summary

This chapter has presented the modeling of an offshore wind power plant. Two modeling approaches have been addressed, the Simulink®-based model and the sequence network model. Both modeling approaches have been used to represent an OWPP base scenario, which has been defined taking into account information of a real OWPP.

The Simulink®-based model comprises the models that have been presented, from chapter 3 to 6, for each power component. The aim of the Simulink®-based model is to determine voltage- and current distortions at different points along the OWPP, the compliance of grid codes in terms of harmonics, and the design and evaluation of technical solutions to detected potential problems. Even though these aspects have not been discussed in detail in this chapter, they are addressed in chapter nine. Regarding the Simulink®-based model of the OWPP base scenario, all the required parameters have been provided to reproduce this scenario. Wake effect has been added to the Simulink®-based model to consider different operation points among WTs. Two case studies have been addressed for this OWPP base scenario. The first case study considers a typical CB-PWM modulation for the GSCs of the WTs while the second case study considers SHE-PWM modulation. For both case studies, the wind blows from east to west and its speed is equal to 16 m/s. For this wind condition, the active power reference of each WT has been defined according to the wake effect. The reactive power reference has been defined so each WT operates with a unity power factor at WTT terminals.

On the other hand, the sequence network model is developed by means of a state-space representation of the OWPP and its implementation in a *.m-file in Matlab®, as carried out in section 7.4. The purpose of the sequence network model is to perform a series of studies whose computation is not an easy task to be performed by the Simulink®-based model in terms of post-processing and time consumption. Among the studies that can be performed with this tool are the frequency response and parameter sensitivity studies of an OWPP. These studies are carried out in next chapter for the OWPP base scenario.

Chapter 8

Frequency Response of an OWPP

This chapter presents the frequency response of an OWPP. These studies are performed by means of the sequence network model and the OWPP base scenario defined in chapter 7. Bode plots of transfer functions, relating voltage- and current variables of different points along the OWPP base scenario, are presented. Special emphasis is taken for transfer functions that relate electrical variables at the PCC point with respect to the voltage-harmonics injected by the GSC of each wind turbine. A discussion about the risk of amplification of the harmonics injected by the WTs is performed according to the spectrums of the modulation strategies evaluated so far, CB-PWM and SHE-PWM. Finally, changes in the frequency response of the OWPP base scenario are presented. These changes are evaluated when varying the electrical parameters of the main power components and when considering an OWPP with an asymmetrical layout. This last can be obtained when considering disconnected wind turbines or when considering an OWPP with distances among WTs quite different.

8.1 Introduction

The concern of power quality has been on the rise in recent years for all kinds of electric power systems. In the offshore wind industry, harmonics are a special concern due to the high penetration of power converters in type-4 wind turbines [6]. This type of WT can be considered as a source of harmonics, which significantly contributes to the overall

harmonic emission at the point of common coupling of the OWPP. Furthermore, this contribution can be worsened due to the presence of resonances that may increase a given voltage- or current-harmonic component. These resonances can be classified into series and parallel resonances and they occur due to capacitive- and inductive behavior of installed power components (e.g. power transformers and submarine cables) in combination with the impedance of the grid.

The goal of studying the frequency response of an OWPP, for the purpose of this Ph.D. thesis, is to aid the understanding of how harmonics injected by the GSC of each wind turbine propagates along the OWPP. In this sense, it is important to study two aspects. The first one is to know the magnitude and phase that see each voltage- and/or current-harmonic at a specific node or point of the OWPP. The second aspect is to know how harmonics of the same order and injected by the GSCs are added, in phase or not.

These two points provide insight into the level of distortion that voltages and currents at different points of the OWPP have and that can endanger the fulfillment of the grid codes in terms of harmonics. Inherently, these aspects also provide insight into what corrective measures can be taken in order to solve certain harmonic problems. Examples of these corrective measures are the installation of passive filters, active damping solutions (which consist on the implementation of additional control blocks in the GSCs that are tuned to attenuate specific harmonics), the implementation of a particular modulation strategy, and the appropriate tuning of controllers (current-loops, DC-link voltage-loop, measurement filters, PLL, etc.).

This chapter presents the frequency response of an OWPP, which is carried out by means of the sequence network model of the OWPP base scenario. This chapter is structured as follows. Section 8.2 presents the analysis of the frequency response of the OWPP base scenario. This task is achieved by means of studying the Bode plots of transfer functions relating voltage- and current variables of different points along the OWPP. Section 8.3 addresses a discussion about the risk of amplification of harmonics injected by wind turbines. This is performed by analyzing the spectrums of the modulation strategies considered in this Ph.D. thesis, CB-PWM and SHE-PWM. Section 8.4 addresses the validation of the sequence network model. The validation is performed by means of a comparison of the results obtained with the Simulink®-based model and the sequence network model. Section 8.5 presents the changes in Bode plots when varying the electrical parameters of the main power components of the OWPP. Section 8.6 carries out two additional studies. First, changes in the frequency response are evaluated when considering the OWPP with disconnected wind turbines. Second, changes in Bode plots are evaluated when considering an OWPP with distances among WTs quite different. Finally, section 8.7 gives the chapter summary.

8.2 Analysis of the Frequency Response of the OWPP Base Scenario

As a starting point, one of the already known aspects is the emission of the voltage harmonics of the grid side converters that are installed in the wind turbines. The spectrums of the modulation strategies considered in this Ph.D. thesis are presented in chapter 3 (subsection 3.5.2). Furthermore, this information can be taken if considering the voltage signals of the GSCs for a specific operation point, such as the one presented in Fig. 7.17 for case study 7.2. It is important not to lose sight that the emission of each GSC changes depending on the operation point of the wind turbine.

According to this information and the way the sequence network model is developed, transfer functions having the voltage of the grid side converter as input are studied in order to aid the understanding of two main aspects. The first one is to know the magnitude and phase that see each voltage harmonic. The second aspect is to know how voltage harmonics of the same order and injected by the wind turbines are added, in phase or not. These two points provide insight about the level of distortion that output variables, voltages and currents at different points of the OWPP, have. Inherently, these aspects also provide insight into what measures can be taken in order to solve certain harmonic problems. For example, the implementation of a particular modulation strategy, as the one considered in case study 7.2, or by means of passive solutions (harmonic filters).

To initiate the studies of this section, attention is paid first, to transfer functions relating the output variables $V_{ab\_PCC}^{+}(s)$ and $I_{a\_PCC}^{+}(s)$, to the input variable $V_{ab\_GSC1}^{+}(s)$. The idea is to gain insight of how the harmonics injected by the GSCs are seen at the PCC point. The results and analyses of other transfer functions of the OWPP base scenario are presented later in this section. It is important to remember that although the notation of the transfer functions refers to the positive-sequence, positive- and negative-sequence are equal due to the assumption considered in section 7.4. Therefore, the presented Bode plots are also valid for the negative-sequence.

Fig. 8.1 and Fig. 8.2 show the Bode plots of transfer functions $V_{ab\_PCC}^{+}(s)\big/V_{ab\_GSC1}^{+}(s)$ and $I_{a\_PCC}^{+}(s)\big/V_{ab\_GSC1}^{+}(s)$, respectively. The magnitude and phase are shown at different frequency values up to a frequency of 5 kHz.

As depicted in these figures, four series resonances can be identified from these transfer functions. Before performing an analysis of how the harmonics emitted by the GSCs are amplified and added by the electrical infrastructure of the OWPP, it is important to identify which components create these resonances. It is worth to mention that several series resonances are created at higher frequencies. These resonances are not shown here because they are out of the frequency range of interest and because they are lower in magnitude than the first four resonances that are studied in this Ph.D. dissertation. In this sense, they can be neglected and attention is paid to the first four resonances.

If it is required to extend the studies for higher frequencies, as pointed out in previous chapters, the harmonics of the GSCs has to be extended together with the frequency-dependent representation of the transformer and submarine cable model. For these aspects, the reader is suggested to review the information presented in chapter 3, chapter 5 and chapter 6.

Fig. 8.1. Bode plot of transfer function $V_{ab\_PCC}^+(s)\big/V_{ab\_GSC1}^+(s)$ of the OWPP base scenario.
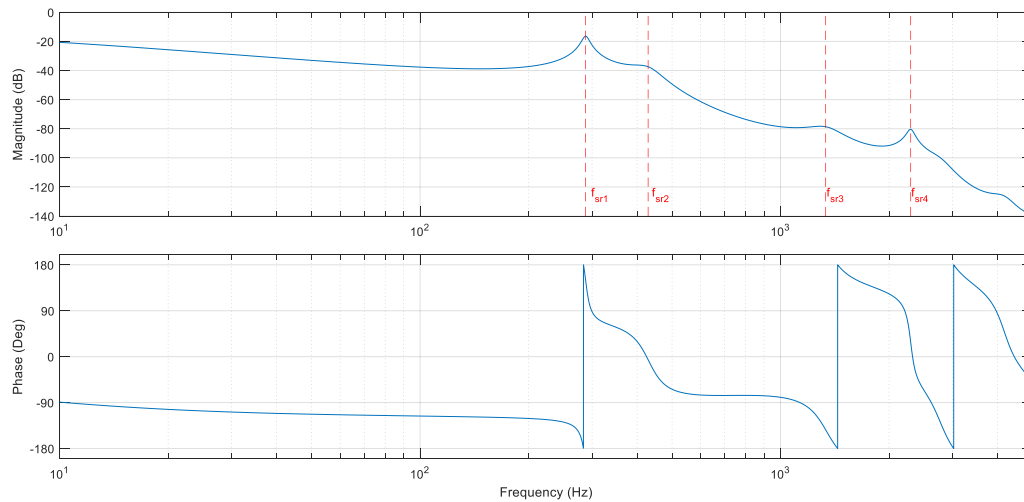
Fig. 8.2. Bode plot of transfer function $I_{a\_PCC}^+(s)\big/V_{ab\_GSC1}^+(s)$ of the OWPP base scenario.

As pointed out, it is important to identify which power components and electrical parameters create the resonances depicted in previous figures. Due to the complexity of the OWPP, i.e. the high number of power components and the high number of elements required to model each power component, the identification process is achieved by means of modal analysis technique. The idea is to identify the eigenvalues, or system poles, that correspond to the first four resonance peaks. This is accomplished by computing the participation factors of the system's matrix $\left[A_{OWPP}^{++} \right]$. An overview of modal analysis is addressed in Appendix D.

The participation factors of each eigenvalue are computed and they are sorted in descendent order. Then, the most important state variables that affect the given modes are presented, the ones with a cumulative weight of 90%. The following figures, Fig. 8.3 to Fig. 8.6, show the participation factors of the eigenvalues that correspond to the resonances depicted in previous figures.
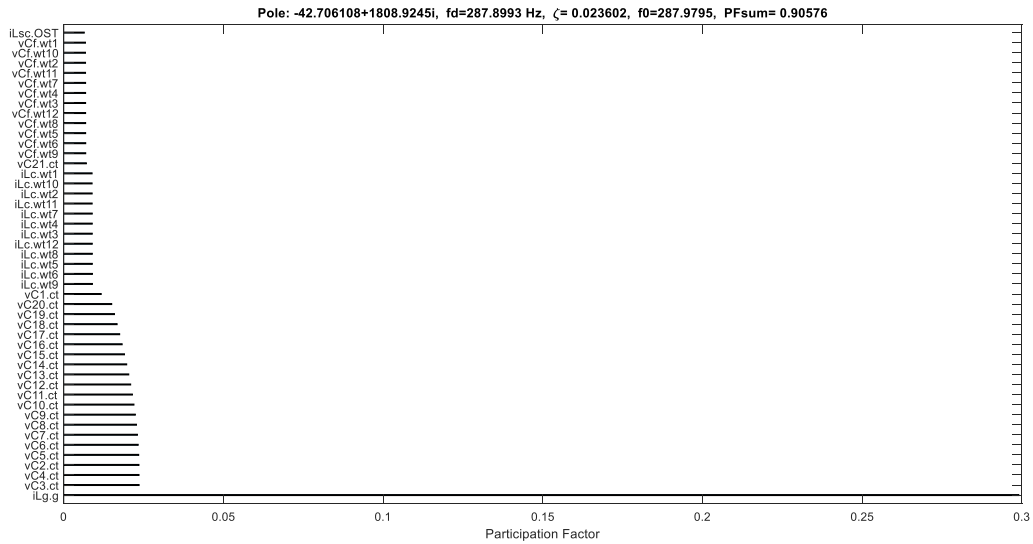
Fig. 8.3. Participation factors of the eigenvalue corresponding to the first series resonance f_{sr1}.
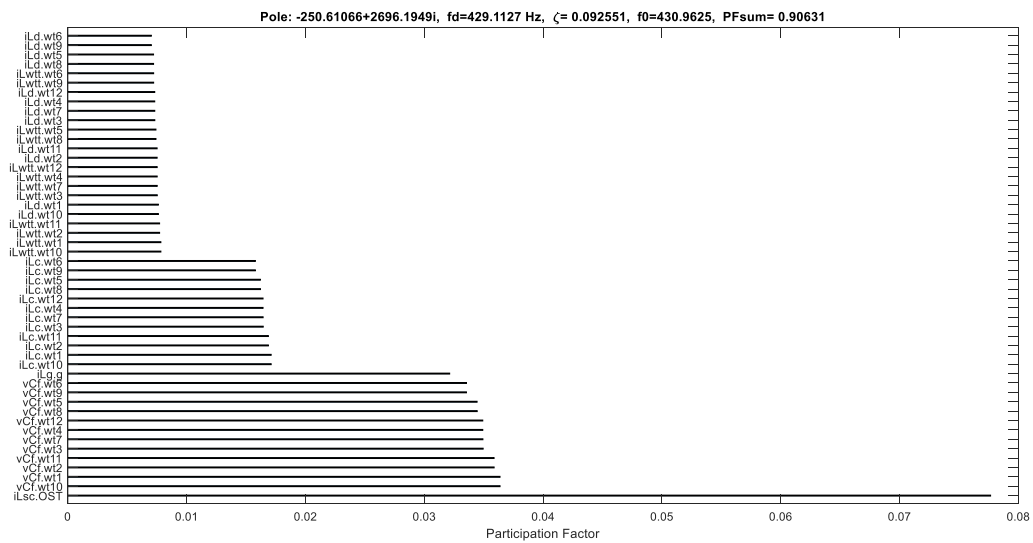
Fig. 8.4. Participation factors of the eigenvalue corresponding to the second series resonance f_{sr2}.

Table 8.1 gives the dominant state variables and power components that create the first four series resonances of the OWPP base scenario. The damped frequency and the damping factor of the eigenvalue of each series resonance are presented too.
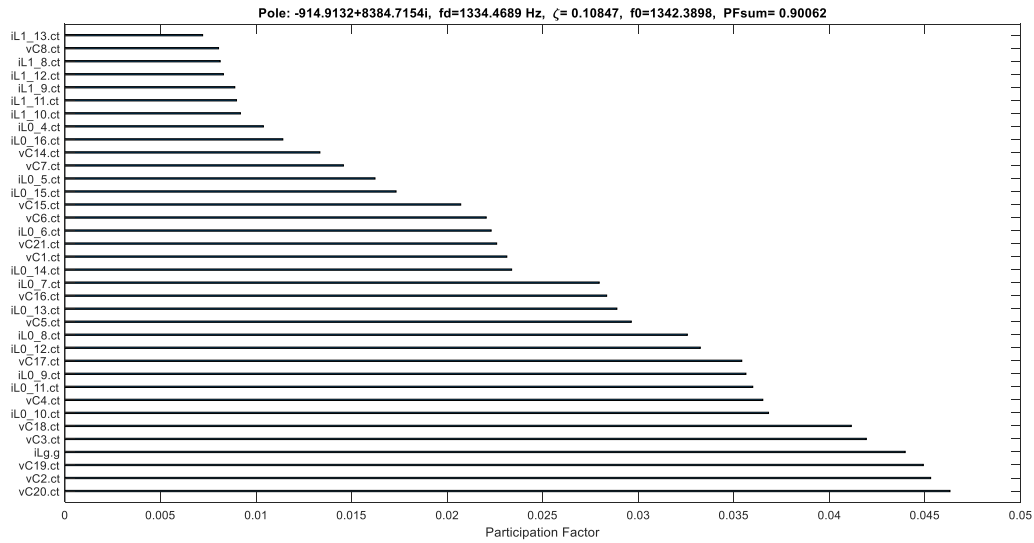
Fig. 8.5. Participation factors of the eigenvalue corresponding to the third series resonance f_{sr3}.
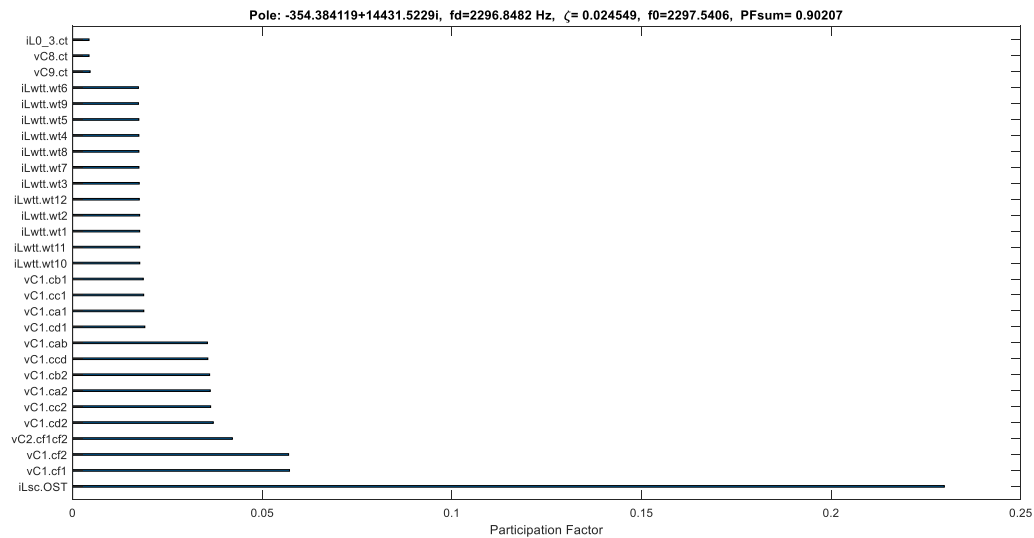
Fig. 8.6. Participation factors of the eigenvalue corresponding to the fourth series resonance f_{sr4}.

Table 8.1. Dominant state variables and power components that create the first four series resonances of the OWPP base scenario.

Series Resonance	Frequency	Damping Factor	Dominant State Variable (Component)
f_{sr1}	287.8993 Hz	0.0236	vC.tc (Transmission cable) iLg (Grid)
f_{sr2}	429.1127 Hz	0.0925	vCf.wti (GSC connection filter) iLc.wti (GSC connection filter) iLwtt.wti (WTT) iLost (OST) iLg (Grid)
f_{sr3}	1334.4689 Hz	0.1084	vC.tc (Transmission cable) iL.tc (Transmission cable) iLg (Grid)
f_{sr4}	2296.8482 Hz	0.0245	vC.cc (Transmission cable) iLost (OST) iLwtt.wti (WTTs)

The previous table reveals important information. The first series resonance f_{sr1} is mainly created by the capacitance of the transmission cable and the equivalent inductance of the grid, which depends on the SCR value. For an OWPP with similar characteristics to the transmission system and the SCR value of the base scenario, the presence of a series resonance around low-frequency values (e.g. few hundreds of Hertz) is inevitable and the WTs will have to deal with this condition.

The second series resonance f_{sr2} is greatly created by the GSC connection filter. Fig. 8.3 also shows that the GSC connection filter affects somehow the first series resonance. In this sense, the GSC connection filter can be also designed considering the effect of this component on the first series resonance.

The resonance f_{sr3} is mainly created by the transmission cable, its second series resonance. Finally, the fourth series resonance f_{sr4} is created by the combination of the capacitance of the submarine cables of the collection network and the inductances of the offshore substation transformer and wind turbine transformers.

Fig. 8.1 and Fig. 8.2 have shown the Bode plots relating the voltage and current signals at the PCC point with respect to the GSC1 point. Now, attention is paid on Bode plots relating the same output variables with remaining GSCs. The aim is to know the differences among Bode plots, in terms of magnitude and phase, due to the location of WTs. When referring to the location of WTs, it means how remote or how close each WT is with respect to the PCC point of the OWPP.

Fig. 8.7 and Fig. 8.8 show the Bode plots of transfer functions $V_{ab\_PCC}^{+}(s)/V_{ab\_GSCi}^{+}(s)$ and $I_{a\_PCC}^{+}(s)/V_{ab\_GSCi}^{+}(s)$, respectively. As shown in these figures, the Bode plots of these transfer functions do not present significative changes; in essence, they are equal for the frequency range of study. For higher frequencies, differences in magnitude and phase can be noticeable as presented in subsection 8.6.2.

An important aspect that can be seen from these two figures is that the electrical infrastructure of the OWPP does not cause a different phase shift (for frequencies up to 5 kHz) among the harmonics injected by the GSCs. In this sense, if the GSCs work at the same operation point, the magnitude of harmonics of the same order will be increased at the PCC point because these harmonics are added in phase. Additional increase of the magnitude of a harmonic can be obtained if a resonance is near a specific harmonic, e.g. the injection of a 5th harmonic voltage coming from the GSCs and the resonance f_{sr1} shown in Fig. 8.7 and Fig. 8.8.

As pointed out, the previous transfer functions do not change significantly depending on which GSCi point the transfer function is seen. This occurs mainly because the OWPP base scenario is symmetrical. Results will be different if considering a different number of wind turbines connected to each radial and different radial cable lengths (feeders and cables that

connect each wind turbine) for this base scenario. These aspects are further addressed in section 8.6.
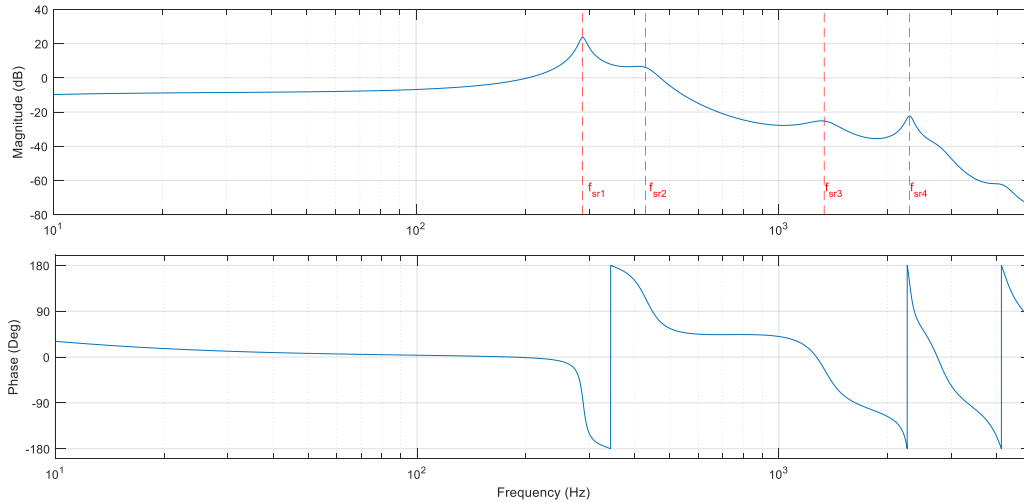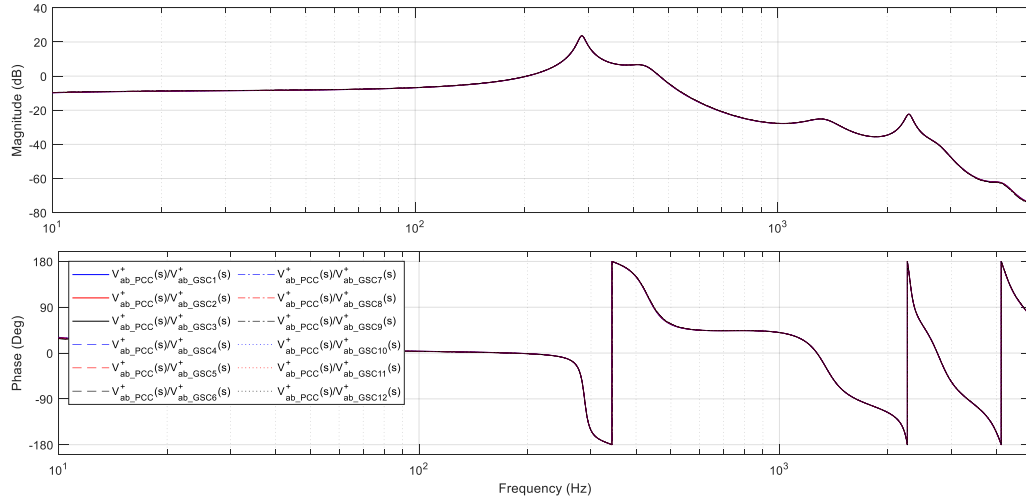

Fig. 8.7. Bode plot of transfer function $V^+_{ab\_PCC}(s)\big/V^+_{ab\_GSCi}(s)$ of the OWPP base scenario.
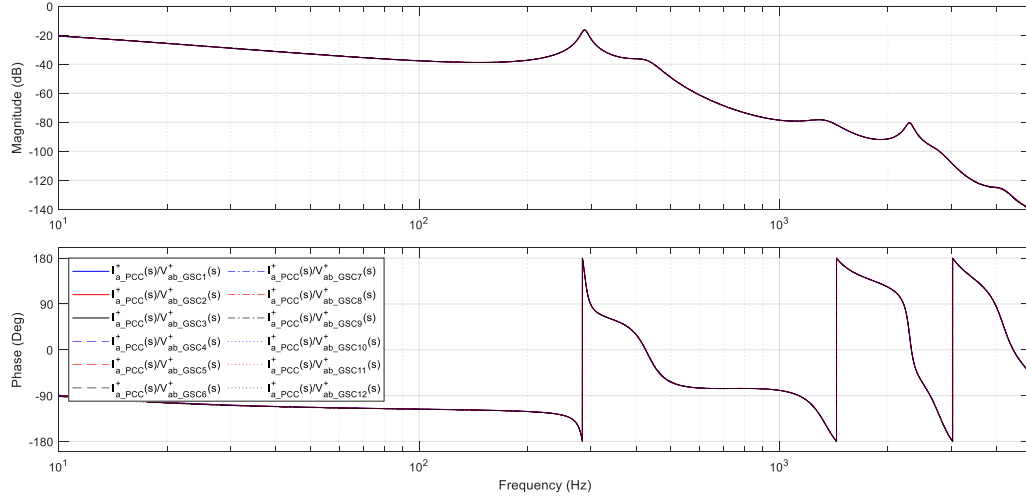
Fig. 8.8. Bode plot of transfer function $I^+_{a\_PCC}(s)\big/V^+_{ab\_GSCi}(s)$ of the OWPP base scenario.

It is also worth to mention that for large OWPPs, the differences in magnitude and phase of the Bode plots are very noticeable as presented in reference [5]. Several factors contribute on these differences, such as a higher number of wind turbines, longer cable lengths, greater differences in distance among WTs to a particular point of the OWPP, the presence of asymmetries in the layout of the OWPP, and other aspects.

Up to now, attention has been paid on how harmonics injected by the GSCs affect the voltage and current signals at the PCC point of the OWPP. Now, the aim is to depict the transfer functions that show how harmonics injected by the GSCs affect the voltage- and current signals of other points of the OWPP.

Fig. 8.9 shows the Bode plots of transfer functions $V^+_{ab\_WT1}(s)\big/V^+_{ab\_GSC1}(s)$, $V^+_{ab\_CP}(s)\big/V^+_{ab\_GSC1}(s)$, and $V^+_{ab\_PCC}(s)\big/V^+_{ab\_GSC1}(s)$. The Bode plots of these transfer

functions present this behavior mainly because of two factors. The first one is because the voltage conversion of transformers. The second one is because the voltage drop for points that are farther away from the source of harmonics.
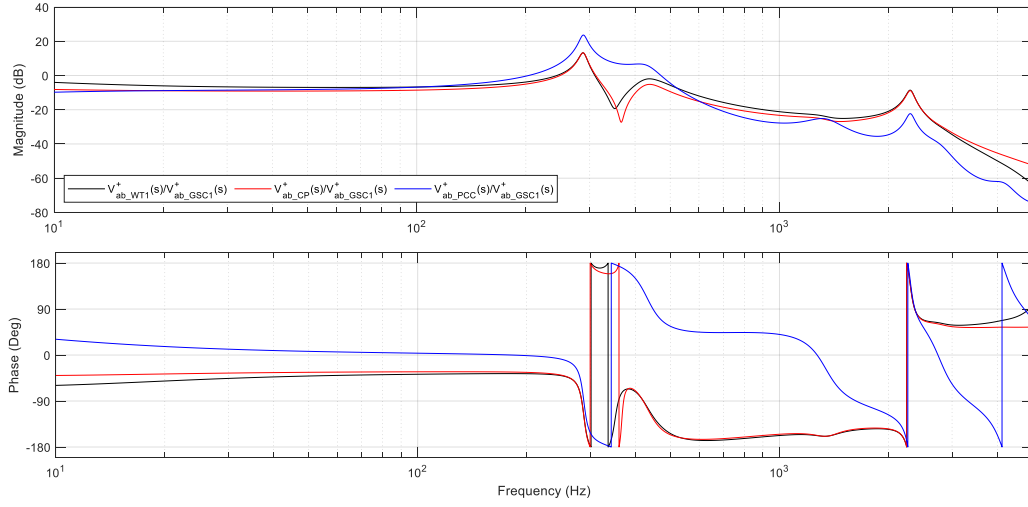
Fig. 8.9. Bode plots of transfer functions: $V^+_{ab\_WT1}(s)\big/V^+_{ab\_GSC1}(s)$, $V^+_{ab\_CP}(s)\big/V^+_{ab\_GSC1}(s)$, and $V^+_{ab\_PCC}(s)\big/V^+_{ab\_GSC1}(s)$ of the OWPP base scenario.

Fig. 8.10 shows the Bode plots of transfer functions $I^+_{a\_WT1}(s)\big/V^+_{ab\_GSC1}(s)$, $I^+_{a\_CP}(s)\big/V^+_{ab\_GSC1}(s)$, and $I^+_{a\_PCC}(s)\big/V^+_{ab\_GSC1}(s)$. It is important to state that for some transfer functions, the aforementioned resonances are barely seen. The reason is mainly that a zero-term cancels or compensates the pole of a resonance. This is a zero-term that is located exactly or near the pole that creates the resonance. For example, this can be seen when comparing Bode plots of transfer functions $I^+_{a\_WT1}(s)\big/V^+_{ab\_GSC1}(s)$ and $I^+_{a\_PCC}(s)\big/V^+_{ab\_GSC1}(s)$ for the first series resonance f_{sr1}.
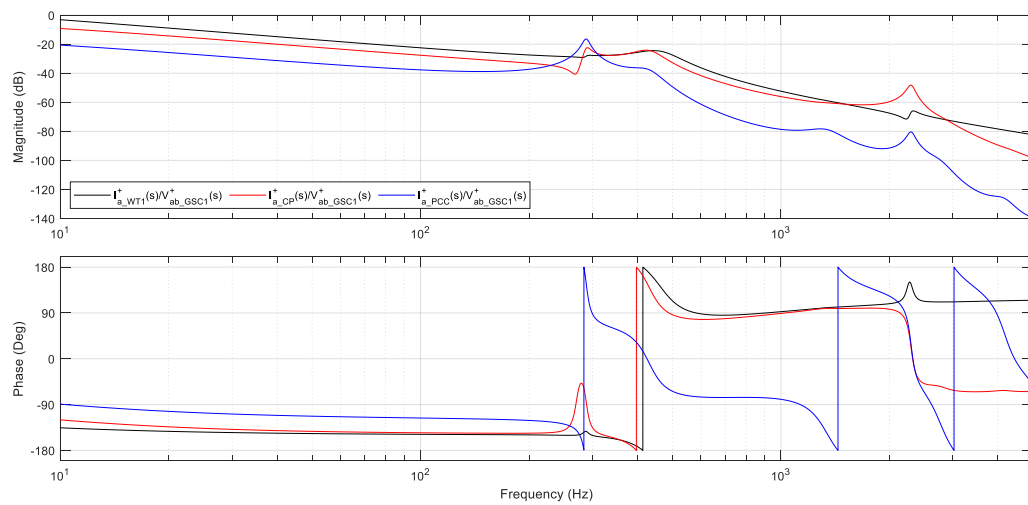
Fig. 8.10. Bode plots of transfer functions $I^+_{a\_WT1}(s)\big/V^+_{ab\_GSC1}(s)$, $I^+_{a\_CP}(s)\big/V^+_{ab\_GSC1}(s)$, and $I^+_{a\_PCC}(s)\big/V^+_{ab\_GSC1}(s)$ of the OWPP base scenario.

173

Up to now, the power grid equivalent has been considered as an ideal voltage source, generating only the fundamental component, with a short-circuit inductance in series. As already mentioned in subsection 7.4.2, there are some scenarios where harmonics, different from the fundamental component, are injected by the grid. In this sense, it is important to study the Bode plots of transfer functions at different points along the OWPP and having the grid voltage as input. In that way, it is possible to deduce how harmonics coming from the grid are seen at each point and if these harmonics may be a potential problem in terms of grid code compliance and stability of the entire OWPP.

Fig. 8.11 depicts the Bode plots of transfer functions $V_{ab\_WT1}^+(s)\big/V_{ab\_g}^+(s)$, $V_{ab\_CP}^+(s)\big/V_{ab\_g}^+(s)$ and $V_{ab\_PCC}^+(s)\big/V_{ab\_g}^+(s)$. On the other hand, Fig. 8.12 shows the Bode plots of transfer functions $I_{a\_WT1}^+(s)\big/V_{ab\_g}^+(s)$, $I_{a\_CP}^+(s)\big/V_{ab\_g}^+(s)$ and $I_{a\_PCC}^+(s)\big/V_{ab\_g}^+(s)$.
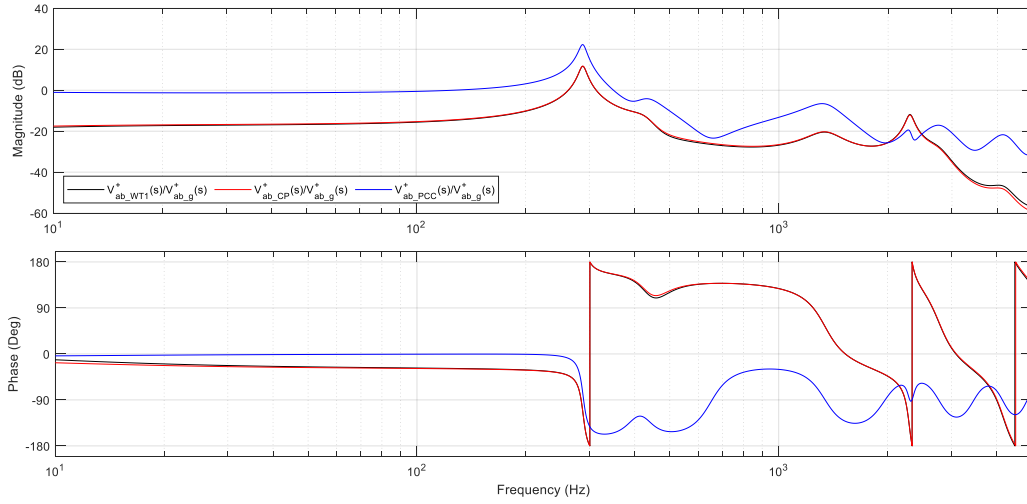
Fig. 8.11. Bode plots of transfer functions: $V_{ab\_WT1}^+(s)\big/V_{ab\_g}^+(s)$, $V_{ab\_CP}^+(s)\big/V_{ab\_g}^+(s)$, and $V_{ab\_PCC}^+(s)\big/V_{ab\_g}^+(s)$ of the OWPP base scenario.
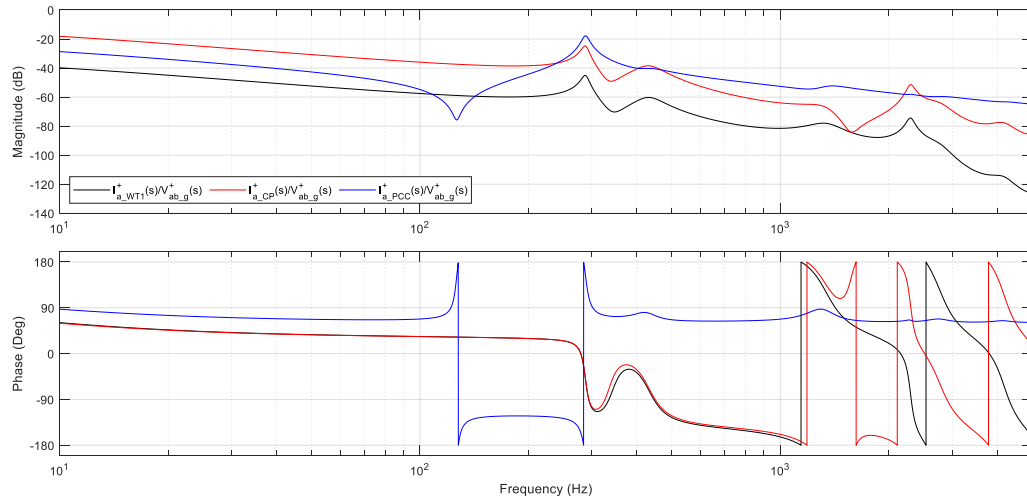
Fig. 8.12. Bode plots of transfer functions $I_{a\_WT1}^+(s)\big/V_{ab\_g}^+(s)$, $I_{a\_CP}^+(s)\big/V_{ab\_g}^+(s)$, and $I_{a\_PCC}^+(s)\big/V_{ab\_g}^+(s)$ of the OWPP base scenario.

8.3 Risk of Amplification of Harmonics injected by WTs

Once the previous aspects have been analyzed, it is important to address a discussion about the risk of amplification of the harmonics injected by wind turbines. This is performed by means of analyzing the spectrums of the modulation strategies considered in this Ph.D. thesis, CB-PWM and SHE-PWM. For simplicity, the risk of harmonic amplification is addressed at the PCC point by studying the transfer functions $V_{ab\_PCC}^+(s)/V_{ab\_GSCi}^+(s)$ and $I_{a\_PCC}^+(s)/V_{ab\_GSCi}^+(s)$. The same analysis can be applied to other transfer functions.

8.3.1 Analysis for WTs operating with CB-PWM modulation

First, the risk of harmonic amplification is addressed for CB-PWM modulation. Fig. 8.13(a) shows the CB-PWM spectrum of the voltage signal $v_{ab\_GSCi}(t)$ in a 2D-plane for different m_a values. As pointed out in chapter 3, the m_f value is equal to 23. Since this value is not a multiple of three, each odd harmonic has positive-, negative-, and zero-sequences and that is the reason why harmonics multiple of three appear in this spectrum. Even though zero-sequence voltage harmonics are also generated, zero-sequence current harmonics do not circulate to the PCC point since there is not a path to let this current flow due to transformer windings connection.

On the other hand, Fig. 8.13(b) depicts the Bode plots of transfer functions $V_{ab\_PCC}^+(s)/V_{ab\_GSC1}^+(s)$ and $I_{a\_PCC}^+(s)/V_{ab\_GSC1}^+(s)$. For these Bode plots, only positive- and negative-sequence harmonics of the signal $v_{ab\_GSCi}(t)$ are considered since these transfer functions are only valid for these sequences. Furthermore, Fig. 8.13(b) highlights the first four series resonances with a red dashed line and the value taken for each harmonic with a black cross marker.

For this modulation strategy, it can be seen that harmonics of order 5th and 7th are heavily affected despite the fact that their magnitudes are very low and that resonance f_{sr1} does not match perfectly with them. These harmonics are amplified for the transfer function $V_{ab\_PCC}^+(s)/V_{ab\_GSC1}^+(s)$. For the case of the transfer function $I_{a\_PCC}^+(s)/V_{ab\_GSC1}^+(s)$, these harmonics are attenuated at the PCC point; however, the attenuation of the system around these frequencies is relatively low. Something similar to the previous situation occurs for the 9th harmonic, which is very close to resonance f_{sr2}.

As pointed out in this chapter, if the GSCs work at the same operation point, the harmonics of the same order are added because they are in phase. Hence, their magnitude is increased by this characteristic at the PCC point. Consequently, these conditions affect the distortion of voltage- and current signals at the PCC point, which might endanger the compliance of the grid codes. In this sense, the aforementioned harmonics might be considered as a problem in terms of level of distortion and compliance of the grid codes.

For harmonics of order 25th and 27th, it can be seen that even their magnitudes are higher than harmonics of low order, the attenuation around f_{sr3} is considerably higher than the previous case. Therefore, it seems that these harmonics might not be a problem.

Finally, the situation changes for harmonics of order 45th and 47th. The magnitude of these harmonics can be much higher when comparing to previous harmonics. Furthermore, the attenuation level around resonance f_{sr4} is very similar to the attenuation level around resonance f_{sr3} for both transfer functions. In this sense, it seems that these harmonics might be considered as problematics for the aspects stated previously. In the next chapter, several scenarios are studied with this type of modulation to corroborate or reject the hypotheses stated so far.

(a)

(b)
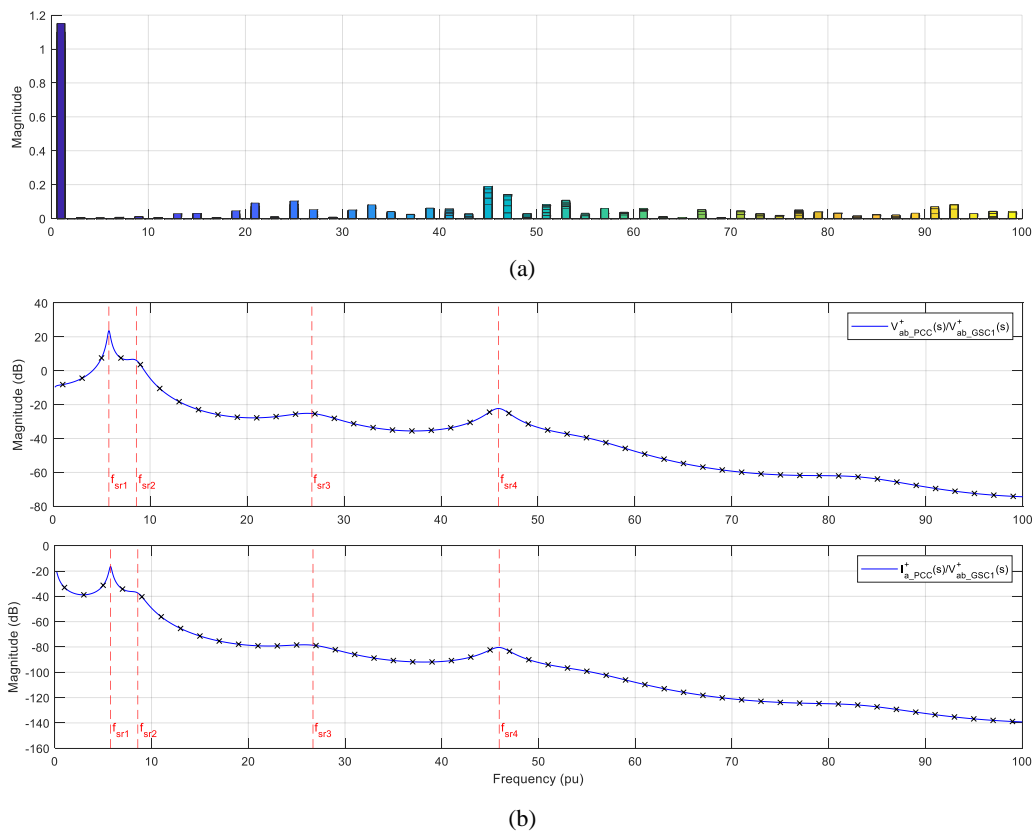
Fig. 8.13. Risk of amplification of harmonics for grid side converters using CB-PWM modulation. (a) CB-PWM spectrum with different m_a values stacked, m_a values ranging from 0.8 to approximately 1.16. (b) Bode plots of transfer functions $V_{ab\_PCC}^{+}(s)/V_{ab\_GSC1}^{+}(s)$ and $I_{a\_PCC}^{+}(s)/V_{ab\_GSC1}^{+}(s)$.

8.3.2 Analysis for WTs operating with SHE-PWM modulation

Now, the same analysis is performed to SHE-PWM modulation. Fig. 8.14(a) shows the SHE-PWM spectrum of the voltage signal $v_{ab\_GSCi}(t)$ in a 2D-plane for different m_a values.

For this type of modulation, each odd harmonic has only one sequence. Positive- and negative-sequence voltage harmonics are shown in Fig. 8.14(a). Zero-sequence voltage harmonics do not appear in this figure, it is the line-to-line voltage spectrum.

On the other hand, Fig. 8.14(b) depicts the Bode plots of transfer functions $V_{ab\_PCC}^{+}(s)\big/V_{ab\_GSC1}^{+}(s)$ and $I_{a\_PCC}^{+}(s)\big/V_{ab\_GSC1}^{+}(s)$. As pointed out, these Bode plots are only valid for the positive- and negative-sequence.

(a)

(b)
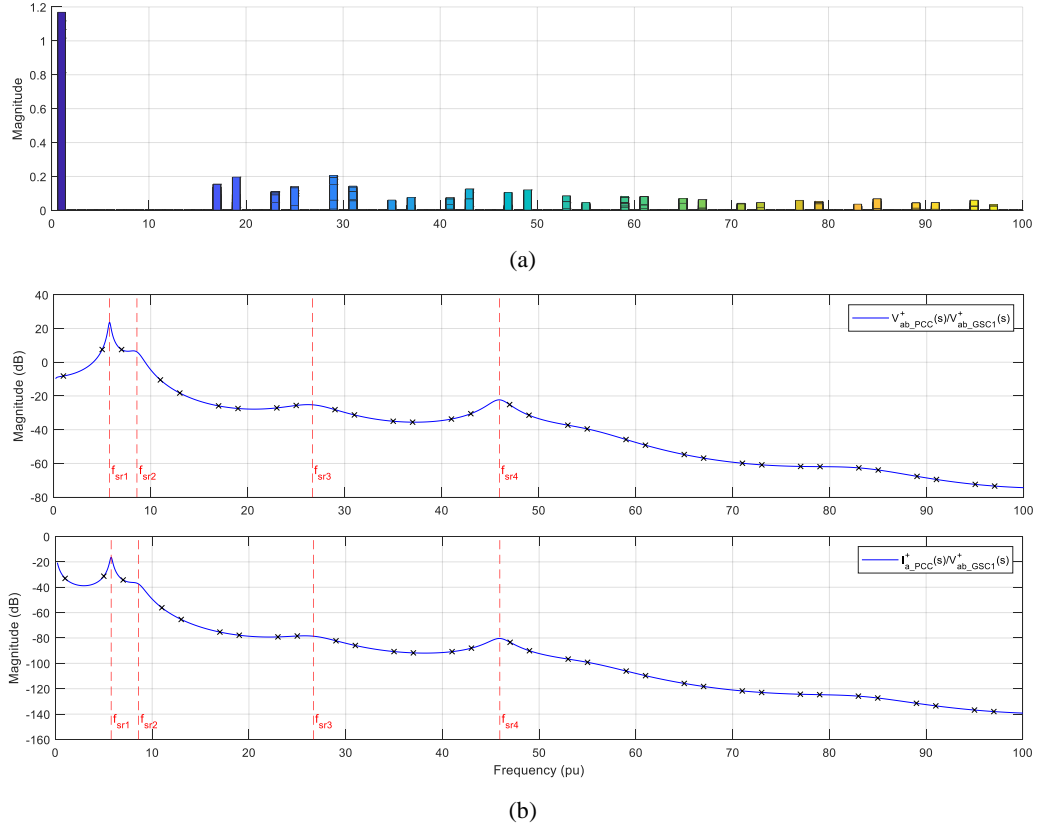
Fig. 8.14. Risk of amplification of harmonics for grid side converters using SHE-PWM modulation. (a) SHE-PWM spectrum with different m_a values stacked, m_a values ranging from 0.8 to approximately 1.16. (b) Bode plots of transfer functions $V_{ab\_PCC}^{+}(s)\big/V_{ab\_GSC1}^{+}(s)$ and $I_{a\_PCC}^{+}(s)\big/V_{ab\_GSC1}^{+}(s)$.

For this modulation strategy, the first two resonances, i.e. f_{sr1} and f_{sr2}, do not represent a problem from a steady-state perspective since low order harmonics are not injected. Harmonics of order 5th, 7th, 11th, and 13th have a null or almost null magnitude as seen in Fig. 8.14(a).

The magnitudes of harmonics of order 17th, 19th, 23rd, 25th, 29th, and 31st are higher when compared with the magnitude of the same harmonic order for the case of CB-PWM. The attenuation level around these harmonics is almost the same. In this sense, some of them might be considered as problematic or be reaching the harmonic limits imposed by the grid codes. In the next chapter, several scenarios are studied with this type of modulation to corroborate or reject the hypotheses stated so far.

8.4   Validation of the Sequence Network based Model

The aim of this section is to validate the sequence network model and the Bode plots presented so far. The validation is performed by means of a comparison of the results obtained with the Simulink®-based model and the sequence network model. The comparison is performed in the frequency-domain for the voltage- and current signals at the PCC point. The results of case study 7.2 (Fig. 7.18 and Fig. 7.19) are taken for this validation.

Fig. 8.15 shows the comparison of the spectrum of the voltage signal $v_{ab\_PCC}(t)$ obtained for both models. Fig. 8.15(a) depicts the magnitude comparison while Fig. 8.15(b) shows the phase comparison. Additionally, the error is presented for both variables considering the exact value the one of the Simulink®-based model.

(a)

(b)
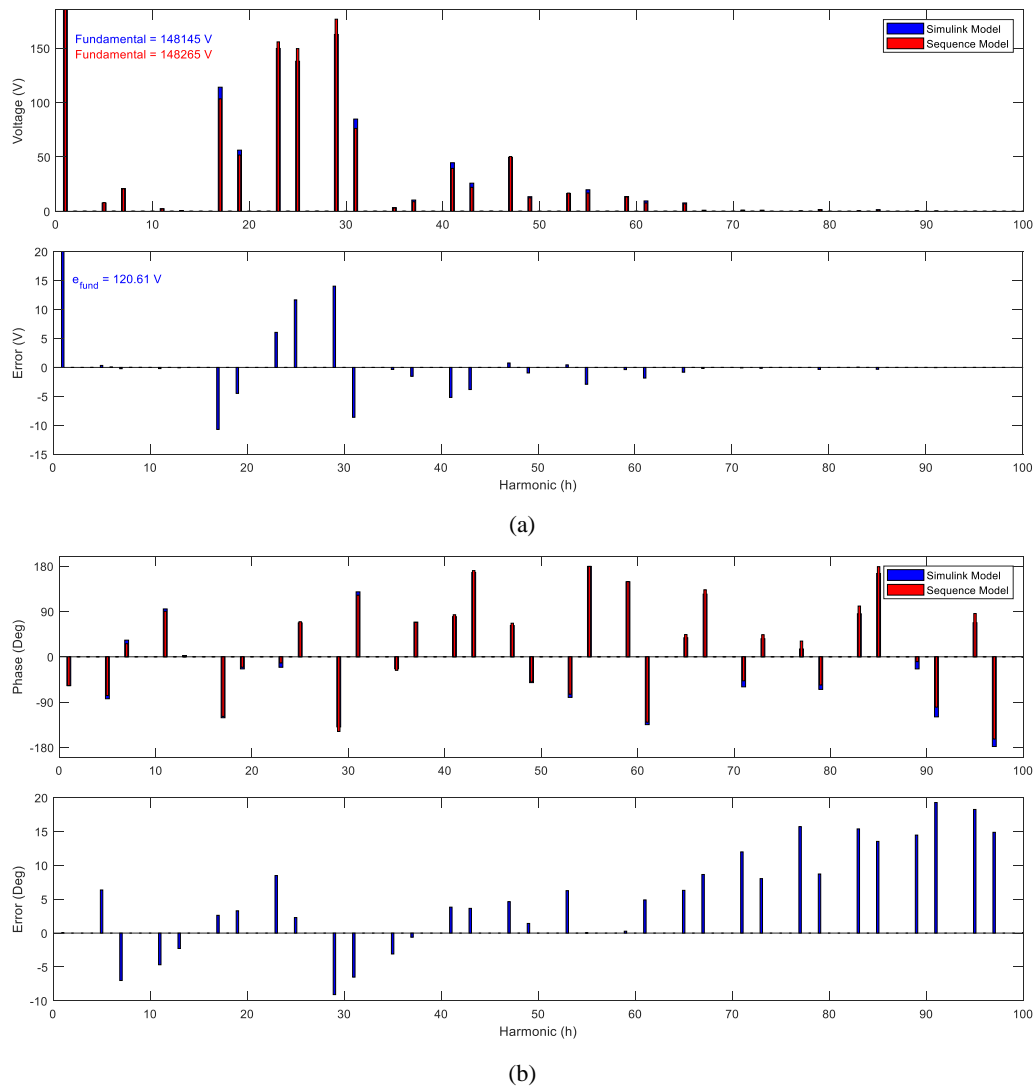
Fig. 8.15. Comparison of the spectrum of voltage signal $v_{ab\_PCC}(t)$ for case study 7.2 with both models, Simulink®-based model and the sequence network model. (a) Magnitude. (b) Phase.

As noticed in this figure, the results obtained with the sequence network model are very similar to the ones obtained with the Simulink® model. Focusing on the magnitude errors for this variable, the error of the fundamental component is 120.61 V, which represents an error of 0.08%. The error of the 17th harmonic is -10.7 V, which represents an error of -9.36%. The error of the 29th harmonic is 14.02 V, which represents an error of 8.61%.

On the other hand, it can be seen that the phase errors are very low for harmonics below the 70th one. The phase error is increased for high-frequency harmonics. This happens mainly because of two factors. The first one is due to the simplifications made for the sequence network model, which are presented in section 7.4, and the fitting process. The second factor is that the phase is the most sensitive variable, especially in the presence of a resonance.

Fig. 8.16 shows the comparison of the spectrum of the current signal $i_{a\_PCC}(t)$ obtained for both models.

(a)

(b)
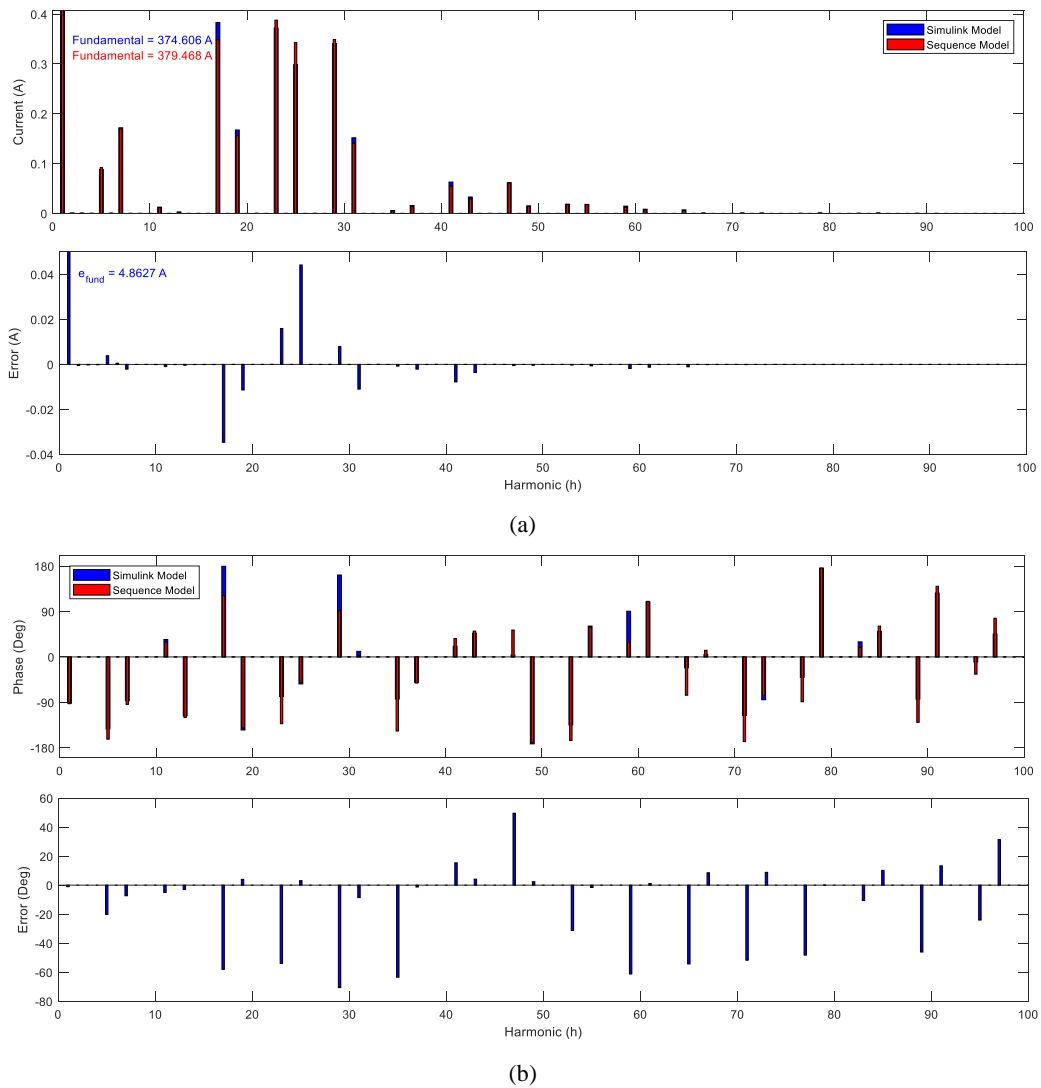
Fig. 8.16. Comparison of the spectrum of current signal $i_{a\_PCC}(t)$ for case study 7.2 with both models, Simulink®-based model and the sequence network model. (a) Magnitude. (b) Phase.

Similar to the previous variable, the results obtained with the sequence network model are similar to the ones obtained with the Simulink® model. The errors are higher when compared with the previous variable. Additionally, phase errors are higher than magnitude errors. The reasons of having these errors are the same of the previous case.

The validations of voltage- and current signals have been performed for other points of the OWPP. For simplicity and due to space constraints, the results are not shown in this document. Finally, it can be stated that Bode plots of transfer functions evaluated so far are valid. In this sense, the sequence network model presented in section 7.4 fulfills the purpose of being used as an analytical tool for the studies presented in this chapter.

8.5 Parameter Sensitivity Studies

This section presents the changes in Bode plots when varying the electrical parameters of the main power components of the OWPP. Additionally, the frequency- and damping factor variation of the main series resonances are shown for each case. The variation is computed with respect to the frequency- and damping factor values of series resonances given in Table 8.1.

Even though the parameter sensitivity studies are shown for the positive-sequence, they are also valid for the negative-sequence. For simplicity, only the variation of the parameters of the GSC connection filter, transmission cable, and power grid are shown. It is worth to mention that the changes depicted in the next subsections are in agreement with the information given by the participation factors, Table 8.1.

8.5.1   Variation of the parameters of the GSC connection filter

The variation of the parameters values of the GSC connection filter, given in Table 7.20 for the OWPP base scenario, are presented in this subsection. Changes of $\pm 20\%$ are done to each parameter.

- Variation of L_c^{++} value

Fig. 8.17 depicts the changes in Bode plots due to a variation in L_c^{++} value. Additionally, Fig. 8.18 shows the values of frequency- and damping factor variation due to changes in the same variable.

The effect of varying the value of inductance L_c^{++} on the first four series resonances, f_{sr1} to f_{sr4}, is shown in previous figures. The following conclusions can be stated.

Regarding the frequency variation, series resonance f_{sr1} decreases while increasing the inductance value. The maximum variation is lower than 10 Hz for the evaluated cases.

(a)   (b)
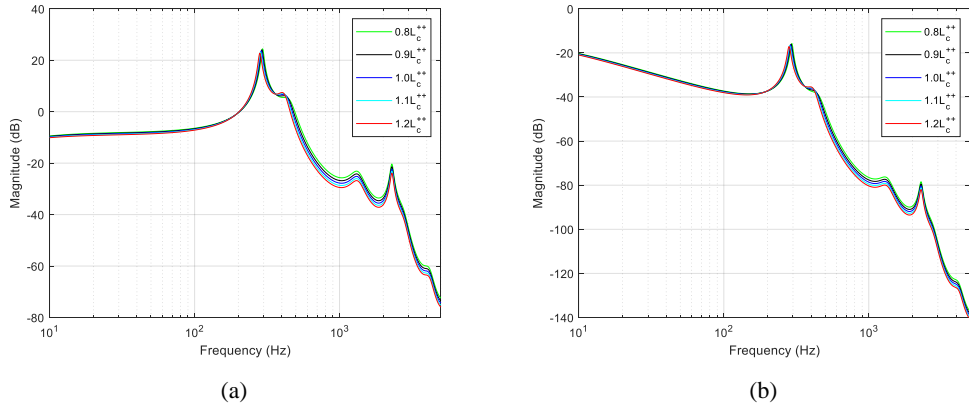
Fig. 8.17. Changes in Bode plots due to a variation in L_c^{++} value. (a) Bode plot of transfer function $V_{ab\_PCC}^{+}(s)\big/V_{ab\_GSC1}^{+}(s)$. (b) Bode plot of transfer function $I_{a\_PCC}^{+}(s)\big/V_{ab\_GSC1}^{+}(s)$.

(a)   (b)
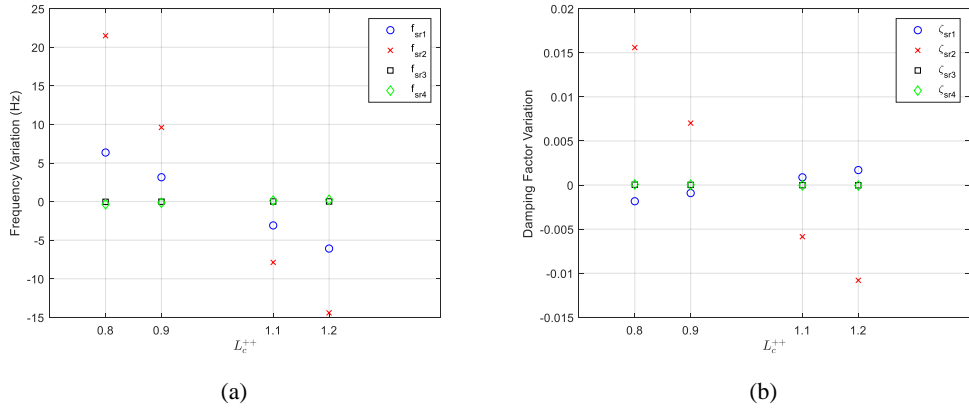
Fig. 8.18. Frequency- and damping factor variation of main series resonances due to a change in L_c^{++} value. (a) Frequency variation. (b) Damping factor variation.

On the other hand, series resonance f_{sr2} is the one that exhibits the highest change as inferred from the participation factors, a maximum variation of approximately 20 Hz for the evaluated cases. This series resonance decreases while increasing the inductance L_c^{++}. Finally, the frequency values of remaining resonances barely change, as shown in Fig. 8.18(a).

Regarding the damping factor variation, the damping factor of resonance f_{sr1} increases while increasing inductance L_c^{++}. The maximum variation is lower than 0.002 for the evaluated cases. On the contrary, the damping factor variation of f_{sr2} is the highest, having a maximum variation of approximately 0.016. Finally, the damping factors of remaining resonances barely change, as shown in Fig. 8.18(b).

- Variation of C_f^{++} value

Fig. 8.19 depicts the changes in Bode plots due to a variation in C_f^{++} value. Additionally, Fig. 8.20 shows the values of frequency- and damping factor variation due to changes in

the same variable. The effect of varying the value of capacitance C_f^{++} on the first four series resonances, f_{sr1} to f_{sr4}, is shown in these figures and briefly described next.

(a)   (b)
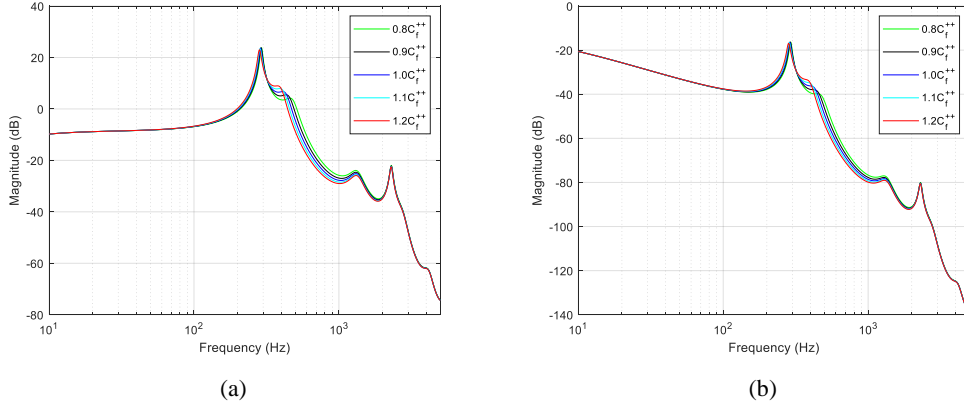
Fig. 8.19. Changes in Bode plots due to a variation in C_f^{++} value. (a) Bode plot of transfer function $V_{ab\_PCC}^+(s)/V_{ab\_GSC1}^+(s)$. (b) Bode plot of transfer function $I_{a\_PCC}^+(s)/V_{ab\_GSC1}^+(s)$.

(a)   (b)
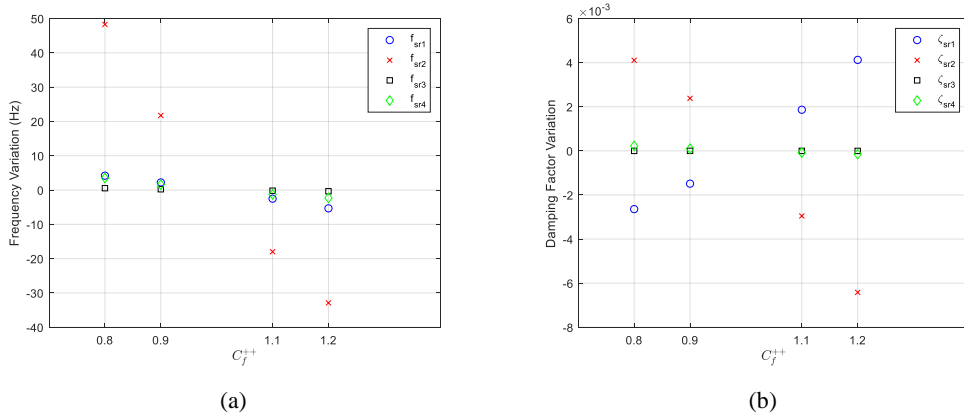
Fig. 8.20. Frequency- and damping factor variation of main series resonances due to a change in C_f^{++} value. (a) Frequency variation. (b) Damping factor variation.

Regarding the frequency variation, series resonance f_{sr2} is the one that exhibits the highest change, a maximum variation of approximately 50 Hz for the evaluated cases. This series resonance decreases while increasing the capacitance value. On the other hand, series resonance f_{sr1} and f_{sr4} present a decrease while increasing the capacitance value. The maximum variation, for both resonances, is approximately equal to ± 5 Hz for the evaluated cases. Finally, series resonance f_{sr3} barely changes, as shown in Fig. 8.20(a).

Regarding the damping factor variation, the damping factor of series resonance f_{sr1} increases while increasing the capacitance value C_f^{++}. The maximum variation is approximately equal to 0.004 for the evaluated cases.

For the case of resonance f_{sr2}, the damping factor variation is the highest, having a maximum variation of approximately -0.006. For this series resonance, the damping factor decreases while increasing the capacitance value.

Finally, the damping factors of remaining resonances barely change, as shown in Fig. 8.20(b).

- Variation of L_d^{++} value

Fig. 8.21 depicts the changes in Bode plots due to a variation in L_d^{++} value. Additionally, Fig. 8.22 shows the values of frequency- and damping factor variation due to changes in the same variable.

(a)   (b)

Fig. 8.21. Changes in Bode plots due to a variation in L_d^{++} value. (a) Bode plot of transfer function $V_{ab\_PCC}^{+}(s)\big/V_{ab\_GSC1}^{+}(s)$. (b) Bode plot of transfer function $I_{a\_PCC}^{+}(s)\big/V_{ab\_GSC1}^{+}(s)$.

(a)   (b)

Fig. 8.22. Frequency- and damping factor variation of main series resonances due to a change in L_d^{++} value. (a) Frequency variation. (b) Damping factor variation.

The effect of varying the value of inductance L_d^{++} on the first four series resonances, f_{sr1} to f_{sr4} , is shown in previous figures. The following conclusions can be stated.

Regarding the frequency variation, series resonance f_{sr2} decreases while increasing the inductance value. The decreasing change exhibits an exponential decay. The maximum

variation is approximately equal to 32 Hz for the evaluated cases. On the other hand, the frequency values of remaining resonances barely change, as shown in Fig. 8.22(a).

Regarding the damping factor variation, the damping factor of series resonance f_{sr2} exhibits an interesting behavior. It decreases for values between $0.8L_d^{++}$ and $0.9L_d^{++}$. On the contrary, it increases when increasing the inductance to values higher than $0.9L_d^{++}$. The maximum variation is approximately equal to 0.018 for the evaluated cases.

The damping factor variation of resonance f_{sr1} increases while increasing the inductance value. The maximum damping factor variation is lower than 0.002 for this resonance. Finally, the damping factors of remaining resonances barely change, see Fig. 8.22(b).

- Variation of R_d^{++} value

Fig. 8.23 depicts the changes in Bode plots due to a variation in the resistance value R_d^{++}. Additionally, Fig. 8.24 shows the values of frequency- and damping factor variation due to changes in the same variable. The following conclusions can be stated from these figures.

(a)   (b)

Fig. 8.23. Changes in Bode plots due to a variation in R_d^{++} value. (a) Bode plot of transfer function $V_{ab\_PCC}^+(s)\big/V_{ab\_GSC1}^+(s)$. (b) Bode plot of transfer function $I_{a\_PCC}^+(s)\big/V_{ab\_GSC1}^+(s)$.

(a)   (b)

Fig. 8.24. Frequency- and damping factor variation of main series resonances due to a change in R_d^{++} value. (a) Frequency variation. (b) Damping factor variation.

Regarding the frequency variation, the four series resonance barely change. For example, the highest change is lower than 10 Hz for the evaluated cases. In general, the frequency value of the resonances barely decrease when increasing the value of resistance R_d^{++}, as shown in Fig. 8.24(a).

Regarding the damping factor variation, the damping factor of series resonance f_{sr2} is the one that exhibits the highest change. It decreases while increasing the resistance value. The maximum variation is approximately equal to -0.006 for the evaluated cases. For the case of series resonance f_{sr4}, the damping factor increases while increasing the resistance value. The maximum variation of the damping factor of resonance f_{sr4} is approximately equal to ±0.002. Finally, the damping factor of remaining resonances barely change, as shown in Fig. 8.24(b).

8.5.2 Variation of the parameters of the transmission cable

The variation of the values of the transmission cable parameters, given in Table 7.17 for the OWPP base scenario, are presented in this subsection. Changes in Bode plots due to the variation of the values of two variables are analyzed. First, the transmission cable length, which is highly dependent on the installation conditions at sea. Second, changes of $\pm20\%$ are performed to the transmission cable capacitance.

- Variation of the transmission cable length

Fig. 8.25 depicts the changes in Bode plots due to a variation in the transmission cable length. Additionally, Fig. 8.26 shows the values of frequency- and damping factor variation due to changes in the same variable. The following conclusions can be stated from these figures.

Regarding the frequency variation, resonance f_{sr3} decreases while increasing the cable length. This resonance exhibits the highest change, a maximum variation of approximately 650 Hz for the evaluated cases. For the case of resonances f_{sr1} and f_{sr2}, they decrease while increasing the transmission cable length. The maximum variations are approximately equal to 50 Hz and 30 Hz for resonances f_{sr1} and f_{sr2}, respectively. Finally, resonance f_{sr4} exhibits a special behavior. It decreases for changes in the transmission cable length between 40km and 70km. For distances higher than 70 km, resonance f_{sr4} increases.

In general, it can be stated that increasing the cable length tends to move the series resonances f_{sr1} and f_{sr3} to lower frequency values. This inherently represents a possible problem in terms of voltage and current distortion at the PCC point if WTs inject low order harmonics and a problem in terms of the tuning requirements of the control loops of the GSCs of the wind turbines. For example, it might not be possible to fulfill with a fast dynamic response while ensuring the stability of the entire OWPP, unless special control strategies (such as active damping loops) are implemented.

(a)   (b)
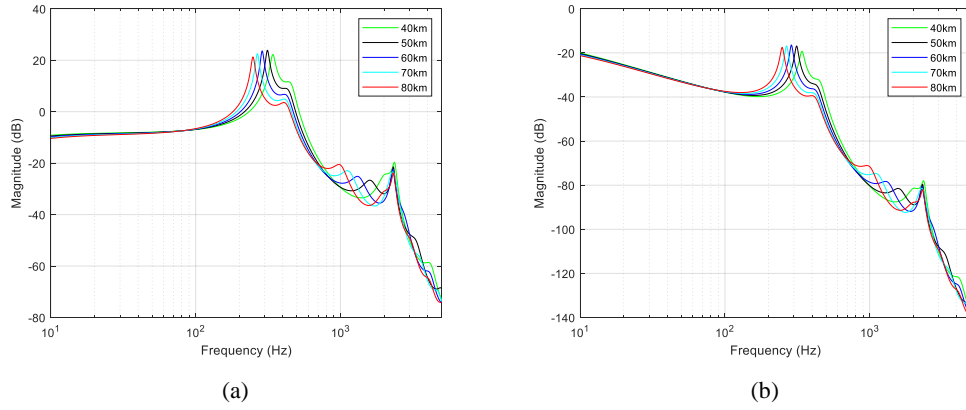
Fig. 8.25. Changes in Bode plots due to a variation of the transmission cable length. (a) Bode plot of transfer function $V_{ab\_PCC}^+(s)\big/V_{ab\_GSC1}^+(s)$. (b) Bode plot of transfer function $I_{a\_PCC}^+(s)\big/V_{ab\_GSC1}^+(s)$.

(a)   (b)
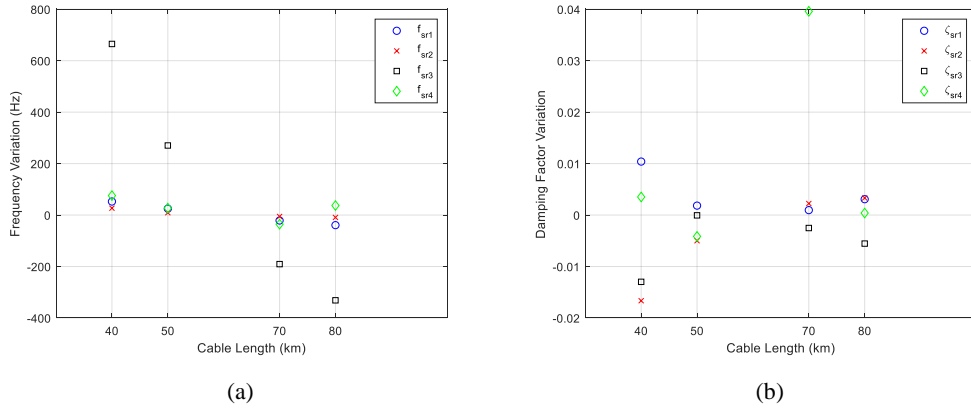
Fig. 8.26. Frequency- and damping factor variation of main series resonances due to a change of the transmission cable length. (a) Frequency variation. (b) Damping factor variation.

Regarding the damping factor variation, the damping factor of series resonance f_{sr2} is the one that exhibits a clear increase over the entire range of variation when increasing the cable length. The maximum damping factor variation is approximately equal to -0.016 for this resonance. On the other hand, the damping factors of remaining resonances increase and decrease for certain ranges of change of cable length, as shown in Fig. 8.26(b).

- Variation of $\hat{C}_{tc}^{++}$ value

Fig. 8.27 depicts the changes in Bode plots due to a variation in $\hat{C}_{tc}^{++}$ value. Additionally, Fig. 8.28 shows the values of frequency- and d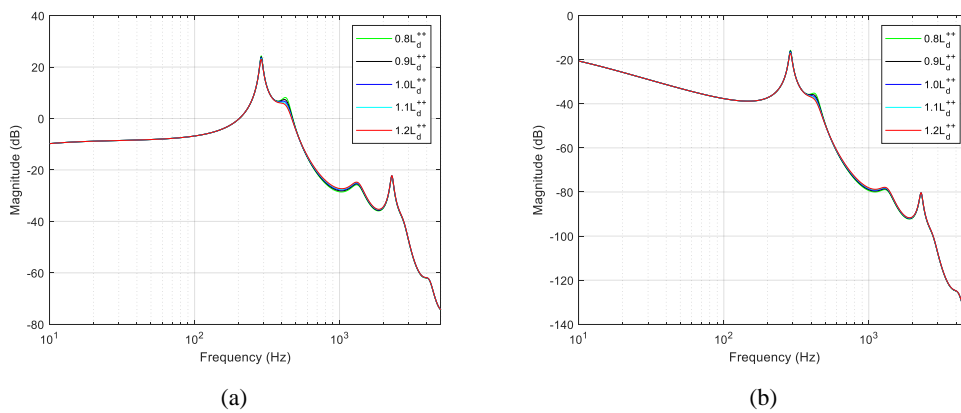amping factor variation due to changes in the same variable. The following conclusions can be stated from these figures.

Regarding the frequency variation, resonances f_{sr1} to f_{sr4} decrease when the capacitance of the transmission cable is increased. The maximum variation is approximately equal to 170 Hz for resonance f_{sr3}. For remaining resonances, the maximum frequency variation is lower than 30 Hz.

(a)   (b)
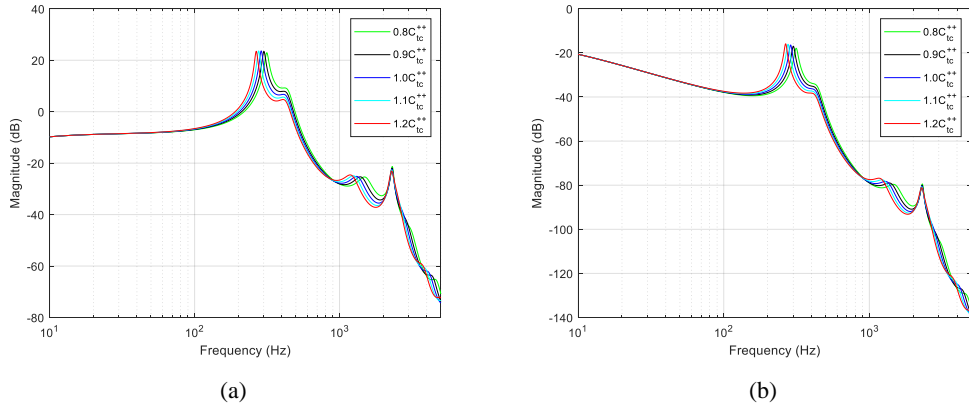
Fig. 8.27. Changes in Bode plots due to a variation in $\hat{C}_{tc}^{++}$ value. (a) Bode plot of transfer function $V_{ab\_PCC}^{+}(s)/V_{ab\_GSC1}^{+}(s)$. (b) Bode plot of transfer function $I_{a\_PCC}^{+}(s)/V_{ab\_GSC1}^{+}(s)$.
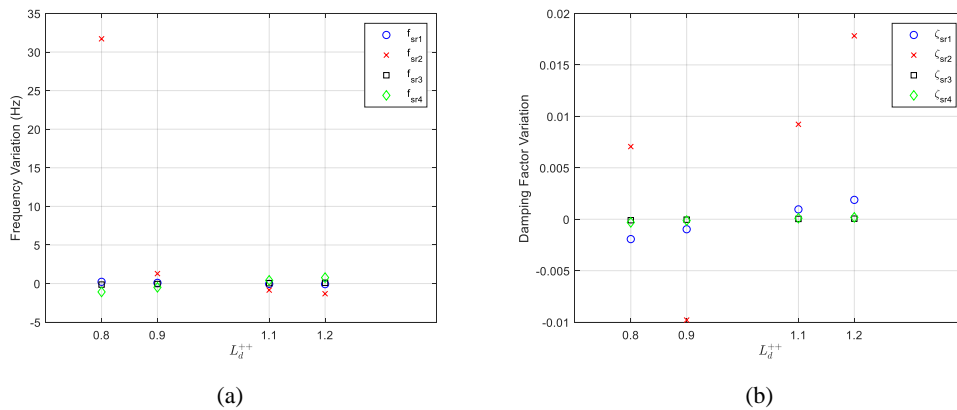

(a)   (b)
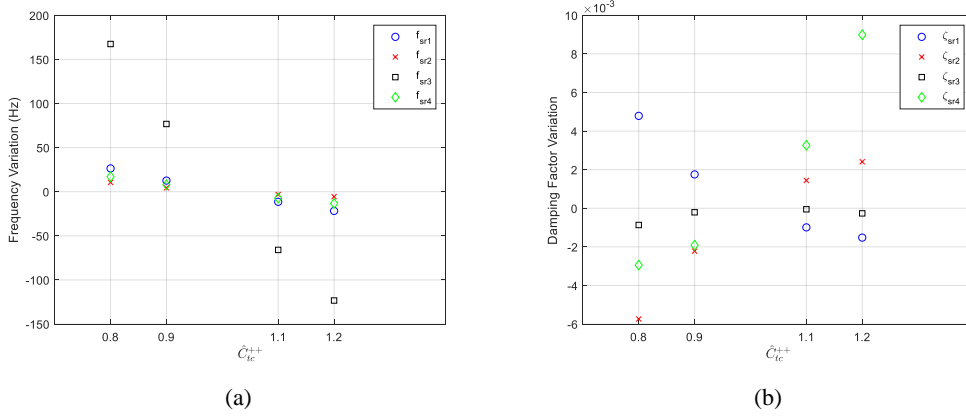
Fig. 8.28. Frequency- and damping factor variation of main series resonances due to a change in $\hat{C}_{tc}^{++}$ value. (a) Frequency variation. (b) Damping factor variation.

Regarding the damping factor variation, the damping factor of resonance f_{sr1} decreases while increasing the capacitance of the transmission cable. The maximum variation of the damping factor is approximately equal to 0.005. Resonances f_{sr2} and f_{sr4} increase when the capacitance of the transmission cable is increased. The maximum damping factors variations are approximately equal to -0.006 and 0.009 for resonances f_{sr2} and f_{sr4}, respectively. Finally, the damping factor of resonance f_{sr3} increases for a range of capacitance variation between $0.8\hat{C}_{tc}^{++}$ and $\hat{C}_{tc}^{++}$. For values higher than $\hat{C}_{tc}^{++}$, the damping factor decreases, as shown in Fig. 8.28(b).

8.5.3 Variation of the Grid Equivalent Impedance

The SCR value is varied from a value of 20 to a value of three with additional intermedium values. An SCR equal to 20 represents a strong grid while an SCR equal to 3 represents a weak grid [202]. Fig. 8.29 depicts the changes in Bode plots due to a variation in the grid strength or SCR value. Additionally, Fig. 8.30 shows the values of frequency- and damping factor variation due to changes in the same variable.

187

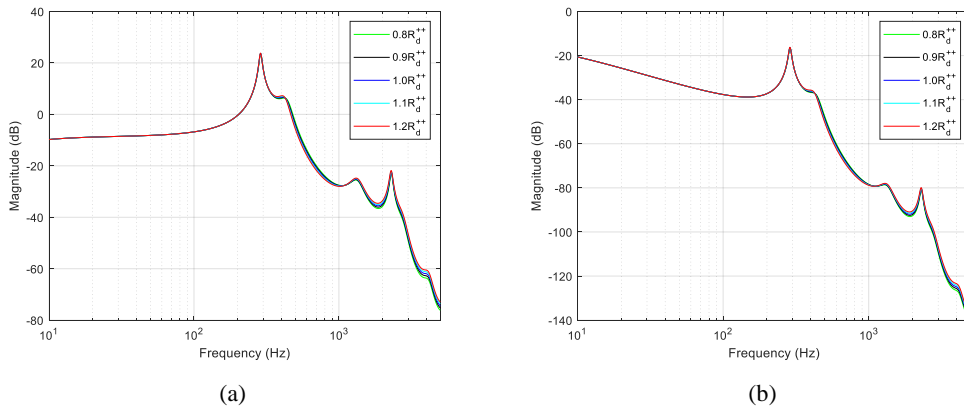(a)   (b)
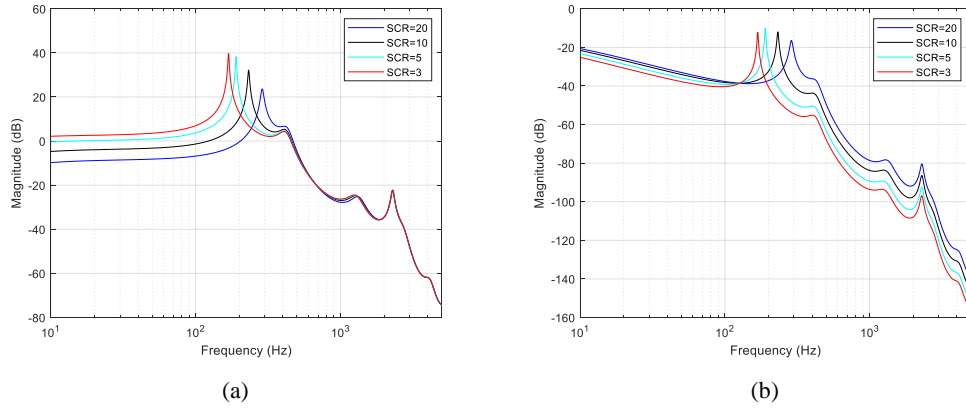
Fig. 8.29. Changes in Bode plots due to a variation of the SCR value. (a) Bode plot of transfer function $V_{ab\_PCC}^{+}(s)\big/V_{ab\_GSC1}^{+}(s)$. (b) Bode plot of transfer function $I_{a\_PCC}^{+}(s)\big/V_{ab\_GSC1}^{+}(s)$.
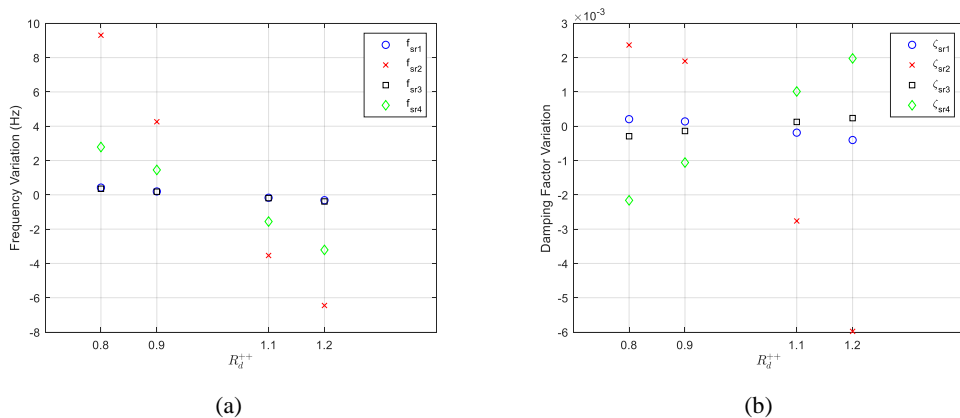

(a)   (b)
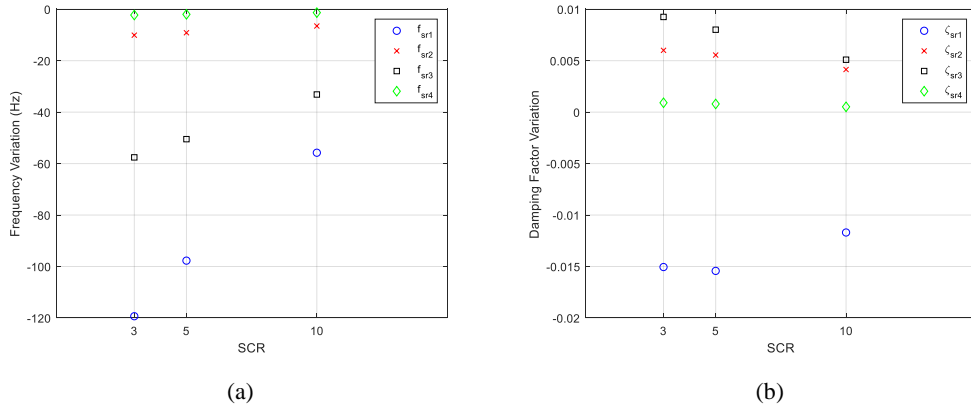
Fig. 8.30. Frequency- and damping factor variation of main series resonances due to a change in SCR value. (a) Frequency variation. (b) Damping factor variation.

Regarding the frequency variation, resonances f_{sr1} to f_{sr4} increase when the SCR value is increased. The maximum variation is approximately equal to -120 Hz for resonance f_{sr1} when having an SCR value equal to three, a weak grid. For the case of resonance f_{sr3}, the maximum variation is approximately equal to -60 Hz for the same SCR value (SCR=3). For remaining resonances, the maximum frequency variation is lower than -10 Hz.

In general, it can be concluded that connecting the OWPP to a weak grid tends to locate the resonance f_{sr1} to lower frequency values. As pointed out in previous subsection, this may cause a potential problem in terms of voltage and current distortion at the PCC point if WTs inject low order harmonics. It may also cause a potential problem in terms of the stability of the entire OWPP. In other words, it may not be possible for WTs to operate with a fast dynamic response while ensuring the stability of the entire OWPP unless special control strategies (such as active damping loops) are implemented.

Regarding the damping factor variation, the damping factor of resonance f_{sr1} exhibits two behaviors. First, it decreases for SCR values between three and five. For SCR values higher than five, the damping factor increases. On the other hand, damping factors of remaining resonances decrease when the SCR value is increased, as shown in Fig. 8.30(b).

8.6 Asymmetrical OWPP Layout

This section addresses two additional studies to the OWPP base scenario. First, the OWPP base scenario is studied when considering a number of disconnected WTs. Second, the OWPP is analyzed when considering an OWPP with distances among WTs and cable feeders quite different.

8.6.1 OWPP with disconnected WTs

In this subsection, the OWPP base scenario is studied with a different number of disconnected wind turbines. Table 8.2 gives information about the wind turbines that are disconnected and the total number of disconnected WTs.

Fig. 8.31 shows the two types of schemes that are analyzed for the disconnected wind turbines. The first scheme is depicted in Fig. 8.31(a) and it considers the IGBTs of the GSCs in off state. The second scheme is shown in Fig. 8.31(b) and it considers the previous condition and the shunt admittance of the filter disconnected. Both schemes represent a WT whose cut-in wind speed has not been reached. The wind turbine transformer is not de-energized for both cases.

Table 8.2. Number of disconnected WTs and the specification of the disconnected WTs.

Number of disconnected WTs	Disconnected WTs
0	None
1	WT1
2	WT1, 10
3	WT1, 10, 2
4	WT1, 10, 2, 11
5	WT1, 10, 2, 11, 4
6	WT1, 10, 2, 11, 4, 7
7	WT1, 10, 2, 11, 4, 7, 3
8	WT1, 10, 2, 11, 4, 7, 3, 12
9	WT1, 10, 2, 11, 4, 7, 3, 12, 5
10	WT1, 10, 2, 11, 4, 7, 3, 12, 5, 8
11	WT1, 10, 2, 11, 4, 7, 3, 12, 5, 8, 6
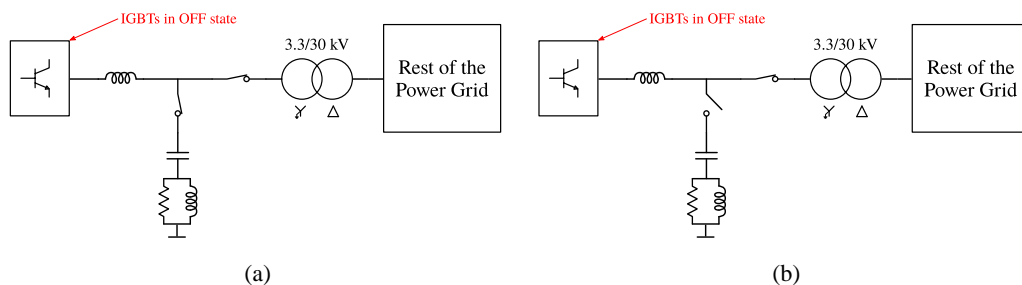
Fig. 8.31. Single-line diagram of disconnected WTs. (a) considering the IGBTs of the GSCs in off state. (b) considering the IGBTs of the GSCs in off state and the shunt capacitor disconnected.

Fig. 8.32 and Fig. 8.33 show the changes in Bode plots for transfer functions $V^+_{ab\_PCC}(s)/V^+_{ab\_GSC9}(s)$ and $I^+_{a\_PCC}(s)/V^+_{ab\_GSC9}(s)$, respectively. These figures show the results considering the scheme of Fig. 8.31(a).

As depicted in these figures, resonances f_{sr1} and f_{sr2} are shifted to lower frequency values. For example, the frequency value of resonance f_{sr1} is reduced to an approximate value of 200 Hz when having eleven disconnected WTs.

Similar to the explanation given in the previous section, this condition may cause a potential problem in terms of voltage- and current distortion at the PCC point if WTs inject low order harmonics. It may also cause a potential problem in terms of the stability of the entire OWPP. In other words, it may not be possible for WTs to operate with a fast dynamic response while ensuring the stability of the entire OWPP unless special control strategies are implemented.
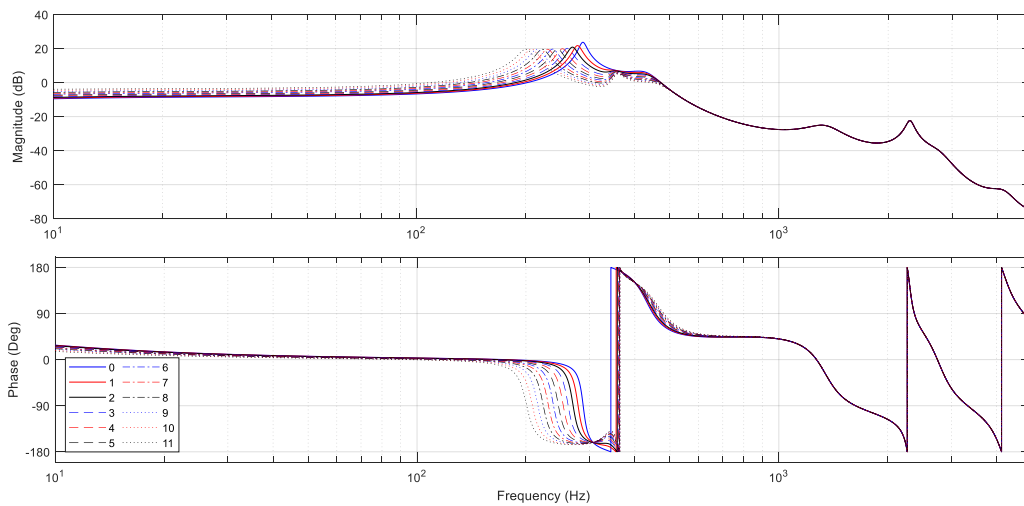
Fig. 8.32. Bode plot of transfer function $V^+_{ab\_PCC}(s)/V^+_{ab\_GSC9}(s)$ depending on the number of disconnected WTs.
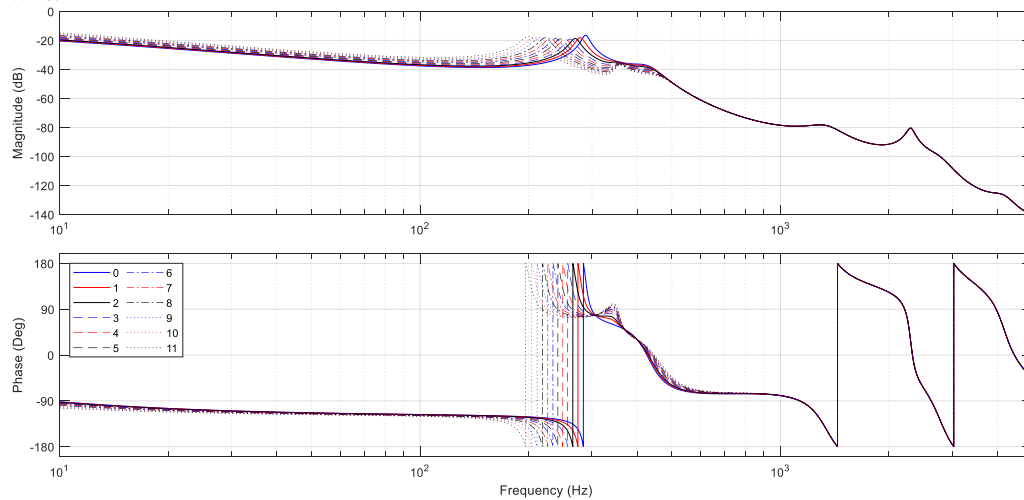
Fig. 8.33. Bode plot of transfer function $I^+_{a\_PCC}(s)/V^+_{ab\_GSC9}(s)$ depending on the number of disconnected WTs.

Finally, it can be seen that resonances f_{sr3} and f_{sr4} are not shifted in frequency. For harmonics close to the frequency values of these resonances, it is a positive aspect that these resonances do not move and the magnitudes of both of them do not increase. This will guarantee that the grid codes in terms of harmonics will be complied too, just if they were fulfilled for previous conditions. It is also important to point out that disconnected WTs do not inject harmonics and the summation of harmonics is lower than considering all the WTs connected.

Now, the same analysis is performed when considering the scheme of Fig. 8.31(b). For this scheme, Fig. 8.34 and Fig. 8.35 show the changes in Bode plots for transfer functions $V_{ab\_PCC}^{+}(s)\big/V_{ab\_GSC9}^{+}(s)$ and $I_{a\_PCC}^{+}(s)\big/V_{ab\_GSC9}^{+}(s)$, respectively.
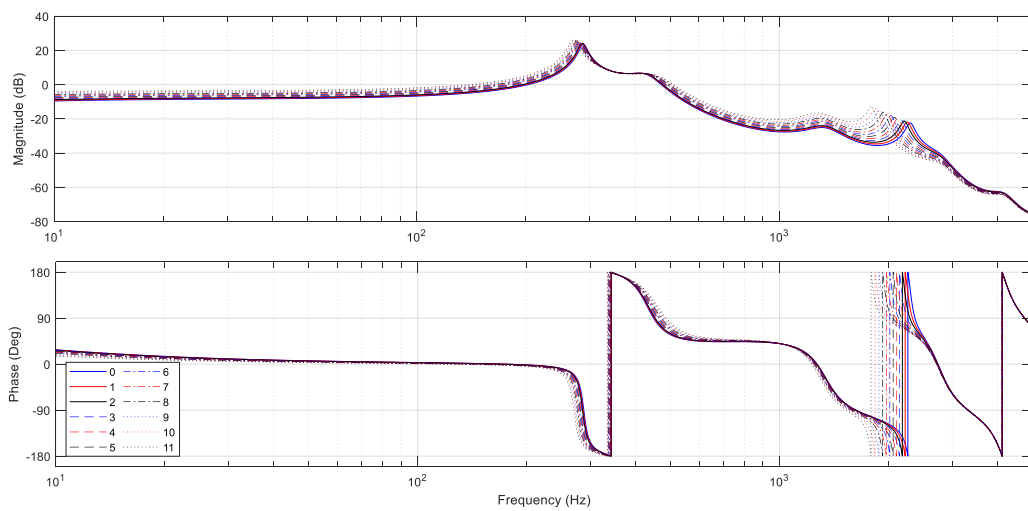
Fig. 8.34. Bode plot of transfer function $V_{ab\_PCC}^{+}(s)\big/V_{ab\_GSC9}^{+}(s)$ depending on the number of disconnected WTs.
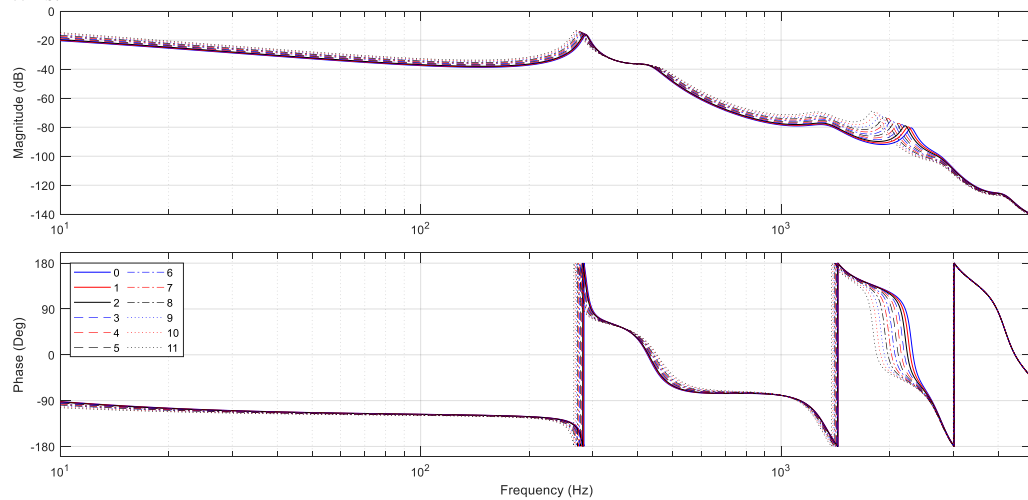
Fig. 8.35. Bode plot of transfer function $I_{a\_PCC}^{+}(s)\big/V_{ab\_GSC9}^{+}(s)$ depending on the number of disconnected WTs.

Contrary to the previous case, resonances f_{sr1} to f_{sr4} are shifted in frequency and their amplitudes are also changed. Focusing on resonances f_{sr1} and f_{sr2}, the changes are lower

than previous case. The lowest frequency value of resonance f_{sr1} is approximately equal to 270 Hz when considering eleven WTs disconnected. Resonance f_{sr2}, on the contrary, is shifted to higher frequency values. Resonances f_{sr3} and f_{sr4} are shifted to lower frequency values. Being resonance f_{sr4}, the one that exhibits the highest change in frequency. This resonance is shifted from approximately 2300 Hz, when all WTs are connected, to a frequency of approximately 1800 Hz when having eleven disconnected WTs.

One important point to notice is that the fact of having a higher number of disconnected WTs increases the magnitude of the Bode plot. This happens because the equivalent impedance of the OWPP is reduced. Finally, it is worth to point out that even though the magnitude plot is increased, disconnected WTs do not inject harmonics and the summation of harmonics is lower than considering all the WTs connected.

8.6.2   OWPP with distances among WTs quite different

One of the conclusions pointed out in section 8.2 is that the electrical infrastructure of the OWPP does not cause a different phase shift among the harmonics injected by the GSCs, this is valid for the frequency range under study (50 Hz to 5 kHz). As already mentioned, this scenario occurs mainly because the OWPP is symmetrical.

Fig. 8.36 shows an asymmetrical layout of the collection network of the OWPP base scenario. The asymmetry of the collection network is obtained by considering the distances among WTs quite different. Changes in the layout of the OWPP are highlighted in red. In order to see the differences with the symmetrical layout, the reader is suggested to compare the schematic of Fig. 7.1(a) and Fig. 8.36.
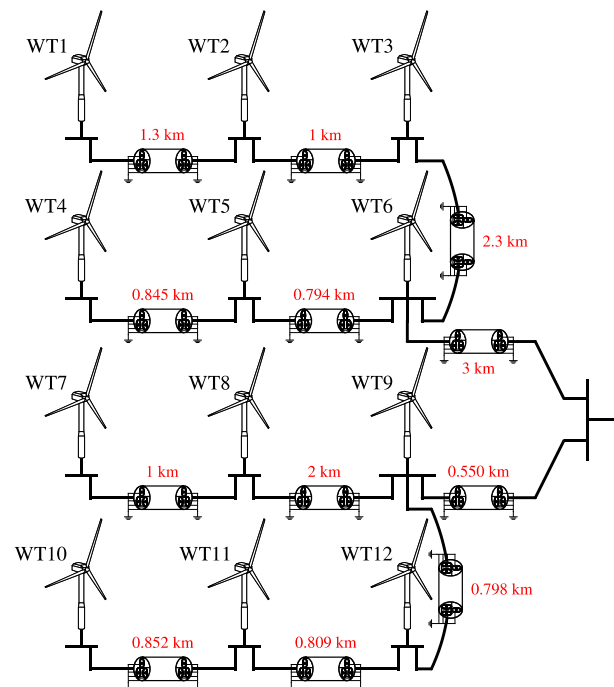
Fig. 8.36. OWPP base scenario considering a collection network with an asymmetrical layout.

Fig. 8.37 shows the Bode plots of transfer function $I^+_{a\_PCC}(s)/V^+_{ab\_GSCi}(s)$ for both, the symmetrical- and asymmetrical layout of the OWPP under study. Fig. 8.37(a) shows the results presented in section 8.2. The frequency response is extended to visualize frequencies up to 10 kHz.

On the other hand, Fig. 8.37(b) shows the results of the asymmetrical layout of the OWPP. As depicted in this figure, different phase shifts among the harmonics injected by the GSCs are visible from a frequency of 3 kHz. Different magnitudes are also noticeable in Bode plots from a frequency of 3 kHz.

(a)

(b)
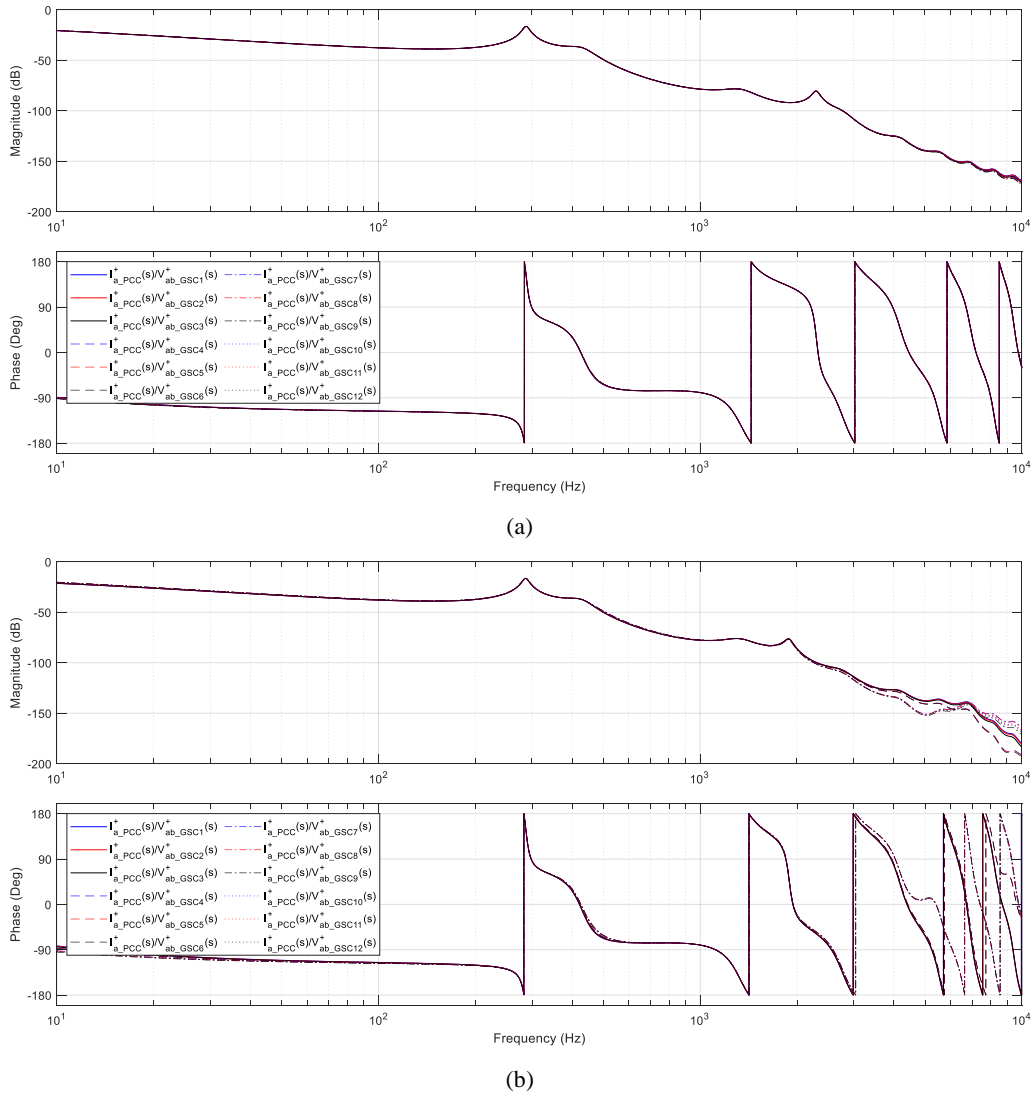
Fig. 8.37. Bode plot of transfer function $I^+_{a\_PCC}(s)/V^+_{ab\_GSCi}(s)$. (a) Symmetrical layout of the OWPP base scenario (All wind turbines are connected and separation distance among WTs is quite similar). (b) Asymmetrical layout of the OWPP base scenario (All wind turbines are connected and separation distance among WTs is quite different).

Resonances f_{sr1} to f_{sr4} have not changed and they are practically the same for all WTs. It is worth to mention that if the separation distances among WTs were made even more asymmetrical and with a higher length, it is possible that resonances f_{sr1} to f_{sr4} could be

affected. In this sense, these resonances may have different magnitudes and they may cause different phase shifts among the harmonics injected by the GSCs.

8.7   Chapter Summary

This chapter has studied the frequency response of the OWPP base scenario. The frequency response has been performed by means of the sequence network model and the OWPP base scenario, given in chapter 7. The following conclusion can be pointed out for this chapter.

One of the main conclusions that have been pointed out in this chapter is that the electrical infrastructure of the OWPP base scenario does not cause a different phase shift (for frequencies up to 5 kHz) among the harmonics injected by the GSCs. In this sense, if the GSCs work at the same operation point, the magnitude of harmonics of the same order will be increased at the PCC point because these harmonics are added in phase. This occurs mainly because the OWPP base scenario is symmetrical. Results may be different when considering an asymmetrical OWPP or a large OWPP. An asymmetrical collection network can be obtained by means of having a different number of wind turbines connected to each radial or by means of different cable lengths among WTs.

Additional increase of the magnitude of a harmonic can be obtained if a resonance is near a specific harmonic, e.g. the injection of a 5th harmonic voltage coming from the GSCs and the presence of resonance f_{sr1} for voltage- and current variables at the PCC point.

Resonances f_{sr1} to f_{sr4} have been identified together with the main components that create them. The identification has been performed with the aid of participation factor technique. According to the studied OWPP, resonance f_{sr1} is created by the capacitance of the transmission cable and the equivalent inductance of the grid model, which depends on the SCR value. Resonance f_{sr2} is created by the GSC connection filter. Resonance f_{sr3} is the second series resonance of the transmission cable (60 km long cable). Finally, resonance f_{sr4} is created by the capacitance of the submarine cables of the collection network and the short-circuit inductance of the transformers, OST and WTTs.

A discussion about the risk of amplification of the harmonics injected by the WTs has been addressed according to the spectrums of the modulation strategies evaluated so far, CB-PWM and SHE-PWM. An important conclusion from this analysis is that a modulation strategy that does not inject low-order harmonics, such as the particular solution of SHE-PWM, is more suited to be used for this base scenario. This is mainly because of the presence of resonance f_{sr1} and the way low-order harmonics are added (in phase).

Chapter 9

Current-Harmonic Evaluation of OWPPs

This chapter presents the steady-state current-harmonic evaluation of an OWPP. The harmonic evaluation is performed by means of computing the spectrum of current signals, the total harmonic distortion (THD) values and the fulfillment of the BDEW grid code. The previous metrics are obtained by means of the Simulink®-based model of the OWPP base scenario. This chapter presents two main studies. First, the harmonic evaluation is performed by considering that wind turbines operate with the typical CB-PWM modulation. For this modulation strategy, the harmonic assessment is performed at wind turbine level and at OWPP level. Several operation points are analyzed for both levels of study. Second, WT manufacturer oriented solutions are proposed with the aim of improving the harmonic emission of the OWPP. The implementation of the particular solution of SHE-PWM modulation is presented together with complementary solutions to further improve the harmonic emission of the OWPP with this type of modulation strategy.

9.1 Introduction

Harmonics are a special concern in the offshore wind industry due to the high penetration of power converters in type-4 wind turbines [5]. Some of the many advantages of installing type-4 wind turbines are presented in subsection 2.2.1. As a side effect, this type of WT can be considered as a source of harmonics, which significantly contributes to the overall harmonic emission at the point of common coupling of the OWPP. Furthermore, this

contribution can be worsened due to the presence of resonances that may increase a given voltage or current harmonic component. These resonances can be classified into series and parallel resonances and they occur due to capacitive- and inductive behavior of installed power components in combination with the impedance of the grid. Submarine cables exhibit a predominant capacitive behavior while transformers behave predominantly as inductors for the frequency range of study of this document, 50 Hz to 5 kHz.

Maximum harmonic injection limits of voltage- and current signals are commonly imposed by grid codes and interconnection agreements. These limits are typically evaluated at the PCC point for the steady-state condition. To determine the compliance with grid code harmonic limits, it is required to perform a harmonic evaluation of the OWPP. This assessment must consider three important factors. First, an accurate representation of the harmonics injected by wind turbines, which clearly depend on modulation strategy and control loops of the GSCs. Second, the frequency-dependent characteristic of installed passive components, e.g. submarine cables and transformers. The third factor to consider is the evaluation of different operation points for each wind turbine, not only for the rated condition. These operation points depend on power factor requirement, wind conditions, and location of each wind turbine. In this sense and with the purpose of including the aforementioned factors, the Simulink®-based model presented in chapter 7 is used to perform the harmonic evaluation.

This chapter presents the steady-state current-harmonic evaluation of the OWPP base scenario. The harmonic assessment is carried out by means of computing the spectrum of current signals, the total harmonic distortion (THD) values and the fulfillment of the BDEW grid code. This chapter is structured as follows. Section 9.2 gives the harmonic injection limits according to the BDEW grid code for both levels of study, WT level and OWPP level. Section 9.3 carries out the harmonic evaluation for wind turbines operating with CB-PWM modulation. For this modulation strategy, the harmonic assessment is performed for both levels of study and for several operation points. In section 9.4, WT manufacturer oriented solutions are proposed with the aim of improving the harmonic emission of the OWPP. The implementation of the particular solution of SHE-PWM modulation is presented together with complementary solutions to further improve the harmonic emission of the OWPP. Finally, section 9.5 gives the chapter summary.

9.2 Specification of Technical Regulations according to the BDEW grid code

This section presents the current-harmonic limits for both, wind turbine level and offshore wind power plant level. The current-harmonic limits, presented next in Fig. 9.1 and Fig. 9.2, are computed according to the procedure and information provided by the BDEW grid code. For a description of other grid codes, references [3,203] are recommended.

9.2.1 Current Harmonics, Interharmonics and Higher Frequency Components

The BDEW technical guideline [97] defines the maximum current injection limit of individual harmonic components, up to 9 kHz, according to Table 9.1.

Table 9.1. BDEW harmonic current injection limits related to the network short-circuit power, which may be fed in total into the MV network. Source [97].

Harmonic (v, μ)	Admissible, related harmonic current i_{v,μ_zul} in A/MVA		
	10 kV network	20 kV network	30 kV network
5	0.058	0.029	0.019
7	0.082	0.041	0.027
11	0.052	0.026	0.017
13	0.038	0.019	0.013
17	0.022	0.011	0.007
19	0.018	0.009	0.006
23	0.012	0.006	0.004
25	0.010	0.005	0.003
$25 < v < 40$ Odd-numbered	$0.01 \cdot 25/v$	$0.005 \cdot 25/v$	$0.003 \cdot 25/v$
Even-numbered	$0.06/v$	$0.03/v$	$0.02/v$
$\mu < 40$	$0.06/\mu$	$0.03/\mu$	$0.02/\mu$
$\mu, v > 40$ Integer and non-integer within a range of 200 Hz	$0.18/\mu$	$0.09/\mu$	$0.06/\mu$

According to the complementary rules [204] done to the original technical guideline, the integer harmonics and high frequency harmonics are calculated (since January 2013) as,

$$I_{v\,Azul} = i_{v\,zul} \cdot S_{kV} \cdot \sqrt{\frac{S_A}{S_{Gesamt}}} \tag{9.1}$$

And the interharmonics are computed as,

$$I_{\mu\,Azul} = i_{\mu\,zul} \cdot S_{kV} \tag{9.2}$$

Being,

S_A: Apparent connection power of the generating plant to be assessed.

S_{Gesamt}: Total connectable or planned feed-in power at the junction point under consideration.

S_{kV}: Short-circuit power at the junction point under consideration.

Furthermore, reference [204] defines some additional rules. Even-numbered harmonic currents are exempted from the calculation. The approval for certification is achieved if no more than 6 calculated values exceed the admissible limit values I_{Azul}. These violations of limits are restricted to a maximum of 200% for harmonics of order 5th, 7th, 11th, 13th, 17th, 19th, 23rd, 25th, and for the remaining frequencies to a maximum of 400% of the limit value. Violations of limit values are not admissible for interharmonic currents.

Current-Harmonic Limits at WT level

In order to determine the BDEW limits at wind turbine level, the parameters of Table 9.2 are considered. An SCR value of 20 is set for the computation of these limits.

Table 9.2. Input parameters for the computation of the BDEW current-harmonic limits at wind turbine level.

Input Parameters	
$S_{A\_WTlevel} = 5\,\text{MVA}$	$S_{Gesamt\_WTlevel} = 30\,\text{MVA}$
$V_{g\_WTlevel} = 30\,\text{kV}$	$S_{kV\_WTlevel} = 20 \cdot S_{A\_WTlevel} = 100\,\text{MVA}$
$I_{r\_WTlevel} = \dfrac{S_{A\_WTlevel}}{\sqrt{3}V_{g\_WTlevel}} \cong 96.23\,\text{A}$	$SCR = 20$

Fig. 9.1 shows the current-harmonic limits at wind turbine level according to the BDEW grid code. The limits are given for integer, non-integer and high frequency harmonics.
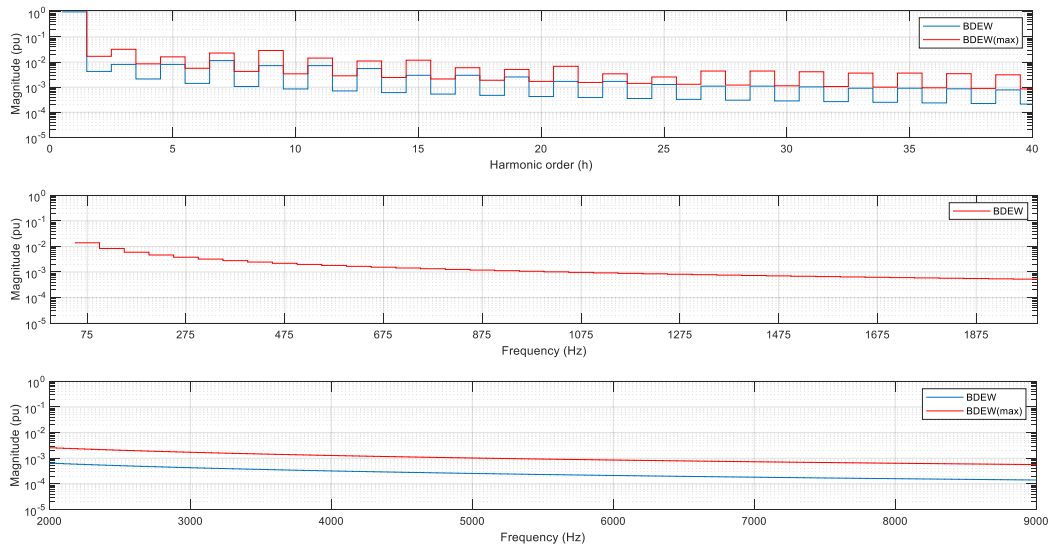
Fig. 9.1. Current-harmonic limits at wind turbine level according to the BDEW grid code.

Current-Harmonic Limits at OWPP level

Similar to the previous case, Table 9.3 gives the input parameters for the computation of the BDEW current-harmonic limits at OWPP level. An SCR value of 20 is set for the computation of these limits.

Table 9.3. Input parameters for the computation of BDEW current-harmonic limits at OWPP level.

Input Parameters	
$S_{A\_OWPPlevel} = 60\,\text{MVA}$	$S_{Gesamt\_OWPPlevel} = 600\,\text{MVA}$
$V_{g\_OWPPlevel} = 110\,\text{kV}$	$S_{kV\_OWPPlevel} = 20 \cdot S_{A\_OWPPlevel} = 1200\,\text{MVA}$
$I_{r\_OWPPlevel} = \dfrac{S_{A\_OWPPlevel}}{\sqrt{3}V_{g\_OWPPlevel}} \cong 314.92\,\text{A}$	$SCR = 20$

Fig. 9.2 shows the current-harmonic limits at OWPP level according to the BDEW grid code. As specified by the grid code, the limits are given for integer, non-integer and high frequency harmonics.
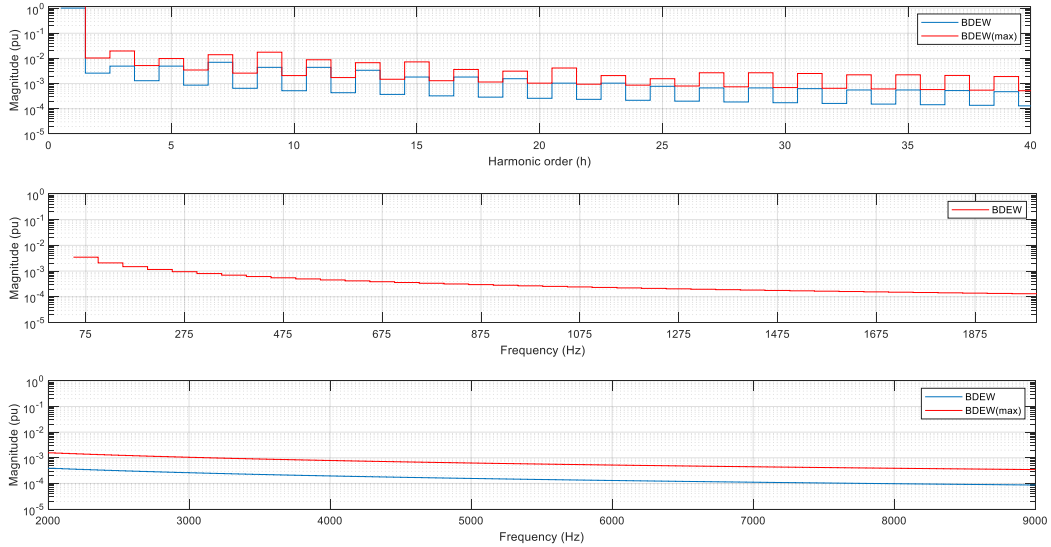
Fig. 9.2. Current-harmonic limits at OWPP level according to the BDEW grid code.

9.2.2   Reactive Power

With active power output, BDEW regulations require the ability to operate the generating plant in any operation point ($V_{grid} \pm 10\%$) with a power factor ranging from -0.95 to +0.95 [97].

9.3   Current-Harmonic Evaluation for WTs operating with CB-PWM modulation

The following subsections present the current-harmonic evaluation for WTs operating with CB-PWM modulation.

9.3.1   Current-Harmonic Evaluation at WT level

The harmonic assessment at wind turbine level is performed by considering the schematic of Fig. 9.3. The models and parameters of each power component are presented in subsection 7.3.1. The only difference for this case is that the wind turbine is connected to an equivalent power grid which is modeled as an ideal voltage source and a short-circuit impedance, see Fig. 7.5. The parameters of the power grid model are computed according to the equivalent SCR value given by Table 9.2.
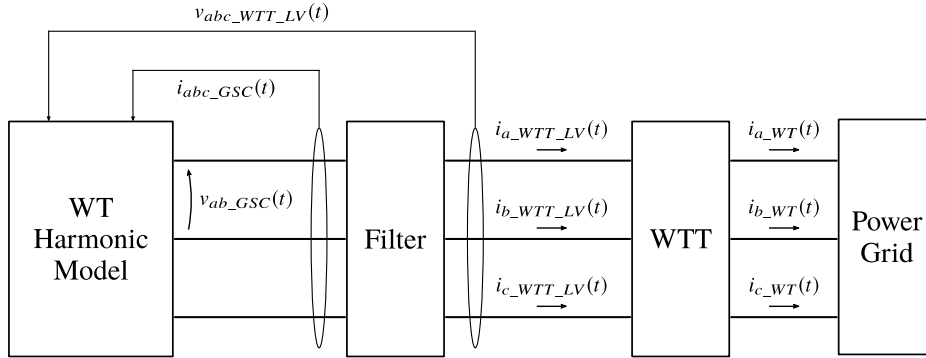
Fig. 9.3. General schematic for the harmonic evaluation at wind turbine level. The control loops of the GSC are implemented. The harmonic evaluation is performed at steady-state.

The current-harmonic evaluation is carried out for several wind turbine power setpoints. For the evaluated cases, the wind turbine is not injecting reactive power to the grid. Table 9.4 gives the total harmonic distortion (THDi) values of the current signal $i_{a\_WT}(t)$ for CB-PWM modulation and for different operation points. The THDi values are computed for the three harmonic subgroups specified by the BDEW grid code.

Table 9.4. Total harmonic distortion (THDi) of the current signal $i_{a\_WT}(t)$ for CB-PWM modulation and for different operation points.

Wind Turbine Power Setpoint	Low Frequency		Interharmonics		High Frequency	
	RMS value (A)	THDi (%)	RMS value (A)	THDi (%)	RMS value (A)	THDi (%)
>95% Pn	96.3224	1.74	0.0541	0.0563	0.2197	0.228
80% Pn	76.8575	1.74	0.0381	0.0397	0.2199	0.229
60% Pn	57.5317	1.73	0.0356	0.0371	0.2201	0.229
40% Pn	38.298	1.71	0.0398	0.0414	0.2203	0.229
20% Pn	19.1148	1.70	0.0310	0.0322	0.2202	0.229

By looking at the results of Table 9.4, it can be noticed that similar THDi values are obtained when comparing the same harmonic subgroup for the evaluated operation points. The THDi values are normalized with respect to the base value at WT level (Table 9.2).

The compliance of the BDEW grid code in terms of harmonics is carried out for the operation points evaluated in Table 9.4. Fig. 9.4 shows the harmonic spectrum of the current signal $i_{a\_WT}(t)$ at rated condition. This figure also shows the current harmonic limits imposed by the BDEW regulations at WT level.

According to this figure and the limits imposed by the grid code, it can be concluded that the wind turbine fulfills the BDEW regulations in terms of harmonics for the rated condition. For simplicity, the graphics of the compliance of the BDEW grid code are not shown for remaining operation points. However, Table 9.5 gives a summary of the fulfillment of the grid code for the evaluated operation points.

It can be stated that for the operation points evaluated so far, the BDEW grid code in terms of harmonics is fulfilled at wind turbine level for CB-PWM modulation.
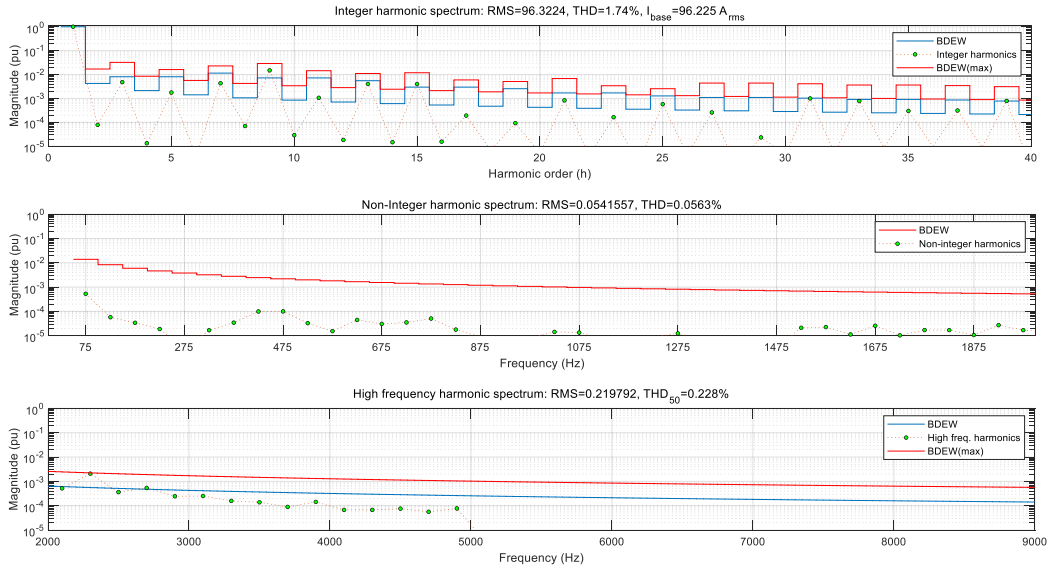
Fig. 9.4. Harmonic spectrum of current signal $i_{a\_WT}(t)$ plotted against the BDEW harmonic current limits at wind turbine level, SCR=20. This graphic considers the following conditions: CB-PWM modulation and wind turbine operating at rated condition.

Table 9.5. Compliance of the BDEW grid code of the current signal $i_{a\_WT}(t)$ for CB-PWM modulation and for different operation points.

Wind Turbine Power Setpoint	BDEW Compliance	Harmonics (h)	Infringement of limits given by BDEW		
			Harmonics of order $6n \pm 1$ ($n = 1 \cdots 4$)	Remaining Harmonics	Interharmonics
		>BDEW limit	>200% BDEW limit	>400% BDEW limit	>BDEW limit
>95% Pn	Yes	9, 15, 45, 47	–	–	–
80% Pn	Yes	9, 15, 45, 47	–	–	–
60% Pn	Yes	9, 15, 45, 47	–	–	–
40% Pn	Yes	9, 15, 45, 47	–	–	–
20% Pn	Yes	9, 15, 45, 47	–	–	–

9.3.2 Current-Harmonic Evaluation at OWPP level

The harmonic assessment at OWPP level is performed by considering the Simulink®-based model presented in section 7.3. The current-harmonic evaluation is carried out for several OWPP power setpoints. As pointed out in previous chapter, these operation points are defined by means of the wind conditions and the wake effect in the OWPP base scenario. Fig. 7.10 and Fig. 7.11 gives the estimated active power generation of each WT and the entire OWPP, respectively. The reactive power reference is defined so each WT operates with a unity power factor at wind turbine transformer terminals. The reader is suggested to review subsection 7.3.2 for the definition and computation of these operation points.

Table 9.6 gives the total harmonic distortion (THDi) values of the current signal $i_{a\_PCC}(t)$ for WTs operating with CB-PWM modulation and for the evaluated operation points. By looking at the results of this table, it can be noticed that similar THDi values are obtained

201

when comparing the same harmonic subgroup for the different operation points. The THDi values are normalized with respect to the base value at the PCC point (Table 9.3).

The compliance of the BDEW grid code in terms of harmonics is evaluated too. Fig. 9.5 shows the harmonic spectrum of the current signal $i_{a\_PCC}(t)$ at rated condition. The figure also shows the current harmonic limits imposed by the BDEW grid code at OWPP level.

For simplicity, the graphics of the compliance of the BDEW grid code are not shown for the remaining operation points. However, Table 9.7 gives a summary of the fulfillment of this grid code for the evaluated operation points.

Table 9.6. Total harmonic distortion (THDi) of the current signal $i_{a\_PCC}(t)$ for CB-PWM modulation and for different operation points.

Wind Direction	Wind speed (m/s)	Low Frequency		Interharmonics		High Frequency	
		RMS value (A)	THDi (%)	RMS value (A)	THDi (%)	RMS value (A)	THDi (%)
West	24	313.495	2.28	0.2930	0.0931	0.7678	0.244
	16	264.962	2.15	0.2489	0.0791	0.7666	0.243
	12.5	188.142	2.03	0.1798	0.0571	0.7652	0.243
	8	83.7304	2.25	0.1158	0.0368	0.7666	0.243
NorthWest	24	313.495	2.28	0.2930	0.0931	0.7678	0.244
	16	301.135	2.26	0.2820	0.0896	0.7676	0.244
	12.5	240.909	2.11	0.2269	0.0721	0.7662	0.243
	8	92.6446	2.26	0.1044	0.0332	0.7668	0.244
North	24	301.102	2.27	0.2820	0.0896	0.7677	0.244
	16	216.833	1.99	0.2046	0.065	0.7649	0.243
	12.5	153.701	1.98	0.1469	0.0467	0.7644	0.243
	8	78.4734	2.24	0.1317	0.0418	0.7664	0.243
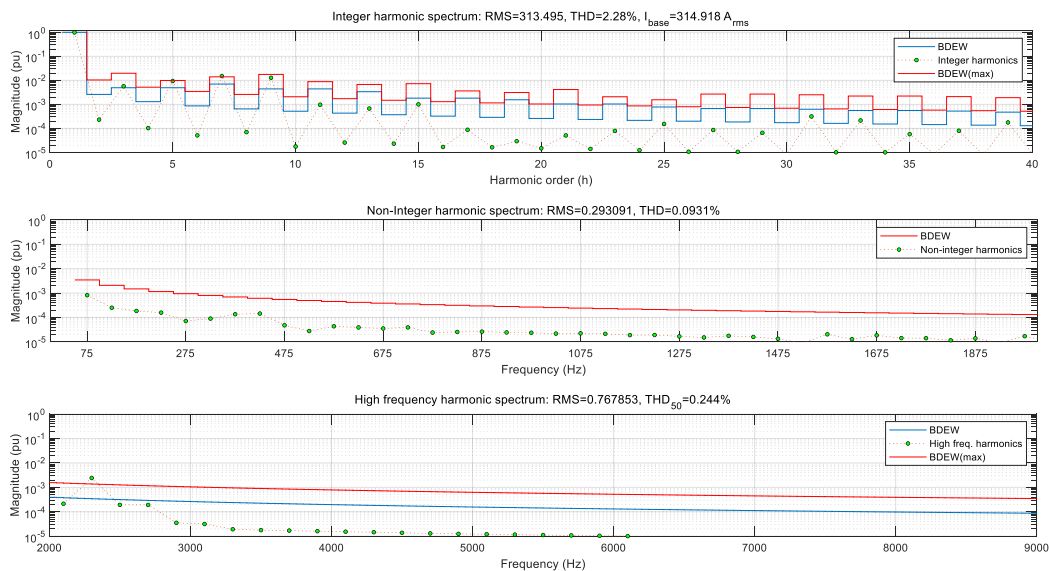
Fig. 9.5. Harmonic spectrum of current signal $i_{a\_PCC}(t)$ plotted against the BDEW harmonic current limits at OWPP level, SCR=20. This graphic considers the following conditions: CB-PWM modulation and wind turbines operating at rated condition (wind direction: west or northwest, wind speed: 24 m/s).

Table 9.7. Compliance of the BDEW grid code of the current signal $i_{a\_PCC}(t)$ for CB-PWM modulation and for different operation points.

| Wind Direction | Wind Speed (m/s) | BDEW Compliance | Harmonics (h) | Infringement of restrictions given by BDEW | | |
| | | | | Harmonics of order $6n \pm 1$ $(n = 1 \cdots 4)$ | Remaining Harmonics | Interharmonics |
			>BDEW limit	>200% BDEW limit	>400% BDEW limit	>BDEW limit
West	24	No	3, 5, 7, 9, 45, 47	7	45, 47	–
	16	No	3, 5, 7, 9, 45, 47	7	45, 47	–
	12.5	No	3, 5, 7, 9, 45, 47	7	45, 47	–
	8	No	3, 5, 7, 9, 45, 47	7	45, 47	–
NorthWest	24	No	3, 5, 7, 9, 45, 47	7	45, 47	–
	16	No	3, 5, 7, 9, 45, 47	7	45, 47	–
	12.5	No	3, 5, 7, 9, 45, 47	7	45, 47	–
	8	No	3, 5, 7, 9, 45, 47	7	45, 47	–
North	24	No	3, 5, 7, 9, 45, 47	7	45, 47	–
	16	No	3, 5, 7, 9, 45, 47	7	45, 47	–
	12.5	No	3, 5, 7, 9, 45, 47	7	45, 47	–
	8	No	3, 5, 7, 9, 45, 47	7	45, 47	–

According to Fig. 9.5 and Table 9.7, the BDEW grid code in terms of harmonics is not fulfilled for the evaluated operation points due to the infringement of harmonics of order 7th, 45th and 47th.

From the results of Table 9.7 and the analysis carried out in section 8.3, it can be concluded that these harmonics are heavily affected due to two reasons. First, the attenuation of the system around these frequencies is relatively low, mainly due to resonances f_{sr1} and f_{sr4} of the OWPP base scenario. Second, the way these harmonics are added, which depend on the operation point of the WTs and the additional phase shift of the electrical infrastructure of the OWPP. The phase shift that sees each WT.

As presented in section 8.2, the electrical infrastructure of the OWPP base scenario does not cause a different phase shift among the harmonics of the same order that are injected by the wind turbines. This last statement is true for the frequency range under study in this Ph.D. thesis, 50 Hz to 5 kHz. In this sense, if wind turbines work at the same or a similar operation point, the magnitudes of harmonics of the same order are added, entirely or partially, in phase at the PCC point.

The results given by Table 9.7 validate the hypothesis stated in subsection 8.3.1. The reader is suggested to see Fig. 8.13 and to review the analysis regarding this figure.

9.3.3 Interleaved operation of WTs of the same radial

The harmonic spectrum of the current signal $i_{a\_PCC}(t)$, shown in Fig. 9.5, can be improved if interleaved operation of wind turbines of the same radial is implemented. The currents of each WT are summed and the phase opposition of some harmonics, due to interleaved operation, leads to a reduced current-harmonic content at the PCC point.

Fig. 9.6 shows the results when implementing interleaved operation of wind turbines of the same radial. Comparing Fig. 9.5 and Fig. 9.6, it can be seen that a reduction of the current-harmonic emission at the PCC point is obtained when performing interleaving. Harmonics of order 45th and 47th are highly reduced at the PCC point and they no longer infringe the limits imposed by the BDEW grid code.

Nevertheless, the results of Fig. 9.6 also reveals that harmonic of order 7th still exceeds the harmonic current resctriction imposed by the grid code. In this sense, it is not worthy to implement this strategy because of two main reasons. First and most important, the BDEW grid code is still not fulfilled. Second, the implementation of such strategy in a real OWPP is not an easy task from the perspective of synchronization of carriers among wind turbines.

Fig. 9.6. Harmonic spectrum of current signal $i_{a\_PCC}(t)$ plotted against the BDEW harmonic current limits at OWPP level, SCR=20. This graphic considers the following conditions: CB-PWM modulation with interleaved operation of WTs of the same radial and wind turbines operating at rated condition (wind direction: west or northwest, wind speed: 24 m/s).

In general, it can be concluded that the typical CB-PWM modulation is not suitable to be implemented in this OWPP base scenario, mainly because of the presence of resonance f_{sr1} and the way harmonics (of the same order and injected by each wind turbine) around this resonance are added.

9.4 WT oriented solutions to improve the Harmonic Emission of the OWPP

Many mitigation techniques have been proposed and implemented in power systems, e.g. offshore wind power plants, to maintain harmonic distortion within the recommended levels. These are [68,205]:

- Harmonic cancellation or mitigation by means of transformer connections. Phase shifting of harmonics is achieved by considering different winding connections (vector groups) or special transformers. For example:
  - Transformers with delta connections to trap and prevent zero-sequence harmonics from entering a specific zone of a power system.
  - Transformers with zigzag connections for cancellation of certain harmonics and compensation of load imbalances.
- Harmonic filters (passive-, active- and hybrid-filters) and power devices, such as Active Power Line Conditioners (APLCs) and Unified Power Quality Conditioners (UPQCs), placed at specific points (e.g. near the source of harmonics, at the PCC point or other problematic point in which the reliability of the entire system or device is not ensure) along the OWPP.
- Dedicated (isolated) line or transformer to attenuate both low- and high frequency electrical noise and transients as they attempt to pass from one bus to another.
- High power quality equipment design: Demand is increasing for designers and manufacturers to produce devices that generate low current distortion.

From the previous mitigation techniques, <u>WT manufacturer oriented solutions are studied with the aim of improving the harmonic emission of the OWPP</u>. According to the conclusions pointed out in the previous subsection, a modulation strategy that does not inject low-order harmonics is more suited to be used for this base scenario. In this sense, the implementation of the particular solution of SHE-PWM modulation, already presented in chapter 3, is studied together with complementary solutions to further improve the harmonic emission of the OWPP. Among the complementary solutions, the variation of the operation point of the wind turbines is performed to make the WTs operate at amplitude modulation indexes that improve the harmonic emission of the OWPP. In some cases, the variation of the operation point might not be possible due to restrictions that are further described in subsection 9.4.2. Finally, the improvement of the harmonic distortion is presented when considering the redesign of the GSC connection filter according to the harmonic spectrum of SHE-PWM modulation.

9.4.1 Current-Harmonic Evaluation for WTs operating with SHE-PWM modulation

The harmonic assessment at OWPP level for WTs operating with SHE-PWM modulation considers the Simulink®-based model presented in section 7.3 and the same conditions

presented in subsection 8.3.2. As pointed out in chapter 3, the particular solution of SHE-PWM does not inject harmonics of order 5th, 7th, 11th and 13th. The first non-eliminated harmonic that appears in the current is the harmonic of order 17th.

Table 9.8 gives the total harmonic distortion (THDi) values of the current signal $i_{a\_PCC}(t)$ for wind turbines operating with SHE-PWM and for the evaluated operation points. In general, the THDi values for the three harmonic subgroups are reduced for this case. Comparing the THDi values of both modulation strategies for a wind speed of 24 m/s, the THDi for the low frequency subgroup is reduced from a value of 2.28% to a value of 0.337%.

Table 9.8. Total harmonic distortion (THDi) of the current signal $i_{a\_PCC}(t)$ for SHE-PWM modulation and for different operation points.

Wind Direction	Wind speed (m/s)	Low Frequency		Interharmonics		High Frequency	
		RMS value (A)	THDi (%)	RMS value (A)	THDi (%)	RMS value (A)	THDi (%)
West	24	313.419	0.337	0.2889	0.0918	0.1239	0.0394
	16	264.878	0.172	0.2433	0.0773	0.0756	0.024
	12.5	188.035	0.113	0.1733	0.055	0.0681	0.0216
	8	83.4327	0.308	0.1063	0.0338	0.0773	0.0246
NorthWest	24	313.419	0.337	0.2889	0.0918	0.1239	0.0394
	16	301.056	0.304	0.2775	0.0881	0.0967	0.0307
	12.5	240.819	0.133	0.2209	0.0702	0.0508	0.0162
	8	92.3723	0.318	0.0927	0.0295	0.0892	0.0283
North	24	301.022	0.316	0.2775	0.0881	0.1036	0.0329
	16	216.743	0.106	0.1988	0.0632	0.0831	0.0264
	12.5	153.576	0.143	0.1414	0.0449	0.0481	0.0153
	8	78.1624	0.3	0.1310	0.0416	0.0689	0.0219

The compliance of the BDEW grid code in terms of harmonics is evaluated too. Fig. 9.7 shows the harmonic spectrum of the current signal $i_{a\_PCC}(t)$ at rated condition. The figure also shows the current harmonic limits imposed by the BDEW grid code at OWPP level.

For simplicity, the figures of the compliance of the BDEW grid code are not shown for the remaining operation points. However, Table 9.9 gives a summary of the fulfillment of the grid code for the evaluated operation points.

According to Fig. 9.7 and Table 9.9, the BDEW grid code is fulfilled for the evaluated operation points.

For this modulation strategy, resonances f_{sr1} and f_{sr2} do not represent a problem from a steady-state perspective since harmonics of order 5th, 7th, 11th and 13th are not injected or are injected with very low value, as shown in Fig. 9.7.

Even though the BDEW grid code is fulfilled, it is important to be aware of harmonics of order 23rd, 25th and 29th since exceeding the BDEW limit will provoke the not fulfillment of the grid code. For the case of harmonic 31st, there is still a margin for reaching the BDEW limit according to the restrictions stated by the grid code. In this sense, this last harmonic does not represent a risk for the compliance of the BDEW limit.

Finally, it can be concluded that this particular solution of SHE-PWM is suitable to be used for this OWPP base scenario. The reasons for this statement were described in previous paragraphs and are validated by the results presented in Table 9.8 and Table 9.9.
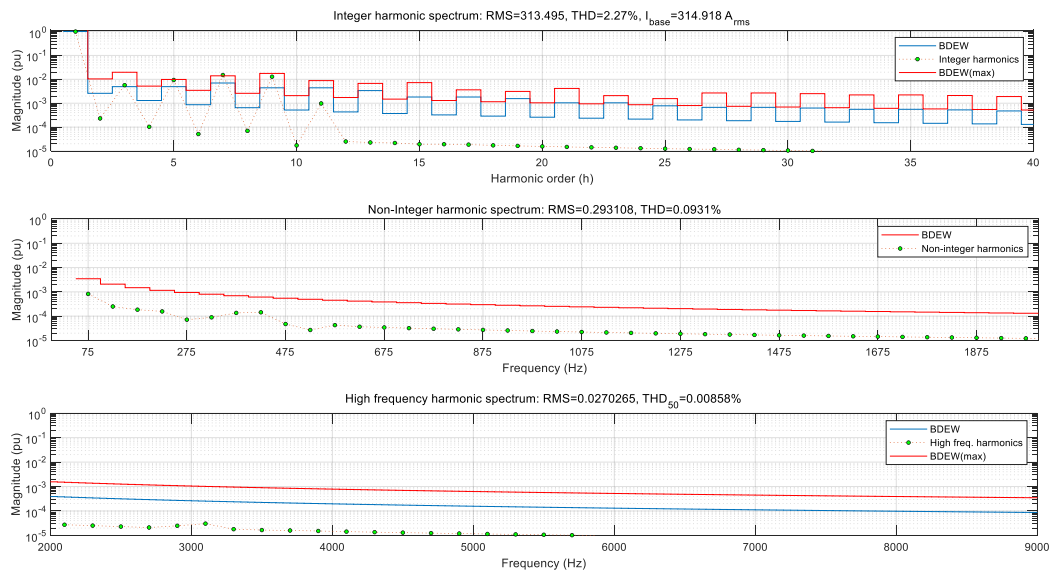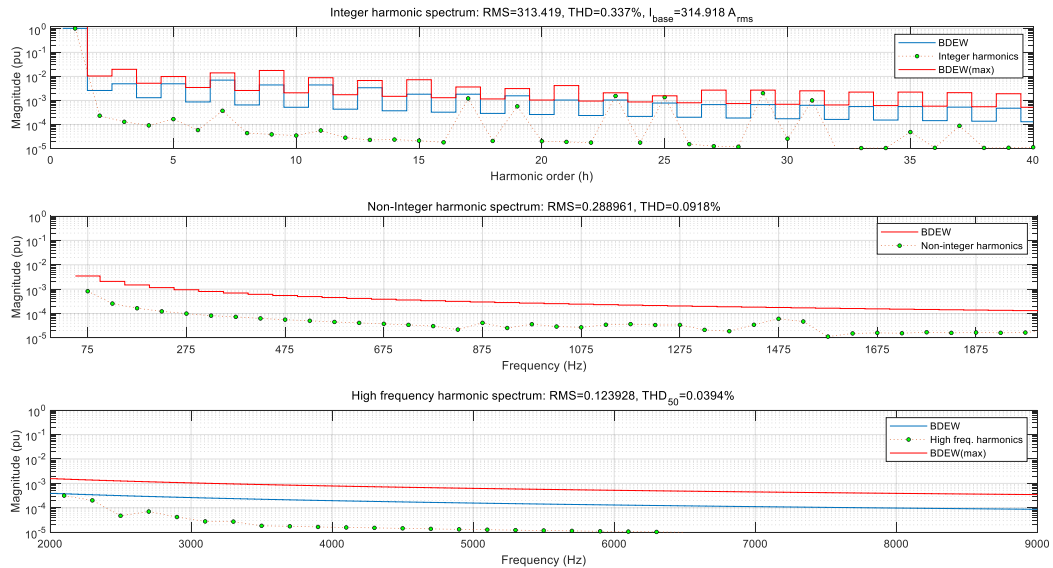

Fig. 9.7. Harmonic spectrum of current signal $i_{a\_PCC}(t)$ plotted against the BDEW harmonic current limits at OWPP level, SCR=20. This graphic considers the following conditions: SHE-PWM modulation and wind turbines operating at rated condition (wind direction: west or northwest, wind speed: 24 m/s).

Table 9.9. Compliance of the BDEW grid code of the current signal $i_{a\_PCC}(t)$ for SHE-PWM modulation and for different operation points.

Wind Direction	Wind Speed (m/s)	BDEW Compliance	Harmonics (h)	Infringement of restrictions given by BDEW		
				Harmonics of order $6n \pm 1$ $(n = 1 \cdots 4)$	Remaining Harmonics	Interharmonics
			>BDEW limit	>200% BDEW limit	>400% BDEW limit	>BDEW limit
West	24	Yes	23, 25, 29, 31	–	–	–
	16	Yes	29	–	–	–
	12.5	Yes	–	–	–	–
	8	Yes	23, 25, 29, 31	–	–	–
NorthWest	24	Yes	23, 25, 29, 31	–	–	–
	16	Yes	23, 25, 29, 31	–	–	–
	12.5	Yes	–	–	–	–
	8	Yes	23, 25, 29, 31	–	–	–
North	24	Yes	23, 25, 29, 31	–	–	–
	16	Yes	–	–	–	–
	12.5	Yes	29	–	–	–
	8	Yes	23, 25, 29, 31	–	–	–

9.4.2 SHE-PWM modulation oriented techniques to improve Power Quality

For the case of SHE-PWM modulation techniques, the implementation of interleaving is not possible. Nevertheless, it is possible to use other techniques with the aim of improving the harmonic emission of the OWPP. Two techniques are described next.

The first technique is to add switching angles to the particular solution of SHE-PWM presented in this dissertation. The addition of these switching angles can be used to eliminate risky harmonics, harmonics approaching the maximum limit restricted by the grid code, such as the harmonic of order 25th depicted in Fig. 9.7.

The second technique is by means of changing the operation point of wind turbines, which can be implemented by changing the DC-link voltage setpoint of the GSC of each WT, the reactive power setpoint of each WT or a combination of both strategies. This is done with the aim of operating with amplitude modulation indexes that result in a lower harmonic distortion level or in the reduction of specific harmonics at the PCC point of the OWPP. Examples of harmonics to reduce are:

- Harmonics that exceed the limits imposed by the grid code.
- Low order harmonics.
- Harmonics amplified by the electrical infrastructure of the OWPP.

Considering the previous ideas, it is important to analyze in detail the harmonic spectrum of the particular solution of SHE-PWM that has been implemented. Fig. 9.8 shows the harmonic spectrum for this type of modulation and for m_a values ranging from 0.8 to 1.16, approximately.
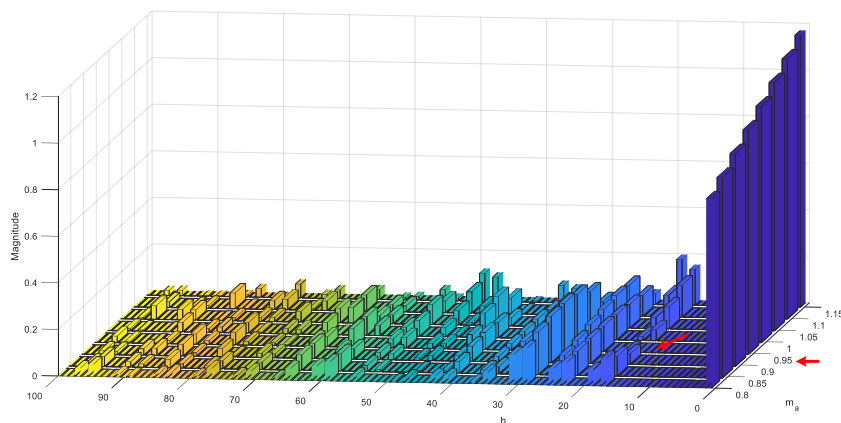
Fig. 9.8. Harmonic spectrum of SHE-PWM modulation for m_a values ranging from 0.8 to 1.16, approximately.

As depicted in Fig. 9.8, the harmonic emission of the OWPP base scenario can be reduced if the GSC of each wind turbine operates around an amplitude modulation index of 0.96. The reason for this statement is that harmonics of order 17th and 19th have small magnitudes for m_a values around 0.96. Additionally, the magnitude of harmonics of order 23rd, 25th, 29th, 31st, 35th, 37th and 41st barely change when compared with the operation point presented in subsection 9.4.1. Despite these aspects, it is still required to evaluate the compliance of the BDEW grid code for the scenario to study with this condition.

Another degree of freedom that can be implemented is the operation with different m_a values for wind turbines of the same radial. The aim is to take advantage of 180 degrees phase shift. This way, for each pair of wind turbines of the same radial, a specific harmonic

can be eliminated or be reduced. The elimination or reduction depends mainly on the magnitudes of harmonics to be added in such condition.

Table 9.10 gives the phase angle of some harmonics for m_a values ranging from 0.86 to 1.16, approximately. For this particular solution of SHE-PWM, a phase shift of 180 degrees is obtained for harmonics of order 17th and 19th when operating at m_a values around 0.96 and 1.06.

Table 9.10. Phase angle (in degrees) of harmonics of order 17th, 19th, 23rd and 25th for different m_a values ranging from 0.86 to 1.16, approximately.

Phase angle (Degrees)		Amplitude modulation index m_a						
		0.8633	0.9142	0.9651	1.0160	1.0670	1.1179	1.1688
Harmonic (h)	17	0	0	0	-180	-180	-180	0
	19	0	0	0	-180	-180	-180	0
	23	0	0	0	0	0	0	0
	25	0	0	0	0	0	0	180

Furthermore, Fig. 9.8 shows that the magnitude of the harmonic of order 17th is very similar for both amplitude modulation indexes. Hence, it is possible that this harmonic will be highly reduced for this scenario. Despite these aspects, it is still required to evaluate the compliance of the BDEW grid code for the scenario under study (with these conditions) and if any other factor could make this idea to be rejected.

Two case studies are given next to exemplify the previous proposals. Before analyzing these case studies, it is worth to emphasize that the variation of the operation point of the wind turbines is not straightforward. For some cases, the implementation of these complementary techniques may not be possible due to several factors. Some of these factors are:

- The particular solution of SHE-PWM modulation.
- The characteristics of the OWPP (e.g. resonances).
- Wind conditions.
- Grid codes.
- Specific conditions required by the grid operator, wich are dependant on power demand, grid events, and other factors.

Case Study 9.1: Change of the DC-link voltage setpoint of GSCs

This case study presents the results when wind turbines operate with amplitude modulation indexes almost equal to 0.96. This m_a value is obtained by means of decreasing the setpoint of the DC-link bus voltage of the grid side converters from a value of 5700 V (OWPP base scenario given in chapter 7) to a value of 5400 V. For this solution, the DC-link Bus voltage is modified slowly (low ramp variation) under certain limits until reaching the desired new DC-link voltage setpoint.

Fig. 9.9 shows the amplitude modulation index and the phase angle of the twelve wind turbines for the rated condition (e.g. wind speed of 24 m/s). Fig. 9.9(a) corroborates that the amplitude modulation index of each wind turbine is almost equal to 0.96.

(a)   (b)

Fig. 9.9. Amplitude modulation index (m_a) and phase angle ($\theta + \delta$) of each wind turbine for case study 9.1. (a) Amplitude modulation index. (b) Phase angle.

Fig. 9.10 shows the harmonic spectrum of the current signal $i_{a\_PCC}(t)$ for this case study. The figure also shows the current harmonic limits imposed by the BDEW grid code at OWPP level. According to this figure, the compliance of the BDEW grid code is fulfilled since the limits imposed by the BDEW regulations are not infringed. Integer harmonics, interharmonics and high frequency harmonics lay within the allowable limits.

Fig. 9.10. Harmonic spectrum of current signal $i_{a\_PCC}(t)$ plotted against the BDEW harmonic current limits at OWPP level, SCR=20. This graphic considers the following conditions: SHE-PWM modulation, parameters of the OWPP base scenario, DC-link voltage setpoint for case study 9.1, and wind turbines operating at rated condition (wind direction: west or northwest, wind speed: 24 m/s).

Table 9.11 gives the THDi values of the current signal $i_{a\_PCC}(t)$ for this case study. This table also shows the THDi values when WTs operate with SHE-PWM modulation and a

DC-link voltage of 5700V (subsection 9.4.1). To give an example, the THDi value for the low frequency subgroup is reduced from a value of 0.337% to a value of 0.304%.

Table 9.11. Comparison of the THDi values of the current signal $i_{a\_PCC}(t)$ for GSCs operating with a DC-link bus voltage of 5400 V (Case Study 9.1) and 5700 V (Base scenario). Both scenarios consider SHE-PWM modulation.

DC-link Bus Voltage (V)	Low Frequency		Interharmonics		High Frequency	
	RMS value (A)	THDi (%)	RMS value (A)	THDi (%)	RMS value (A)	THDi (%)
5400	313.418	0.304	0.2888	0.0917	0.1648	0.0523
5700	313.419	0.337	0.2889	0.0918	0.1239	0.0394

Fig. 9.11 shows the comparison of the spectrums of the current signal $i_{a\_PCC}(t)$ for both scenarios, base scenario and case study 9.1. This figure shows a reduction of harmonics of order 17th and 19th. The harmonic of order 17th is reduced from a value of 0.12% to a value of 0.01%. For the case of harmonic 19th, this is reduced from a value of 0.06% to a value of 0.017%. The variation of the magnitude of remaining harmonics is lower compared to these two harmonics, as shown in Fig. 9.11.

(a)

(b)
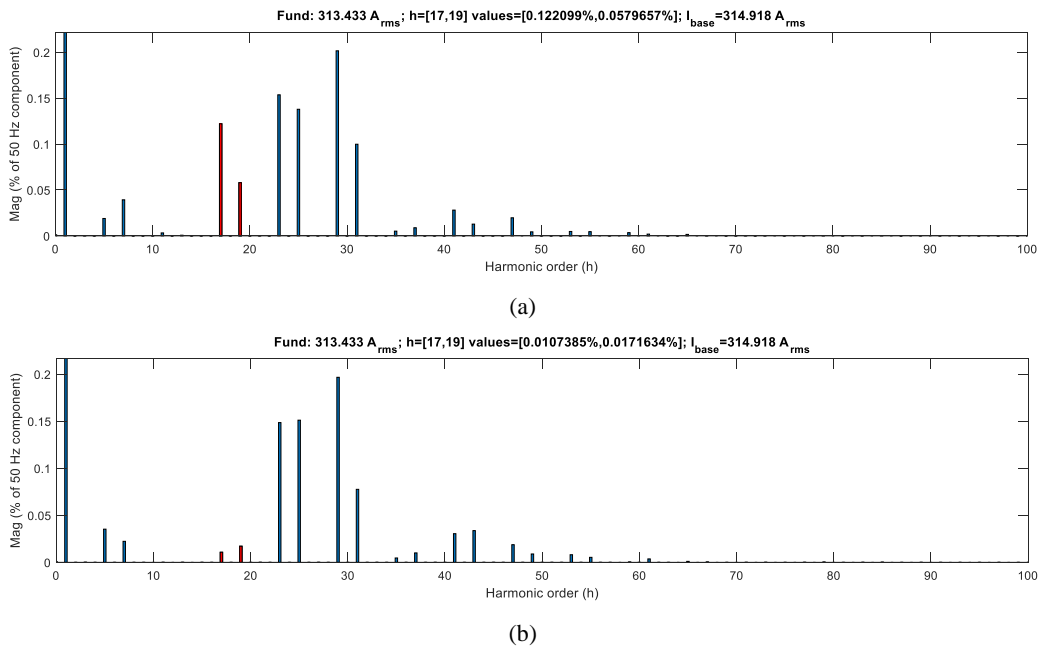
Fig. 9.11. Harmonic spectrum of current signal $i_{a\_PCC}(t)$ for the last 20 ms time window. (a) DC-link bus voltage equal to 5700 V. (b) DC-link bus voltage equal to 5400 V, case study 9.1.

Case Study 9.2: Change of the reactive power setpoint of each wind turbine

This case study presents the results when wind turbines operate with amplitude modulation indexes ranging from 0.92 to 0.97, approximately. The m_a values are obtained by means of changing the reactive power setpoint of each wind turbine. The OWPP is working with a power factor almost equal to one. Each wind turbine injects the rated active power (5MW). Some wind turbines are injecting reactive power while others are absorbing

reactive power. Table 9.12 gives the active power, reactive power and power factor values of the OWPP and of each wind turbine.

Table 9.12. Active-, reactive power and power factor values of the OWPP and each wind turbine for case study 9.2.

Active power, reactive power and power factor values of the OWPP		
$P_{PCC} = 56.6157$ MW	$Q_{PCC} = 6.7476$ MVAR	$\text{pf}_{PCC} = 0.9929 \quad (\text{pf} \approx 1)$
Reactive power and power factor of each WT		
Capacitive Mode	Inductive Mode	Capacitive Mode
$Q_{WT1} = 1.1866$ MVAR	$Q_{WT2} = -0.2505$ MVAR	$Q_{WT3} = 0.4663$ MVAR
$\text{pf}_{WT1} = 0.9730$	$\text{pf}_{WT2} = 0.9987$	$\text{pf}_{WT3} = 0.9957$
$Q_{WT4} = 1.1866$ MVAR	$Q_{WT5} = -0.2505$ MVAR	$Q_{WT6} = 0.4663$ MVAR
$\text{pf}_{WT4} = 0.9730$	$\text{pf}_{WT5} = 0.9987$	$\text{pf}_{WT6} = 0.9957$
$Q_{WT7} = 1.1866$ MVAR	$Q_{WT8} = -0.2505$ MVAR	$Q_{WT9} = 0.4663$ MVAR
$\text{pf}_{WT7} = 0.9730$	$\text{pf}_{WT8} = 0.9987$	$\text{pf}_{WT9} = 0.9957$
$Q_{WT10} = 1.1866$ MVAR	$Q_{WT11} = -0.2505$ MVAR	$Q_{WT12} = 0.4663$ MVAR
$\text{pf}_{WT10} = 0.9730$	$\text{pf}_{WT11} = 0.9987$	$\text{pf}_{WT12} = 0.9957$

Fig. 9.12 shows the amplitude modulation index and the phase angle of the twelve wind turbines. Fig. 9.12(a) corroborates the values of the amplitude modulation index of each wind turbine for this case study.
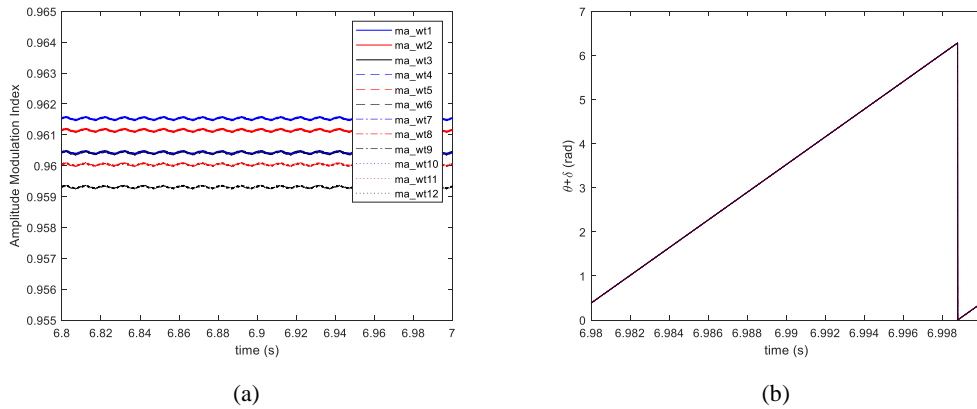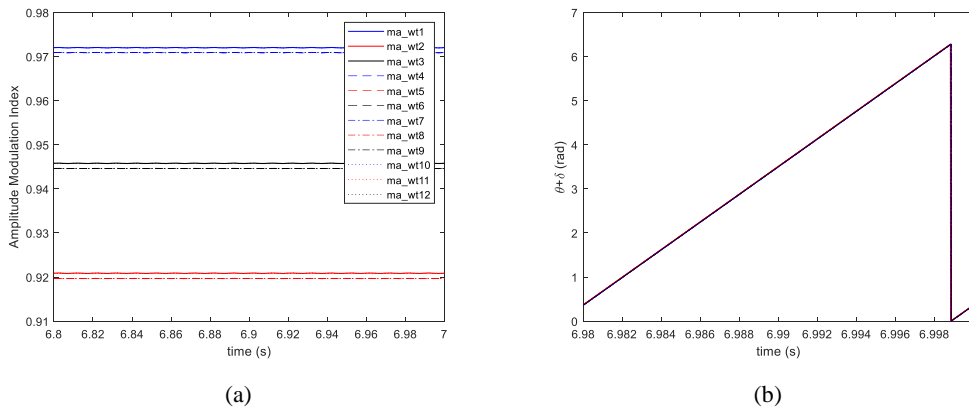

Fig. 9.12. Amplitude modulation index (m_a) and phase angle ($\theta + \delta$) of each wind turbine for case study 9.2. (a) Amplitude modulation index. (b) Phase angle.

Fig. 9.13 shows the harmonic spectrum of the current signal $i_{a\_PCC}(t)$ for this case study. The figure also shows the current harmonic limits imposed by the BDEW grid code at OWPP level. According to this figure, the compliance of the BDEW grid code is fulfilled since the limits imposed by the BDEW grid code are not infringed. Integer harmonics, interharmonics and high frequency harmonics lay within the allowable limits.

Table 9.13 gives the THDi values of the current signal $i_{a\_PCC}(t)$ for this case study. This table also shows the THDi values presented in subsection 9.4.1 for the rated condition (e.g. wind speed of 24 m/s). The THDi value for the low frequency subgroup is reduced from a value of 0.337% to a value of 0.318%.

Similar to the previous case, harmonics of order 17th and 19th are reduced. The harmonic of order 17th is reduced from a value of 0.12% to a value of 0.06%. For the case of harmonic 19th, this is reduced from a value of 0.06% to a value of 0.032%. The variation of the magnitude of remaining harmonics is lower compared to these two harmonics.
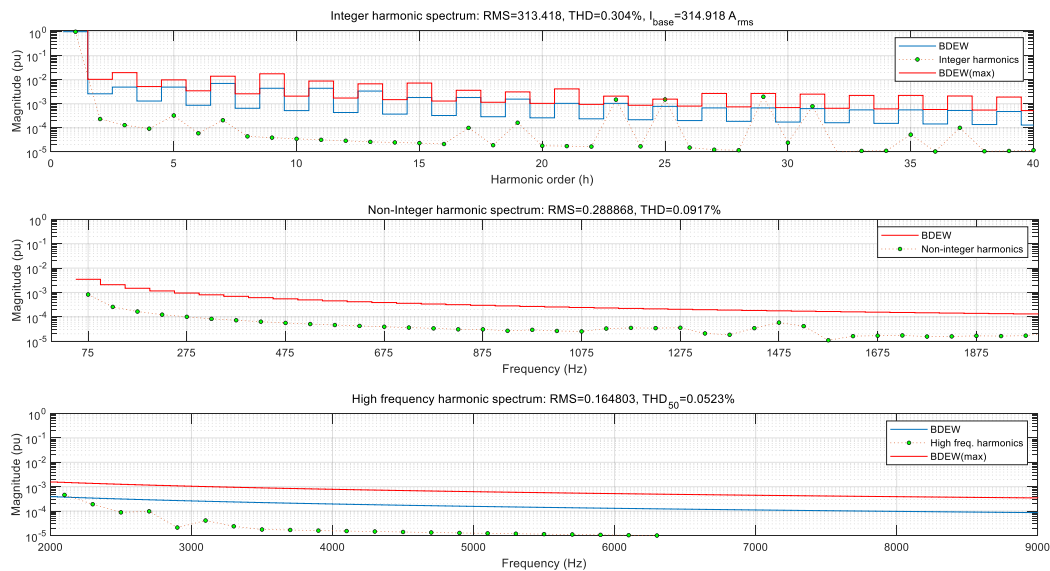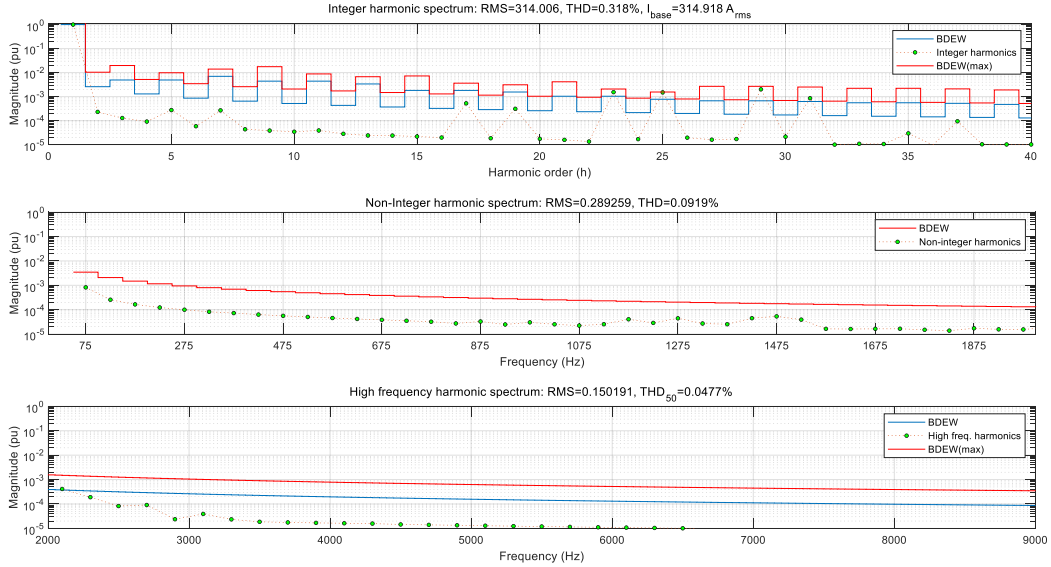

Fig. 9.13. Harmonic spectrum of current signal $i_{a\_PCC}(t)$ plotted against the BDEW harmonic current limits at OWPP level, SCR=20. This graphic considers the following conditions: SHE-PWM modulation, parameters of the OWPP base scenario and wind turbines working at operation points given by Table 9.12.

Table 9.13. Comparison of the THDi values of the current signal $i_{a\_PCC}(t)$ for case study 9.2 and for the base scenario.

Scenario	Low Frequency		Interharmonics		High Frequency	
	RMS value (A)	THDi (%)	RMS value (A)	THDi (%)	RMS value (A)	THDi (%)
Case Study 9.2	314.006	0.318	0.2892	0.0919	0.1501	0.0477
Base Scenario	313.419	0.337	0.2889	0.0918	0.1239	0.0394

Even though the THDi values for this case study are reduced compared to the results presented in subsection 9.4.1, it is worth to point out that this solution is the most restrictive since it highly depends on wind conditions, grid codes and specific requirements demanded by the grid operator. In this sense, the technical solution presented in case study 9.1 is more advantageous compared with case study 9.2. For case study 9.1, proper design of the DC-link (DC-bus capacitors, crowbar, voltage control loops, etc.) of the GSC must be done to be able to change the voltage setpoint of the DC-link over a specified range.

9.4.3 SHE-PWM modulation oriented filter

In this subsection, the GSC connection filter is redesigned by taking into account the harmonic spectrum of SHE-PWM modulation. The redesign of the LCL-rl filter is performed by following the methodology presented in reference [90]. Table 9.14 gives the parameters of the LCL-rl filter for the particular solution of SHE-PWM.

Table 9.14. Parameters of the SHE-PWM modulation oriented LCL-rl filter (Simulink®-based model). Source [90].

SHE-PWM modulation oriented LCL-rl filter			
$L_{c\_wt} = 675\,\mu H$	$C_{f\_wt} = 365\,\mu F$	$L_{d\_wt} = 95\,\mu H$	$R_{d\_wt} = 50\,\Omega$

Fig. 9.14 shows the SHE-PWM spectrum and the Bode plot of the transfer function $I_{a\_PCC}^{+}(s)\big/V_{ab\_GSC1}^{+}(s)$, which is also valid for the negative-sequence. The SHE-PWM spectrum is depicted for several stacked m_a values.

As shown in Fig. 9.14, the LCL-rl filter is designed so that the resonance frequency lays close to the harmonic of order 9th. This is done to guarantee that no excitation is possible since the modulation eliminates the surrounding harmonics. Furthermore, the LCL-rl filter is designed so that the anti-resonant frequency lays on the 17th harmonic, which is the first non-eliminated harmonic that appears in the current. The attenuation level for this harmonic is high, almost equal to -120 dB.

(a)

(b)
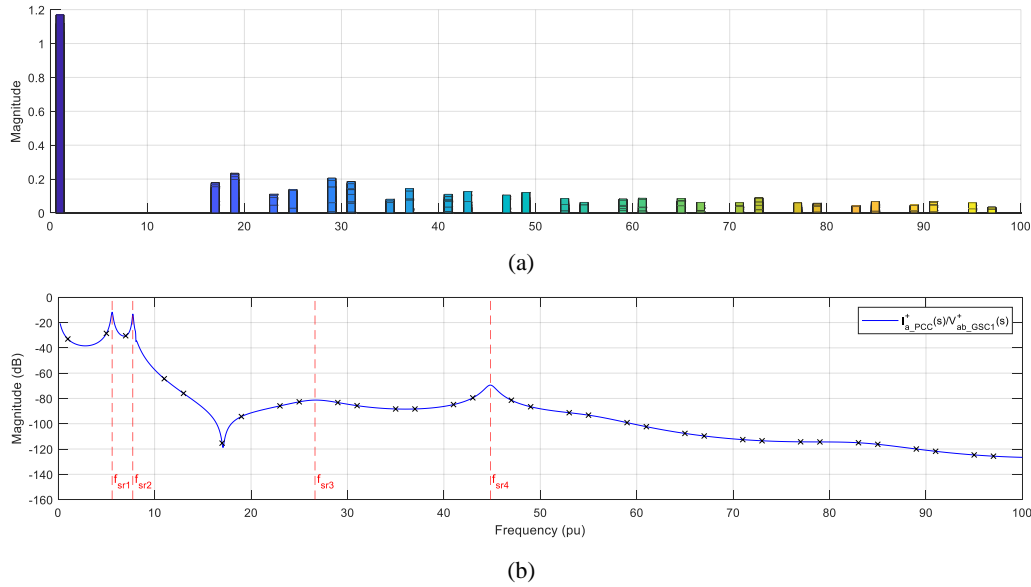
Fig. 9.14. SHE-PWM spectrum and Bode plot of the transfer function $I_{a\_PCC}^{+}(s)\big/V_{ab\_GSC1}^{+}(s)$. (a) SHE-PWM spectrum with several stacked m_a values, normalized line-to-line voltage of the GSC. (b) Bode plot of transfer function $I_{a\_PCC}^{+}(s)\big/V_{ab\_GSC1}^{+}(s)$. Frequency values of series resonances: $f_{sr1} = 279.547\,\text{Hz}$, $f_{sr2} = 402.761\,\text{Hz}$, $f_{sr3} = 1331.6966\,\text{Hz}$, $f_{sr4} = 2241.1881\,\text{Hz}$.

Fig. 9.15 shows the harmonic spectrum of the current signal $i_{a\_PCC}(t)$ at rated condition. The figure also shows the current harmonic limits imposed by the BDEW grid code at OWPP level. According to this figure, the compliance of the BDEW grid code is fulfilled since the restrictions imposed by this grid code are not infringed. Integer harmonics, interharmonics and high frequency harmonics lay within the allowable limits.
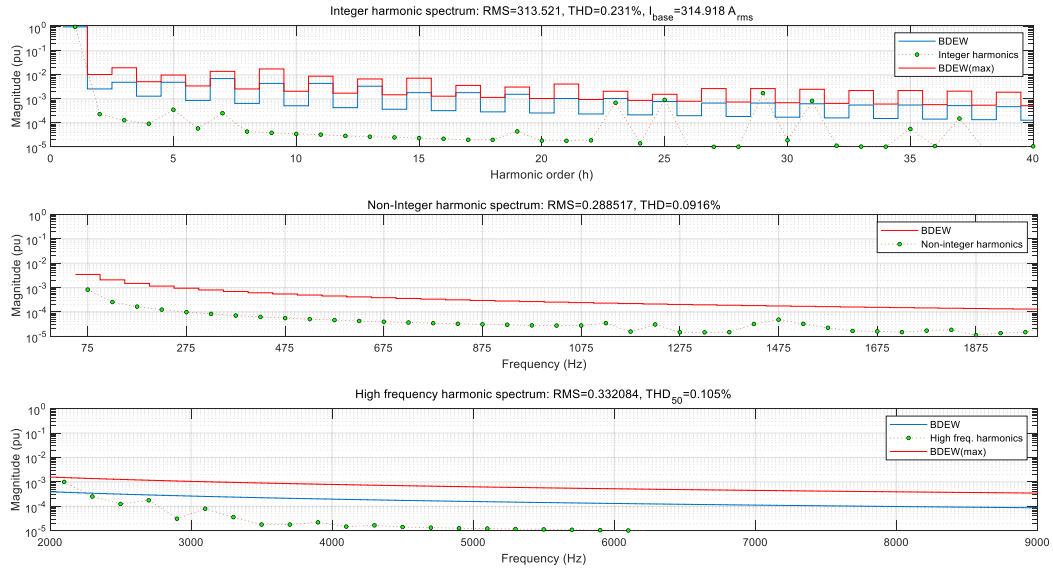
Fig. 9.15. Harmonic spectrum of current signal $i_{a\_PCC}(t)$ plotted against the BDEW harmonic current limits at OWPP level, SCR=20. This graphic considers the following conditions: SHE-PWM modulation, GSC connection filter of Table 9.14 and wind turbines operating at rated condition (wind direction: west or northwest, wind speed: 24 m/s).

Table 9.15 gives the THDi values of the current signal $i_{a\_PCC}(t)$ for this scenario. This table also gives the THDi values of previous cases for comparative purposes. It can be seen that lower THDi values are obtained when considering the SHE-PWM oriented filter of Table 9.14.

Table 9.15. Comparison of the THDi values of the current signal $i_{a\_PCC}(t)$ considering SHE-PWM oriented filter, case study 9.1, case study 9.2, and base scenario.

Scenario	Low Frequency		Interharmonics		High Frequency	
	RMS value (A)	THDi (%)	RMS value (A)	THDi (%)	RMS value (A)	THDi (%)
SHE-PWM oriented filter and DC-link voltage of 5400 V	313.521	0.231	0.2885	0.0916	0.3320	0.105
Case Study 9.1	313.418	0.304	0.2888	0.0917	0.1648	0.0523
Case Study 9.2	314.006	0.318	0.2892	0.0919	0.1501	0.0477
Base Scenario	313.419	0.337	0.2889	0.0918	0.1239	0.0394

The THDi value for the low frequency subgroup is further reduced to a value of 0.231%. Fig. 9.16 shows the spectrum of the current signal $i_{a\_PCC}(t)$ for this scenario and for the last 20 ms time window, for better visualization. As depicted in this figure, harmonics of order 17th and 19th are highly reduced compared to case study 9.1, see Fig. 9.16 and Fig. 9.11(b).

It is worth to point out that this solution has been tested with the control strategy presented in subsection 7.3.1 and that the GSCs have reached the steady-state. Finally, it can be concluded that the harmonic emission of the OWPP base scenario can be improved when considering the particular solution of SHE-PWM modulation and the parameters of the GSC connection filter given in Table 9.14.
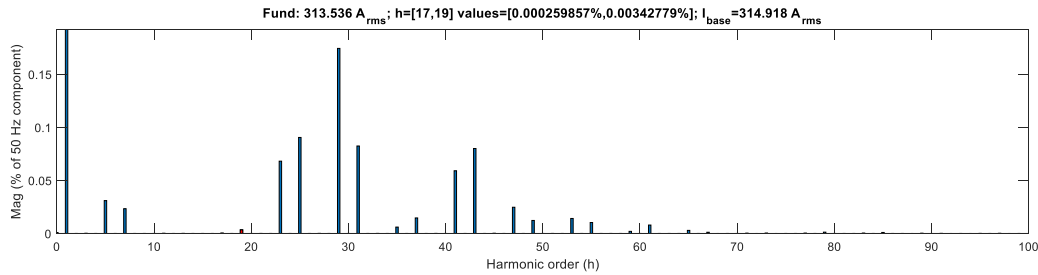
Fig. 9.16. Harmonic spectrum of current signal $i_{a\_PCC}(t)$ for the last 20 ms time window. SHE-PWM modulation oriented filter is considered for this scenario.

9.5 Chapter Summary

This chapter has presented the steady-state current-harmonic evaluation of the OWPP base scenario. The harmonic assessment has been performed by means of computing the spectrum of current signals, the THDi values and the fulfillment of the BDEW grid code. The following conclusions can be pointed out for this chapter.

The harmonic assessment must be carried out not only at wind turbine level but also at wind farm developer level (OWPP level). As presented in section 9.3 for WTs operating with the commonly used CB-PWM modulation, the harmonic evaluation at wind turbine level gives low THDi values and the fulfillment of the BDEW grid codes. However, the fulfillment of the grid code might not be achieved for several operation points when performing the harmonic evaluation for an offshore wind farm with resonances at low frequency values. Thus, additional wind turbine analyses for specific applications (i.e. wind farm layout, transmission link distance, short-circuit ratio of the grid, and other characteristics of the electrical network) are needed.

An example of the aforementioned application is carried out in subsection 9.3.2 for the OWPP base scenario presented in chapter 7. For this scenario, three important factors heavily affect the current harmonic emission and the compliance of the BDEW grid code at the PCC point of the OWPP. First, the magnitude of the harmonics injected by the GSCs. Second, the attenuation level of the system around these harmonics, especially if a resonance matches or is close to a certain harmonic or harmonics. Third, the way harmonics of the same order are added at a specific point of the OWPP. The summation of harmonics depends mainly on the operation point of the wind turbines and the phase shift of the electrical infrastructure of the OWPP that sees each WT.

To improve the harmonic emission of the OWPP and the compliance of the grid code in terms of harmonics, a modulation strategy that does not inject low-order harmonics is more suited to be used for OWPPs having a resonance at a low-frequency value (around 100Hz to 400 Hz). In section 9.4, WT manufacturer oriented solutions are proposed with the aim of improving the harmonic emission of the OWPP. The implementation of the particular

solution of SHE-PWM modulation is presented together with complementary solutions to further improve the harmonic emission of the OWPP.

Among the complementary solutions, the variation of the operation point of the wind turbines is performed to make the WTs operate at amplitude modulation indexes that improve the harmonic emission of the OWPP. This can be implemented by means of changing the DC-link voltage setpoint of the GSC of each wind turbine, the reactive power setpoint of each WT or a combination of both strategies. The objective is to operate with amplitude modulation indexes that result in a lower harmonic distortion level or in the reduction of specific harmonics at the PCC point of the OWPP. Examples of harmonics to reduce are harmonics that exceed the limits imposed by the grid code, low-order harmonics or harmonics that are amplified by the resonances of the OWPP.

From the complementary solutions, it is worth to point out that the change of the reactive power setpoint is the most restrictive since it highly depends on wind conditions, grid codes and specific requirements demanded by the grid operator. In this sense, the change of the DC-link voltage setpoint of the GSC of each wind tubine is more advantageous. For this solution, proper design of the DC-link of the GSC must be done to be able to change the voltage setpoint of the DC-link over a specified range.

Finally, the harmonic emission of the OWPP can be improved by means of the redesign of the GSC connection filter according to the harmonic spectrum of SHE-PWM modulation, as presented in subsection 9.4.3. This last case, together with the complementary solutions presented for SHE-PWM, results in the lowest THDi values for the scenarios studied so far.

Chapter 10

Conclusions and Future Work

This chapter details the conclusions, contributions, and guidelines for future work within the framework of this Ph.D. thesis.

10.1 Conclusions

After presenting the work done in this Ph.D. dissertation, the following general conclusions can be summarized.

To account for an appropriate harmonic assessment of an OWPP, it is required to consider three important factors. First, an accurate representation of the harmonics injected by the wind turbines, which clearly depend on modulation strategy and control loops of the GSCs. Second, the frequency-dependent characteristic of installed passive components, e.g. submarine cables and transformers. The third factor to consider is the evaluation of different operation points for each wind turbine, not only for the rated condition. These operation points depend on power factor requirements, wind conditions, and location of each wind turbine. The most important points to support the requirement of these factors are described next.

- A wind turbine harmonic model has been proposed to represent the behavior of a wind turbine and its harmonics, up to 5 kHz. The distinctive structure of this model consists of implementing a voltage source containing both the fundamental

component and the harmonics emitted by the converter. According to the validation results of the wind turbine harmonic model, it can represent reasonably well the wind turbine in normal operation. Three main advantages are identified: relative simplicity of implementation, reduction in the computational burden and the possibility to disclose the simulation model to third parties.

- Wind turbine wake effect (Jensen's model) has been added to the Simulink®-based model to estimate the mean wind speed at each wind turbine. This estimation is computed according to the spatial distribution of the OWPP and wind conditions, i.e. wind speed and wind direction. This allows to represent the different estimated active power generation of the wind turbines according to reality.

- The FD-STC model has been presented for the representation of the power transformers in the Simulink®-based model. The transformer model includes four main parameters. These are the frequency-dependent behavior of the winding resistance, the impedance of the transformer core, stray capacitances and the zero-sequence impedance. The impedance of the transformer core is considered linear. Guidelines for transformer model parameterization have been described in chapter 5. These approaches are manufacturer datasheets, parameter estimation, design information, and laboratory tests. In this Ph.D. thesis, emphasis has been paid to a combination between datasheets and parameter estimation mainly due to the lack of information to represent accurately the behavior of a transformer in frequency.

- The FDPi model has been proposed to reproduce the behavior of a three-core submarine cable for frequencies up to 5 kHz. The model consists of N cascaded FDPi sections. Each section incorporates the magnetic coupling, the electrical coupling, the frequency-dependent variation of the conductive layers by means of Foster equivalent networks and the loss mechanism of the cable. All these four points allow an easy implementation of the model by means of discrete RLC components. Parameterization of the model is described in detail and is performed according to analytical equations, which includes skin effect. The validation of the FDPi model is performed with a reference model, the ULM. The results obtained from this validation process show a very good agreement of the FDPi model in representing the behavior of a three-core submarine cable for frequencies up to 5 kHz.

- Two complementary modeling approaches have been presented to model and perform harmonic analysis in AC OWPPs. These are the Simulink®-based model, which implements and connects the models described from chapter 3 to 6, and the analytical sequence network based model of the passive components of an OWPP. The aim of the Simulink®-based model is to determine voltage and current distortion at different points along the OWPP, the BDEW grid code compliance in terms of harmonics, and the design and evaluation of technical solutions to potential problems. On the other hand, the purpose of the sequence network model is to perform a series of studies whose computation is not an easy task to be performed by the Simulink®-based model in terms of post-processing and time

consumption. Among these studies are the frequency response and parameter sensitivity studies of an OWPP.

The definition of an OWPP base scenario is required for the parameterization and connection of the models of the power components. The base scenario was defined taking into account information of a real OWPP. The main conclusions from the analysis of the OWPP base scenario are the following.

- The electrical infrastructure of the OWPP base scenario does not cause a different phase shift (for frequencies up to 5 kHz) among the harmonics injected by the GSCs. In this sense, if the GSCs work at the same operation point, the magnitude of harmonics of the same order will be increased at the PCC point because these harmonics are added in phase. This occurs mainly because the OWPP base scenario is symmetrical. Results may be different when considering an asymmetrical OWPP or a large OWPP.

- Series resonances f_{sr1} to f_{sr4} have been identified together with the main components that create them. The identification has been performed with the aid of participation factor technique. According to the studied OWPP, resonance f_{sr1} is created by the capacitance of the transmission cable and the equivalent inductance of the grid model, which depends on the SCR value. Resonance f_{sr2} is created by the GSC connection filter. Resonance f_{sr3} is the second series resonance of the transmission cable (60 km long cable). Finally, resonance f_{sr4} is mainly created by the capacitance of the submarine cables of the collection network and the short-circuit inductance of the transformers, OST and WTTs.

- The connection of the OWPP to a weak grid tends to locate the resonance f_{sr1} to lower frequency values. This may cause a potential problem in terms of voltage and current distortion at the PCC point if WTs inject low order harmonics. It may also cause a potential problem in terms of the stability of the entire OWPP. In other words, it may not be possible for WTs to operate with a fast dynamic response while ensuring the stability of the entire OWPP unless special control strategies (such as active damping loops) are implemented.

- For WTs operating with the commonly used CB-PWM modulation, the harmonic evaluation at wind turbine level gives low THDi values and the fulfillment of the BDEW grid codes. However, the fulfillment of the grid code is not achieved for several operation points when performing the harmonic evaluation at the PCC point of the OWPP. This is mainly due to resonances at low frequency values.

- For CB-PWM, the total harmonic current distortion remains about the same as a function of the produced active power; whereas the total interharmonic current distortion presents an increase with produced active power.

- A modulation strategy that does not inject low-order harmonics, such as the particular solution of SHE-PWM presented in this research work, is more suited to

be used for this base scenario. This is mainly because of the presence of resonance f_{sr1} and the way low-order harmonics are added (in phase).

- For SHE-PWM, the total harmonic current distortion (in rms amperes) does not remains constant as in the case of CB-PWM. There are certain operation points, e.g. the ones with estimated active power generation given by wind speeds of 12.5 and 16 m/s, in where the THDi values are lower. For the case of interharmonics, the total interharmonic current distortion presents an increase with produced active power.

- The implementation of the particular solution of SHE-PWM modulation together with complementary solutions have shown a further improvement of the harmonic emission of the OWPP. Among the complementary solutions, the variation of the operation point of the wind turbines has been performed to make the WTs operate with amplitude modulation indexes that result in a lower harmonic distortion level or in the reduction of specific harmonics at the PCC point of the OWPP. This has been implemented by means of changing the DC-link voltage setpoint of the GSC of each wind turbine, the reactive power setpoint of each WT or a combination of both strategies.

- The change of the DC-link voltage setpoint of the GSC of each wind tubine is more advantageous. For this solution, proper design of the DC-link of the GSC must be done to be able to change the voltage setpoint of the DC-link over a specified range. On the contrary, the change of the reactive power setpoint is the most restrictive since it highly depends on wind conditions, grid codes and specific requirements demanded by the grid operator.

- The harmonic emission of the OWPP is improved by means of the redesign of the GSC connection filter according to the harmonic spectrum of SHE-PWM modulation. This last case, together with the complementary solutions presented for SHE-PWM, results in the lowest THDi values for all the scenarios evaluated.

In general and applicable not only for the OWPP base scenario, the following main conclusions can be stated:

- The harmonic assessment must be carried out not only at wind turbine level but also at wind farm developer level (OWPP level). Additional wind turbine analyses for specific applications (i.e. wind farm layout, transmission link distance, short-circuit ratio of the grid, and other characteristics of the electrical network) are needed.

- Three important factors heavily affect the current harmonic emission and the compliance of the BDEW grid code at the PCC point of the OWPP. First, the magnitude of the harmonics that are injected by the GSCs. Second, the attenuation level of the system around these harmonics, especially if a resonance matches or is close to a certain harmonic or harmonics. Third, the way harmonics of the same order are added at a specific point of the OWPP. The summation of harmonics

depends mainly on the operation point of the wind turbines and the phase shift of the electrical infrastructure of the OWPP that sees each WT.

- To improve the harmonic emission of an OWPP and the compliance of the grid code in terms of harmonics, a modulation strategy that does not inject low-order harmonics is more suited to be used for OWPPs having a resonance or resonances at low-frequency values (e.g. around 100Hz to 600 Hz).

10.2 Scientific Contributions

As a result of this work, one journal paper and a conference paper have been accepted.

- Ruiz, C.; Abad, G.; Zubiaga, M.; Madariaga, D.; Arza, J. Frequency-Dependent Pi Model of a Three-Core Submarine Cable for Time and Frequency Domain Analysis. *Energies* **2018**, *11*, doi:10.3390/en11102778.
- Ruiz, C.; Zubiaga, M.; Abad, G.; Madariaga, D.; Arza, J. Validation of a Wind Turbine Harmonic Model based on the Generic Type 4 Wind Turbine Standard. *20Th Eur. Conf. Power Electron. Appl.* **2018**, 10.

10.3 Future Lines

Additionally, possible future lines to work into can be listed as follows:

- A comparison of the simulation time between the proposed wind turbine harmonic model and a detailed representation of the wind turbine, e.g. a wind turbine model oriented to perform EMT studies. Following this line, a deep study must be performed to analyze the transient state of the solutions presented in chapter 9, also with the aid of a detailed EMT representation of the wind turbine.
- It will be valuable to perform an experimental characterization of the LCL-rl filter at Ingeteam's facilities. In this sense, the frequency-dependent behavior of the LCL-rl filter can be incorporated into the harmonic analysis of the OWPP scenarios that will be required to model.
- More modulation schemes can be evaluated for the OWPP base scenario. For example, different particular solutions of SHM-PWM modulation, which is briefly described in subsection 3.3.2, can be implemented and be compared with the results presented in chapter 9.
- The main power components are modeled to represent harmonics up to 5 kHz. This frequency can be set to a higher value, e.g. 9 kHz to cover all the frequency range defined by the BDEW technical guideline. In this sense, the modeling of the main

power components must be extended with their particular requirements. For submarine cables and power transformers, the models presented in chapters 5 and 6 have to be modified to account for a good representation of the frequency-dependent effects at higher frequencies. For the case of the wind turbine harmonic model, the harmonic representation of the grid side converter has to be extended but the model itself will not require to be modified (at least conceptually).

- The implementation of advanced control strategies and/or additional filtering capabilities to reduce the unwanted oscillations that can be noticed in the results presented in chapter 9. As commented in subsection 3.3.3, a possible solution to further reduce these unwanted oscillations is the notch-filter-based active damping method. Another possible solution is by implementing notch filters to the measured signals in dq-frame that are fed back to the current controller. For both cases, stability has to be evaluated.

- Following the previous point, a complementary analysis addressing the stability of the OWPP will be interesting. For this future task, the analytical sequence-network based model presented in section 7.4 can be modified and upgraded to incorporate the control algorithm of the grid side converters. The sequence network parameters must be converted to other representation domain, e.g. parameters in dq frame. The converter can be represented, as suggested in many references cited in chapter 1, as a Norton equivalent. The equivalent impedance of this representation should include not only passive components of the wind turbine but also the grid side converter internal impedance given by the control scheme and operation point. The upgraded analytical tool will allow to study the stability of the system and will provide guidelines to tune the controllers appropriately. In general, the tool will provide a deeper understanding of the system.

References

1.   GWEC *Global Wind Report 2018*; 2019;

2.   WindEurope *Offshore Wind in Europe. Key trends and Statistics 2018*; 2018;

3.   Ackermann, T. *Wind Power in Power Systems*; 2nd ed.; John Wiley & Sons, Ltd, 2012; ISBN 0815505752.

4.   Anaya-Lara, O. *Offshore Wind Energy Generation. Control, Protection and Integration to Electrical Systems*; Wiley, 2014; ISBN 9781118701539.

5.   Kocewiak, L. H. Harmonics in large offshore wind farms, Aalborg University, 2012.

6.   Larumbe, L. B. Introduction to the Analysis of Harmonics and Resonances in Large Offshore Wind Power Plants. *2018 IEEE 18th Int. Power Electron. Motion Control Conf.* **2018**, 393–400.

7.   Xin, Z.; Wang, X.; Loh, P. C. Grid-Current Feedback Control for LCL-Filtered Grid Converters with Enhanced Stability. *IEEE Trans. Power Electron.* **2016**, *8993*, doi:10.1109/TPEL.2016.2580543.

8.   Uski-Joutsenvuo, S.; Niskanen, S. *Wind turbine models - Status report of model development and verification measurements*; 2012;

9.   Bradt, M.; Badrzadeh, B.; Camm, E.; Mueller, D.; Schoene, J.; Siebert, T.; Smith, T.; Starke, M.; Walling, R. Harmonics and Resonance Issues in Wind Power Plants. *2011 IEEE Power Energy Soc. Gen. Meet.* **2012**, 1–8.

10.   Kocewiak, Ł. H.; Álvarez, C.; Muszynski, P. Wind Turbine Harmonic Model and Its Application. Overview , Status and Outline of the new IEC Technical Report. In *14th International Workshop on Large-Scale Integration of Wind Power into Power System*; 2015; p. 6.

11.   CIGRE WG-02 *Guidelines for representation of network elements when calculating transients*; 1990;

12.   IEEE Working Group PES-TR7 *Modeling and Analysis of System Transients Using Digital Programs Part 2*; 1998;

13.   Martinez, J. A.; Mahseredjian, J.; Walling, R. a. Parameter determination: procedure for modeling system transients. *IEEE Power Energy Mag.* **2005**, *3*, 16–28, doi:10.1109/MPAE.2005.1507018.

14.   Siemens PSS-E Available online: http://w3.siemens.com/smartgrid/global/en/products-systems-solutions/software-solutions/planning-data-management-software/planning-simulation/pages/pss-e.aspx.

15.   Manitoba HVDC Research Centre PSCAD Available online: https://hvdc.ca/pscad/.

16.   Electric, G. PSLF - General Electric Available online: http://www.geenergyconsulting.com/insights/grid-planning-software-insights.

17. Powertech TSAT Available online: http://www.powertechlabs.com/areas-of-focus/software-technologies/dsatools-software/transient-security-assessment-tool/.

18. Corporation, P. PowerWorld Available online: https://www.powerworld.com/.

19. EEUG ATP-EMTP Available online: http://eeug-test.hostingkunde.de/.

20. Solutions, P. EMTP-RV Available online: http://emtp-software.com/.

21. DIGSILENT PowerFactory Available online: http://www.digsilent.de/index.php/products-powerfactory.html.

22. MathWorks Simscape Power Systems Available online: https://es.mathworks.com/products/simpower.html.

23. EMD WindPro Available online: https://www.emd.dk/windpro/.

24. DTU WAsP Available online: http://www.wasp.dk/.

25. WindSim Available online: https://windsim.com/.

26. ReSoft WindFarm Available online: http://www.resoft.co.uk.

27. Zubiaga, M.; Abad, G.; Barrena, J. A. *Energy Transmission and Grid Integration of AC Offshore Wind Farms*; Intech, 2012; ISBN 978-953-51-0368-4.

28. Yang, K. On Harmonic Emission, Propagation and Aggregation in Wind Power Plants, Lulea University of Technology, 2015.

29. Glasdam, J. B. Harmonics in Offshore Wind Power Plants Employing Power Electronic Devices in the Transmission System, Aalborg University, 2015.

30. Ghassemi, F.; Koo, K. Equivalent Network for Wind Farm Harmonic Assessments. *IEEE Trans. Power Deliv.* **2010**, *25*, 1808–1815.

31. Monjo, L.; Sainz, L.; Liang, J.; Pedra, J. Study of resonance in wind parks. *Electr. Power Syst. Res.* **2015**, *128*, 30–38, doi:10.1016/j.epsr.2015.06.017.

32. Zhang, S.; Jiang, S.; Lu, X.; Ge, B.; Peng, F. Z. Resonance issues and damping techniques for grid-connected inverters with long transmission cable. *IEEE Trans. Power Electron.* **2014**, *29*, 110–120, doi:10.1109/TPEL.2013.2253127.

33. Sainz, L.; Monjo, L.; Pedra, J.; Cheah-Mane, M.; Liang, J.; Gomis-Bellmunt, O. Effect of wind turbine converter control on wind power plant harmonic response and resonances. *IET Electr. Power Appl.* **2016**, *11*, 157–168, doi:10.1049/iet-epa.2016.0241.

34. Kocewiak, Ł. H.; Hjerrild, J.; Bak, C. L. Wind turbine converter control interaction with complex wind farm systems. *IET Renew. Power Gener.* **2013**, 380–389, doi:10.1049/iet-rpg.2012.0209.

35. Bakhshizadeh, M. K.; Hjerrild, J.; Kocewiak, L.; Hesselbaek, B.; Sorensen, T.; Blaabjerg, F.; Bak, C. L.; Da Silva, F. F. Harmonic modelling, propagation and mitigation for large wind power plants connected via long HVAC cables: Review and outlook of current research. In *2016 IEEE International Energy Conference, ENERGYCON 2016*; 2016.

36. Svendsen, H. G.; Marvik, J. I.; Ceballos, S. *Report on deep offshore wind farm grid integration aspects including a case study*; 2015;

37. Wu, B.; Lang, Y.; Zargari, N.; Kouro, S. *Power Conversion and Control of Wind Energy Systems*; Wiley - IEEE Press, 2011; ISBN 0470593652.

38. Erlich, I.; Shewarega, F.; Feltes, C.; Koch, F. W.; Fortmann, J. Offshore Wind

Power Generation Technologies. *Proceeding IEEE* **2012**, 15.

39.   Teodorescu, R.; Liserre, M.; Rodriguez, P. *Grid Converters for Photovoltaic and Wind Power Systems*; Wiley - IEEE, 2011; ISBN 9780470057513.

40.   WindEurope *Wind energy in Europe in 2018 Trends and Statistics*; 2018;

41.   Madariaga, A.; De Alegría, I. M.; Martín, J. L.; Eguía, P.; Ceballos, S. Current facts about offshore wind farms. *Renew. Sustain. Energy Rev.* **2012**, *16*, 3105–3116, doi:10.1016/j.rser.2012.02.022.

42.   Ng, C.; Ran, L. *Offshore Wind Farms: Technologies, Design and Operation*; Woodhead Publishing, 2016; ISBN 9780081007808.

43.   Declercq, J.; Van Schevensteen, R. Challenges for Reliable Offshore Transformers Maximising the Value of Wind Energy. *Wind. Int.* **2008**.

44.   Martinez Velasco, J. *Power System Transients: Parameter Determination*; CRC Press, 2010; ISBN 9781420065299.

45.   da Silva, F. F.; Bak, C. L. *Electromagnetic Transients in Power Cables*; Springer, 2013; ISBN 9781447152354.

46.   Ametani, A.; Ohno, T.; Nagaoka, N. *Cable System Transients: Theory, Modeling and Simulation*; IEEE Press Wiley, 2015; ISBN 9781118702123.

47.   Svendsen, H. G.; Faiella, L. *Design procedure for inter-array electric design*; 2013;

48.   Nexans *Submarine Power Cables*; 2013;

49.   McDonald, J. *Electric Power Substations Engineering*; 3rd ed.; CRC Press, 2012; ISBN 0849317037.

50.   Lumbreras, S.; Ramos, A. Optimal design of the electrical layout of an offshore wind farm applying decomposition strategies. *IEEE Trans. Power Syst.* **2013**, *28*, 1434–1441, doi:10.1109/TPWRS.2012.2204906.

51.   Quinonez-Varela, G.; Ault, G. W.; Anaya-Lara, O.; McDonald, J. R. Electrical Collector System Options for Large Offshore Wind Farms. *Renew. Power Gener. IET* **2007**, *1*, 8, doi:10.1049/iet-rpg.

52.   Bresesti, P.; Kling, W. L.; Hendriks, R. L.; Vailati, R. HVDC connection of offshore wind farms to the transmission system. *IEEE Trans. Energy Convers.* **2007**, *22*, 37–43, doi:10.1109/TEC.2006.889624.

53.   Arrillaga, J. *High Voltage Direct Current Transmission*; 2nd ed.; IET, 2008; Vol. 29; ISBN 9780852969410.

54.   Montilla-Djesus, M. E.; Santos-Martin, D.; Arnaltes, S.; Castronuovo, E. D. Optimal operation of offshore wind farms with line-commutated HVDC link connection. *IEEE Trans. Energy Convers.* **2010**, *25*, 504–513, doi:10.1109/TEC.2009.2033575.

55.   Xu, J.; Liu, B.; Torres-Olguin, R. E.; Undeland, T. Grid integration of large offshore wind energy and oil & gas installations using LCC HVDC transmission system. *Int. Symp. Power Electron. Electr. Drives, Autom. Motion* **2010**, 784–791, doi:10.1109/SPEEDAM.2010.5542225.

56.   Arrillaga, J.; Watson, N.; Liu, Y. *Flexible Power Transmission The HVDC Options*; John Wiley & Sons, Ltd, 2007; ISBN 9780470056882.

57.   Cole, S.; Belmans, R. Transmission of bulk power. *IEEE Ind. Electron. Mag.* **2009**, *3*, 19–24, doi:10.1109/MIE.2009.933884.

58. Bahrman, M. P.; Johnson, B. K. The ABCs of HVDC transmission technologies. *IEEE Power Energy Mag.* **2007**, *5*, 32–44, doi:10.1109/MPAE.2007.329194.

59. Flourentzou, N.; Agelidis, V. G.; Demetriades, G. D. VSC-Based HVDC Power Transmission Systems: An Overview. *IEEE Trans. Power Electron.* **2009**, *24*, 592–602, doi:10.1109/TPEL.2008.2008441.

60. Salam, M. A.; Rahman, Q. M. *Power Systems Grounding*; Springer, 2016; ISBN 978-981-10-0444-5.

61. IEEE Committee C62 *IEEE Guide for the Application of Neutral Grounding in Electrical Utility Systems, Part I: Introduction*; 2000;

62. Feltes, C.; Van De Sandt, R.; Koch, F.; Shewarega, F.; Erlich, I. Neutral grounding in wind farm medium voltage collector grids. In *2011 IEEE/PES Power Systems Conference and Exposition, PSCE 2011*; 2011; pp. 1–7.

63. Jeppsson, J.; Larsen, P. E.; Larsson, A. *Technical Description Lillgrund Wind Power Plant*; 2008;

64. Shaarbafi, K. *Transformer Modeling Guide*; 2014;

65. Shuai, L.; Jensen, K. H.; Kocewiak, Ł. H. Application of Type 4 Wind Turbine Harmonic Model for Wind Power Plant Harmonic Study. **2016**.

66. Pourbeik, P. *Specification of the Second Generation Generic Models for Wind Turbine Generators*; 2014;

67. IEC IEC 61400-27-1:2015 Available online: https://collections.iec.ch/std/series/iec61400-27-1%7Bed1.0%7Den.nsf/doc.xsp.

68. Wu, B. *HIGH-POWER CONVERTERS AND AC DRIVES*; IEEE Press Wiley, 2006; ISBN 9780471731719.

69. Blaabjerg, F. *Control of Power Electronic Converters and Systems - Volume I*; Academic Press, 2018; ISBN 978-0-12-805245-7.

70. Holmes, D. G.; Lipo, T. *Pulse Width Modulation for Power Converters*; IEEE Press Wiley, 2003; ISBN 0471234397.

71. McGrath, B. P.; Holmes, D. G. Multicarrier PWM Strategies for Multilevel Inverters. *IEEE Trans. Ind. Electron.* **2002**, *49*, 858–867.

72. Leon, J. I.; Kouro, S.; Franquelo, L. G.; Rodriguez, J.; Wu, B. The Essential Role and the Continuous Evolution of Modulation Techniques for Voltage Source Inverters in Past , Present and Future Power Electronics. *IEEE Trans. Ind. Electron.* **2016**, *0046*, 14, doi:10.1109/TIE.2016.2519321.

73. Leon, J. I.; Vazquez, S.; Franquelo, L. G. Multilevel Converters: Control and Modulation Techniques for Their Operation and Industrial Applications. *Proc. IEEE* **2017**, *105*, 2066–2081.

74. Timbus, A.; Liserre, M.; Teodorescu, R.; Rodriguez, P.; Blaabjerg, F. Evaluation of Current Controllers for Distributed Power Generation Systems. *IEEE Trans. Power Electron.* **2009**, *24*, 654–664.

75. Liserre, M.; Teodorescu, R.; Blaabjerg, F. Multiple Harmonics Control for Three-Phase Grid Converter Systems With the Use of PI-RES Current Controller in a Rotating Frame. *IEEE Trans. Power Electron.* **2006**, *21*, 836–841.

76. Yepes, A. G. Digital Resonant Current Controllers for Voltage Source Converters, Universidade Vigo, 2011.

77. Golestan, S.; Member, S.; Guerrero, J. M. Three-Phase PLLs : A Review of Recent Advances. *IEEE Trans. Power Electron.* **2016**, 14, doi:10.1109/TPEL.2016.2565642.

78. Freijedo, F. D.; Doval-gandoy, J.; López, Ó.; Acha, E.; Member, S. Tuning of Phase-Locked Loops for Power Converters Under Distorted Utility Conditions. *IEEE Trans. Ind. Appl.* **2009**, *45*, 2039–2047.

79. Golestan, S.; Ramezani, M.; Guerrero, J. M.; Member, S.; Freijedo, F. D. Moving Average Filter Based Phase-Locked Loops : Performance Analysis and Design Guidelines. *IEEE Trans. Power Electron.* **2014**, *29*, 2750–2763.

80. Robles, E.; Ceballos, S.; Pou, J.; Mart, L. Variable-Frequency Grid-Sequence Detector Based on a Quasi-Ideal Low-Pass Filter Stage and a Phase-Locked Loop. *IEEE Trans. Power Electron.* **2010**, *25*, 2552–2563.

81. Freijedo, F. D.; Yepes, A. G.; Member, S.; López, Ó.; Fernández-comesaña, P.; Member, S.; Doval-gandoy, J. An Optimized Implementation of Phase Locked Loops for Grid Applications. *IEEE Trans. Instrum. Meas.* **2011**, *60*, 3110–3119.

82. González-Espín, F.; Figueres, E.; Member, S.; Garcerá, G. An Adaptive Synchronous-Reference-Frame Phase-Locked Loop for Power Quality Improvement in a Polluted Utility Grid. *IEEE Trans. Ind. Electron.* **2012**, *59*, 2718–2731.

83. Zobaa, A. F.; Member, S.; Hossam, S.; Abdel, E. A New Approach for Harmonic Distortion Minimization in Power Systems Supplying Nonlinear Loads. *IEEE Trans. Ind. Informatics* **2014**, *10*, 1401–1412.

84. Peña-Alzola, R.; et al LCL-filter Design for Robust Active Damping in Grid Connected Converters. *IEEE Trans. Ind. Informatics* **2014**, *3203*, 1–12, doi:10.1109/TII.2014.2361604.

85. Yin, J.; Duan, S.; Liu, B. Stability Analysis of Grid-Connected Inverter with LCL Filter Adopting A Digital Single-Loop Controller with Inherent Damping Characteristic. *IEEE Trans. Ind. Informatics* **2013**, 1–9.

86. Wu, W.; He, Y.; Tang, T.; Blaabjerg, F. A New Design Method for the Passive Damped LCL and LLCL Filter-Based Single-Phase Grid-Tied Inverter. *IEEE Trans. Ind. Electron.* **2013**, 1–12.

87. Ruan, X.; Wang, X.; et al *Control Techniques for LCL -Type Grid- Connected Inverters*; Springer, 2018; ISBN 9789811042768.

88. Rockhill, A. A.; Liserre, M.; Teodorescu, R.; Rodriguez, P. Grid-Filter Design for a Multimegawatt Medium-Voltage Voltage-Source Inverter. *IEEE Trans. Ind. Electron.* **2011**, *58*, 1205–1217.

89. Peña-Alzola, R.; Liserre, M.; Blaabjerg, F.; Sebastián, R.; Fuchs, F. W. Analysis of the Passive Damping Losses in LCL-Filter-Based Grid Converters. *IEEE Trans. Power Electron.* **2013**, *28*, 2642–2646.

90. Zabaleta, M.; Burguete, E.; Madariaga, D.; Zubimendi, I.; Zubiaga, M.; Larrazabal, I. LCL grid filter design of a multimegawatt medium-voltage converter for offshore wind turbine using SHEPWM modulation. *IEEE Trans. Power Electron.* **2016**, *31*, 1993–2001, doi:10.1109/TPEL.2015.2442434.

91. Zou, Z.; Wang, Z.; Cheng, M. Modeling , Analysis , and Design of Multifunction Grid-Interfaced Inverters With Output LCL Filter. *IEEE Trans. Power Electron.* **2014**, *29*, 3830–3839.

92. Dannehl, J.; Fuchs, F. W.; Hansen, S.; Thøgersen, P. B. Investigation of Active Damping Approaches for PI-Based Current Control of Grid-Connected Pulse Width Modulation Converters With LCL Filters. *IEEE Trans. Ind. Appl.* **2010**, *46*, 1509–1517.

93. Xu, J.; Xie, S.; Tang, T. Active Damping-Based Control for Grid-Connected LCL-Filtered Inverter With Injected Grid Current Feedback Only. *IEEE Trans. Ind. Electron.* **2014**, *61*, 4746–4758.

94. Liserre, M.; Blaabjerg, F.; Teodorescu, R. Grid Impedance Estimation via Excitation of LCL-Filter Resonance. *IEEE Trans. Ind. Appl.* **2007**, *43*, 1401–1407.

95. Ruiz, C.; Zubiaga, M.; Abad, G.; Madariaga, D.; Arza, J. Validation of a Wind Turbine Harmonic Model based on the Generic Type 4 Wind Turbine Standard. *20Th Eur. Conf. Power Electron. Appl.* **2018**, 10.

96. IEEE Working Group PQ-Harmonics *IEEE Std 519-2014 - IEEE Recommended Practice and Requirements for Harmonic Control in Electric Power Systems*; 2014;

97. BDEW *Technical Guideline - Generating Plants Connected to the Medium-Voltage Network*; 2008;

98. INGETEAM INGECON WIND MV100 Datasheet Available online: http://www.ingeteam.com/es-es/sectores/energia-eolica/p15_23_252_22/full-converter-mv-3000-10000.aspx.

99. Brantsæter, H.; Kocewiak, Ł.; Årdal, A. R.; Tedeschi, E. Passive filter design and offshore wind turbine modelling for system level harmonic studies. In *Energy Procedia 80*; Elsevier B.V., 2015; Vol. 80, pp. 401–410.

100. Zubiaga, M.; Larrazabal, I.; Madariaga, D.; Aguirrezabal, J.; Zubimendi, I.; Nuñez, G.; Garin, I.; Burguete, E.; Zabaleta, M. *Low scale grid emulator test bench for in-house validation of high power converters oriented to offshore*;

101. Jacobsen, E.; Lyons, R. The sliding DFT. *IEEE Signal Process. Mag.* **2003**, *20*, 74–80, doi:10.1109/MSP.2003.1184347.

102. Lyons, R. *Streamlining Digital Signal Processing*; Wiley - IEEE, 2012; ISBN 9781118316948.

103. González-Longatt, F.; Wall, P. P.; Terzija, V. Wake effect in wind farm performance: Steady-state and dynamic behavior. *Renew. Energy* **2012**, *39*, 329–338, doi:10.1016/j.renene.2011.08.053.

104. Kiranoudis, C. T.; Maroulis, Z. B. Effective short-cut modelling of wind park efficiency. *Renew. Energy* **1997**, *11*, 439–457, doi:10.1016/S0960-1481(97)00011-6.

105. Shakoor, R.; Hassan, M. Y.; Raheem, A.; Wu, Y. K. Wake effect modeling: A review of wind farm layout optimization using Jensen's model. *Renew. Sustain. Energy Rev.* **2016**, *58*, 1048–1059, doi:10.1016/j.rser.2015.12.229.

106. Wußow, S.; Sitzki, L.; Hahm, T. 3D-simulation of the turbulent wake behind a wind turbine. *J. Phys. Conf. Ser.* **2007**, *75*, 12–33, doi:10.1088/1742-6596/75/1/012033.

107. Sanderse, B. *Aerodynamics of wind turbine wakes: Literature review*; 2009;

108. Jensen, N. O. A note on wind generator interaction. **1983**, 1–16, doi:Riso-M-2411.

109. Katic, I.; Hojstrup, J.; Jensen, N. O. A Simple Model for Cluster Efficiency. *EWEC Proc.* **1986**, *1*.

110. Charhouni, N.; Arbaoui, A.; Sallaou, M. Analysis of wake impact on wind farm performance using two analytical models. *IEEE* **2014**, 1–5.

111. Larsen, G. C. *A Simple Wake Calculation Procedure*; 1988; Vol. No. 2760;

112. Frandsen, S.; Barthelmie, R.; Pryor, S. *Analytical modelling of wind speed deficit in large offshore wind farms*; 2006;

113. Ainslie, J. F. Calculating the flowfield in the wake of wind turbines. *J. Wind Eng. Ind. Aerodyn.* **1988**, *27*, 213–224, doi:10.1016/S0167-6105(13)00239-0.

114. Schepers, J. G. *ENDOW: Validation and improvement of ECN's wake model*; 2003;

115. Mikkelsen, R. Actuator Disc Methods Applied to Wind Turbines, Technical University of Denmark, 2003.

116. Troldborg, N.; Sørensen, J. Numerical simulations of wake characteristics of a wind turbine in uniform inflow. *Wind Energy* **2010**, *13*, 86–99, doi:10.1002/we.

117. Ammara, I.; Leclerc, C.; Masson, C. A Viscous Three-Dimensional Differential/Actuator-Disk Method for the Aerodynamic Analysis of Wind Farms. *J. Sol. Energy Eng.* **2002**, *124*, 345–356, doi:10.1115/1.1510870.

118. Lange B.; et al Modeling of offshore wind turbine wakes with the wind farm program FLaP. *Proc. OWEMES Conf.* **2003**.

119. Dekker, J. W. M.; Pierik, J. T. G. *European Wind Turbine Standards II*; 1998;

120. Frandsen, S. T. Turbulence and turbulence- generated structural loading in wind turbine clusters, Technical University of Denmark, 2007, Vol. 1188.

121. De-Prada-Gil, M.; Alías, C. G.; Gomis-Bellmunt, O.; Sumper, A. Maximum wind power plant generation by reducing the wake effect. *Energy Convers. Manag.* **2015**, *101*, 73–84, doi:10.1016/j.enconman.2015.05.035.

122. Barthelmie, R. J.; Folkerts, L.; Larsen, G. C.; Rados, K.; Pryor, S. C.; Frandsen, S. T.; Lange, B.; Schepers, G. Comparison of wake model simulations with offshore wind turbine wake profiles measured by sodar. *J. Atmos. Ocean. Technol.* **2006**, *23*, 888–901, doi:10.1175/JTECH1886.1.

123. Thørgersen, M.; Sørensen, T.; Nielsen, P. *WindPRO/PARK: Introduction to Wind Turbine Wake Modelling and Wake Generated Turbulence*; 2005;

124. Gil, M. D. P. Design , operation and control of novel electrical concepts for offshore wind power plants, Universitat Politecnica de Catalunya, 2014.

125. Koch, F.; Gresch, M.; Shewarega, F.; Erlich, I.; Bachmann, U. Consideration of wind farm wake effect in power system dynamic simulation. *2005 IEEE Russ. Power Tech* **2005**, *2*, 1–7, doi:10.1109/PTC.2005.4524572.

126. Martinez Velasco, J.; Mork, B. a. Transformer modeling for low-and mid-frequency transients-a review. *IEEE Trans. Power Deliv.* **2005**, *20*, 1625–1632, doi:10.1109/TPWRD.2004.833884.

127. Dommel, H. W. *Electromagnetic Transients Program Theory Book*; 1986;

128. Velasco, J. A.; Walling, R.; Mork, B. A.; Martin-Arnedo, J.; Durbak, D. Parameter determination for modeling system transients-Part III: Transformers. *IEEE Trans. Power Deliv.* **2005**, *20*, 2051–2062, doi:10.1109/TPWRD.2005.848752.

129. Haginomori, E.; Koshiduka, T.; Arai, J.; Ikeda, H. *Power System Transient Analysis . Theory and Practice using Simulation Programs (ATP-EMTP).*; 1st ed.; Wiley, 2016; ISBN 9781118737538.

130. Chen, X. Negative inductance and numerical instability of the saturable transformer component in EMTP. *IEEE Trans. Power Deliv.* **2000**, *15*, 1199–1204, doi:10.1109/61.891503.

131. Henriksen, T. How to avoid unstable time domain responses caused by transformer models. *IEEE Trans. Power Deliv.* **2002**, *17*, 516–522, doi:10.1109/61.997928.

132. Dick, E. P.; Watson, W. Transformer models for transient studies based on field measurements. *IEEE Trans. Power Appar. Syst.* **1981**, *PAS-100*, 409–419, doi:10.1109/TPAS.1981.316870.

133. de Leon, F.; Semlyen, A. Complete transformer model for electromagnetic transients. *IEEE Trans. Power Deliv.* **1994**, *9*, 231–239, doi:10.1109/61.277694.

134. Mork, B. A.; Gonzalez, F.; Ishchenko, D.; Stuehm, D. L.; Mitra, J. Hybrid transformer model for transient simulation - Part I: Development and parameters. *IEEE Trans. Power Deliv.* **2007**, *22*, 248–255, doi:10.1109/TPWRD.2006.883000.

135. Mork, B.; Gonzalez, F.; Ishchenko, D.; Stuehm, D.; Mitra, J. Hybrid Transformer Model for Transient Simulation : Part II - Laboratory Measurements and Benchmarking. *IEEE Trans. Power Deliv.* **2007**, *22*, 4244.

136. Hoidalen, H. K.; Mork, B. A.; Gonzalez, F.; Ishchenko, D.; Chiesa, N. Implementation and verification of the Hybrid Transformer model in ATPDraw. *Electr. Power Syst. Res.* **2009**, *79*, 454–459, doi:10.1016/j.epsr.2008.09.003.

137. Chiesa, N.; Mork, B. A.; Hidalen, H. K. Transformer model for inrush current calculations: Simulations, measurements and sensitivity analysis. *IEEE Trans. Power Deliv.* **2010**, *25*, 2599–2608, doi:10.1109/TPWRD.2010.2045518.

138. Hatziargyriou, N. D.; Prousalidis, J. M.; Papadias, B. C. Generalised transformer model based on the analysis of its magnetic core circuit. *IEE Proc. -Generation, Transm. Distrib.* **1993**, *140*, 269, doi:10.1049/ip-c.1993.0040.

139. Arrillaga, J.; Enright, W.; Watson, N. R.; Wood, A. R. Improved simulation of HVDC converter transformers in electromagnetic transient programs. *Proc. Inst. Elect. Eng., Gen. Transm. Distrib.* **1997**, *144*, 100–106, doi:10.1049/ip-gtd:19970849.

140. Manitoba HVDC Research Centre *EMTDC Transient Analysis for PSCAD Power System Simulation*; 2010;

141. Hoidalen, H. K.; Lotfi, A.; Zirka, S.; Moroz, Y.; Chiesa, N.; Mork, B. A. Benchmarking of hysteretic elements in topological transformer model. In *Electric Power Systems Research*; 2016; Vol. 138, pp. 33–40.

142. Chiesa, N. Power Transformer Modeling for Inrush Current Calculation, Norwegian University of Science and Technology, 2010.

143. Zirka, S. E.; Moroz, Y. I.; Harrison, R. G.; Chiesa, N. Inverse hysteresis models for transient simulation. *IEEE Trans. Power Deliv.* **2014**, *29*, 552–559, doi:10.1109/TPWRD.2013.2274530.

144. Chiesa, N.; Høidalen, H. K. Hysteretic iron-core inductor for transformer inrush current modelling in EMTP. In *16th Power Systems Computaction Conference*; 2008; pp. 1–7.

145. de León, F.; Semlyen, A. Time Domain Modeling of Eddy Current Effects for Transformer Transients. *IEEE Trans. Power Deliv.* **1993**, *8*, doi:10.1109/61.296301.

146. Leon, F. De; Semlyen, A. Eddy current add-on for frequency dependent representation of winding losses in transformer models used in computing electromagnetic transients. In *IEE Proceedings -Generation, Transmission and Distribution*; 1994; Vol. 141.

147. Tarasiewicz, E. J.; Morched, A. S.; Narang, A.; Dick, E. P. Frequency Dependant Eddy Current Models for Nonlinear Iron Cores. *IEEE Trans. Power Syst.* **1993**, *8*, 588–597, doi:10.1109/59.260823.

148. Chiesa, N.; Gustavsen, B. Frequency-dependent modeling of transformer winding impedance from R(w)/L measurements. *IEEE Trans. Power Deliv.* **2014**, *29*, 1511–1513, doi:10.1109/TPWRD.2014.2301597.

149. Tziouvaras, D. A.; McLaren, P.; Alexander, G.; Dawson, D.; Esztergalyos, J.; Fromen, C.; Glinkowski, M.; Hasenwinkle, I.; Kezunovic, M.; Kojovic, L.; Kotheimer, B.; Kuffel, R.; Nordstrom, J.; Zocholl, S. Mathematical models for current, voltage, and coupling capacitor voltage transformers. *IEEE Trans. Power Deliv.* **2000**, *15*, 62–72, doi:10.1109/61.847230.

150. Chiesa, N. Power Transformer Modelling Advanced Core Model, Politecnico di Milano, 2005.

151. Cho, S. D. Parameter Estimation for Transformer Modeling, Michigan Technological University, 2002.

152. Neves, W. L. A. Transformer Modelling for Transient Studies, The University of British Columbia, 1994.

153. Das, J. C. Surges transferred through transformers. In *Conference Record of the 2002 Annual Pulp and Paper Industry Technical Conference (Cat. No.02CH37352)*; 2002; pp. 139–147.

154. Arana, I. Switching overvoltages in offshore wind power grids, Technical University of Denmark (DTU), 2011.

155. Azzouz, Z.; Foggia, A.; Meunier, G.; Pierrat, L. 3D Finite Element Computation of the High Frequency Parameters of Power Transformer Windings. *IEEE Trans. Magn.* **1993**, *29*, 1407–1410, doi:10.1109/20.250666.

156. Del Vecchio, R.; Poulin, B.; Feghali, P.; Shah, D.; Ahuja, R. *Transformer Design Principles*; 2nd ed.; CRC Press, 2010; ISBN 978-1-4398-0582-4.

157. Mork, B. A.; Gonzalez, F.; Ishchenko, D. *Parameter estimation and advancements in transformer models for EMTP simulations. Task MTU-6: Parameter Estimation*; 2003;

158. Schellmanns, A.; Keradec, J. P.; Schanen, J. L. Electrical equivalent circuit for frequency dependant impedance: minimum lumped elements for a given precision. In *Conference Record of the 2000 IEEE Industry Applications Conference. Thirty-Fifth IAS Annual Meeting and World Conference on Industrial Applications of Electrical Energy (Cat. No.00CH37129)*; 2000; Vol. 5, pp. 3105–3110.

159. Mitra, J. *Laboratory Testing of 3-leg and 5-leg Distribution Transformers*; 2002;

160. Mitra, J. *Frequency Dependence of Parameters of 3-leg and 5-leg Distribution Transformers*; 2003;

161. Watson, N.; Arrillaga, J. *Power Systems Electromagnetic Transients Simulation*; IET, 2003; Vol. 39; ISBN 9780852961063.

162. D'Arco, S.; Beerten, J.; Suul, J. A. Cable Model Order Reduction for HVDC

Systems Interoperability Analysis. In *11th IET International Conference on AC and DC Power Transmission*; Birmingham, 2015; p. 10.

163. Meredith, R. EMTP Modeling of Electromagnetic Transients in Multi-Mode Coaxial Cables By Finite Sections. *IEEE Trans. Power Deliv.* **1997**, *12*, 489–496.

164. Sakis, A. P.; Masson, J.-F. Modeling and Analysis of URD Cable Systems. *IEEE Trans. Power Deliv.* **1990**, *5*, 806–815.

165. Macias, J. A. R.; Exposito, A. G.; Soler, A. B. A Comparison of Techniques for State-Space Transient Analysis of Transmission Lines. *IEEE Trans. Power Deliv.* **2005**, *20*, 894–903, doi:10.1109/TPWRD.2005.844271.

166. Ruiz, C.; Abad, G.; Zubiaga, M.; Madariaga, D.; Arza, J. Frequency-Dependent Pi Model of a Three-Core Submarine Cable for Time and Frequency Domain Analysis. *Energies* **2018**, *11*, doi:10.3390/en11102778.

167. da Silva, F. M. F. Analysis and simulation of electromagnetic transients in HVAC cable transmission grids, Aalborg University, 2011.

168. Arrillaga, J.; Watson, N. *Power System Harmonics*; 2nd ed.; John Wiley & Sons, Ltd, 2003; ISBN 978-1-119-03572-5.

169. Tleis, N. D. *Power Systems Modelling and Fault Analysis: Theory and Practice*; Elsevier - Newnes, 2008; ISBN 9780750680745.

170. Gudmundsdottir, U. S. Modelling of long High Voltage AC Cables in the Transmission System, Aalborg University, 2010.

171. Hoshmeh, A.; Schmidt, U. A full frequency-dependent cable model for the calculation of fast transients. *Energies* **2017**, *10*, 1–19, doi:10.3390/en10081158.

172. Torrez, P.; Costa, E. C. M.; Kurokawa, S. Frequency-dependent multiconductor line model based on the Bergeron method. *Electr. Power Syst. Res.* **2015**, *127*, 314–322, doi:10.1016/j.epsr.2015.05.019.

173. Pagnetti, A. Cable Modeling for Electromagnetic Transients in Power Systems, Universite Blaise Pascal, 2012.

174. Marti, J. R. Accurate modelling of frequency-dependent transmission lines in electromagnetic transient simulations. *IEEE Trans. Power Appar. Syst.* **1982**, *PAS-101*, 147–157, doi:10.1109/TPAS.1982.317332.

175. Hoogendorp, G. Steady State and transient behavior of underground cables in 380 kV transmission grids, Delft University of Technology, 2016.

176. Morched, A.; Gustavsen, B.; Tartibi, M. A Universal Model for Accurate Calculation of Electromagnetic Transients on Overhead lines and Underground cables. *IEEE Trans. Power Deliv.* **1999**, *14*, 1032–1038.

177. Yu, T. Full Frequency-Dependent Modelling of Underground Cables for Electromagnetic Transient Analysis, University of British Columbia, 2001.

178. Yu, T. C.; Martí, J. R. A robust phase-coordinates frequency-dependent underground cable model (zCable) for the EMTP. *IEEE Trans. Power Deliv.* **2003**, *18*, 189–194, doi:10.1109/TPWRD.2002.807749.

179. Lorenzo, E. Di The Maxwell Capacitance Matrix. **2011**, 1–3.

180. Ametani, A. A general formulation of impedance and admittance of cables. *IEEE Trans. Power Appar. Syst.* **1980**, *PAS-99*, 902–910, doi:10.1109/TPAS.1980.319718.

181. Asada, T.; Baba, Y.; Member, S.; Nagaoka, N.; Ametani, A.; Fellow, L.; Mahseredjian, J.; Yamamoto, K. A Study on Basic Characteristics of the Proximity Effect on Conductors. *IEEE Trans. Power Deliv.* **2017**, *32*, 1790–1799, doi:10.1109/TPWRD.2016.2590962.

182. Tsiamitros, D. A.; Papagiannis, G. K.; Dokopoulos, P. S. Earth return impedances of conductor arrangements in multilayer soils - Part II: Numerical results. *IEEE Trans. Power Deliv.* **2008**, *23*, 2401–2408, doi:10.1109/TPWRD.2008.923999.

183. Gustavsen, B.; Bruaset, A.; Bremnes, J. J.; Hassel, A. A finite-element approach for calculating electrical parameters of umbilical cables. *IEEE Trans. Power Deliv.* **2009**, *24*, 2375–2384, doi:10.1109/TPWRD.2009.2028481.

184. Yin, Y.; Dommel, H. W. Calculation of frequency-dependent impedances of underground power cables with finite element method. *IEEE Trans. Magn.* **1989**, *25*, 3025–3027, doi:10.1109/20.34358.

185. Pagnetti, A.; Xemard, A.; Paladian, F.; Nucci, C. A. An improved method for the calculation of the internal impedances of solid and hollow conductors with the inclusion of proximity effect. *IEEE Trans. Power Deliv.* **2012**, *27*, 2063–2072, doi:10.1109/TPWRD.2012.2212466.

186. De Arizon, P.; Dommel, H. W. Computation of Cable Impedances Based on Subdivision of Conductors. *IEEE Trans. Power Deliv.* **1987**, *PER-7*, doi:10.1109/MPER.1987.5527296.

187. Patel, U. R.; Gustavsen, B.; Triverio, P. An equivalent surface current approach for the computation of the series impedance of power cables with inclusion of skin and proximity effects. *IEEE Trans. Power Deliv.* **2013**, *28*, 2474–2482, doi:10.1109/TPWRD.2013.2267098.

188. Patel, U. R.; Triverio, P. MoM-SO: A Complete Method for Computing the Impedance of Cable Systems Including Skin, Proximity, and Ground Return Effects. *IEEE Trans. Power Deliv.* **2015**, *30*, 2110–2118, doi:10.1109/TPWRD.2014.2378594.

189. Patel, U. R.; Triverio, P. Accurate Impedance Calculation for Underground and Submarine Power Cables Using MoM-SO and a Multilayer Ground Model. *IEEE Trans. Power Deliv.* **2016**, *31*, 1233–1241, doi:10.1109/TPWRD.2015.2469599.

190. Gustavsen, B. Panel session on data for modeling system transients insulated cables. *2001 IEEE Power Eng. Soc. Winter Meet. Conf. Proc. (Cat. No.01CH37194)* **2001**, *2*, 718–723, doi:10.1109/PESW.2001.916943.

191. Gustavsen, B.; Semlyen, A. Rational Approximation of Frequency Domain Responses by Vector Fitting. *IEEE Trans. Power Deliv.* **1999**, *14*, 1052–1061.

192. Gustavsen, B. Improving the pole relocating properties of vector fitting. *IEEE Trans. Power Deliv.* **2006**, *21*, 1587–1592, doi:10.1109/TPWRD.2005.860281.

193. ABB *XLPE Submarine Cable Systems*; 2014;

194. Gustavsen, B.; Martinez, J. A.; Durbak, D. Parameter determination for modeling system transients - Part II: Insulated cables. *IEEE Trans. Power Deliv.* **2005**, *20*, 2045–2050, doi:10.1109/TPWRD.2005.848774.

195. Alphaventus *Fact-sheet alpha ventus*; 2015;

196. Westerhellweg, A.; Cañadillas, B.; Kinder, F.; Neumann, T. Wake measurements at alpha ventus - Dependency on stability and turbulence intensity. *J. Phys. Conf.*

Ser. **2014**, *555*, doi:10.1088/1742-6596/555/1/012106.

197. Westerhellweg, A.; Canadillas, B.; Kinder, F.; Neumann, T. Detailed analysis of offshore wakes based on two years data of Alpha Ventus and comparison with CFD simulations. In *DEWI Magazine*; 2013; p. 7.

198. AlphaVentus Alpha Ventus Available online: https://www.alpha-ventus.de/english.

199. Wang, X.; Blaabjerg, F. Harmonic Stability in Power Electronic Based Power Systems: Concept, Modeling, and Analysis. *IEEE Trans. Smart Grid* **2018**, *3053*, 1–12, doi:10.1109/TSG.2018.2812712.

200. Kundur, P. *Power System Stability And Control*; McGraw-Hill, 1994; ISBN 9780070359581.

201. Abad, G.; Laka, A.; Saavedra, G.; Barrena, J. A. Analytical modeling approach to study harmonic mitigation in AC grids with active impedance at selective frequencies. *Energies* **2018**, *11*, doi:10.3390/en11061337.

202. Gupta, M.; Martinez, A.; Saylors, S. Experiences with Wind Power Plants with Low SCR 2015, 1–24.

203. Xu, D.; Blaabjerg, F.; Chen, W.; Zhu, N. *Advanced Control of Doubly Fed Induction Generator For Wind Power Systems*; 1st ed.; IEEE Press Wiley, 2018; ISBN 9781119172062.

204. BDEW *Rules and transitional periods for specific requirements complementary to the technical guideline : Generating plants connected to the medium- voltage network - Guideline for generating plants ' connection to and parallel operation with the medium-voltage*; 2013;

205. Fuchs, E. F.; Masoum, M. *Power Quality in Power Systems and Electrical Machines*; 2nd ed.; Academic Press, 2015; ISBN 9780128007822.

206. Velasco, J. A. *Transient Analysis of Power Systems: Solution Techniques, Tools and Applications*; Wiley - IEEE Press, 2015; ISBN 978-1-118-35234-2.

207. Bañuelos-Cabral, E. S.; Gutiérrez-Robles, J. A.; Gustavsen, B.; Naredo, J. L.; García-Sánchez, J. L.; Sotelo-Castañón, J.; Galván-Sánchez, V. A. Enhancing the accuracy of rational function-based models using optimization. *Electr. Power Syst. Res.* **2015**, *125*, 83–90, doi:10.1016/j.epsr.2015.04.001.

208. Gustavsen, B.; De Silva, H. M. J. Inclusion of rational models in an electromagnetic transients program: Y-Parameters, Z-Parameters, S-parameters, transfer functions. *IEEE Trans. Power Deliv.* **2013**, *28*, 1164–1174, doi:10.1109/TPWRD.2013.2247067.

209. Gustavsen, B. *User's Guide for Vector Fitting Matrix Toolbox*; 2009;

210. Gustavsen, B. *User's Guide for Vector Fitting*; 2008;

211. Deschrijver, D.; Mrozowski, M.; Dhaene, T.; De Zutter, D. Macromodeling of multiport systems using a fast implementation of the vector fitting method. *IEEE Microw. Wirel. Components Lett.* **2008**, *18*, 383–385, doi:10.1109/LMWC.2008.922585.

212. Gustavsen, B. Fast passivity enforcement for S-parameter models by perturbation of residue matrix eigenvalues. *IEEE Trans. Adv. Packag.* **2010**, *33*, 257–265, doi:10.1109/TADVP.2008.2010508.

213. Rettenmeier, A.; Blasche, K.; Huesmann, M.; Schneehorst, A.; Wessel, A.; Al, E. *RAVE-Research on the offshore test field*; 2009;

214. Sharples, M. *Offshore Electrical Cable Burial for Wind Farms: State of the Art, Standards and Guidance & Acceptable*; 2011;

215. ABB *Transformer Technical Features* .;

216. Wasynczuk, O.; De Carlo, R. A. The Component Connection Model and Structure Preserving Model Order Reduction. *Int. Fed. Autom. Control* **1981**, *17*, 619–626.

217. Wang, Y.; Wang, X.; Blaabjerg, F.; Chen, Z. Small-Signal Stability Analysis of Inverter-Fed Power Systems Using Component Connection Method. *IEEE Trans. Smart Grid* **2017**, 1–1, doi:10.1109/TSG.2017.2686841.

218. Bakhshizadeh, M. K.; Yoon, C.; Hjerrild, J.; Bak, C. L.; Kocewiak, L. H.; Blaabjerg, F.; Hesselbaek, B. The Application of Vector Fitting to Eigenvalue-Based Harmonic Stability Analysis. *IEEE J. Emerg. Sel. Top. Power Electron.* **2017**, *5*, 1487–1498, doi:10.1109/JESTPE.2017.2727503.

219. Pérez-Arriaga, I. J.; Verghese, G. C.; Schweppe, F. C. Selective Modal Analysis With Applications to Electric Power Systems, Part I: Heuristic Introduction. *IEEE Trans. Power Appar. Syst.* **1982**, *PAS-101*, 3117–3125, doi:10.1109/TPAS.1982.317524.

220. Verghese, G.; Perez-arriaga, I.; Schweppe, F. Selective Modal Analysis With Applications to Electric Power Systems, Part II: The Dynamic Stability Problem. *IEEE Trans. Power Appar. Syst.* **1982**, *PAS-101*, 3126–3134, doi:10.1109/TPAS.1982.317525.

221. Sauer, P.; Pai, M. A.; Chow, J. *Power System Dynamics and Stability With Synchrophasor Measurement and Power System Toolbox*; Second Edi.; IEEE Press Wiley, 2018; ISBN 9781119355793.

Appendix A

Rational Modeling of Frequency-Dependent Components

Several power system components, e.g. submarine cables and power transformers, are characterized by strongly frequency-dependent effects in their behaviour. The accurate simulation of these power system components requires taking into account this effect.

One way of modeling such components is by characterizing their behavior in the frequency domain and then performing a circuit representation. The use of rational functions is a key aspect of such modeling as it leads to highly efficient time-domain simulations.

This annex focuses on the modeling of terminal equivalents. The frequency-dependent behavior of the power components under study is treated in previous chapters. A list of the most common rational fitting methods is presented together with the reasons for their use and the constraints that rational function based models must fulfill for time-domain simulations. Then, a brief description of the two most widely used fitting methods in EMTP-type tools is presented.

A.1   Rational Functions

The goal of a rational function $f(s)$ is to approximate its frequency response, as closely as possible, to the one of a physical element or system $h(s)$, as given in equation (A.1).

$$f(s) \cong h(s) \tag{A.1}$$

A rational function can be formulated in the frequency-domain in various forms [206]. These are:

- Polynomial form, given by equation (A.2).

$$f(s) = \frac{a_N s^N + \cdots + a_1 s + a_0}{b_N s^N + \cdots + b_1 s + 1} \tag{A.2}$$

- Pole-zero form, given by equation (A.3).

$$f(s) = k \frac{\displaystyle\prod_{m=1}^{N}(s - z_m)}{\displaystyle\prod_{m=1}^{N}(s - p_m)} \tag{A.3}$$

- Pole-residue form, given by equation (A.4).

$$f(s) = r_0 + \sum_{m=1}^{N} \frac{r_m}{s - p_m} \tag{A.4}$$

- State-space form, given by equation (A.5).

$$f(s) = [C]\{s[I] - [A]\}^{-1}[B] + [D] \tag{A.5}$$

There are two reasons for the use of rational functions. First, it allows a direct transformation from the frequency-domain into the time-domain, i.e. it generates an equivalent lumped circuit. Second, it leads to highly efficient simulations in the time-domain via recursive convolution [206], given by equations (A.6) and (A.7). This formulation can be interfaced to Simulink® or EMTP-type programs via a Norton equivalent, where the current source is updated in each time step.

$$f(s) = \sum_{m=1}^{N} \frac{r_m}{s - p_m} \qquad \rightarrow \qquad f(t) = \sum_{m=1}^{N} r_m e^{p_m t} \tag{A.6}$$

$$y(t) = f(t) * u(t) \qquad \rightarrow \qquad \begin{cases} x_n = \alpha x_{n-1} + u_{n-1} \\ y_n = \beta x_n + \xi u_n \end{cases} \tag{A.7}$$

The first approach has the main drawback of being less efficient for complex systems. This is mainly because its representation is performed with large circuits in comparison with the recursive convolution approach.

A rational function based model is required to fulfill with four constraints associated with the behavior of physical systems [207]. These are:

- Stability: The model must have all its poles in the left half-plane.
- Realness: All model parameters must be real or come in complex conjugate pairs.

- Reciprocity: The state-space model may be required to be symmetrical with respect to its terminals (for example an admittance representation) for the case of multi-port systems.
- Passivity: The model cannot generate power.

A.2   Fitting Techniques

The two most widely used fitting techniques in EMTP-type tools are described below.

Bode's Asymptotic Fitting

The asymptotic approximation known as Bode was introduced in 1945 and afterwards applied by J. R. Marti for transmission line modeling in 1982 [174]. Using Bode fitting leads to a pole-zero form given by equation (A.3).

In this fitting technique, the poles and zeros are successively added to the total response function by tracing the resulting asymptote of the approximation to the magnitude function of the given response. To simplify the development of this technique, it is assumed that the full set of poles and zeros are of first order, real, different and lie in the left half-plane. The method gives a magnitude function given by equation (A.8).

$$\left|f(j\omega)\right| = \frac{K_0 \left|\dfrac{j\omega}{z_1}-1\right|\left|\dfrac{j\omega}{z_2}-1\right|\cdots\left|\dfrac{j\omega}{z_n}-1\right|}{\left|\omega\right|\left|\dfrac{j\omega}{p_1}-1\right|\left|\dfrac{j\omega}{p_2}-1\right|\cdots\left|\dfrac{j\omega}{p_m}-1\right|} \tag{A.8}$$

Being K_0,

$$K_0 = \frac{k\prod\limits_{n=1}^{N} z_n}{\prod\limits_{m=1}^{M} p_m} \tag{A.9}$$

Equation (A.8) can be expressed by equation (A.10).

$$\log_{10}\left|f(j\omega)\right| = \log_{10}\left|K_0\right| + \log_{10}\left|\frac{j\omega}{z_1}-1\right| + \cdots + \log_{10}\left|\frac{j\omega}{z_n}-1\right|$$
$$- \log_{10}\left|\omega\right| - \log_{10}\left|\frac{j\omega}{p_1}-1\right| - \cdots - \log_{10}\left|\frac{j\omega}{p_m}-1\right| \tag{A.10}$$

In the implementation, the fitting process starts at the lowest frequency sample and compares the function to be fitted with the sum of the line segments given by the approximation of each term of equation (A.10). When the asymptote deviates from the

target function by a tolerance value [174], a pole or zero is added to improve the approximation. For transmission line modeling, a relative tolerance criterion is normally used.

The realness criterion is enforced by restricting all poles and zeros to be real. The stability criterion is enforced by restricting the poles to lie in the left half-plane by giving a minimum-phase shift function [174]. In the implementation by Marti, the accuracy is enhanced by shifting the poles and zeros around their first asymptotes. In general, this fitting technique is applied in the case of physical systems with smooth frequency response.

Vector Fitting

Vector Fitting (VF) is applicable to smooth and non-smooth data. Thus, it is considered as a more general fitting approach in comparison with other fitting techniques that are only used for smooth frequency response. The user can choose between an approximation with real-only parameters and with real and complex conjugate parameters. A general description of the algorithm is described below. Details can be found in references [208–210].

The goal of Vector Fitting (VF) is to calculate a rational model on pole-residue form, as given by equation (A.11), by relocating a set of initial poles through an iterative procedure [191]. Coefficients d and e are optional terms and can be zero.

$$f(s) \approx \sum_{n=1}^{N} \frac{c_n}{s - p_n} + d + se \qquad (A.11)$$

Being,

c_n : the residues of the approximation.

p_n : the poles of the approximation.

Some characteristics of VF are summarized next:

- VF iteratively relocates an initial set of poles to better positions by solving a linear least squares formulation [191].
- Stability of the poles is ensured by flipping any unstable pole into the left half-plane. The pole identification is followed by a residue identification step.
- A single call to the routine gives a single iteration, better approximations can be obtained if several iterations are performed.
- A relaxed non-triviality constraint is used in the pole identification step of VF for achieving faster convergence and less biasing [192].
- The linear problem associated with the pole identification step of VF is solved in a faster way by using a matrix structure [211].
- VF can be extended or be used for fitting a matrix of elements in the case of multiport systems. Details of the VF Matrix Toolbox can be found in reference [209].

- Although a model extracted by VF has stable poles only, the model may still yield unstable results when included in a time-domain simulation. This is because the model may generate power under certain terminal conditions, since VF does not guarantee the passivity of the extracted model. Passivity can, however, be enforced by a post-processing step. The vectfit3.m routine developed by SINTEF and used in this project includes a passivity enforcement scheme based on perturbation of the residue matrix eigenvalues (spectral perturbation) in order to reduce the computational effort. Details of the scheme of passivity enforcement can be found in reference [212].

Appendix B

Supporting Information for the Parameterization of the OWPP Base Scenario

The purpose of this appendix is to provide supporting information for the parameterization of the OWPP base scenario. As pointed out in section 7.2, the OWPP base scenario is defined taking into account information of a real OWPP. In this sense, Alpha Ventus is taken as a reference OWPP where several characteristics, such as the number and rated power of WTs, spatial disposition of WTs, length of the transmission system, voltage levels, electrical connections, and others are considered. The main goal is to study an OWPP base scenario that is not far away from reality.

It is also important to mention that transformer and submarine cable parameterization are based on datasheets of real components that are, to a certain degree, similar to the ones installed in the OWPP. In this sense, the values needed for certain parameters are obtained via scaling the per-unit values of the components or by adopting the same value in cases where this can be applied, e.g. a given characteristic or parameter of a similar submarine cable. Due to the previous reasons, the datasheets of these power components are presented as well.

B.1 Alpha Ventus OWPP

Alpha Ventus was commissioned as the first OWPP installed in Germany in April 2010 [195]. The OWPP has a total capacity of 60 MW. This amount of power is generated from 12 WTs, each one with a power rating of 5 MW. The WTs are clustered into groups of three. A collector network then links all the WTs to an offshore platform, which steps up the voltage to 110 kV, transmission system level. The link between the offshore substation to the onshore substation is done by a submarine cable of approximately 60 km long. Fig. B.1 shows a simplified schematic of Alpha Ventus OWPP. Fig. B.2 shows the layout of the offshore wind farm, which provides information about the separation distances among WTs.
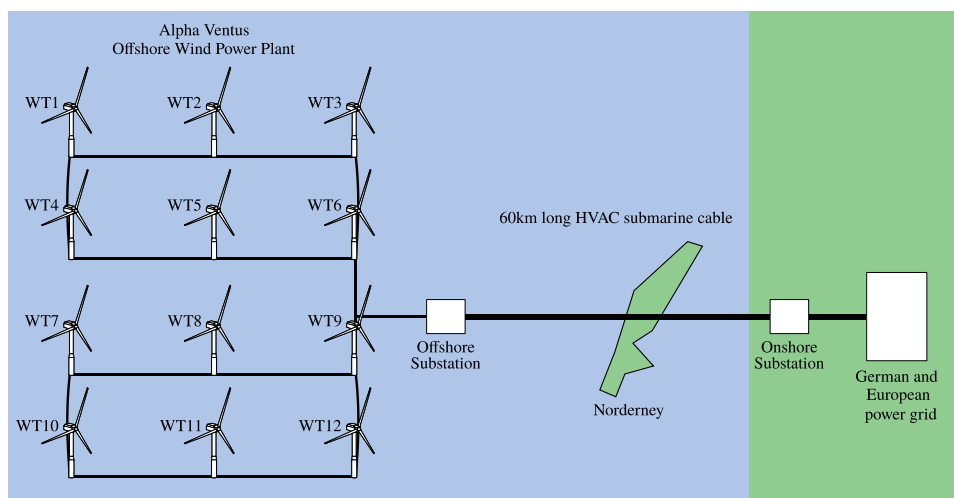

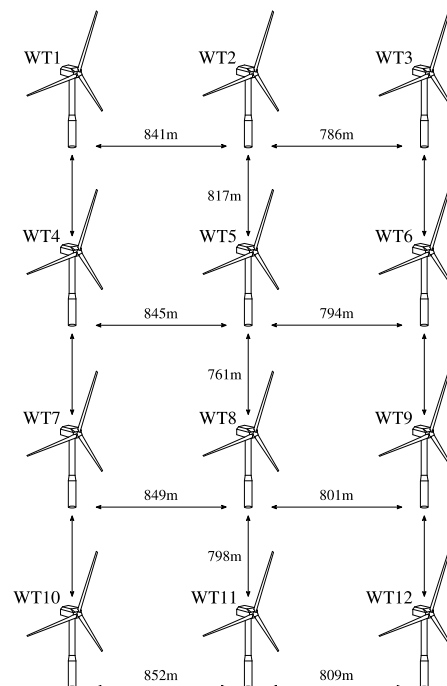Fig. B.1. Simplified schematic of Alpha Ventus OWPP. Source [198].

Fig. B.2. Alpha Ventus wind farm layout. Source [213].

Two types of WT models are installed; the Multibrid M5000 from AREVA manufacturer and the Senvion 5M from Repower Systems SE manufacturer [198]. Table B.1 gives the available technical data of these wind turbine models.

Table B.1. Technical data of WTs installed at Alpha Ventus OWPP. Source [198].

Parameters	Wind Turbine Model	
	Senvion 5M	Multibrid M5000
Rotor diameter	126 m	116 m
Hub height	92 m	90 m
Rated Power	5 MW	5 MW
Speed	6.9-12.1 rpm	5.9-14.8 rpm
Cut-in wind speed	3.5 m/s	3.5 m/s
Rated wind speed	13 m/s	12.5 m/s
Cut-out wind speed	30 m/s	25 m/s

The available electrical information of the offshore substation transformer and protections are given in Table B.2.

Table B.2. Available technical data for the OST and protections of Alpha Ventus OWPP. Source [198].

Offshore Substation Transformer (OST)	
Nominal Voltage	110/30 kV
Nominal Power	75 MVA
Manufacturer	AREVA
Protections	
Switchgear	110 kV GIS from AREVA
Neutral earthing transformer	Zig-zag
Fire extinguishing system	
Emergency generator	

Table B.3 and Table B.4 provide the technical information of the MVAC and HVAC submarine cable, respectively. The MVAC submarine cable is installed for the collection network while the HVAC is installed for the transmission system.

Table B.3. Available technical data of the MVAC submarine cables installed at Alpha Ventus OWPP for the collection network. Source [214].

MVAC submarine cable	
Nominal Voltage	30 kV
Number of cores	3 (Single 3-core submarine cable)
Core cross section	240 mm^2
Diameter	125 mm
Burial depth	0.6 m
Manufacturer	NSW (General Cable)

Table B.4. Available technical data of the HVAC submarine cable installed at Alpha Ventus OWPP for the transmission system. Source [214].

HVAC submarine cable	
Nominal Voltage	110 kV
Number of cores	3 (Single 3-core submarine cable)
Core cross section	240 mm^2
Cable length	60 km
Manufacturer	Prysmian

B.2 ABB 2.35 MVA Transformer Datasheet

Table B.5 gives the basic nameplate data of a 2.35 MVA Wind Turbine Transformer from ABB manufacturer. The parameters of the equivalent standard circuit at the nominal frequency and for a Y-connected transformer are given in Table B.6. Real values are given at the HV side of the transformer.

Table B.5. Basic nameplate data of a 2.35 MVA ABB Wind Turbine Transformer. Source [215].

ABB Transformer: Basic Nameplate Data	
Rated Power	2350 kVA
Load Losses (at rated power)	19800 W
No load Losses (at rated power)	4700 W
Short-circuit Impedance (at rated power)	9.5% at 690 V $U_x = 9.46\%$ $U_r = 0.84\%$
No load current (at rated power)	0.5% I_{rated}
Rated Voltage (HV)	30 kV
Rated current (HV Delta Connection)	45.23 A
Rated Voltage (LV)	690 V

Table B.6. Parameters of the equivalent standard circuit, given by ABB manufacturer. Source [215].

Real values	PU values
$R_{HV} = 1.77\,\Omega$	$R_{HV} = 0.0046$ pu
$R_{LV} = 1.45\,\Omega$	$R_{LV} = 0.0038$ pu
$X_{HV} = 18.12\,\Omega$	$X_{HV} = 0.0473$ pu
$X_{LV} = 18.12\,\Omega$	$X_{LV} = 0.0473$ pu
$R_{Fe} = 191489\,\Omega$	$R_{Fe} = 500$ pu
$X_{mu} = 83573\,\Omega$	$X_{mu} = 218.22$ pu

B.3   MVAC Submarine Cable of the Collection Network

This section presents supporting information for the parameterization of the FDPi model representing the collection network cables of the OWPP base scenario.

Table B.7 gives the constructional data of the Nexans 2XS2YRAA 18/30(36) kV three-core submarine cable. Table B.8, on the other hand, gives the electrical data for this cable. The information provided by these tables is taken from a datasheet given by Nexans.

Table B.7. Constructional data of Nexans 2XS2YRAA 18/30(36) kV submarine cable. Source [48].

	Constructional Data				
1.	Nominal cross-sectional area of conductor (mm^2)	240	6.	Bedding wall thickness (mm)	2
2.	Conductor copper round stranded diameter over conductor (mm)	18.6	7.	Armour steel wires round galvanized diameter (mm)	5.0
3.	Insulation XLPE wall thickness (mm)	8.0	8.	Serving bitumen fiber material and lime wash wall thickness (mm)	4.0
4.	Screen copper wires and counter helix cross-sectional area (mm^2)	25	9.	Outer diameter of cable (mm)	114
5.	Core sheath PE black	Wall thickness (mm)	2.5	10.	Cable weight (t/km)	22.0
		Diameter (mm)	43			

Table B.8. Electrical data of Nexans 2XS2YRAA 18/30(36) kV submarine cable. Source [48].

Electrical Data	
Conductor resistance DC 20ºC (Ω/km)	0.0754
Conductor resistance AC 90ºC (Ω/km)	0.10
Screen resistance 20ºC (Ω/km)	0.73
Capacitance (μF/km)	0.23
Inductance (mH/km)	0.35

Table B.9 gives information about the simplified geometrical and material properties of the submarine cable after the conversion procedure (detailed in section 6.4) is performed. Table B.10, on the other hand, gives information about the installation conditions, burial depth and surrounding medium properties.

Table B.9. Simplified geometrical and material parameters of the MVAC submarine cable for the parameterization of the collection network cables of the OWPP base scenario.

Layer	Parameters
1.	$r_1 = 9.3 \, \text{mm}$, $\rho_c = 2.0487 \cdot 10^{-8} \, \Omega\text{m}$, $\mu_{rc} = 1$
2.	$r_2 = 18.7894 \, \text{mm}$, $\mu_{rins1} = 1$, $\varepsilon_{rins1} = 2.9076$
3.	$r_3 = 19 \, \text{mm}$, $\rho_s = 1.825 \cdot 10^{-8} \, \Omega\text{m}$, $\mu_{rs} = 1$
4.	$r_4 = 21.5 \, \text{mm}$, $\mu_{rins2} = 1$, $\varepsilon_{rins2} = 2.3$
5.	$r_5 = 48 \, \text{mm}$, $\mu_{rins3} = 1$, $\varepsilon_{rins3} = 2.3$
6.	$r_6 = 53 \, \text{mm}$, $\rho_p = 18 \cdot 10^{-8} \, \Omega\text{m}$, $\mu_{rp} = 1$
7.	$r_7 = 57 \, \text{mm}$, $\mu_{rins4} = 1$, $\varepsilon_{rins4} = 2.1$

Table B.10. Installation conditions of the MVAC submarine cable for the parameterization of the collection network cables of the OWPP base scenario.

Installation conditions		
$\rho_{seabed} = 20 \, \Omega\text{m}$	$\mu_{rseabed} = 1$	$h_{burialdepth\_cc} = 0.6 \, \text{m}$

B.4   HVAC Submarine Cable of the Transmission System

This section presents supporting information for the parameterization of the FDPi model representing the transmission system cable of the OWPP base scenario.

Table B.11 gives the constructional data of the ABB HVAC 110(130) kV three-core submarine cable. Table B.12, on the other hand, gives the electrical data for this cable. The information provided by these tables is taken from a datasheet given by ABB.

Table B.11. Constructional data of ABB HVAC 110(130) kV three-core submarine cable. Source [193].

Constructional Data				
1.	Cross-section of conductor (mm^2)	240	5. Lead sheath thickness (mm)	2
2.	Diameter of conductor (mm)	18.1	6. Outer diameter of the cable (mm)	157
3.	Insulation thickness (mm)	15	7. Cable weight Aluminium (kg/m)	38
4.	Diameter over insulation (mm)	50.5	8. Cable weight Copper (kg/m)	42.5

Table B.12. Electrical data of ABB HVAC 110(130) kV three-core submarine cable. Source [193].

Electrical Data	
Capacitance (μF/km)	0.15
Inductance (mH/km)	0.43

Table B.13 gives information about the simplified geometrical and material properties of the submarine cable after the conversion procedure (detailed in Section 6.4) is performed. Table B.14, on the other hand, gives information about the installation conditions, burial depth and surrounding medium properties.

Table B.13. Simplified geometrical and material parameters of the HVAC submarine cable for the parameterization of the transmission system cable of the OWPP base scenario.

Layer	Parameters
1.	$r_1 = 9.05\,\mathrm{mm}$, $\rho_c = 1.8483 \cdot 10^{-8}\,\Omega\mathrm{m}$, $\mu_{rc} = 1$
2.	$r_2 = 26.45\,\mathrm{mm}$, $\mu_{rins1} = 1$, $\varepsilon_{rins1} = 2.8918$
3.	$r_3 = 28.45\,\mathrm{mm}$, $\rho_s = 22 \cdot 10^{-8}\,\Omega\mathrm{m}$, $\mu_{rs} = 1$
4.	$r_4 = 30.25\,\mathrm{mm}$, $\mu_{rins2} = 1$, $\varepsilon_{rins2} = 2.3$
5.	$r_5 = 67.2\,\mathrm{mm}$, $\mu_{rins3} = 1$, $\varepsilon_{rins3} = 2.3$
6.	$r_6 = 72.2\,\mathrm{mm}$, $\rho_p = 18 \cdot 10^{-8}\,\Omega\mathrm{m}$, $\mu_{rp} = 1$
7.	$r_7 = 78.5\,\mathrm{mm}$, $\mu_{rins4} = 1$, $\varepsilon_{rins4} = 2.1$

Table B.14. Installation conditions of the HVAC submarine cable for the parameterization of the transmission system cable of the OWPP base scenario.

Installation conditions		
$\rho_{seabed} = 20\,\Omega\mathrm{m}$	$\mu_{rseabed} = 1$	$h_{burialdepth\_tc} = 0.6\,\mathrm{m}$

Appendix C

Component Connection Method

The Component Connection Method (CCM) is basically a reformulation of the conventional state-space model [216]. Fig. C.1 shows a comparison between the modeling procedures of the general state-space representation and the CCM.

$$\frac{d}{dt}[x] = [A][x] + [B][u]$$
$$[y] = [C][x] + [D][u]$$

System State-Space Model

$$|[A] - [\lambda][I]| = 0$$

eig(A)=system poles

(a)

Composite Component
State-Space Model

$$\frac{d}{dt}[x] = [F][x] + [G][a]$$
$$[b] = [H][x] + [J][a]$$

$$\frac{d}{dt}[x_i] = [F_i][x_i] + [G_i][a_i]$$
$$[b_i] = [H_i][x_i] + [J_i][a_i]$$

i^{th} Component State-Space Model

$$[a] = [L_{11}][b] + [L_{12}][u]$$
$$[y] = [L_{21}][b] + [L_{22}][u]$$

Connection Matrices: $[L_{ij}]$
Linear algebraic

Modularity
Scalability

$$\frac{d}{dt}[x] = [A][x] + [B][u]$$
$$[y] = [C][x] + [D][u]$$

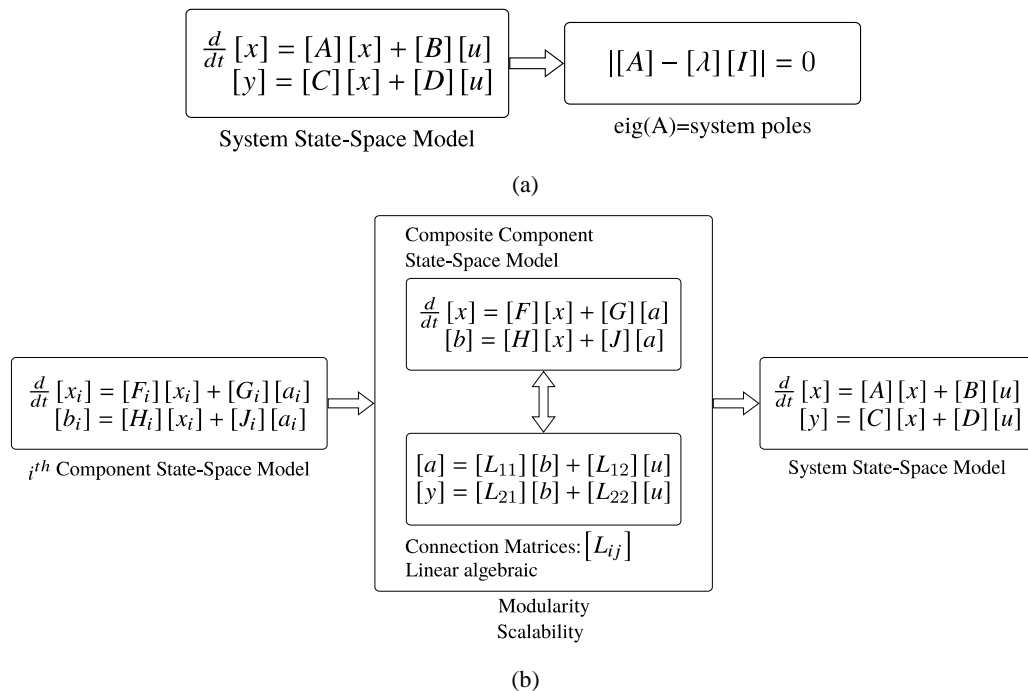System State-Space Model

(b)

Fig. C.1. Comparison between the modeling procedures of the general state-space representation and the Component Connection Method (CCM). (a) General state-space model. (b) CCM-based model. Source [199].

The component connection model of a linear dynamical system consists of a set of two vector matrix equations, which describe in a separate way the component dynamics and

component interconnections. Interconnections are linear algebraic and they are performed by using the well-known Kirchoff Voltage Law (KVL) and Kirchoff Current Law (KCL).

Let the ith component have input vector $[a_i]$, output vector $[b_i]$, and state vector $[x_i]$. The linear state model for the ith component is given by equation (C.1).

$$\frac{d}{dt}[x_i] = [F_i][x_i] + [G_i][a_i]$$
$$[b_i] = [H_i][x_i] + [J_i][a_i]$$

(C.1)

The composite component state model is constructed by stacking the $n-$ component equations together, as given by equation (C.2).

$$\frac{d}{dt}[x] = [F][x] + [G][a]$$
$$[b] = [H][x] + [J][a]$$

(C.2)

Being,

$$[F] = \begin{bmatrix} [F_1] & [0] & \cdots & [0] \\ [0] & [F_2] & \cdots & [0] \\ \vdots & \vdots & \ddots & \vdots \\ [0] & [0] & \cdots & [F_n] \end{bmatrix} \quad ; \quad [G] = \begin{bmatrix} [G_1] & [0] & \cdots & [0] \\ [0] & [G_2] & \cdots & [0] \\ \vdots & \vdots & \ddots & \vdots \\ [0] & [0] & \cdots & [G_n] \end{bmatrix}$$

(C.3)

$$[H] = \begin{bmatrix} [H_1] & [0] & \cdots & [0] \\ [0] & [H_2] & \cdots & [0] \\ \vdots & \vdots & \ddots & \vdots \\ [0] & [0] & \cdots & [H_n] \end{bmatrix} \quad ; \quad [J] = \begin{bmatrix} [J_1] & [0] & \cdots & [0] \\ [0] & [J_2] & \cdots & [0] \\ \vdots & \vdots & \ddots & \vdots \\ [0] & [0] & \cdots & [J_n] \end{bmatrix}$$

(C.4)

The interconnection of the components is given by equation (C.5).

$$[a] = [L_{11}][b] + [L_{12}][u]$$
$$[y] = [L_{21}][b] + [L_{22}][u]$$

(C.5)

Being,

$[u]$: system input vector.

$[y]$: system output vector.

$[L_{ij}]$: connection matrices.

Assuming that the composite component state vector $[x]$ is equal to the composite system state vector, then the CCM results in a composite system state model, if and only if the condition given by equation (C.6) is met.

$$\left(\left[I\right]-\left[L_{11}\right]\left[J\right]\right)^{-1}\neq 0 \tag{C.6}$$

The composite system state model is given by the well-known equation (C.7).

$$\frac{d}{dt}\left[x\right]=\left[A\right]\left[x\right]+\left[B\right]\left[u\right]$$
$$\left[y\right]=\left[C\right]\left[x\right]+\left[D\right]\left[u\right] \tag{C.7}$$

The matrices defining the system state-space model are given by equations (C.8) to (C.11).

$$\left[A\right]=\left[F\right]+\left[G\right]\left(\left[I\right]-\left[L_{11}\right]\left[J\right]\right)^{-1}\left[L_{11}\right]\left[H\right] \tag{C.8}$$

$$\left[B\right]=\left[G\right]\left(\left[I\right]-\left[L_{11}\right]\left[J\right]\right)^{-1}\left[L_{12}\right] \tag{C.9}$$

$$\left[C\right]=\left[L_{21}\right]\left(\left[I\right]-\left[J\right]\left[L_{11}\right]\right)^{-1}\left[H\right] \tag{C.10}$$

$$\left[D\right]=\left[L_{21}\right]\left[J\right]\left(\left[I\right]-\left[L_{11}\right]\left[J\right]\right)^{-1}\left[L_{12}\right]+\left[L_{22}\right] \tag{C.11}$$

The reader is suggested to see references [199,216–218] for detailed information about CCM.

Appendix D

Modal Analysis Overview

Due to the large size and complexity of power systems, it is often necessary to develop reduced-order models for dynamic stability studies by preserving only a few modes. The appropriate definition and determination as to which state variables significantly participate in the selected modes become very important. This requires a tool for identifying the state variables that have significant participation in a selected mode. Verghese et al. [219,220] have suggested a related but dimensionless measure of state participation called participation factors. The following is a brief description of modal analysis. The reader is suggested to review references [200,219–221] for details and examples.

D.1   Eigenvalues

The eigenvalues of the system matrix $[A]$ are the roots of the characteristic equation, equation (D.1).

$$\left\| [A] - [\lambda][I] \right\| = 0 \tag{D.1}$$

Considering a pair of complex conjugate eigenvalues $\lambda_{1,2} = \alpha \pm j\beta$, real and imaginary parts are given by equations (D.2) and (D.3).

$$\alpha = -\zeta \omega_0 \tag{D.2}$$

$$\beta = \omega_d = \omega_0 \sqrt{1 - \zeta^2} \tag{D.3}$$

The undamped frequency ω_0 is given by equation (D.4). The frequency ω_0 is also called the frequency of resonance. However, the frequency that can be observed during a transient is the damped frequency ω_d. The damped frequency depends on the damping factor ζ, as

given by equation (D.3). The frequency of resonance coincides with the damped frequency only if $\alpha = 0$.

$$\omega_0 = \sqrt{\alpha^2 + \beta^2} \tag{D.4}$$

The damping factor ζ is given by equation (D.5). The damping factor is positive if the mode is stable, $\alpha < 0$.

$$\zeta = -\frac{\alpha}{\omega_0} \tag{D.5}$$

D.2 Eigenvectors

For each eigenvalue λ_i there exists a right eigenvector $[v_i]$ and a left eigenvector $[w_i]$, as given by equations (D.6) and (D.7) [200]. If λ_i is complex, then $[v_i]$ and $[w_i]$ have complex entries.

$$[A][v_i] = \lambda_i [v_i] \tag{D.6}$$

$$[w_i]^T [A] = [w_i]^T \lambda_i \tag{D.7}$$

Right- and left eigenvectors have the special property of being orthogonal, equations (D.8) and (D.9) are fulfilled.

$$[w_i]^T [v_i] \neq 0 \tag{D.8}$$

$$[w_i]^T [v_j] = 0 \qquad ; \qquad i \neq j \tag{D.9}$$

D.3 Participation Factor

Participation factor analysis aids in the identification of how each state variable affects a given eigenvalue [221]. A participation factor is a sensitivity measure of an eigenvalue to a diagonal entry of the system matrix $[A]$. This is given by equation (D.10).

$$p_{ki} = \frac{\partial \lambda_i}{\partial a_{kk}} = \frac{w_{ki} v_{ki}}{[w_i]^T [v_i]} \tag{D.10}$$

Being,

$\lambda_i : i^{th}$ system eigenvalue.

a_{kk} : diagonal entry of the system $[A]$ matrix.

$w_{ki} : k^{th}$ entry of the left eigenvector associated with the ith eigenvalue.

$v_{ki} : k^{th}$ entry of the right eigenvector associated with the ith eigenvalue.

p_{ki} : participation factor relating the kth state variable to the ith eigenvalue.

The sum of all participation factors associated with a given eigenvalue is equal to one [221], equation (D.11). This property is useful, since all participation factors lie on a scale from zero to one.

$$\sum_{k=1}^{n} p_{ki} = 1 \tag{D.11}$$

The eigenvectors corresponding to a complex eigenvalue will have complex elements. Hence, p_{ki} can be defined by equation (D.12) for this case [221].

$$p_{ki} = \frac{|v_{ki}||w_{ki}|}{\sum_{k=1}^{n} |v_{ki}||w_{ki}|} \tag{D.12}$$

The participation matrix $[P]$ can be computed according to equation (D.13).

$$[P] = [W]^T \odot [V] \tag{D.13}$$

Being,

$$[V] = \left[[v_1] \quad [v_2] \quad \cdots \quad [v_n] \right] \tag{D.14}$$

$$[W] = \left[[w_1] \quad [w_2] \quad \cdots \quad [w_n] \right] \tag{D.15}$$

Operator $\odot$ is the element-by-element product.